

1

2

3

4

5

Simultaneous Measurement of Oscillation Parameters in Beam and Atmospheric Neutrino Data from Tokai-to-Kamioka and Super-Kamiokande Experiments

6

Daniel Robert Clement Barrow

7

8

Magdalen College,
Oxford University

9

Version 1.1

10

A Dissertation Submitted to Oxford University
11 for the Degree of Doctor of Philosophy

13 **Simultaneous Measurement of**

14 **Oscillation Parameters in Beam and**

15 **Atmospheric Neutrino Data from**

16 **Tokai-to-Kamioka and**

17 **Super-Kamiokande Experiments**

18 *Abstract*

19 Lorem ipsum dolor sit amet, consectetur adipiscing elit, sed do eiusmod tempor incididunt ut labore et dolore magna aliqua. Nulla aliquet porttitor lacus luctus accumsan tortor posuere. Pulvinar neque laoreet suspendisse interdum. Sem viverra aliquet eget sit. Nunc sed velit dignissim sodales ut eu sem integer vitae. At erat pellentesque adipiscing commodo elit at imperdiet dui accumsan. Fames ac turpis egestas integer eget aliquet nibh. Scelerisque eu ultrices vitae auctor eu augue. Purus non enim praesent elementum facilisis leo vel. Sollicitudin nibh sit amet commodo. Vitae auctor eu augue ut. Vel quam elementum pulvinar etiam. A condimentum vitae sapien pellentesque habitant morbi tristique senectus. Viverra accumsan in nisl nisi scelerisque eu ultrices. Sed viverra ipsum nunc aliquet bibendum enim.

32 Declaration

33 This dissertation is the result of my own work, except where ex-
34 plicit reference is made to the work of others, and has not been sub-
35 mitted for another qualification to this or any other university. This
36 dissertation does not exceed the word limit for the respective Degree
37 Committee.

38 Daniel Robert Clement Barrow

39 ©The copyright of this thesis rests with the author and is made available under a Creative
40 Commons Attribution Non-Commercial No Derivatives licence. Researchers are free to copy,
41 distribute or transmit the thesis on the condition that they attribute it, that they do not use
42 it for commercial purposes and that they do not alter, transform or build upon it. For any
43 reuse or redistribution, researchers must make clear to others the licence terms of this work.

44

Acknowledgements

45 at pretium nibh ipsum. Eget nunc scelerisque viverra mauris in aliquam. Arcu vitae
46 elementum curabitur vitae nunc sed velit dignissim. Sed arcu non odio euismod lacinia
47 at quis risus sed. Vitae tempus quam pellentesque nec nam aliquam sem et tortor.
48 Viverra aliquet eget sit amet tellus cras adipiscing. Purus sit amet luctus venenatis
49 lectus magna. In aliquam sem fringilla ut morbi tincidunt augue. Fermentum dui
50 faucibus in ornare. Aliquam malesuada bibendum arcu vitae elementum curabitur
51 vitae nunc sed.

52 Ultricies leo integer malesuada nunc vel risus commodo. Tellus cras adipiscing
53 enim eu turpis egestas pretium. Dictumst quisque sagittis purus sit amet volutpat
54 consequat mauris nunc. Vitae congue mauris rhoncus aenean vel elit scelerisque
55 mauris pellentesque. Vel facilisis volutpat est velit egestas dui id ornare. Suscipit
56 adipiscing bibendum est ultricies. At in tellus integer feugiat scelerisque varius
57 morbi enim. Cras semper auctor neque vitae tempus. Commodo sed egestas egestas
58 fringilla phasellus faucibus. Cras pulvinar mattis nunc sed blandit. Pretium viverra
59 suspendisse potenti nullam ac tortor vitae. Purus sit amet volutpat consequat. Orci
60 sagittis eu volutpat odio facilisis mauris. Sit amet massa vitae tortor condimentum
61 lacinia quis. Commodo sed egestas egestas fringilla phasellus. Sed libero enim sed
62 faucibus turpis. Vitae tempus quam pellentesque nec.

63 Blandit massa enim nec dui. Viverra tellus in hac habitasse platea dictumst vestibulu-
64 lum. Bibendum enim facilisis gravida neque convallis. Sagittis nisl rhoncus mattis
65 rhoncus urna neque. Nisl rhoncus mattis rhoncus urna neque. Ac tortor vitae purus
66 faucibus ornare. Aenean sed adipiscing diam donec adipiscing tristique risus. Sapien
67 nec sagittis aliquam malesuada bibendum. Et leo duis ut diam quam nulla. Tellus
68 rutrum tellus pellentesque eu tincidunt tortor aliquam nulla facilisi.

Contents

1	Introduction	1
2	Neutrino Oscillation Physics	2
2.1	Discovery of Neutrinos	2
2.2	Theory of Neutrino Oscillation	4
2.2.1	Three Flavour Oscillations	4
2.2.2	The MSW Effect	8
2.3	Neutrino Oscillation Measurements	9
2.3.1	Solar Neutrinos	11
2.3.2	Atmospheric Neutrinos	13
2.3.3	Accelerator Neutrinos	16
2.3.4	Reactor Neutrinos	18
2.4	Summary	20
3	T2K and SK Experiment Overview	23
3.1	The Super-Kamiokande Experiment	23
3.1.1	The SK Detector	24
3.1.2	Calibration	28
3.1.3	Data Acquisition and Triggering	31
3.1.4	Cherenkov Radiation	33
3.2	The Tokai to Kamioka Experiment	35
3.2.1	The Neutrino Beam	37
3.2.2	The Near Detector at 280m	40
3.2.2.1	Fine Grained Detectors	43
3.2.2.2	Time Projection Chambers	44

93	3.2.2.3	π^0 Detector	46
94	3.2.2.4	Electromagnetic Calorimeter	46
95	3.2.2.5	Side Muon Range Detector	48
96	3.2.3	The Interactive Neutrino GRID	48
97	4	Bayesian Statistics and Markov Chain Monte Carlo Techniques	50
98	4.1	Bayesian Statistics	51
99	4.2	Monte Carlo Simulation	52
100	4.2.1	Markov Chain Monte Carlo	53
101	4.2.2	Metropolis-Hastings Algorithm	56
102	4.2.3	MCMC Optimisation	58
103	4.3	Understanding the MCMC Results	61
104	4.3.1	Marginalisation	62
105	4.3.2	Parameter Estimation and Credible Intervals	63
106	4.3.3	Bayesian Model Comparisons	65
107	4.3.4	Comparison of MCMC Output to Expectation	66
108	5	Simulation, Reconstruction, and Event Reduction	68
109	5.1	Simulation	68
110	5.2	Event Reconstruction at SK	73
111	5.3	Event Reduction at SK	84
112	6	Sample Selections and Systematics	90
113	6.1	Atmospheric Samples	92
114	6.2	Near Detector Beam Samples	99
115	6.3	Far Detector Beam Samples	102
116	6.4	Systematic Uncertainties	107
117	6.4.1	Beam Flux	107
118	6.4.2	Atmospheric Flux	109

119	6.4.3	Neutrino Interaction	110
120	6.4.4	Near Detector	116
121	6.4.5	Far Detector	118
122	6.4.5.1	Beam Samples	119
123	6.4.5.2	Atmospheric Samples	122
124	6.4.5.3	Correlated Detector Model	124
125	7	Oscillation Probability Calculation	131
126	7.1	Overview	132
127	7.2	Treatment of Fast Oscillations	140
128	7.3	Calculation Engine	146
129	7.4	Matter Density Profile	149
130	7.5	Production Height Averaging	155
131	Bibliography		159
132	List of Figures		172
133	List of Tables		183

¹³⁵ **Chapter 1**

¹³⁶ **Introduction**

¹³⁷ **Chapter 2**

¹³⁸ **Neutrino Oscillation Physics**

¹³⁹ When first proposed, neutrinos were expected to be massless fermions that only in-
¹⁴⁰ teract through weak and gravitational forces. This meant they were very difficult to
¹⁴¹ detect as they can pass through significant amounts of matter without interacting. De-
¹⁴² spite this, experimental neutrino physics has developed with many different detection
¹⁴³ techniques and neutrino sources being used today. In direct tension with standard
¹⁴⁴ model physics, neutrinos have been determined to oscillate between different lepton
¹⁴⁵ flavours, requiring them to have mass.

¹⁴⁶ The observation techniques which lead to the discovery of the neutrino are doc-
¹⁴⁷ umented in section 2.1. The theory underpinning neutrino oscillation is described
¹⁴⁸ in section 2.2 and includes the approximations which can be made to simplify the
¹⁴⁹ understanding of neutrino oscillation in the two-flavour approximation. Past, current,
¹⁵⁰ and future neutrino experiments are detailed in section 2.3, including the reactor,
¹⁵¹ atmospheric, and long-baseline accelerator neutrino sources that have been used to
¹⁵² successfully constrain oscillation parameters. Finally, the current state of oscillation
¹⁵³ parameter measurements are summarised in section 2.4.

¹⁵⁴ **2.1 Discovery of Neutrinos**

¹⁵⁵ At the start of the 20th century, the electrons emitted from the β -decay of the nucleus
¹⁵⁶ were found to have a continuous energy spectrum [1,2]. This observation seemingly
¹⁵⁷ broke the energy conservation invoked within that period's nuclear models. Postulated

158 in 1930 by Pauli as the solution to this problem, the neutrino (originally termed
159 “neutron”) was theorized to be an electrically neutral spin-1/2 fermion with a mass of
160 the same order of magnitude as the electron [3]. This neutrino was to be emitted with
161 the electron in β -decay to alleviate the apparent breaking of energy conservation. As a
162 predecessor of today’s weak interaction model, Fermi’s theory of β -decay developed
163 the understanding by coupling the four constituent particles; electron, proton, neutron,
164 and neutrino, into a consistent model [4].

165 Whilst Pauli was not convinced of the ability to detect neutrinos, the first observa-
166 tions of the particle were made in the mid-1950s when neutrinos from a reactor were
167 observed via the inverse β -decay (IBD) process, $\bar{\nu}_e + p \rightarrow n + e^+$ [5, 6]. The detector
168 consisted of two parts: a neutrino interaction medium and a liquid scintillator. The
169 interaction medium was built from two water tanks. These were loaded with cadmium
170 chloride to allow increased efficiency of neutron capture. The positron emitted from
171 IBD annihilates, $e^+ + e^- \rightarrow 2\gamma$, generating a prompt signal and the neutron is captured
172 on the cadmium via $n + {}^{108}Cd \rightarrow {}^{109*}Cd \rightarrow {}^{109}Cd + \gamma$, producing a delayed signal. An
173 increase in the coincidence rate was observed when the reactor was operating which
174 was interpreted as interactions from neutrinos generated in the reactor.

175 After the discovery of the ν_e , the natural question of how many flavours of neutrino
176 exist was asked. In 1962, a measurement of the ν_μ was conducted at the Brookhaven
177 National Laboratory [7]. A proton beam was directed at a beryllium target, generating
178 a π -dominated beam which then decayed via $\pi^\pm \rightarrow \mu^\pm + (\nu_\mu, \bar{\nu}_\mu)$, and the subsequent
179 interactions of the ν_μ were observed. As the subsequent interaction of the neutrino
180 generates muons rather than electrons, it was determined the ν_μ was fundamentally
181 different from ν_e . The final observation to be made was that of the ν_τ from the DONUT
182 experiment [8]. Three neutrinos seem the obvious solution as it mirrors the known
183 number of charged lepton (as they form weak isospin doublets) but there could be

¹⁸⁴ evidence of more. Several neutrino experiments have found anomalous results [9, 10]
¹⁸⁵ which could be attributed to sterile neutrinos. However, cosmological observations
¹⁸⁶ indicate the number of neutrino species $N_{eff} = 2.99 \pm 0.17$ [11], as measured from
¹⁸⁷ the cosmic microwave background power spectrum, and LEP measured the number
¹⁸⁸ of active neutrino flavours to be $N_\nu 2.9840 \pm 0.0082$ [12] from measurements of the
¹⁸⁹ Z -decay width.

¹⁹⁰ 2.2 Theory of Neutrino Oscillation

¹⁹¹ As direct evidence of beyond Standard Model physics, a neutrino generated with
¹⁹² lepton flavour α can change into a different lepton flavour β after propagating some
¹⁹³ distance. This phenomenon is called neutrino oscillation and requires that neutrinos
¹⁹⁴ must have a non-zero mass (as seen in subsection 2.2.1). This observation is direct
¹⁹⁵ evidence of beyond standard model physics. This behaviour has been characterised
¹⁹⁶ by the Pontecorvo-Maki-Nakagawa-Sakata (PMNS) [13–15] mixing matrix which
¹⁹⁷ describes how the flavour and mass of neutrinos are associated. This is analogous to
¹⁹⁸ the Cabibbo-Kobayashi-Maskawa (CKM) [16] matrix measured in quark physics.

¹⁹⁹ 2.2.1 Three Flavour Oscillations

²⁰⁰ The PMNS parameterisation defines three flavour eigenstates, ν_e , ν_μ and ν_τ (indexed
²⁰¹ ν_α), which are eigenstates of the weak interaction and three mass eigenstates, ν_1 , ν_2 and
²⁰² ν_3 (indexed ν_i). Each mass eigenstate is the superposition of all three flavour states,

$$|\nu_i\rangle = \sum_\alpha U_{\alpha i} |\nu_\alpha\rangle. \quad (2.1)$$

203 Where U is the PMNS matrix which is unitary and connects the mass and flavour

204 eigenstates.

205 The weak interaction couples to flavour eigenstates so neutrinos interact with

206 leptons of the same flavour. The propagation of a neutrino flavour eigenstate, in a

207 vacuum, can be re-written as a plane-wave solution to the time-dependent Schrödinger

208 equation,

$$|\nu_\alpha(t)\rangle = \sum_i U_{\alpha i}^* |\nu_i\rangle e^{-i\phi_i}. \quad (2.2)$$

209 The probability of observing a neutrino of flavour eigenstate β from one which

210 originated as flavour α can be calculated as,

$$P(\nu_\alpha \rightarrow \nu_\beta) = |\langle \nu_\beta | \nu_\alpha(t) \rangle|^2 = \sum_{i,j} U_{\alpha i}^* U_{\beta i} U_{\alpha j} U_{\beta j}^* e^{-i(\phi_j - \phi_i)} \quad (2.3)$$

211 The ϕ_i term can be expressed in terms of the energy, E_i , and magnitude of the

212 three momenta, p_i , of the neutrino, $\phi_i = E_i t - p_i x$ (t and x being time and position

213 coordinates). Therefore,

$$\phi_j - \phi_i = E_j t - E_i t - p_j x + p_i x. \quad (2.4)$$

214 For a relativistic particle, $E_i \gg m_i$,

$$p_i = \sqrt{E_i^2 - m_i^2} \approx E_i - \frac{m_i^2}{2E_i}. \quad (2.5)$$

215 Making the approximations that neutrinos are relativistic, the mass eigenstates
216 were created with the same energy and that $x = L$, where L is the distance traveled by
217 the neutrino, Equation 2.4 then becomes

$$\phi_j - \phi_i = \frac{\Delta m_{ij}^2 L}{2E}, \quad (2.6)$$

218 where $\Delta m_{ij}^2 = m_j^2 - m_i^2$. This, combined with further use of unitarity relations
219 results in Equation 2.3 becoming

$$P(\nu_\alpha \rightarrow \nu_\beta) = \delta_{\alpha\beta} - 4 \sum_{i>j} \Re \left(U_{\alpha i}^* U_{\beta i} U_{\alpha j} U_{\beta j}^* \right) \sin^2 \left(\frac{\Delta m_{ij}^2 L}{4E} \right) + (-) 2 \sum_{i>j} \Im \left(U_{\alpha i}^* U_{\beta i} U_{\alpha j} U_{\beta j}^* \right) \sin \left(\frac{\Delta m_{ij}^2 L}{2E} \right). \quad (2.7)$$

220 Where $\delta_{\alpha\beta}$ is the Kronecker delta function and the negative sign on the last term is
221 included for the oscillation probability of antineutrinos.

222 Typically, the PMNS matrix is parameterised into three mixing angles, a charge
223 parity (CP) violating phase δ_{CP} , and two Majorana phases $\alpha_{1,2}$,

$$U = \underbrace{\begin{pmatrix} 1 & 0 & 0 \\ 0 & c_{23} & s_{23} \\ 0 & -s_{23} & c_{23} \end{pmatrix}}_{\text{Atmospheric, Accelerator}} \underbrace{\begin{pmatrix} c_{13} & 0 & s_{13}e^{-i\delta_{CP}} \\ 0 & 1 & 0 \\ -s_{13}e^{-i\delta_{CP}} & 0 & c_{13} \end{pmatrix}}_{\text{Reactor, Accelerator}} \underbrace{\begin{pmatrix} c_{12} & s_{12} & 0 \\ -s_{12} & c_{12} & 0 \\ 0 & 0 & 1 \end{pmatrix}}_{\text{Reactor, Solar}} \underbrace{\begin{pmatrix} e^{i\alpha_1/2} & 0 & 0 \\ 0 & e^{i\alpha_2/2} & 0 \\ 0 & 0 & 1 \end{pmatrix}}_{\text{Majorana}}. \quad (2.8)$$

²²⁴ Where $s_{ij} = \sin(\theta_{ij})$ and $c_{ij} = \cos(\theta_{ij})$. The oscillation parameters are often
²²⁵ grouped; (1,2) as “solar”, (2,3) as “atmospheric” and (1,3) as “reactor”. Many
²²⁶ neutrino experiments aim to measure the PMNS parameters from a wide array of
²²⁷ origins, as is the purpose of this thesis.

²²⁸ The Majorana phase, $\alpha_{1,2}$, included within the fourth matrix in Equation 2.8 is only
²²⁹ included for completeness. For an oscillation analysis experiment, any terms contain-
²³⁰ ing this phase disappear due to taking the expectation value of the PMNS matrix.
²³¹ Measurements of these phases are typically performed by experiments searching for
²³² neutrino-less double β -decay [17].

²³³ A two flavour approximation can be obtained when one assumes the third mass
²³⁴ eigenstate is degenerate with another. As discussed in section 2.3, it is found that
²³⁵ $\Delta m_{21}^2 \ll |\Delta m_{31}^2|$. This results in the two flavour approximation being reasonable for
²³⁶ understanding the features of the oscillation. In this two flavour case, the mixing
²³⁷ matrix becomes,

$$U_{2 \text{ Flav.}} = \begin{pmatrix} \cos(\theta) & \sin(\theta) \\ -\sin(\theta) & \cos(\theta) \end{pmatrix}. \quad (2.9)$$

²³⁸ This culminates in the oscillation probability,

$$\begin{aligned} P(\nu_\alpha \rightarrow \nu_\alpha) &= 1 - \sin^2(2\theta) \sin^2\left(\frac{\Delta m^2 L}{4E}\right), \\ P(\nu_\alpha \rightarrow \nu_\beta) &= \sin^2(2\theta) \sin^2\left(\frac{\Delta m^2 L}{4E}\right). \end{aligned} \quad (2.10)$$

²³⁹ Where $\alpha \neq \beta$. For a fixed neutrino energy, the oscillation probability is a sinusoidal
²⁴⁰ function depending upon the distance over which the neutrino propagates. The
²⁴¹ frequency and amplitude of oscillation are dependent upon $\Delta m^2/4E$ and $\sin^2 2\theta$,
²⁴² respectively. The oscillation probabilities presented thus far assume $c = 1$, where
²⁴³ c is the speed of light in vacuum. In more familiar units, the maximum oscillation
²⁴⁴ probability for a fixed value of θ is given at $L[km]/E[GeV] \sim 1.27/\Delta m^2$. It is this
²⁴⁵ calculation that determines the best L/E value for a given experiment to be designed
²⁴⁶ around for measurements of a specific value of Δm^2 .

²⁴⁷ 2.2.2 The MSW Effect

²⁴⁸ The theory of neutrino oscillation in a vacuum has been described in subsection 2.2.1.
²⁴⁹ However, the beam neutrinos and atmospheric neutrinos originating from below the
²⁵⁰ horizon propagate through matter in the Earth. The coherent scattering of neutrinos
²⁵¹ from a material target modifies the Hamiltonian of the system. This results in a change
²⁵² in the oscillation probability. Notably, charged current scattering ($\nu_e + e^- \rightarrow \nu_e + e^-$,
²⁵³ propagated by a W boson) only affects electron neutrinos whereas the neutral current
²⁵⁴ scattering ($\nu_l + l^- \rightarrow \nu_l + l^-$, propagated by a Z^0 boson) interacts through all neutrino
²⁵⁵ flavours equally. In the two-flavour approximation, the effective mixing parameter
²⁵⁶ becomes

$$\sin^2(2\theta) \rightarrow \sin^2(2\theta_m) = \frac{\sin^2(2\theta)}{(A/\Delta m^2 - \cos(2\theta))^2 + \sin^2(2\theta)}, \quad (2.11)$$

where $A = 2\sqrt{2}G_F N_e E$, N_e is the electron density of the medium and G_F is Fermi's constant. It is clear to see that there exists a value of $A = \Delta m^2 \cos(2\theta)$ for $\Delta m^2 > 0$ which results in a divergent mixing parameter. This resonance is termed the Mikheyev-Smirnov-Wolfenstein (MSW) effect (or more colloquially, the matter resonance) which regenerates the electron neutrino component of the neutrino flux [18–20]. The density at which the resonance occurs is given by

$$N_e = \frac{\Delta m^2 \cos(2\theta)}{2\sqrt{2}G_F E}. \quad (2.12)$$

At densities lower than this critical value, the oscillation probability will be much closer to that of vacuum oscillation. For antineutrinos, $N_e \rightarrow -N_e$ [21]. The resonance occurring from the MSW effect depends on the sign of Δm^2 . Therefore, any neutrino oscillation experiment which observes neutrinos and antineutrinos which have propagated through matter can have some sensitivity to the ordering of the neutrino mass eigenstates.

2.3 Neutrino Oscillation Measurements

As evidence of beyond standard model physics, the 2015 Nobel Prize in Physics was awarded to the Super-Kamiokande (SK) [22] and Sudbury Neutrino Observatory (SNO) [23] collaborations for the first definitive observation of solar and atmospheric

²⁷³ neutrino oscillation [24]. Since then, the field has seen a wide array of oscillation
²⁷⁴ measurements from a variety of neutrino sources. As seen in subsection 2.2.1, the
²⁷⁵ neutrino oscillation probability is dependent on the ratio of the propagation baseline, L ,
²⁷⁶ to the neutrino energy, E . It is this ratio that determines the type of neutrino oscillation
²⁷⁷ a particular experiment is sensitive to.

²⁷⁸ As illustrated in Figure 2.1, there are many neutrino sources that span a wide
²⁷⁹ range of energies. The least energetic neutrinos are from diffuse supernovae and
²⁸⁰ terrestrial neutrinos at $O(1)$ MeV whereas the most energetic neutrinos originate from
²⁸¹ atmospheric and galactic neutrinos of $> O(1)$ TeV.

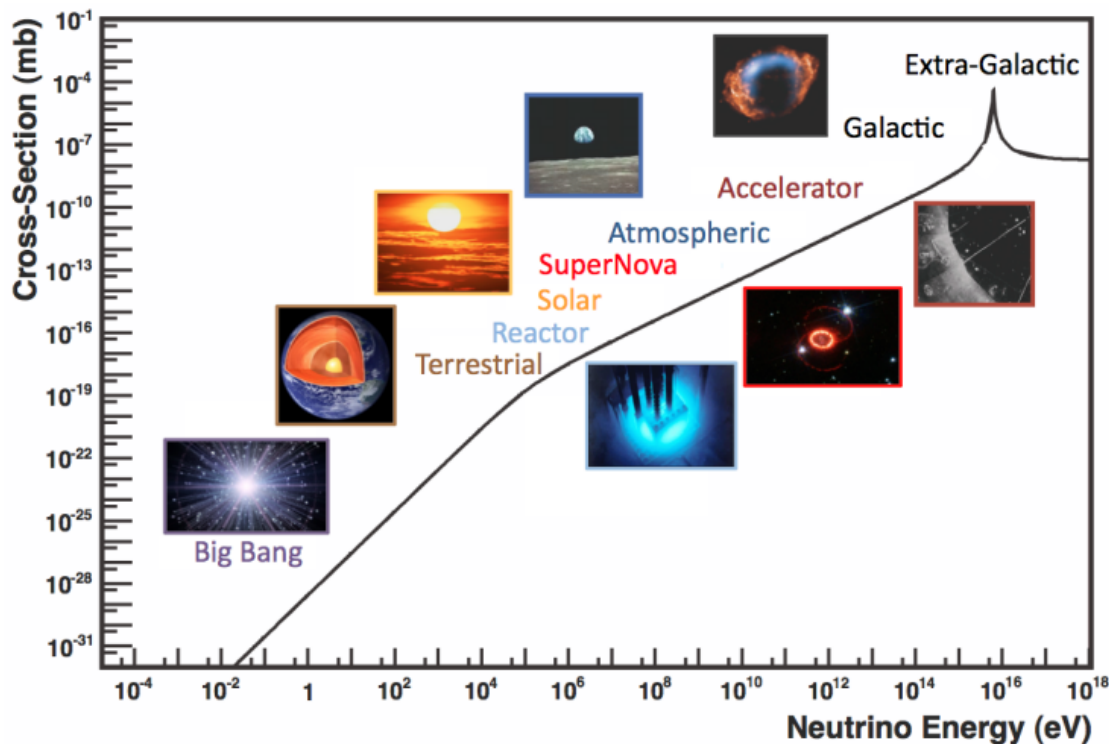


Figure 2.1: The cross-section of neutrinos from various natural and man-made sources as a function of neutrino energy. Taken from [25]

²⁸² 2.3.1 Solar Neutrinos

²⁸³ Solar neutrinos are emitted from fusion reaction chains at the center of the Sun. The
²⁸⁴ solar neutrino flux, given as a function of neutrino energy for different fusion and
²⁸⁵ decay chains, is illustrated in Figure 2.2. Whilst proton-proton fusion generates the
²⁸⁶ largest flux of neutrinos, the neutrinos are of low energy and are difficult to reconstruct
²⁸⁷ due to the IBD interaction threshold of 1.8MeV. Consequently, most experiments focus
²⁸⁸ on the neutrinos from the decay of 8B (via $^8B \rightarrow ^8Be^* + e^+ + \nu_e$), which are higher
²⁸⁹ energy.

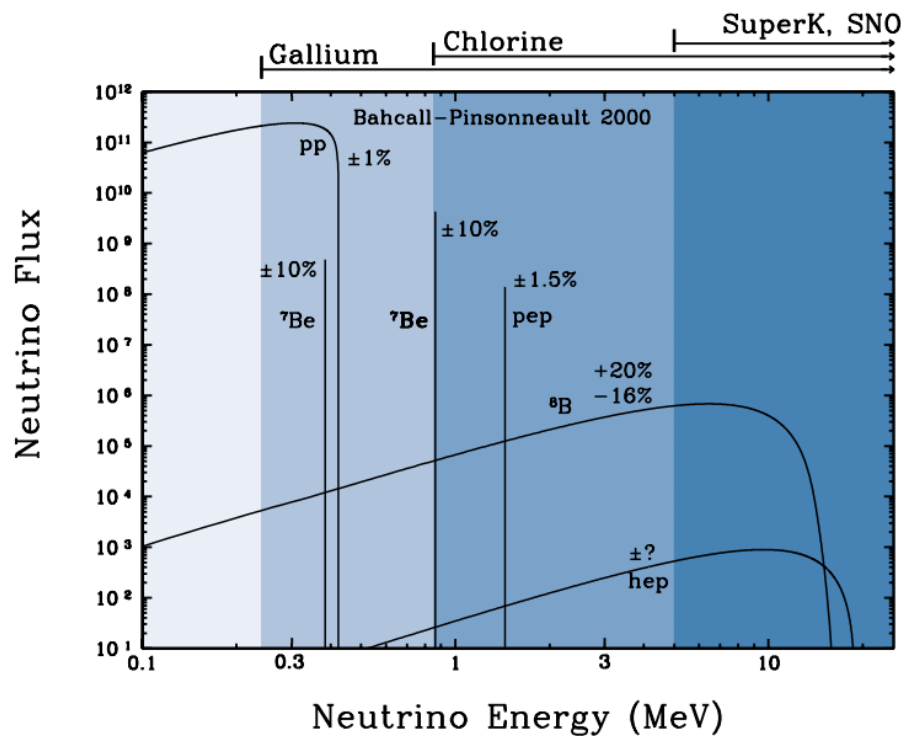
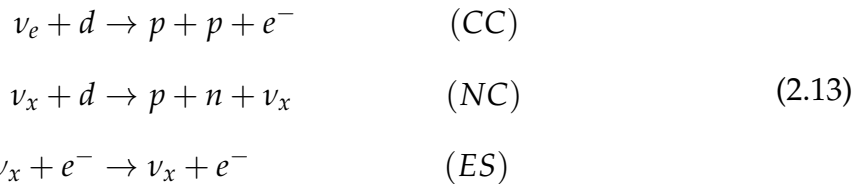


Figure 2.2: The solar neutrino flux as a function of neutrino energy for various fusion reactions and decay chains as predicted by the Standard Solar Model. Taken from [26].

²⁹⁰ The first measurements of solar neutrinos observed a significant reduction in the
²⁹¹ event rate compared to predictions from the Standard Solar Model [27, 28]. The
²⁹² proposed solution to this “solar neutrino problem” was $\nu_e \leftrightarrow \nu_\mu$ oscillations in a

²⁹³ precursory version of the PMNS model [29]. The Kamiokande [30], Gallex [31] and
²⁹⁴ Sage [32] experiments confirmed the ~ 0.5 factor deficit of solar neutrinos.

²⁹⁵ The conclusive solution to this problem was determined by the SNO collaboration
²⁹⁶ [33]. Using a deuterium water target to observe 8B neutrinos, the event rate of charged
²⁹⁷ current (CC), neutral current (NC), and elastic scattering (ES) interactions (Given in
²⁹⁸ Equation 2.13) was simultaneously measured. CC events can only occur for electron
²⁹⁹ neutrinos, whereas the NC channel is agnostic to neutrino flavour, and the ES reaction
³⁰⁰ has a slight excess sensitivity to electron neutrino interactions. This meant that there
³⁰¹ were direct measurements of the ν_e and ν_x neutrino flux. It was concluded that the
³⁰² CC and ES interaction rates were consistent with the deficit previously observed.
³⁰³ Most importantly, the NC reaction rate was only consistent with the others under the
³⁰⁴ hypothesis of flavour transformation.



³⁰⁵ Many experiments have since measured the neutrino flux of different interaction
³⁰⁶ chains within the sun [34–36]. The most recent measurement was that of CNO neutrinos
³⁰⁷ which were recently observed with 5σ significance by the Borexino collaboration.
³⁰⁸ Future neutrino experiments aim to further these spectroscopic measurements of
³⁰⁹ different fusion chains within the Sun [37–39]. Solar neutrinos act as an irreducible
³¹⁰ background for dark matter experiments like DARWIN but oscillation parameter
³¹¹ measurements can be made [40].

³¹² 2.3.2 Atmospheric Neutrinos

- ³¹³ The interactions of primary cosmic ray protons in Earth's upper atmosphere generate
³¹⁴ showers of energetic hadrons. These are mostly pions and kaons which when they
³¹⁵ decay produce a natural source of neutrinos spanning energies of MeV to TeV [41].
³¹⁶ The main decay is via

$$\begin{aligned} \pi^\pm &\rightarrow \mu^\pm + (\nu_\mu, \bar{\nu}_\mu) \\ \mu^\pm &\rightarrow e^\pm + (\nu_e, \bar{\nu}_e) + (\nu_\mu, \bar{\nu}_\mu) \end{aligned} \tag{2.14}$$

³¹⁷ such that for a single pion decay, three neutrinos are typically produced. The
³¹⁸ atmospheric neutrino flux energy spectra as predicted by the Bartol [42], Honda
³¹⁹ [43–45], and FLUKA [46] models are illustrated in Figure 2.3. The flux distribution
³²⁰ peaks at an energy of $O(10)\text{GeV}$. The uncertainties associated with these models
³²¹ are dominated by the hadronic production of kaon and pions as well as the primary
³²² cosmic flux.

³²³ Unlike long-baseline experiments which have a fixed baseline, the distance at-
³²⁴ mospheric neutrinos propagate is dependent upon the zenith angle at which they
³²⁵ interact. This is illustrated in Figure 2.4. Neutrinos that are generated directly above
³²⁶ the detector ($\cos(\theta) = 1.0$) have a baseline equivalent to the height of the atmosphere
³²⁷ whereas neutrinos that interact directly below the detector ($\cos(\theta) = -1.0$) have to
³²⁸ travel a length equal to the diameter of the Earth. This means atmospheric neutrinos
³²⁹ have a baseline that varies from $O(20)\text{km}$ to $O(6 \times 10^3)\text{km}$. Any neutrino generated
³³⁰ at or below the horizon will be subject to matter effects as they propagate through the
³³¹ Earth.

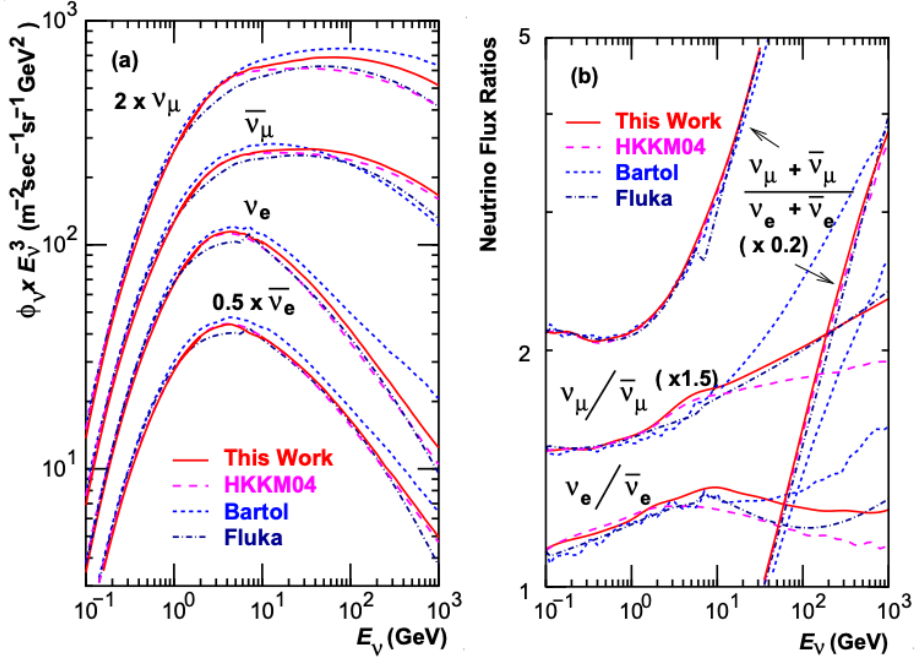


Figure 2.3: Left panel: The atmospheric neutrino flux for different neutrino flavours as a function of neutrino energy as predicted by the 2007 Honda model (“This work”) [43], the 2004 Honda model (“HKKM04”) [44], the Bartol model [42] and the FLUKA model [46]. Right panel: The ratio of the muon to electron neutrino flux as predicted by all the quoted models. Both figures taken from [43].

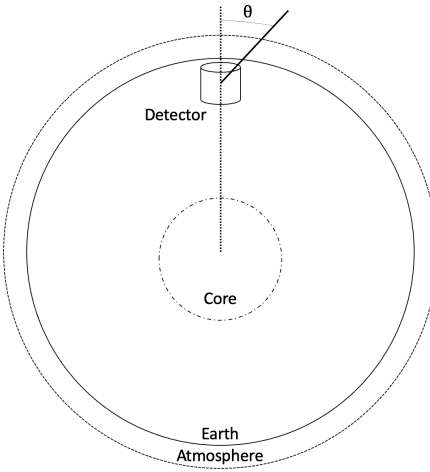


Figure 2.4: A diagram illustrating the definition of zenith angle as used in the Super Kamiokande experiment [47].

Figure 2.5 highlights the neutrino flux as a function of the zenith angle for different

slices of neutrino energy. For medium to high-energy neutrinos (and to a lesser degree

for low-energy neutrinos), the flux is approximately symmetric around $\cos(\theta) = 0$.

To the accuracy of this approximation, the systematic uncertainties associated with atmospheric flux for comparing upward-going and down-going neutrino cancels. This allows the down-going events, which are mostly insensitive to oscillation probabilities, to act as an unoscillated prediction (similar to a near detector in an accelerator neutrino experiment).

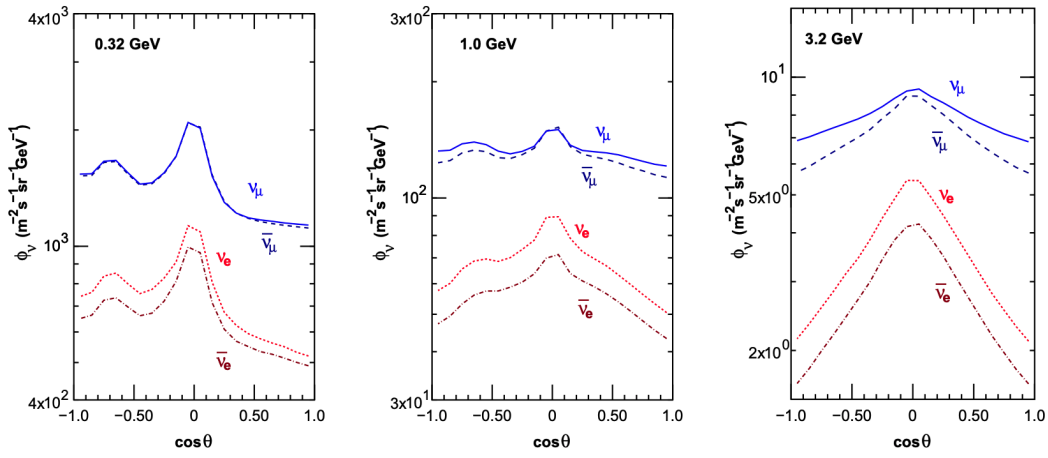


Figure 2.5: Prediction of $\nu_e, \bar{\nu}_e, \nu_\mu, \bar{\nu}_\mu$ fluxes as a function of zenith angle as calculated by the HKKM model [45]. The left, middle and right panels represent three values of neutrino energy, 0.32GeV, 1.0GeV and 3.2GeV respectively. Predictions for other models including Bartol [42], Honda [43] and FLUKA [46] are given in [47].

Precursory hints of atmospheric neutrinos were observed in the mid-1960s searching for $\nu_\mu + X \xrightarrow{(-)} X^* + \mu^\pm$ [48], although it was called an anomaly at the time of measurement. This was succeeded with the IMB-3 [49] and Kamiokande [50] experiments which measured the ratio of muon neutrinos compared to electron neutrinos $R(\nu_\mu/\nu_e)$. Both experiments were found to have a consistent deficit of muon neutrinos, with $R(\nu_\mu/\nu_e) = 0.67 \pm 0.17$ and $R(\nu_\mu/\nu_e) = 0.60^{+0.07}_{-0.06} \pm 0.05$. Super-Kamiokande (SK) [47] extended this analysis by fitting oscillation parameters in $P(\nu_\mu \rightarrow \nu_\tau)$ which found best fit parameters $\sin^2(2\theta) > 0.92$ and $1.5 \times 10^{-3} < \Delta m^2 < 3.4 \times 10^{-3}$ eV 2 .

Since then, atmospheric neutrino experiments have been making precision measurements of the $\sin^2(\theta_{23})$ and Δm^2_{32} oscillation parameters. Atmospheric neutrino oscillation is dominated by $P(\nu_\mu \rightarrow \nu_\tau)$, where SK observed a 4.6σ discovery of ν_τ

³⁵¹ appearance [51]. Figure 2.6 illustrates the current estimates on the atmospheric mixing
³⁵² parameters from a wide range of atmospheric and accelerator neutrino observatories.

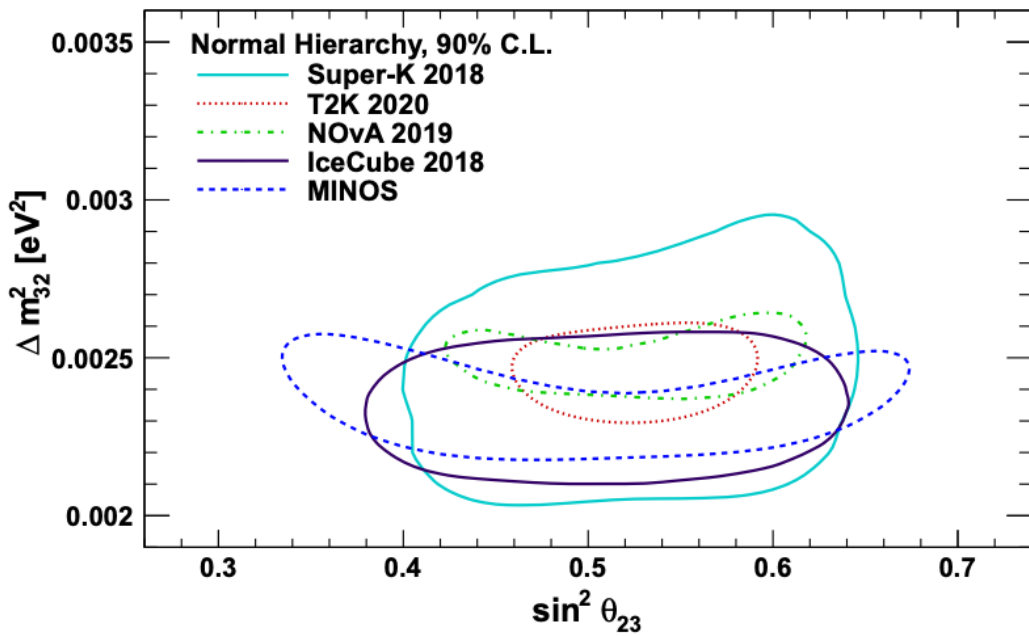


Figure 2.6: Constraints on the atmospheric oscillation parameters, $\sin^2(\theta_{23})$ and Δm_{32}^2 , from atmospheric and long baseline experiments: SK [52], T2K [53], NOvA [54], IceCube [55] and MINOS [56]. Figure taken from [57].

³⁵³ 2.3.3 Accelerator Neutrinos

³⁵⁴ The concept of using a man-made “neutrino beam” was first realised in 1962 [58].
³⁵⁵ Since then, many experiments have followed which all use the same fundamental
³⁵⁶ concepts. Typically, a proton beam is aimed at a target producing charged mesons that
³⁵⁷ decay to neutrinos. The mesons can be sign-selected by the use of magnetic focusing
³⁵⁸ horns to generate a neutrino or antineutrino beam. Pions are the primary meson that
³⁵⁹ decay and depending on the orientation of the magnetic field, a muon (anti-)neutrino
³⁶⁰ beam is generated via $\pi^+ \rightarrow \mu^+ + \nu_\mu$ or $\pi^- \rightarrow \mu^- + \bar{\nu}_\mu$. The decay of muons and
³⁶¹ kaons does result in an irreducible intrinsic electron neutrino background. In T2K,
³⁶² this background contamination is $O(< 1\%)$ [59]. There is also an approximately $\sim 5\%$

³⁶³ “wrong-sign” neutrino background of $\bar{\nu}_\mu$ generated via the same decays. As the beam is
³⁶⁴ generated by proton interactions (rather than anti-proton interactions), the wrong-sign
³⁶⁵ component in the antineutrino beam is larger when operating in neutrino mode.

³⁶⁶ Tuning the proton energy in the beam and using beam focusing techniques allows
³⁶⁷ the neutrino energy to be set to a value that maximises the disappearance oscillation
³⁶⁸ probability in the L/E term in Equation 2.10. This means that accelerator experiments
³⁶⁹ are typically more sensitive to the mixing parameters as compared to a natural neutrino
³⁷⁰ source. However, the disadvantage compared to atmospheric neutrino experiments is
³⁷¹ that the baseline has to be shorter due to the lower flux. Consequently, there is typically
³⁷² less sensitivity to matter effects and the ordering of the neutrino mass eigenstates.

³⁷³ A neutrino experiment measures

$$R(\vec{x}) = \Phi(E_\nu) \times \sigma(E_\nu) \times \epsilon(\vec{x}) \times P(\nu_\alpha \rightarrow \nu_\beta), \quad (2.15)$$

³⁷⁴ where $R(\vec{x})$ is the event rate of neutrinos at position \vec{x} , $\Phi(E_\nu)$ is the flux of neutrinos
³⁷⁵ with energy E_ν , $\sigma(E_\nu)$ is the cross-section of the neutrino interaction and $\epsilon(\vec{x})$ is the
³⁷⁶ efficiency and resolution of the detector. In order to leverage the most out of an
³⁷⁷ accelerator neutrino experiment, the flux and cross-section systematics need to be
³⁷⁸ constrained. This is typically done via the use of a “near detector”, situated at a baseline
³⁷⁹ of $O(1)$ km. This detector observes the unoscillated neutrino flux and constrains the
³⁸⁰ parameters used within the flux and cross-section model.

³⁸¹ The first accelerator experiments to precisely measure oscillation parameters were
³⁸² MINOS [60] and K2K [61]. These experiments confirmed the ν_μ disappearance seen in
³⁸³ atmospheric neutrino experiments by finding consistent parameter values for $\sin^2(\theta_{23})$
³⁸⁴ and Δm_{23}^2 . The current generation of accelerator neutrino experiments, T2K and NO ν A

385 extended this field by observing $\bar{\nu}_\mu \rightarrow \bar{\nu}_e$ and lead the sensitivity to atmospheric mix-
 386 ing parameters as seen in Figure 2.6 [62]. The two experiments differ in their peak
 387 neutrino energy, baseline, and detection technique. The NO ν A experiment is situated
 388 at a baseline of 810km from the NuMI beamline which delivers 2GeV neutrinos. The
 389 T2K neutrino beam is peaked around 0.6GeV and propagates 295km. The NO ν A
 390 experiment also uses functionally identical detectors (near and far) which allow the
 391 approximate cancellation of detector systematics whereas T2K uses a plastic scintil-
 392 lator technique at the near detector and a water Cherenkov far detector. The future
 393 generation experiments DUNE [63] and Hyper-Kamiokande [64] will succeed these
 394 experiments as the high-precision era of neutrino oscillation parameter measurements
 395 develops.

396 Several anomalous results have been observed in the LSND [9] and MiniBooNE [10]
 397 detectors which were designed with purposefully short baselines. Parts of the neu-
 398 trino community attributed these results to oscillations induced by a fourth “sterile”
 399 neutrino [65] but several searches in other experiments, MicroBooNE [66] and KAR-
 400 MEN [67], found no hints of additional neutrino species. The solution to the anomalous
 401 results is still being determined.

402 2.3.4 Reactor Neutrinos

403 As illustrated in the first discovery of neutrinos (section 2.1), nuclear reactors are a very
 404 useful man-made source of electron antineutrinos. For reactors that use low-enriched
 405 uranium ^{235}U as fuel, the antineutrino flux is dominated by the β -decay fission of ^{235}U ,
 406 ^{238}U , ^{239}Pu and ^{241}Pu [68] as illustrated in Figure 2.7.

407 Due to their low energy, reactor electron antineutrinos predominantly interact
 408 via the inverse β -decay (IBD) interaction. The typical signature contains two signals

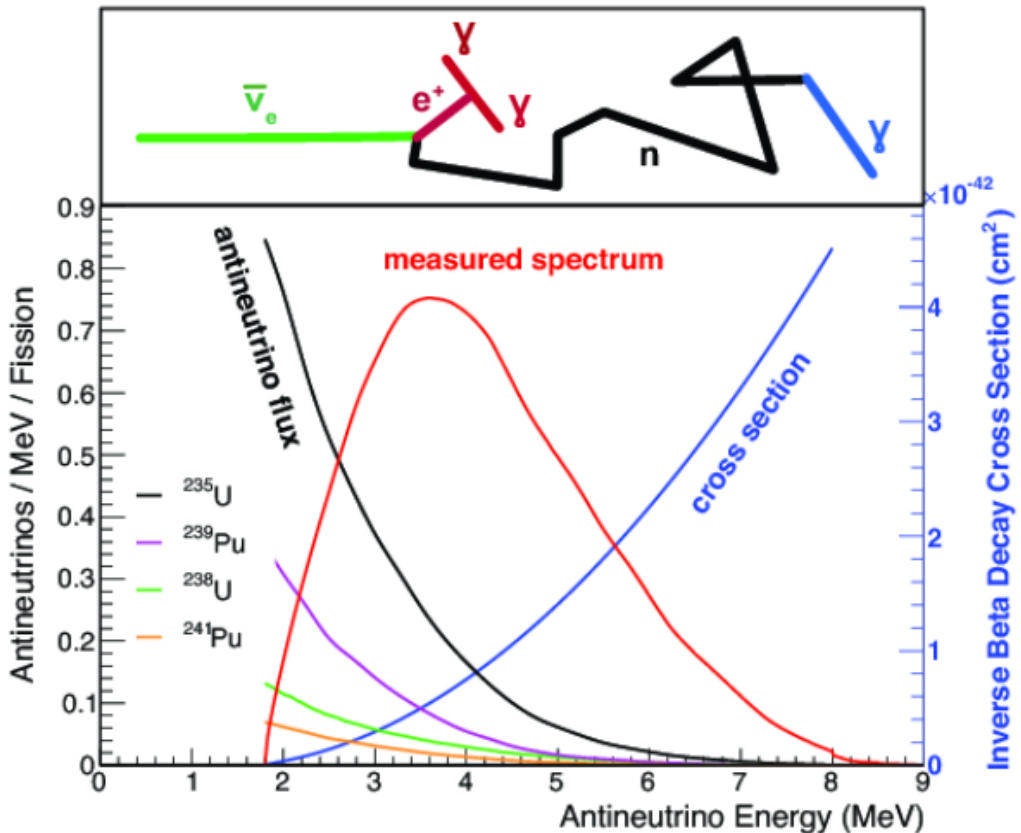


Figure 2.7: Reactor electron antineutrino fluxes for ^{235}U (Black), ^{238}U (Green), ^{239}Pu (Purple), and ^{241}Pu (Orange) isotopes. The inverse β -decay cross-section (Blue) and corresponding measurable neutrino spectrum (Red) are also given. Top panel: Schematic of Inverse β -decay interaction including the eventual capture of the emitted neutron. This capture emits a γ -ray which provides a second signal of the event. Taken from [69].

delayed by $O(200)\mu\text{s}$; firstly the prompt photons from positron annihilation, and secondly the photons emitted ($E_{tot}^\gamma = 2.2\text{MeV}$) from de-excitation after neutron capture on hydrogen. Searching for both signals improves the detector's ability to distinguish between background and signal events [70]. Recently, SK included gadolinium dopants into the ultra-pure water to increase the energy released from the photon cascade to $\sim 8\text{MeV}$ and reduce the time of the delayed signal to $\sim 28\mu\text{s}$.

There are many short baseline experiments ($L \sim O(1)\text{km}$) that have measured the $\sin^2(\theta_{13})$ and Δm_{23}^2 oscillation parameters. Daya Bay [71], RENO [72] and Double Chooz [73] have all provided precise measurements, with the first discovery of a

418 non-zero θ_{13} made by Daya Bay and RENO (and complemented by T2K [73]). The
419 constraints on $\sin^2(\theta_{13})$ by the reactor experiments lead the field and are often used as
420 external inputs to accelerator neutrino experiments to improve their sensitivity to δ_{CP}
421 and mass hierarchy determination. JUNO-TAO [74], a small collaboration within the
422 larger JUNO experiment, is a next-generation reactor experiment that aims to precisely
423 measure the isotopic antineutrino yields from the different fission chains. Alongside
424 this, it aims to explain the ‘5MeV excess’ [75–77] by conducting a search for sterile
425 neutrinos with a mass scale of around 1eV.

426 Kamland [78] is the only experiment to have observed reactor neutrinos using a
427 long baseline (flux weighted averaged baseline of $L \sim 180\text{km}$) which allows it to have
428 sensitivity to Δm_{12}^2 . Combined with the SK solar neutrino experiment, the combined
429 analysis puts the most stringent constraint on Δm_{12}^2 [79].

430 2.4 Summary

431 Since observing the first evidence of neutrino oscillations in the late 1990’s, numerous
432 measurements of the mixing parameters have been made. Many experiments use
433 neutrinos as a tool for discovery of new physics (diffuse supernova background,
434 neutrinoless double beta decay and others) so the PMNS parameters are summarised
435 in the Particle Data Group (PDG) review tables. The analysis presented in this thesis
436 focuses on the 2020 T2K oscillation analysis presented in [80] where the 2018 PDG
437 constraints [81] were used. These constraints are outlined in Table 2.1.

438 The $\sin^2(\theta_{13})$ measurement stems from the electron antineutrino disappearance,
439 $P(\bar{\nu}_e \rightarrow \bar{\nu}_e)$, and is take as the average best-fit from the combination of Daya Bay,
440 Reno and Double Chooz. It is often used as a prior uncertainty within other neu-
441 trino oscillation experiments, typically termed the reactor constraint. The $\sin^2(\theta_{12})$

Parameter	2018 Constraint
$\sin^2(\theta_{12})$	0.307 ± 0.013
Δm_{21}^2	$(7.53 \pm 0.18) \times 10^{-5} \text{ eV}^2$
$\sin^2(\theta_{13})$	$(2.12 \pm 0.08) \times 10^{-2}$
$\sin^2(\theta_{23})$ (I.H., Q1)	$0.421^{+0.033}_{-0.025}$
$\sin^2(\theta_{23})$ (I.H., Q2)	$0.592^{+0.023}_{-0.030}$
$\sin^2(\theta_{23})$ (N.H., Q1)	$0.417^{+0.025}_{-0.028}$
$\sin^2(\theta_{23})$ (N.H., Q2)	$0.597^{+0.024}_{-0.030}$
Δm_{32}^2 (I.H.)	$(-2.56 \pm 0.04) \times 10^{-3} \text{ eV}^2$
Δm_{32}^2 (N.H.)	$(2.51 \pm 0.05) \times 10^{-3} \text{ eV}^2$

Table 2.1: The 2018 Particle Data Group constraints of the oscillation parameters taken from [81]. The value of Δm_{23}^2 is given for both normal hierarchy (N.H.) and inverted hierarchy (I.H.) and $\sin^2(\theta_{23})$ is broken down by whether its value is below (Q1) or above (Q2) 0.5.

parameter is predominantly measured through electron neutrino disappearance, $P(\nu_e \rightarrow \nu_{\mu,\tau})$, in solar neutrino experiments. The long-baseline reactor neutrino experiment Kamland also has sensitivity to this parameter and is used in a joint fit to solar data from SNO and SK, using the reactor constraint. Measurements of $\sin^2(\theta_{23})$ are made by long-baseline and atmospheric neutrino experiments. The PDG value is a joint fit of T2K, NOvA, MINOS and IceCube DeepCore experiments. The latest T2K-only measurement, provided at Neutrino2020 and is the basis of this thesis, is given as $\sin^2(\theta_{23}) = 0.546^{+0.024}_{-0.046}$ [80]. The PDG constraint on Δm_{12}^2 is provided by the KamLAND experiment using solar and geoneutrino data. This measurement utilised a $\sin^2(\theta_{13})$ constraint from accelerator (T2K, MINOS) and reactor neutrino (Daya Bay, RENO, Double Chooz) experiments. Accelerator measurements make some of the most stringent constraints on Δm_{23}^2 although atmospheric experiments have more sensitivity to the mass hierarchy determination. The PDG performs a joint fit of accelerator and atmospheric data, in both normal and inverted hierarchy separately. The latest T2K-only result is $\Delta m_{32}^2 = 2.49^{+0.058}_{-0.082} \times 10^{-3} \text{ eV}^2$ favouring normal hierarchy [80]. The value of δ_{CP} is largely undetermined. CP-conserving values of 0 and π were

458 rejected with $\sim 2\sigma$ intervals, as published in Nature, although more recent analysis
459 have reduced the rejection intervals to 90%. Since the 2018 PDG publication, there has
460 been a new measurement of $\sin^2(\theta_{13}) = (2.20 \pm 0.07) \times 10^{-2}$ [82], alongside updated
461 Δm_{23}^2 and $\sin^2(\theta_{23})$ measurements.

462 Throughout this thesis, several sample spectra predictions and contours are pre-
463 sented which require oscillation parameters to be assumed. Table 2.2 defines two sets
464 of oscillation parameters, with “Asimov A” set being close to the preferred values
465 from a previous T2K-only fit [83] and “Asimov B” being CP-conserving and further
466 from maximal θ_{23} mixing.

Parameter	Asimov A	Asimov B
Δm_{12}^2	$7.53 \times 10^{-5} \text{ eV}^2$	
Δm_{32}^2	$2.509 \times 10^{-3} \text{ eV}^2$	
$\sin^2(\theta_{12})$	0.304	
$\sin^2(\theta_{13})$	0.0219	
$\sin^2(\theta_{23})$	0.528	0.45
δ_{CP}	-1.601	0.0

Table 2.2: Reference values of the neutrino oscillation parameters for two different oscillation parameter sets.

467 **Chapter 3**

468 **T2K and SK Experiment Overview**

469 As the successor of the Kamiokande experiment, the Super-Kamiokande (SK) collabora-
470 ration has been leading atmospheric neutrino oscillation analyses for over two decades.
471 The detector has provided some of the strongest constraints on proton decay and the
472 first precise measurements of the Δm_{23}^2 and $\sin^2(\theta_{23})$ neutrino oscillation parameters.
473 The ability of the detector to low-energy neutrino events has been significantly im-
474 proved with the recent gadolinium doping of the ultra-pure water target. The history,
475 detection technique, and operation of the SK detector is described in section 3.1.

476 The Tokai-to-Kamioka (T2K) experiment was one of the first long-baseline ex-
477 periments to use both neutrino and antineutrino beams to precisely measure the
478 charge parity violation within the neutrino sector. With the SK detector observing
479 the oscillated neutrino flux, the T2K experiment observed the first hints of a non-zero
480 $\sin^2(\theta_{13})$ measurement and continues to lead the field with the constraints it provides
481 on $\sin^2(\theta_{13})$, $\sin^2(\theta_{23})$, Δm_{23}^2 and δ_{CP} . The techniques which T2K uses in gener-
482 ating its neutrino beam as well as the near-detector used to constrain the flux and
483 cross-section parameters used in this analysis are documented in section 3.2.

484 **3.1 The Super-Kamiokande Experiment**

485 The SK experiment began taking data in 1996 [84] and has had many modifications
486 throughout its lifespan. There have been seven defined periods of data taking as
487 noted in Table 3.1. Data taking began in SK-I which ran for five years. Between the

488 SK-I and SK-II periods, a significant proportion of the PMTs were damaged during
 489 maintenance. Those that survived were equally distributed throughout the detector
 490 in the SK-II era, which resulted in a reduced photo-coverage. From SK-III onwards,
 491 repairs to the detector meant the full suite of PMTs was operational. Before the
 492 start of SK-IV, the data acquisition and electronic systems were upgraded. Between
 493 SK-IV and SK-V, a significant effort was placed into tank open maintenance and
 494 repair/replacement of defective PMTs, a task for which the author of this thesis was
 495 required. Consequently, the detector conditions were significantly different between
 496 the two operational periods. SK-VI saw the start of the 0.01% gadolinium doped water.
 497 SK-VII, which started during the writing of this thesis, has increased the gadolinium
 498 concentration to 0.03% for continued operation [85].

Period	Start Date	End Date	Live-time (days)
I	April 1996	July 2001	1489.19
II	October 2002	October 2005	798.59
III	July 2006	September 2008	518.08
IV	September 2008	May 2018	3244.4
V	January 2019	July 2020	461.02
VI	July 2020	May 2022	583.3
VII	May 2022	Ongoing	N/A

Table 3.1: The various SK periods and respective live-time. The SK-VI live-time is calculated until 1st April 2022. SK-VII started during the writing of this thesis.

499 3.1.1 The SK Detector

500 The basic structure of the Super-Kamiokande (SK) detector is a cylindrical tank with a
 501 diameter 39.3m and height 41.1m filled with ultrapure water [86]. A diagram of the
 502 significant components of the SK detector is given in Figure 3.1. The SK detector is
 503 situated in the Kamioka mine in Gifu, Japan. The mine is underground with roughly
 504 1km rock overburden (2.7km water equivalent overburden) [87]. At this depth, the

505 rate of cosmic ray muons is significantly decreased to a value of $\sim 2\text{Hz}$. The top of
 506 the tank is covered with stainless steel which is designed as a working platform for
 507 maintenance, calibration, and location for high voltage and data acquisition electronics.

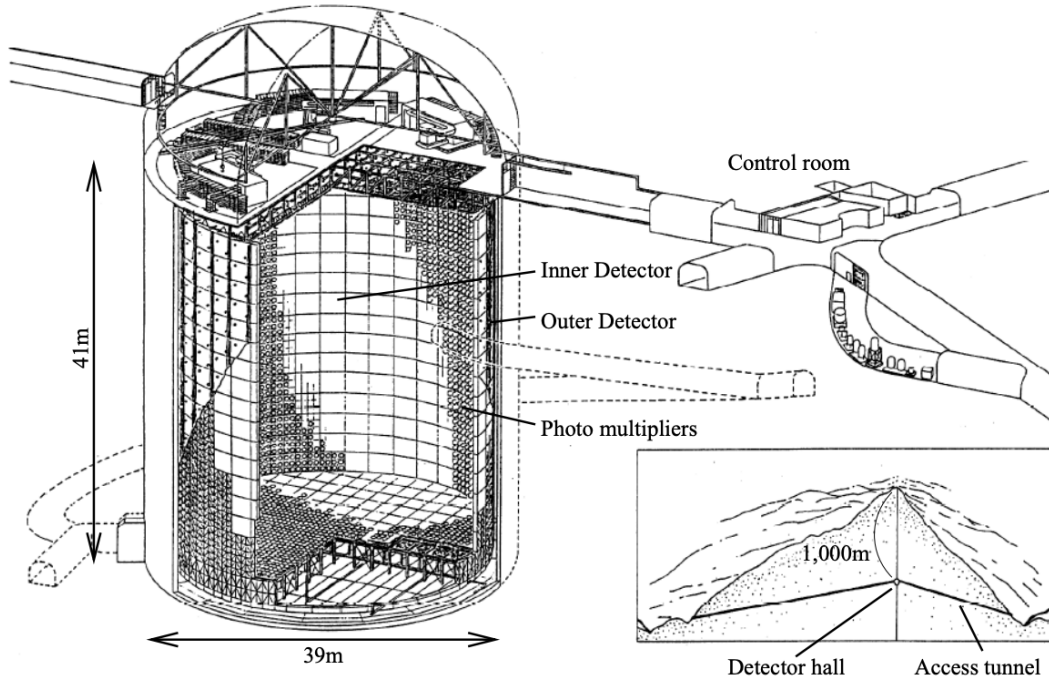


Figure 3.1: A schematic diagram of the Super-Kamiokande Detector. Taken from [88].

508 A smaller cylindrical structure (36.2m diameter, 33.8m height) is situated inside the
 509 tank, with an approximate 2m gap between this structure and the outer tank wall. The
 510 purpose of this structure is to support the photomultiplier tubes (PMTs). The volume
 511 inside and outside the support structure is referred to as the inner detector (ID) and
 512 outer detector (OD), respectively. In the SK-IV era, the ID and OD are instrumented
 513 by 11,129 50cm and 1,885 20cm PMTs respectively [86]. The ID contains a 32kton
 514 mass of water. Many analyses performed at SK use a “fiducial volume” defined by the
 515 volume of water inside the ID excluding some distance to the ID wall. This reduces the
 516 volume of the detector which is sensitive to neutrino events but reduces radioactive
 517 backgrounds and allows for better reconstruction performance. The nominal fiducial

518 volume is defined as the area contained inside 2m from the ID wall for a total of
519 22.5kton water [89].

520 The two regions of the detector (ID and OD) are optically separated with opaque
521 black plastic. The purpose of this is to determine whether a track entered or exited
522 the ID. This allows cosmic ray muons and partially contained events to be tagged and
523 separated from neutrino events entirely contained within the ID. This black plastic is
524 also used to cover the area between the ID PMTs to reduce photon reflection from the
525 ID walls. Opposite to this, the OD is lined with a reflective material to allow photons to
526 reflect around inside the OD until collected by one of the PMTs. Furthermore, each OD
527 PMT is backed with $50 \times 50\text{cm}$ plates of wavelength shifting acrylic which increases
528 the efficiency of light collection [87].

529 In the SK-IV data-taking period, the photocathode coverage of the detector, or the
530 fraction of the ID wall instrumented with PMTs, is $\sim 40\%$ [87]. The PMTs have a
531 quantum efficiency (the ratio of detected electrons to incident photons) of $\sim 21\%$ for
532 photons with wavelengths of $360\text{nm} < \lambda < 390\text{nm}$. The proportion of photoelectrons
533 that produce a signal in the dynode of a PMT, termed the collection efficiency, is
534 $> 70\%$ [87]. The PMTs used within SK are most sensitive to photons with wavelength
535 $300\text{nm} \leq \lambda \leq 600\text{nm}$ [87]. One disadvantage of using PMTs as the detection media
536 is that the Earth's geomagnetic field can modify its response. Therefore, a set of
537 compensation coils is built around the inner surface of the detector to mitigate this
538 effect [90].

539 As mentioned, the SK detector is filled with ultrapure water, which in a perfect
540 world would contain no impurities. However, bacteria and organic compounds can
541 significantly degrade the water quality. This decreases the attenuation length, which
542 reduces the total number of photons that hit a PMT. To combat this, a sophisticated
543 water treatment system has been developed [87, 91]. UV lights, mechanical filters,

544 and membrane degasifiers are used to reduce the bacteria, suspended particulates,
545 and radioactive materials from the water. The flow of water within the tank is also
546 critical as it can remove stagnant bacterial growth or build-up of dust on the surfaces
547 within the tank. Gravity drifts impurities in the water towards the bottom of the
548 tank which, if left uncontrolled, can create asymmetric water conditions between
549 the top and bottom of the tank. Typically, the water entering the tank is cooled
550 below the ambient temperature of the tank to control convection and inhibit bacteria
551 growth. Furthermore, the rate of dark noise hits within PMTs is sensitive to the PMT
552 temperature [92] so controlling the temperature gradients within the tank is beneficial
553 for stable measurements.

554 SK-VI is the first phase of the SK experiment to use gadolinium dopants within
555 the ultrapure water [85]. As such, the SK water system had to be replaced to avoid
556 removing the gadolinium concentrate from the ultrapure water [93]. For an inverse
557 β -decay (IBD) interaction in a water target, the emitted neutron is thermally captured
558 on hydrogen. This process releases 2.2MeV γ rays which are difficult to detect as
559 the resulting Compton scattered electrons are very close to the Cherenkov threshold,
560 limiting the number of photons produced. Thermal capture of neutrons on gadolin-
561 ium generates γ rays with higher energy (8MeV [70]) meaning they are more easily
562 detected. SK-VI has 0.01% Gd loading (0.02% gadolinium sulphate by mass) which
563 causes \approx 50% of neutrons emitted by IBD to be captured on gadolinium [94, 95].
564 Whilst predominantly useful for low energy analyses, Gd loading allows better $\nu/\bar{\nu}$
565 separation for atmospheric neutrino event selections [96]. Efforts are currently in place
566 to increase the gadolinium concentrate to 0.03% for \approx 75% neutron capture efficiency
567 on gadolinium [97]. The final stage of loading targets 0.1% concentrate.

568 3.1.2 Calibration

569 The calibration of the SK detector is documented in [86] and summarised below. The
570 analysis presented within this thesis is dependent upon ‘high energy events’ (Charged
571 particles with $O(> 100)\text{MeV}$ momenta). These are events that are expected to generate
572 a larger number of photons such that each PMT will be hit with multiple photons.
573 The reconstruction of these events depends upon the charge deposited within each
574 PMT and the timing response of each individual PMT. Therefore, the most relevant
575 calibration techniques to this thesis are outlined.

576 Before installation, 420 PMTs were calibrated to have identical charge responses
577 and then distributed throughout the tank in a cross-shape pattern (As illustrated by
578 Figure 3.2). These are used as a standardised measure for the rest of the PMTs installed
579 at similar geometric positions within SK to be calibrated against. To perform this
580 calibration, a xenon lamp is located at the center of the SK tank which flashes uniform
581 light at 1Hz. This allows for geometrical effects, water quality variation, and timing
582 effects to be measured in-situ throughout normal data-taking periods.

583 When specifically performing calibration of the detector (in out-of-data taking
584 mode), the water in the tank was circulated to avoid top/bottom asymmetric water
585 quality. Any non-uniformity within the tank significantly affects the PMT hit proba-
586 bility through scattering or absorption. This becomes a dominant effect for the very
587 low-intensity light sources discussed later which are designed such that only one
588 photon is incident upon a given PMT.

589 The “gain” of a PMT is defined as the ratio of the total charge of the signal produced
590 compared to the charge of photoelectrons emitted by the photocathodes within the
591 PMT. To calibrate the signal of each PMT, the “relative” and “absolute” gain values are

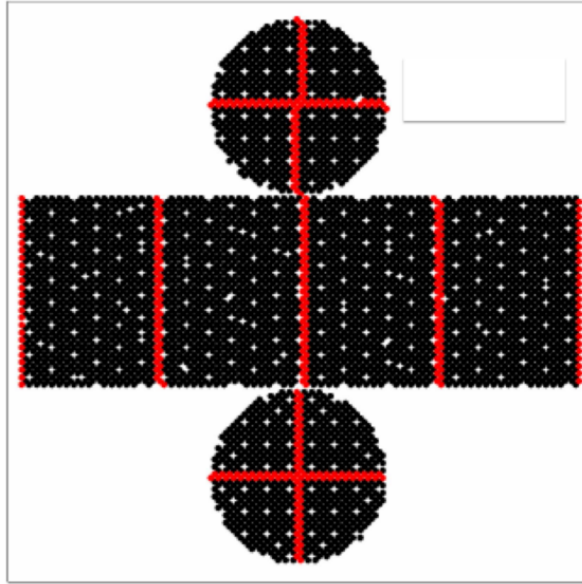


Figure 3.2: The location of “standard PMTs” (red) inside the SK detector. Taken from [86].

592 measured. The relative gain is the variation of gain among each of the PMTs whereas
 593 the absolute gain is the average gain of all PMTs.

594 The relative gain is calibrated as follows. A laser is used to generate two measure-
 595 ments: a high-intensity flash that illuminates every PMT with a sufficient number of
 596 photons, and a low-intensity flash in which only a small number of PMTs collect light.
 597 The first measurement creates an average charge, $Q_{obs}(i)$ on PMT i , whereas the second
 598 measurement ensures that each hit PMT only generates a single photoelectron. For the
 599 low-intensity measurement, the number of times each PMT records a charge larger
 600 than 1/4 photoelectrons, $N_{obs}(i)$, is counted. The values measured can be expressed as

$$\begin{aligned} Q_{obs}(i) &\propto I_H \times f(i) \times \epsilon(i) \times G(i), \\ N_{obs}(i) &\propto I_L \times f(i) \times \epsilon(i), \end{aligned} \tag{3.1}$$

601 Where I_H and I_L is the intensity of the high and low flashes, $f(i)$ is the acceptance
 602 efficiency of the i^{th} PMT, $\epsilon(i)$ is the product of the quantum and collection efficiency

of the i^{th} PMT and $G(i)$ is the gain of the i^{th} PMT. The relative gain for each PMT can be determined by taking the ratio of these quantities.

The absolute gain calibration is performed by observing fixed energy γ -rays of $E_{\gamma} \sim 9\text{MeV}$ emitted isotropically from neutron capture on a NiCf source situated at the center of the detector. This generates a photon yield of about 0.004 photoelectrons/PMT/event, meaning that $> 99\%$ of PMT signals are generated from single photoelectrons. A charge distribution is generated by performing this calibration over all PMTs, and the average value of this distribution is taken to be the absolute gain value.

As mentioned in subsection 3.1.1, the average quantum and collection efficiency for the SK detector is $\sim 21\%$ and $> 70\%$ respectively. However, these values do differ between each PMT and need to be calibrated accordingly. Consequently, the NiCf source is also used to calibrate the “quantum \times collection” efficiency (denoted “QE”) value of each PMT. The NiCf low-intensity source is used as the PMT hit probability is proportional to the QE ($N_{\text{obs}}(i) \propto \epsilon(i)$ in Equation 3.1). A Monte Carlo prediction which includes photon absorption, scattering, and reflection is made to estimate the number of photons incident on each PMT and the ratio of the number of predicted to observed hits is calculated. The difference is attributed to the QE efficiency of that PMT. This technique is extended to calculate the relative QE efficiency by normalizing the average of all PMTs which removes the dependence on the light intensity.

Due to differing cable lengths and readout electronics, the timing response between a photon hitting the PMT and the signal being captured by the data acquisition can be different between each PMT. Due to threshold triggers (Described in subsection 3.1.3), the time at which a pulse reaches a threshold is dependent upon the size of the pulse. This is known as the ‘time-walk’ effect and also needs to be accounted for in each PMT. To calibrate the timing response, a pulse of light with width 0.2ns is emitted into the

629 detector through a diffuser. Two-dimensional distributions of time and pulse height
630 (or charge) are made for each PMT and are used to calibrate the timing response. This
631 is performed in-situ during data taking with the light source pulsing at 0.03Hz.

632 The top/bottom water quality asymmetry is measured using the NiCf calibration
633 data and cross-referencing these results to the “standard PMTs”. The water attenuation
634 length is continuously measured by the rate of vertically-downgoing cosmic-ray
635 muons which enter via the top of the tank.

636 Dark noise is the phenomenon where a PMT registers a pulse that is consistent
637 with a single photoelectron emitted from photon detection despite the PMT being in
638 complete darkness. This is predominately caused by two processes. Firstly there is
639 intrinsic dark noise which is where photoelectrons gain enough thermal energy to be
640 emitted from the photocathode, and secondly, the radioactive decay of contaminants
641 inside the structure of the PMT. Typical dark noise rate for PMTs used within SK are
642 $O(3)$ kHz [87]. This is lower than the expected number of photons generated for a ‘high
643 energy event’ (As described in subsection 3.1.4) but instability in this value can cause
644 biases in reconstruction. Dark noise is related to the gain of a PMT and is calibrated
645 using hits inside a time window recorded before an event trigger [98].

646 3.1.3 Data Acquisition and Triggering

647 The analysis presented in this thesis only uses the SK-IV period of the SK experiment
648 so this subsection focuses on the relevant points of the data acquisition and triggering
649 systems to that SK period. The earlier data acquisition and triggering systems are
650 documented in [99, 100].

651 Before the SK-IV period started, the existing front-end electronics were replaced
652 with “QTC-Based Electrons with Ethernet, QBEE” systems [101]. When the QBEE

observes a signal above a 1/4 photoelectron threshold, the charge-to-time (QTC) converter generates a rectangular pulse. The start of the rectangular pulse indicates the time at which the analog photoelectron signal was received and the width of the pulse indicates the total charge integrated throughout the signal. This is then digitized by time-to-digital converters and sent to the “front-end” PCs. The digitized signal from every QBEE is then chronologically ordered and sent to the “merger” PCs. It is the merger PCs that apply the software trigger. Any triggered events are passed to the “organizer” PC. This sorts the data stream of multiple merger PCs into chronologically ordered events which are then saved to disk. The schematic of data flow from PMTs to disk is illustrated in Figure 3.3.

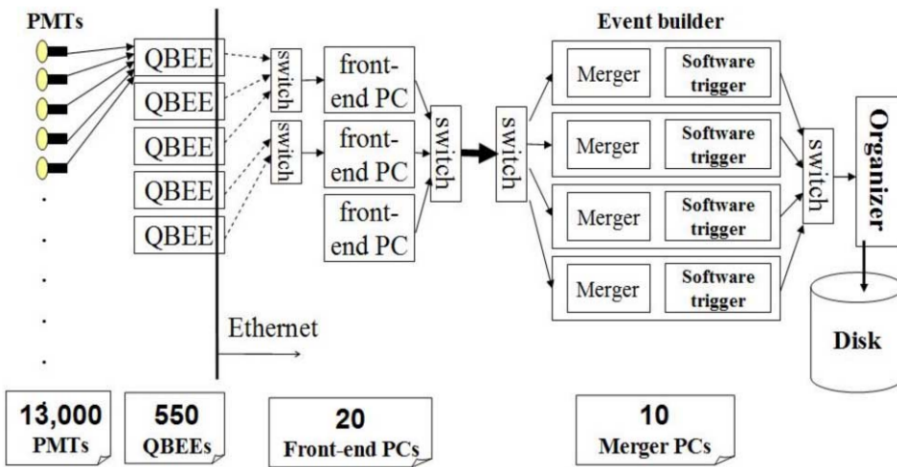


Figure 3.3: Schematic view of the data flow through the data acquisition and online system. Taken from [102].

The software trigger (described in [103]) operates by determining the number of PMT hits within a 200ns sliding window, N_{200} . This window coincides with the maximum time that a Cherenkov photon would take to traverse the length of the SK tank [100]. For lower energy events that generate fewer photons, this technique is useful for eliminating background processes like dark noise and radioactive decay which would be expected to separate in time. When the value of N_{200} exceeds some threshold, a software trigger is issued. There are several trigger thresholds used within

670 the SK-IV period which are detailed in Table 3.2. If one of these thresholds is met, the
 671 PMT hits within an extended time window are also read out and saved to disk. In
 672 the special case of an event that exceeds the SHE trigger but does not exceed the OD
 673 trigger, the AFT trigger looks for delayed coincidences of 2.2MeV gamma rays emitted
 674 from neutron capture in a $535\mu\text{s}$ window after the SHE trigger. A similar but more
 675 complex “Wideband Intelligent Trigger (WIT)” has been deployed and is described
 676 in [104].

Trigger	Acronym	Condition	Extended time window (μs)
Super Low Energy	SLE	>34/31 hits	1.3
Low Energy	LE	>47 hits	40
High Energy	HE	>50 hits	40
Super High Energy	SHE	>70/58 hits	40
Outer Detector	OD	>22 hits in OD	N/A

Table 3.2: The trigger thresholds and extended time windows saved around an event which were utilised throughout the SK-IV period. The exact thresholds can change and the values listed here represent the thresholds at the start and end of the SK-IV period.

677 3.1.4 Cherenkov Radiation

678 Cherenkov light is emitted from any highly energetic charged particle traveling
 679 with relativistic velocity, β , greater than the local speed of light in a medium [105].
 680 Cherenkov light is formed at the surface of a cone with characteristic pitch angle,

$$\cos(\theta) = \frac{1}{\beta n}. \quad (3.2)$$

where n is the refractive index of the medium. Consequently, the Cherenkov momentum threshold, P_{thres} , is dependent upon the mass, m , of the charged particle moving through the medium,

$$P_{thres} = \frac{m}{\sqrt{n^2 - 1}} \quad (3.3)$$

For water, where $n = 1.33$, the Cherenkov threshold momentum and energy for various particles are given in Table 3.3. In contrast, γ -rays are detected indirectly via the combination of photons generated by Compton scattering and pair production. The threshold for detection in the SK detector is typically higher than the threshold for photon production. This is due to the fact that the attenuation of photons in the water means that typically $\sim 75\%$ of Cherenkov photons reach the ID PMTs. Then the collection and quantum efficiencies described in subsection 3.1.1 result in the number of detected photons being lower than the number of photons which reach the PMTs.

Particle	Threshold Momentum (MeV)	Threshold Energy (MeV)
Electron	0.5828	0.7751
Muon	120.5	160.3
Pion	159.2	211.7
Proton	1070.0	1423.1

Table 3.3: The threshold momentum and energy for a particle to generate Cherenkov light in ultrapure water, as calculated in Equation 3.2 in ultrapure water which has refractive index $n = 1.33$.

The Frank-Tamm equation [106] describes the relationship between the number of Cherenkov photons generated per unit length, dN/dx , the wavelength of the photons generated, λ , and the relativistic velocity of the charged particle,

$$\frac{d^2N}{dxd\lambda} = 2\pi\alpha \left(1 - \frac{1}{n^2\beta^2}\right) \frac{1}{\lambda^2}. \quad (3.4)$$

where α is the fine structure constant. For a 100MeV momentum electron, approximately 330 photons will be produced per centimeter in the $300\text{nm} \leq \lambda \leq 700\text{nm}$ region which the ID PMTs are most sensitive to [87].

3.2 The Tokai to Kamioka Experiment

The Tokai to Kamioka (T2K) experiment is a long-baseline neutrino oscillation experiment located in Japan. Proposed in the early 2000s [107, 108] to replace K2K [109], T2K was designed to observe electron neutrino appearance whilst precisely measuring the oscillation parameters associated with muon neutrino disappearance [110]. The experiment consists of a neutrino beam generated at the Japan Proton Accelerator Research Complex (J-PARC), a suite of near detectors situated 280m from the beam target, and the Super Kamiokande far detector positioned at a 295km baseline. The cross-section view of the T2K experiment is drawn in Figure 3.4.

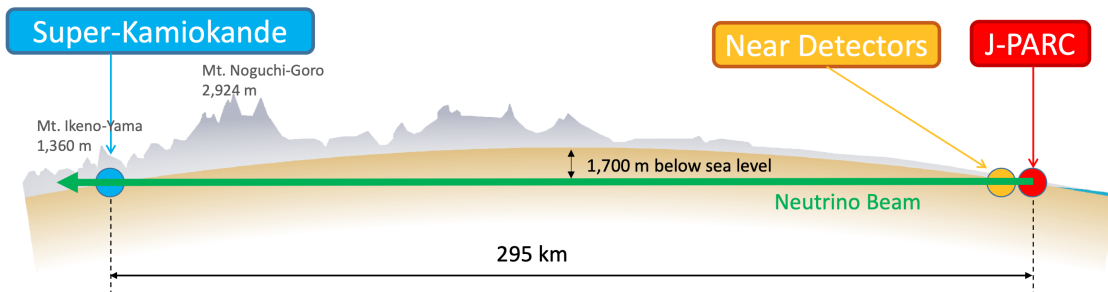


Figure 3.4: The cross-section view of the Tokai to Kamioka experiment illustrating the beam generation facility at J-PARC, the near detector situated at a baseline of 280m and the Super Kamiokande far detector situated 295km from the beam target.

The T2K collaboration makes world-leading measurements of the $\sin^2(\theta_{23})$, Δm_{23}^2 , and δ_{CP} oscillation parameters. Improvements in the precision and accuracy of parameter estimates are still being made by including new data samples and developing the models which describe the neutrino interactions and detector responses [111]. Electron neutrino appearance was first observed at T2K in 2014 [112] with 7.3σ significance.

The near detectors provide constraints on the beam flux and cross-section model parameters used within the oscillation analysis by observing the unoscillated neutrino beam. There are a host of detectors situated in the near detector hall (As illustrated in Figure 3.5): ND280 (subsection 3.2.2), INGRID (subsection 3.2.3), NINJA [113], WAGASCI [114], and Baby-MIND [115]. The latter three are not currently used within the oscillation analysis presented within this thesis.

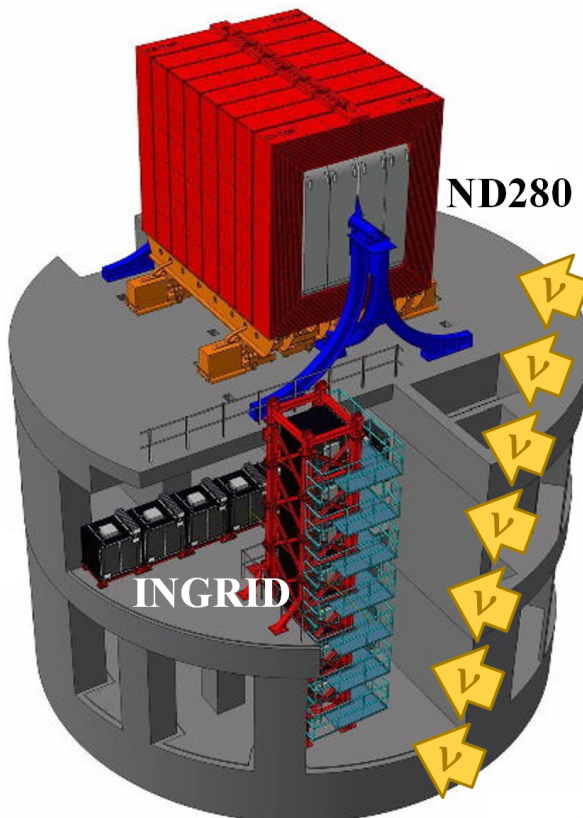


Figure 3.5: The near detector suite for the T2K experiment showing the ND280 and INGRID detectors. The distance between the detectors and the beam target is 280m.

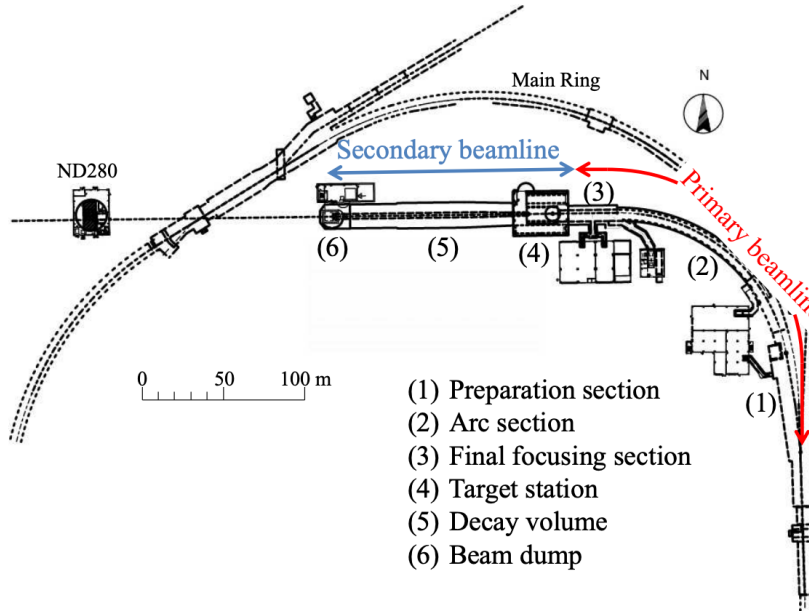
Whilst this thesis presents the ND280 in terms of its purpose for the oscillation analysis, the detector can also make many cross-section measurements at neutrino energies of $O(1)$ GeV for the different targets within the detector [116, 117]. These measurements are of equal importance as they can lead the way in determining the model parameters used in the interaction models for the future high-precision era of neutrino physics.

DB: Discuss BANFF, PTheta, MaCh3 and covariance

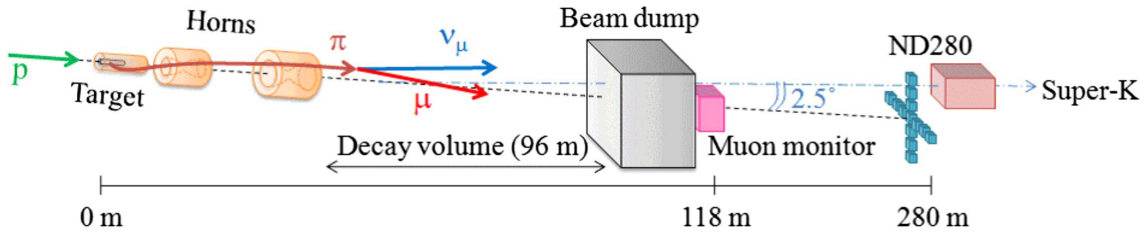
3.2.1 The Neutrino Beam

The neutrino beam used within the T2K experiment is described in [59, 118] and summarised below. The accelerating facility at J-PARC is composed of two sections; the primary and secondary beamlines. Figure 3.6 illustrates a schematic of the beamline, focusing mostly on the components of the secondary beamline. The primary beamline has three accelerators that progressively accelerate protons; a linear accelerator, a rapid-cycling synchrotron, and the main-ring (MR) synchrotron. Once fully accelerated by the MR, the protons have a kinetic energy of 30GeV. Eight bunches of these protons, separated by 500ns, are extracted per “spill” from the MR and directed towards a graphite target (a rod of length 91.4cm and diameter 2.6cm). Spills are extracted at 0.5Hz with $\sim 3 \times 10^{14}$ protons contained per spill.

The secondary beamline consists of three main components: the target station, the decay volume, and the beam dump. The target station is comprised of the target, beam monitors, and three magnetic focusing horns. The proton beam interacts with the graphite target to form a secondary beam of mostly pions and kaons. The secondary beam travels through a 96m long decay volume, generating neutrinos through the following decays [59],



(a) Primary and secondary beamline



(b) Secondary beamline

Figure 3.6: Top panel: Bird's eye view of the most relevant part of primary and secondary beamline used within the T2K experiment. The primary beamline is the main-ring proton synchrotron, kicker magnet, and graphite target. The secondary beamline consists of the three focusing horns, decay volume, and beam dump. Figure taken from [118]. Bottom panel: The side-view of the secondary beamline including the focusing horns, beam dump and neutrino detectors. Figure taken from [119].

$$\begin{array}{ll}
 \pi^+ \rightarrow \mu^+ + \nu_\mu & \pi^- \rightarrow \mu^- + \bar{\nu}_\mu \\
 K^+ \rightarrow \mu^+ + \nu_\mu & K^- \rightarrow \mu^- + \bar{\nu}_\mu \\
 \rightarrow \pi^0 + e^+ + \nu_e & \rightarrow \pi^0 + e^- + \bar{\nu}_e \\
 \rightarrow \pi^0 + \mu^+ + \nu_\mu & \rightarrow \pi^0 + \mu^- + \bar{\nu}_\mu \\
 K_L^0 \rightarrow \pi^- + e^+ + \nu_e & K_L^0 \rightarrow \pi^+ + e^- + \bar{\nu}_e \\
 \rightarrow \pi^- + \mu^+ + \nu_\mu & \rightarrow \pi^+ + \mu^- + \bar{\nu}_\mu \\
 \mu^+ \rightarrow e^+ + \bar{\nu}_\mu + \nu_e & \mu^- \rightarrow e^- + \nu_\mu + \bar{\nu}_e
 \end{array}$$

The electrically charged component of the secondary beam is focused towards the far detector by the three magnetic horns. These horns direct charged particles of a particular polarity towards SK whilst defocusing the oppositely charged particles. This allows a mostly neutrino or mostly antineutrino beam to be used within the experiment, denoted as “forward horn current (FHC)” or “reverse horn current (RHC)” respectively.

Figure 3.7 illustrates the different contributions to the FHC and RHC neutrino flux.

The low energy flux is dominated by the decay of pions whereas kaon decay becomes the dominant source of neutrinos for $E_\nu > 3\text{GeV}$. The “wrong-sign” component, which is the $\bar{\nu}_\mu$ background in a ν_μ beam, and the intrinsic irreducible ν_e background, are predominantly due to muon decay for $E_\nu < 2\text{GeV}$. As the antineutrino production cross-section is smaller than the neutrino cross-section, the wrong-sign component is more dominant in the RHC beam as compared to that in the FHC beam.

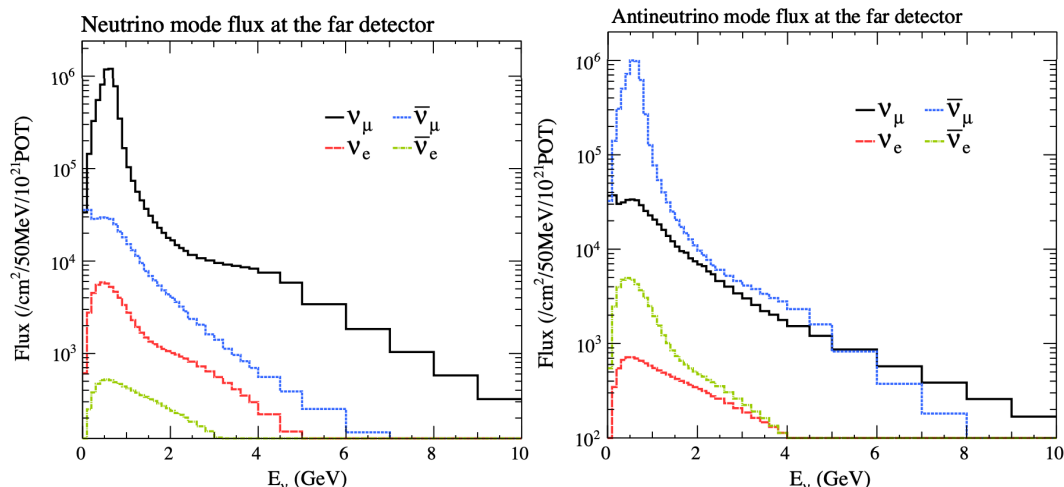


Figure 3.7: The Monte Carlo prediction of the energy spectrum for each flavour of neutrino (ν_e , $\bar{\nu}_e$, ν_μ and $\bar{\nu}_\mu$) in the neutrino dominated beam FHC mode (Left) and antineutrino dominated beam RHC mode (Right) expected at SK. Taken from [120].

The beam dump, situated at the end of the decay volume, stops all charged particles other than highly energetic muons ($p_\mu > 5\text{GeV}$). The MuMon detector monitors the

758 penetrating muons to determine the beam direction and intensity which is used to
759 constrain some of the beam flux systematics within the analysis [119, 121].

760 The T2K experiment uses an off-axis beam to narrow the neutrino energy distribution.
761 This was the first implementation of this technique in a long-baseline neutrino
762 oscillation experiment after its original proposal [122]. Pion decay, $\pi \rightarrow \mu + \nu_\mu$, is a
763 two-body decay. Consequently, the neutrino energy, E_ν , can be determined based on
764 the pion energy, E_π , and the angle at which the neutrino is emitted, θ ,

$$E_\nu = \frac{m_\pi^2 - m_\mu^2}{2(E_\pi - p_\pi \cos(\theta))}, \quad (3.5)$$

765 where m_π and m_μ are the mass of the pion and muon respectively. For a fixed
766 energy pion, the neutrino energy distribution is dependent upon the angle at which the
767 neutrinos are observed from the initial pion beam direction. For the 295km baseline at
768 T2K, $E_\nu = 0.6\text{GeV}$ maximises the electron neutrino appearance probability, $P(\nu_\mu \rightarrow \nu_e)$,
769 whilst minimising the muon disappearance probability, $P(\nu_\mu \rightarrow \nu_\mu)$. Figure 3.8
770 illustrates the neutrino energy distribution for a range of off-axis angles, as well as the
771 oscillation probabilities most relevant to T2K.

772 3.2.2 The Near Detector at 280m

773 Whilst all the near detectors are situated in the same “pit” located at 280m from the
774 beamline, the “ND280” detector is the off-axis detector which is situated at the same
775 off-axis angle as the Super-Kamiokande far detector. It has two primary functions;
776 firstly it measures the neutrino flux and secondly it counts the event rates of different
777 types of neutrino interactions. Both of these constrain the flux and cross-section

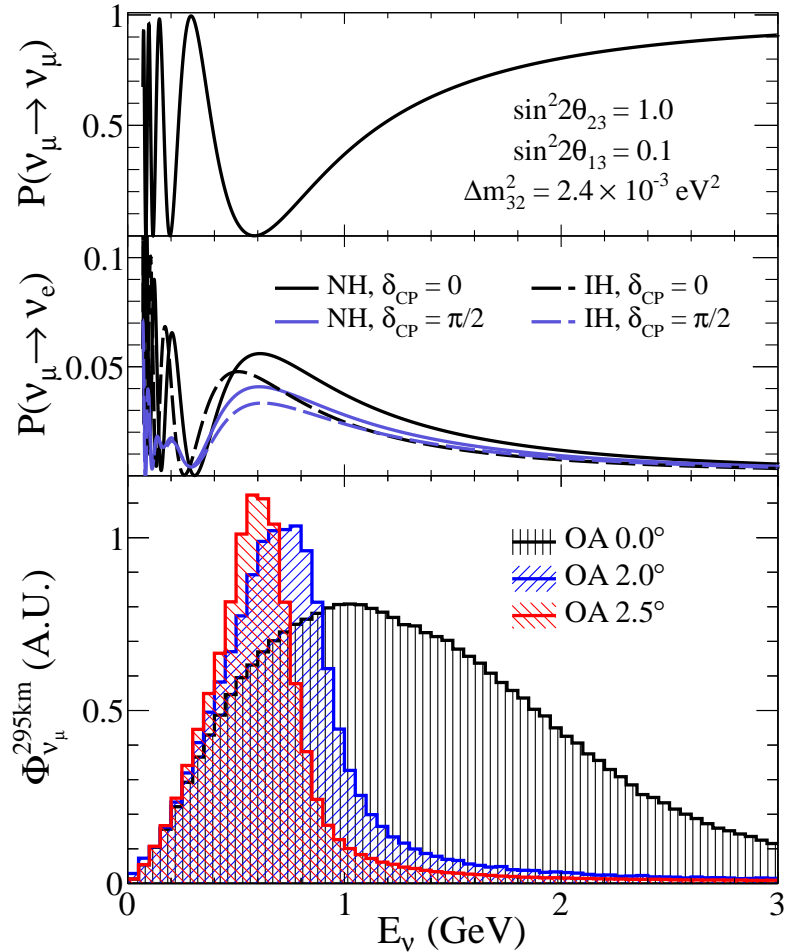


Figure 3.8: Top panel: T2K muon neutrino disappearance probability as a function of neutrino energy. Middle panel: T2K electron neutrino appearance probability as a function of neutrino energy. Bottom panel: The neutrino flux distribution for three different off-axis angles (Arbitrary units) as a function of neutrino energy.

systematics invoked within the model for a more accurate prediction of the expected event rate at the far detector.

As illustrated in Figure 3.9, the ND280 detector consists of several sub-detectors. The most important part of the detector for this analysis is the tracker region. This is comprised of two time projection chambers (TPCs) sandwiched between three fine grain detectors (FGDs). The FGDs contain both hydrocarbon plastics and water targets for neutrino interactions and provide track reconstruction near the interaction vertex. The emitted charged particles can then propagate into the TPCs which provide particle identification and momentum reconstruction. The FGDs and TPCs are

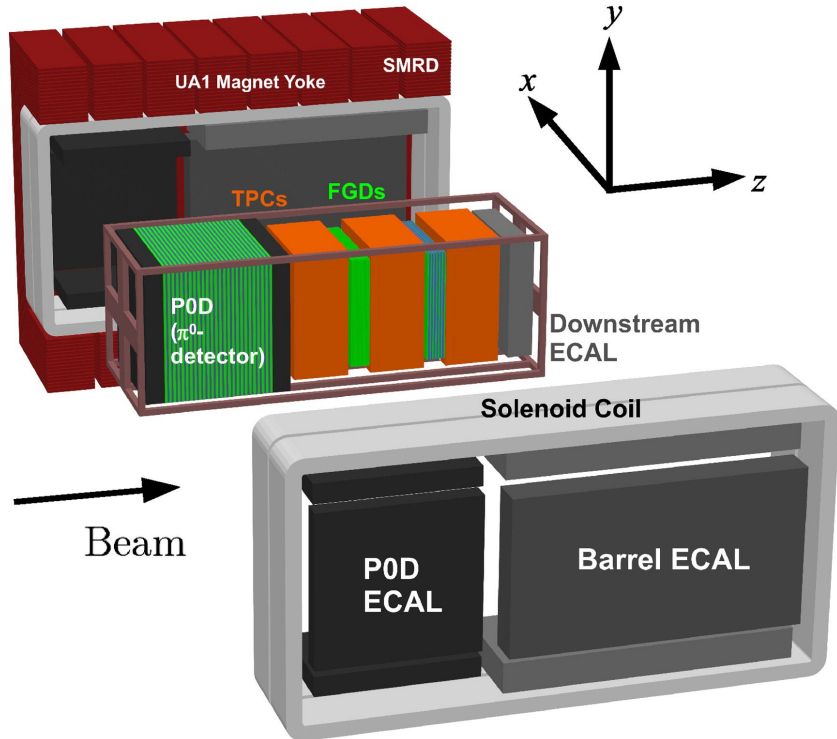


Figure 3.9: The components of the ND280 detector. The neutrino beam travels from left to right. Taken from [118].

787 further described in subsubsection 3.2.2.1 and subsubsection 3.2.2.2 respectively. The
 788 electromagnetic calorimeter (ECAL) encapsulates the tracker region alongside the π^0
 789 detector (P0D). The ECAL measures the deposited energy from photons emitted from
 790 interactions within the FGD. The P0D constrains the cross-section of neutral current
 791 interactions which generate neutral pions, which is one of the largest backgrounds in
 792 the electron neutrino appearance oscillation channel. The P0D and ECAL detectors
 793 are detailed in subsubsection 3.2.2.3 and subsubsection 3.2.2.4 respectively. The entire
 794 detector is located within a large yoke magnet which produces a 0.2T magnetic field.
 795 This design of the magnet also includes a scintillating detector called the side muon
 796 range detector (SMRD) which is used to track high-angle muons as well as acting as a
 797 cosmic veto. The SMRD is described in subsubsection 3.2.2.5.

798 3.2.2.1 Fine Grained Detectors

799 The T2K tracker region is comprised of two fine grained detectors (FGD) and three
800 Time Projection Chambers (TPC). A detailed description of the FGD design, construc-
801 tion, and assembly is found in [123] and summarised below. The FGDs are the primary
802 target for neutrino interactions with a mass of 1.1 tonnes per FGD. Alongside this,
803 the FGDs are designed to be able to track short-range particles which do not exit the
804 FGD. Typically, short-range particles are low momentum and are observed as tracks
805 that deposit a large amount of energy per unit length. This means the FGD needs
806 good granularity to resolve these particles. The FGDs have the best timing resolution
807 ($\sim 3\text{ns}$) of any of the sub-detectors of the ND280 detector. As such, the FGDs are
808 used for time of flight measurements to distinguish forward going positively charged
809 particles from backward going negatively charged particles. Finally, any tracks which
810 pass through multiple sub-detectors are required to be track matched to the FGD.

811 Both FGDs are made from square scintillator planes of side length 186cm and
812 width 2.02cm. Each plane consists of two layers of 192 scintillator bars in an X or Y
813 orientation. A wavelength shifting fiber is threaded through the center of each bar and
814 is read out by a multi-pixel photon counter (MPPC). FGD1 is the most upstream of
815 the two FGDs and contains 15 planes of carbon plastic scintillator which is a common
816 target in external neutrino scattering data. As the far detector is a pure water target, 7
817 of the 15 scintillator planes in FGD2 have been replaced with a hybrid water-scintillator
818 target. Due to the complexity of the nucleus, nuclear effects can not be extrapolated
819 between different nuclei. Therefore having the ability to take data on one target which
820 is the same as external data and another target which is the same as the far detector
821 target is beneficial for reliable model parameter estimates.

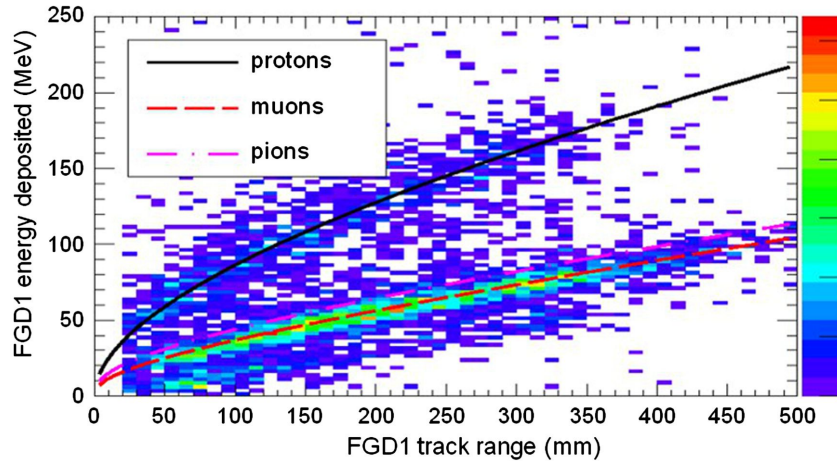


Figure 3.10: Comparison of data to Monte Carlo prediction of integrated deposited energy as a function of track length for particles that stopped in FGD1. Taken from [123].

The integrated deposited energy is used for particle identification. The FGD can distinguish protons from other charged particles by comparing the integrated deposited energy from data to Monte Carlo prediction as seen in Figure 3.10.

3.2.2.2 Time Projection Chambers

The majority of particle identification and momentum measurements within ND280 are provided by three Time Projection Chambers (TPCs) [124]. The TPCs are located on either side of the FGDs. They are located inside of the magnetic field meaning the momentum of a charged particle can be determined from the bending of the track.

Each TPC module consists of two gas-tight boxes, as shown in Figure 3.11, which are made of non-magnetic material. The outer box is filled with CO₂ which acts as an electrical insulator between the inner box and the ground. The inner box forms the field cage which produces a uniform electric drift field of $\sim 275\text{V}/\text{cm}$ and is filled with an argon gas mixture. Charged particles moving through this gas mixture ionize the gas and the ionised charge is drifted towards micromegas detectors which measure the ionization charge. The time and position information in the readout allows a three-dimensional image of the neutrino interaction.

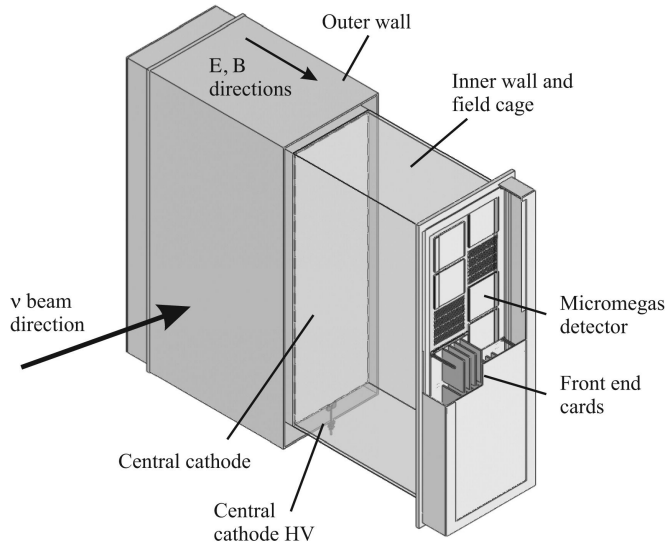


Figure 3.11: Schematic design of a Time Projection Chamber detector. Taken from [124].

The particle identification of tracks that pass through the TPCs is performed using

dE/dx measurements. Figure 3.12 illustrates the data to Monte Carlo distributions of the energy lost by a charged particle passing through the TPC as a function of the reconstructed particle momentum. The resolution is $7.8 \pm 0.2\%$ meaning that electrons and muons can be distinguished. This allows reliable measurements of the intrinsic ν_e component of the beam.

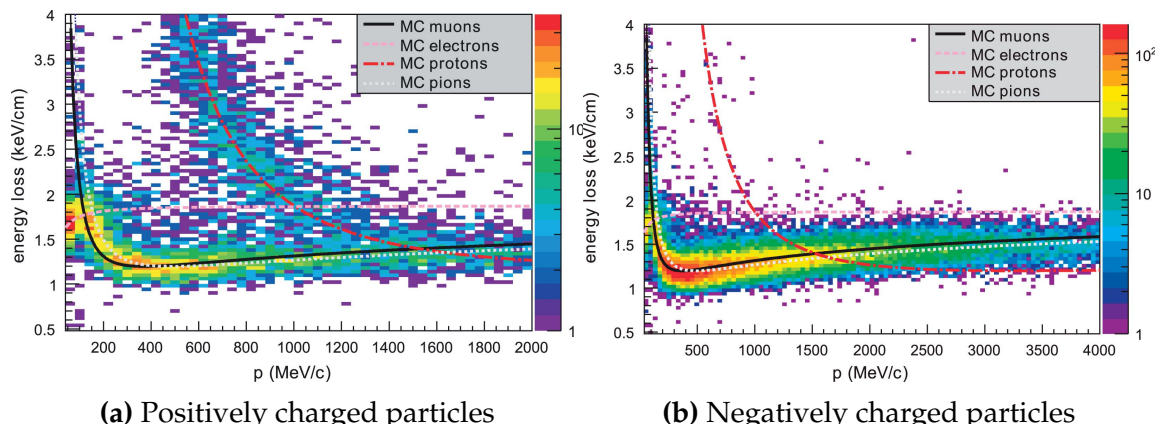


Figure 3.12: The distribution of energy loss as a function of reconstructed momentum for charged particles passing through the TPC, comparing data to Monte Carlo prediction. Taken from [124].

⁸⁴⁴ 3.2.2.3 π^0 Detector

⁸⁴⁵ If one of the γ -rays from a $\pi^0 \rightarrow 2\gamma$ decay is missed at the far detector, the recon-
⁸⁴⁶ struction will determine that event to be a charge current ν_e -like event. This is one of
⁸⁴⁷ the main backgrounds hindering the electron neutrino appearance searches. The π^0
⁸⁴⁸ detector (P0D) measures the cross-section of the neutral current induced neutral pion
⁸⁴⁹ production on a water target to constrain this background.

⁸⁵⁰ The P0D is a cube of approximately 2.5m length consisting of layers of scintillating
⁸⁵¹ bars, brass and lead sheets, and water bags as illustrated in Figure 3.13. Two electro-
⁸⁵² magnetic calorimeters are positioned at the most upstream and most downstream
⁸⁵³ position in the sub-detector and the water target is situated in between them. The
⁸⁵⁴ scintillator layers are built from two triangular bars orientated in opposite directions
⁸⁵⁵ to form a rectangular layer. Each triangular scintillator bar is threaded with optical
⁸⁵⁶ fiber which is read out by MPPCs. The high-Z brass and lead regions produce electron
⁸⁵⁷ showers from the photons emitted in π^0 decay.

⁸⁵⁸ The sub-detector can generate measurements of NC1 π^0 cross-sections on a water
⁸⁵⁹ target by measuring the event rate both with and without the water target, with the
⁸⁶⁰ cross-section on a water target being determined as the difference. The total active
⁸⁶¹ mass is 16.1 tonnes when filled with water and 13.3 tonnes when empty.

⁸⁶² 3.2.2.4 Electromagnetic Calorimeter

⁸⁶³ The electromagnetic calorimeter [126] (ECal) encapsulates the P0D and tracking sub-
⁸⁶⁴ detectors. Its primary purpose is to aid π^0 reconstruction from any interaction in
⁸⁶⁵ the tracker. To do this, it measures the energy and direction of photon showers from
⁸⁶⁶ $\pi^0 \rightarrow 2\gamma$ decay. It can also distinguish pion and muon tracks depending on the shape
⁸⁶⁷ of the photon shower deposited.

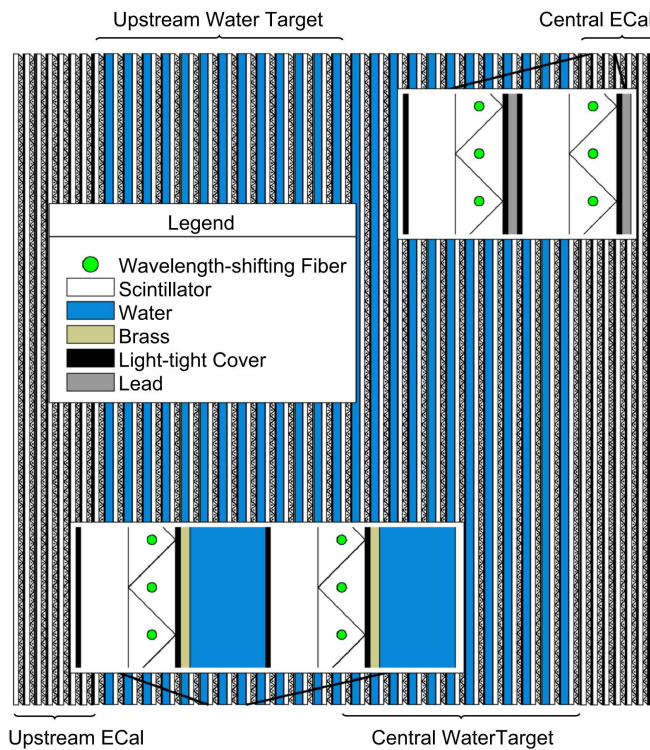


Figure 3.13: A schematic of the P0D side-view. Taken from [125].

The ECal is comprised of three sections; the P0D ECal which surrounds the P0D, the barrel ECal which encompasses the tracking region, and the downstream ECal which is situated downstream of the tracker region. The barrel and downstream ECals are tracking calorimeters that focus on electromagnetic showers from high-angle particles emitted from the tracking sub-detectors. Particularly in the TPC, high-angle tracks (those which travel perpendicularly to the beam-axis) can travel along a single scintillator bar resulting in very few hits. The width of the barrel and downstream ECal corresponds to ~ 11 electron radiation lengths to ensure a significant amount of the π^0 energy is contained. As the P0D has its own calorimetry which reconstructs showers, the P0D ECal determines the energy which escapes the P0D.

Each ECal is constructed of multiple layers of scintillating bars sandwiched between lead sheets. The scintillating bars are threaded with optical fiber and read out by MPPCs. Each sequential layer of the scintillator is orientated perpendicular to the previous which allows a three dimensional event reconstruction. The target mass

882 of the P0D ECal, barrel ECal, and downstream ECal are 1.50, 4.80 and 6.62 tonnes
883 respectively.

884 **3.2.2.5 Side Muon Range Detector**

885 As illustrated in Figure 3.9, the ECal, FGDs, P0D, and TPCs are enclosed within the
886 UA1 magnet. Originally designed for the NOMAD [127] experiment and reconditioned
887 for use in the T2K experiment [128], the UA1 magnet provides a uniform horizontal
888 magnetic field of 0.2T with an uncertainty of 2×10^{-4} T.

889 Built into the UA1 magnet, the side muon range detector (SMRD) [129] monitors
890 high-energy muons which leave the tracking region and permeate through the ECal.
891 It additionally acts as a cosmic muon veto and trigger.

892 **3.2.3 The Interactive Neutrino GRID**

893 The Interactive Neutrino GRID (INGRID) detector is situated within the same “pit” as
894 the other near detectors. It is aligned with the beam in the “on-axis” position and mea-
895 sures the beam direction, spread, and intensity. The detector was originally designed
896 with 16 identical modules [118] (two modules have since been decommissioned) and a
897 “proton” module. The design of the detector is cross-shaped with length and height
898 10m × 10m as illustrated in Figure 3.14.

899 Each module is composed of iron sheets interlaced with eleven tracking scintillator
900 planes for a total target mass of 7.1 tonnes per module. The scintillator design is an X-Y
901 pattern of 24 bars in both orientations, where each bar contains wave-length shifting
902 fibers which are connected to multi-pixel photon counters (MPPCs). Each module is
903 encapsulated inside veto planes to aid the rejection of charged particles entering the
904 module.

905 The proton module is different from the other modules in that it consists of entirely
 906 scintillator planes with no iron target. The scintillator bars are also smaller than those
 907 used in the other modules to increase the granularity of the detector and improve
 908 tracking capabilities. The module sits in the center of the beamline and is designed to
 909 give precise measurements of quasi-elastic charged current interactions to evaluate
 910 the performance of the Monte Carlo simulation of the beamline.

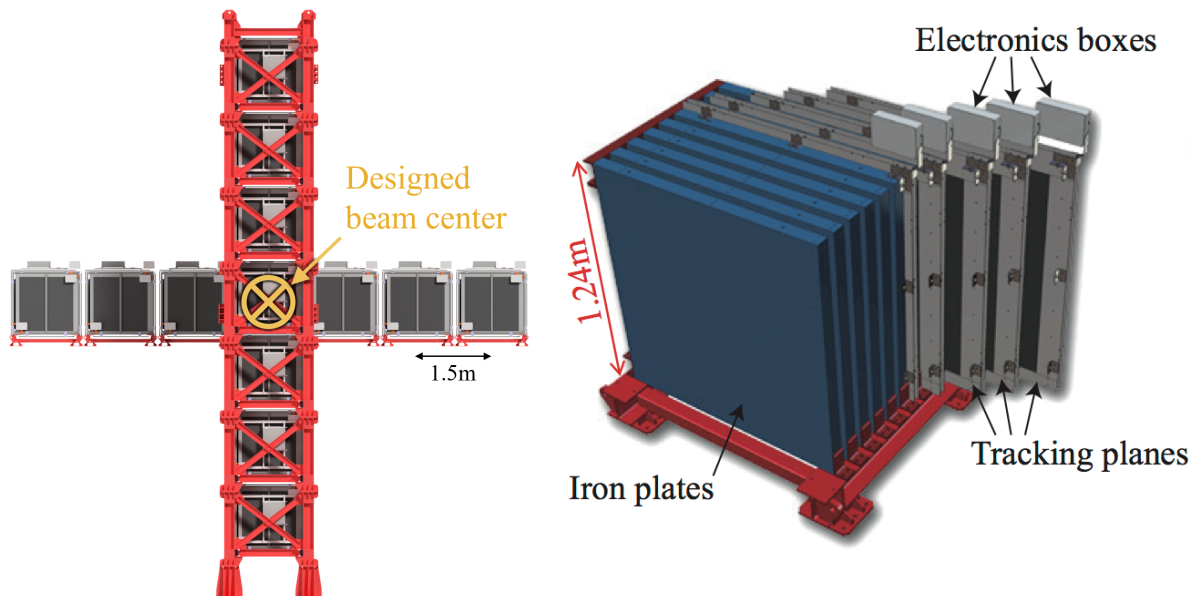


Figure 3.14: Left panel: The Interactive Neutrino GRID on-axis Detector. 14 modules are arranged in a cross-shape configuration, with the center modules being directly aligned with the on-axis beam. Right panel: The layout of a single module of the INGRID detector. Both figures are recreated from [118].

911 The INGRID detector can measure the beam direction to an uncertainty of 0.4mrad
 912 and the beam center within a resolution of 10cm [118]. The beam direction in both the
 913 vertical and horizontal directions is discussed in [130] and it is found to be in good
 914 agreement with the MUMON monitor described in subsection 3.2.1.

915 **Chapter 4**

916 **Bayesian Statistics and Markov Chain**
917 **Monte Carlo Techniques**

918 This thesis presents a Bayesian oscillation analysis. To extract the oscillation parameters,
919 a Markov Chain Monte Carlo (MCMC) method is used. This chapter explains
920 the theory of how parameter estimates can be determined using this technique and
921 condenses the material found in the literature [131–134].

922 The oscillation parameter determination presented within this thesis is built upon
923 a simultaneous fit to neutrino beam data in the near detector, beam data at SK and
924 atmospheric data at SK. In total, there are four oscillation parameters of interest
925 ($\sin^2(\theta_{23})$, $\sin^2(\theta_{13})$, Δm_{23}^2 , and δ_{CP}), two oscillation parameters to which this study
926 will not be sensitive ($\sin^2(\theta_{12})$, Δm_{12}^2) and many nuisance parameters that control the
927 systematic uncertainty models invoked within this study.

928 The MCMC technique generates a multi-dimensional probability distribution across
929 all of the model parameters used in the fit. To determine the parameter estimate of a
930 single parameter, this multi-dimensional object is integrated over all other parameters.
931 This process is called Marginalisation and is further described in subsection 4.3.1.
932 Monte Carlo techniques approximate the probability distribution of each parameter
933 within the limit of generating infinite samples. As ever, generating a large number of
934 samples is time and resource-dependent. Therefore, an MCMC technique is utilised
935 within this analysis to reduce the required number of steps to sufficiently sample the
936 parameter space. This technique is described in further detail in subsection 4.2.1.

⁹³⁷ 4.1 Bayesian Statistics

⁹³⁸ Bayesian inference treats observable data, D , and model parameters, $\vec{\theta}$, on equal
⁹³⁹ footing such that a probability model of both data and parameters is required. This is
⁹⁴⁰ the joint probability distribution $P(D, \vec{\theta})$ and can be described by the prior distribution
⁹⁴¹ for model parameters $P(\vec{\theta})$ and the likelihood of the data given the model parameters
⁹⁴² $P(D|\vec{\theta})$,

$$P(D, \vec{\theta}) = P(D|\vec{\theta})P(\vec{\theta}). \quad (4.1)$$

⁹⁴³ The prior distribution, $P(\vec{\theta})$, describes all previous knowledge about the parameters
⁹⁴⁴ within the model. For example, if the risk of developing health problems is known
⁹⁴⁵ to increase with age, the prior distribution would describe the increase. For the
⁹⁴⁶ purpose of this analysis, the prior distribution is typically the best-fit values taken
⁹⁴⁷ from external data measurements with a Gaussian uncertainty. The prior distribution
⁹⁴⁸ can also contain correlations between model parameters. In an analysis using Monte
⁹⁴⁹ Carlo techniques, the likelihood of measuring some data assuming some set of model
⁹⁵⁰ parameters is calculated by comparing the Monte Carlo prediction generated at that
⁹⁵¹ particular set of model parameters to the data.

⁹⁵² It is parameter estimation that is important for this analysis and as such, we apply
⁹⁵³ Bayes' theorem [135] to calculate the probability for each parameter to have a certain
⁹⁵⁴ value given the observed data, $P(\vec{\theta}|D)$, which is known as the posterior distribution
⁹⁵⁵ (often termed the posterior). This can be expressed as

$$P(\vec{\theta}|D) = \frac{P(D|\vec{\theta})P(\vec{\theta})}{\int P(D|\vec{\theta})P(\vec{\theta})d\vec{\theta}}. \quad (4.2)$$

956 The denominator in Equation 4.2 is the integral of the joint probability distribution

957 over all values of all parameters used within the fit. For brevity, we say that the
958 posterior distribution is

$$P(\vec{\theta}|D) \propto P(D|\vec{\theta})P(\vec{\theta}). \quad (4.3)$$

959 In subsection 4.3.1, we see that for the cases used within this analysis, it is reason-
960 able to know the posterior to some normalisation constant.

961 4.2 Monte Carlo Simulation

962 Monte Carlo techniques are used to numerically solve a complex problem that does
963 not necessarily have an analytical solution. These techniques rely on building a large
964 ensemble of samples from an unknown distribution and then using the ensemble to
965 approximate the properties of the distribution.

966 An example that uses Monte Carlo techniques is to calculate the area underneath
967 a curve. For example, take the problem of calculating the area under a straight line
968 with gradient $M = 0.4$ and intercept $C = 1.0$. Analytically, one can calculate the area
969 under the line is equal to 30 units for $0 \leq x \leq 10$. Using Monte Carlo techniques,
970 one can calculate the area under this line by throwing many random values for the x
971 and y components of each sample and then calculating whether that point falls below

the line. The area can then be calculated by the ratio of points below the line to the total number of samples thrown multiplied by the total area in which samples were scattered. The study is shown in Figure 4.1 highlights this technique and finds the area under the curve to be 29.9 compared to an analytical solution of 30.0. The deviation of the numerical to analytical solution can be attributed to the number of samples used in the study. The accuracy of the approximation in which the properties of the Monte Carlo samples replicate those of the desired distribution is dependent on the number of samples used. Replicating this study with a differing number of Monte Carlo samples used in each study (As shown in Figure 4.2) highlights how the Monte Carlo techniques are only accurate within the limit of a high number of samples.

Whilst the above example has an analytical solution, these techniques are just as applicable to complex solutions. Clearly, any numerical solution is only as useful as its efficiency. As discussed, the accuracy of the Monte Carlo technique is dependent upon the number of samples generated to approximate the properties of the distribution. Furthermore, if the positions at which the samples are evaluated are not ‘cleverly’ picked, the efficiency of the Monte Carlo technique significantly drops. Given the example in Figure 4.1, if the region in which the samples are scattered significantly extends passed the region of interest, many calculations will be calculated but do not add to the ability of the Monte Carlo technique to achieve the correct result. For instance, any sample evaluated at a $y \geq 5$ could be removed without affecting the final result. This does bring in an aspect of the ‘chicken and egg’ problem in that to achieve efficient sampling, one needs to know the distribution beforehand.

4.2.1 Markov Chain Monte Carlo

This analysis utilises a multi-dimensional probability distribution, with some dimensions being significantly more constrained than others. This could be from prior

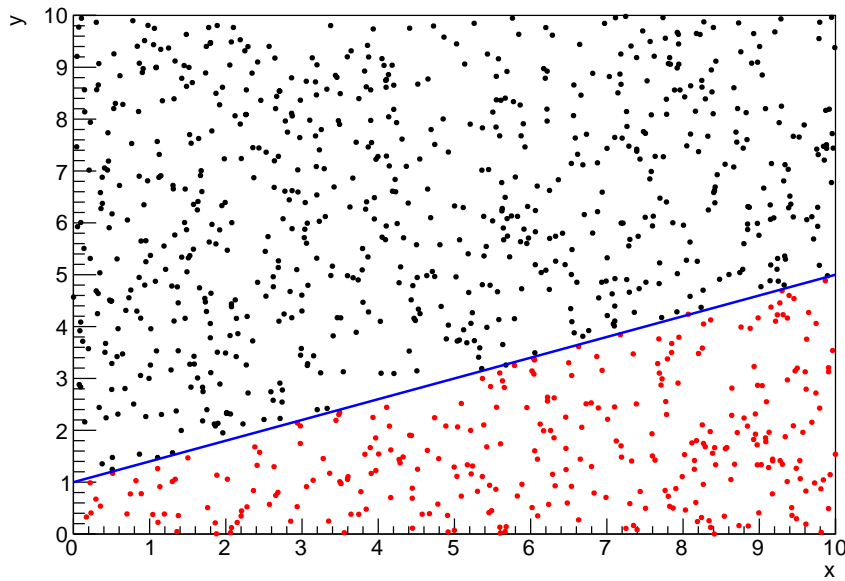


Figure 4.1: Example of using Monte Carlo techniques to find the area under the blue line. The gradient and intercept of the line are 0.4 and 1.0 respectively. The area found to be under the curve using one thousand samples is 29.9 units.

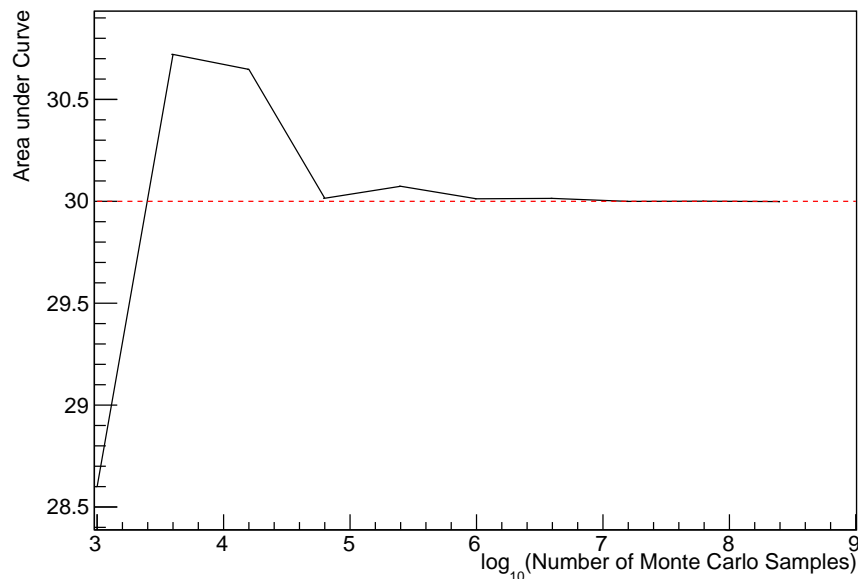


Figure 4.2: The area under a line of gradient 0.4 and intercept 1.0 for the range $0 \leq x \leq 10$ as calculated using Monte Carlo techniques as a function of the number of samples used in each repetition. The analytical solution to the area is 30 units as given by the red line.

knowledge of parameter distributions from external data or un-physical regions in which parameters can not exist. Consequently, the Monte Carlo techniques used need to be as efficient as possible. For this analysis, the Markov Chain Monte Carlo (MCMC) technique is chosen. An MCMC technique is a Monte Carlo technique that uses a Markov chain to select which points at which to sample the parameter distribution. This technique performs a semi-random stochastic walk through the allowable parameter space. This builds a posterior distribution which has the property that the density of sampled points is proportional to the probability density of that parameter. This does mean that the samples produced by this technique are not statistically independent but they will cover the space of the distribution.

A Markov chain functions by selecting the position of step \vec{x}_{i+1} based on the position of \vec{x}_i . The space in which the Markov chain selects samples is dependent upon the total number of parameters utilised within the fit, where a discrete point in this space is described by the N-dimensional space \vec{x} . In a perfectly operating Markov chain, the position of the next step depends solely on the previous step and not on the further history of the chain (\vec{x}_0, \vec{x}_1 , etc.). However, in solving the multi-dimensionality of the fit used within this analysis, each step becomes correlated with several of the steps preceding itself. This behaviour is further explained in subsection 4.2.3. Providing the MCMC chain is well optimised, it will begin to converge towards a unique stationary distribution. The period between the chain's initial starting point and the convergence to the unique stationary distribution is colloquially known as the burn-in period. This is discussed further in subsection 4.2.3. Once the chain reaches the stationary distribution, all points sampled after that point will look like samples from that distribution.

1021 Further details of the theories underpinning MCMC techniques are discussed
1022 in [132] but can be summarised by the requirement that the chain satisfies the three
1023 ‘regularity conditions’:

- 1024 • Irreducibility: From every position in the parameter space \vec{x} , there must exist a
1025 non-zero probability for every other position in the parameter space to be reached.
- 1026 • Recurrence: Once the chain arrives at the stationary distribution, every step fol-
1027 lowing from that position must be samples from the same stationary distribution.
- 1028 • Aperiodicity: The chain must not repeat the same sequence of steps at any point
1029 throughout the sampling period.

1030 The output of the chain after burn-in (ie. the sampled points after the chain
1031 has reached the stationary distribution) can be used to approximate the posterior
1032 distribution and model parameters $\vec{\theta}$. To achieve the requirement that the unique
1033 stationary distribution found by the chain be the posterior distribution, one can use
1034 the Metropolis-Hastings algorithm. This guides the stochastic process depending on
1035 the likelihood of the current proposed step compared to that of the previous step.
1036 Implementation and other details of this technique are discussed in subsection 4.2.2.

1037 4.2.2 Metropolis-Hastings Algorithm

1038 As a requirement for MCMCs, the Markov chain implemented in this technique must
1039 have a unique stationary distribution that is equivalent to the posterior distribution.
1040 To ensure this requirement and that the regularity conditions are met, this analysis
1041 utilises the Metropolis-Hastings (MH) algorithm [136,137]. For the i^{th} step in the chain,
1042 the MH algorithm determines the position in the parameter space to which the chain
1043 moves to based on the current step, \vec{x}_i , and the proposed step, \vec{y}_{i+1} . The proposed step
1044 is randomly selected from some proposal function $f(\vec{x}_{i+1} | \vec{x}_i)$, which depends solely

1045 on the current step (ie. not the further history of the chain). The next step in the chain
 1046 \vec{x}_{i+1} can be either the current step or the proposed step determined by whether the
 1047 proposed step is accepted or rejected. To decide if the proposed step is selected, the
 1048 acceptance probability, $\alpha(\vec{x}_i, \vec{y}_i)$, is calculated as

$$\alpha(\vec{x}_i, \vec{y}_{i+1}) = \min \left(1, \frac{P(\vec{y}_{i+1}|D)f(\vec{x}_i|\vec{y}_{i+1})}{P(\vec{x}_i|D)f(\vec{y}_{i+1}|\vec{x}_i)} \right). \quad (4.4)$$

1049 Where $P(\vec{y}_{i+1}|D)$ is the posterior distribution as introduced in section 4.1. To
 1050 simplify this calculation, the proposal function is required to be symmetric such that
 1051 $f(\vec{x}_i|\vec{y}_{i+1}) = f(\vec{y}_{i+1}|\vec{x}_i)$. In practice, a multi-variate Gaussian distribution is used to
 1052 throw parameter proposals from. This reduces Equation 4.4 to

$$\alpha(\vec{x}_i, \vec{y}_{i+1}) = \min \left(1, \frac{P(\vec{y}_{i+1}|D)}{P(\vec{x}_i|D)} \right). \quad (4.5)$$

1053 After calculating this quantity, a random number, β , is generated uniformly be-
 1054 tween 0 and 1. If $\beta \leq \alpha(\vec{x}_i, \vec{y}_{i+1})$, the proposed step is accepted. Otherwise, the chain
 1055 sets the next step equal to the current step and this procedure is repeated. This can be
 1056 interpreted as if the posterior probability of the proposed step is greater than that of
 1057 the current step, ($P(\vec{y}_{i+1}|D) \geq P(\vec{x}_i|D)$), the proposed step will always be accepted.
 1058 If the opposite is true, ($P(\vec{y}_{i+1}|D) \leq P(\vec{x}_i|D)$), the proposed step will be accepted
 1059 with probability $P(\vec{x}_i|D)/P(\vec{y}_{i+1}|D)$. This ensures that the Markov chain does not get
 1060 trapped in any local minima in the potentially non-Gaussian posterior distribution.
 1061 The outcome of this technique is that the density of steps taken in a discrete region is
 1062 directly proportional to the probability density in that region.

¹⁰⁶³ 4.2.3 MCMC Optimisation

¹⁰⁶⁴ As discussed in subsection 4.2.2, the proposal function invoked within the MH algo-
¹⁰⁶⁵ rithm can take any form and the chain will still converge to the stationary distribution.
¹⁰⁶⁶ At each set of proposed parameter values, a prediction of the same spectra has to be
¹⁰⁶⁷ generated which requires significant computational resources. Therefore, the number
¹⁰⁶⁸ of steps taken before the unique stationary distribution is found should be minimised
¹⁰⁶⁹ as only steps after convergence add information to the oscillation analysis. Further-
¹⁰⁷⁰ more, the chain should entirely cover the allowable parameter space to ensure that all
¹⁰⁷¹ values have been considered. Tuning the distance that the proposal function jumps
¹⁰⁷² between steps on a parameter-by-parameter basis can both minimise the length of the
¹⁰⁷³ burn-in period and ensure that the correlation between step \vec{x}_i and \vec{x}_j is sufficiently
¹⁰⁷⁴ small.

¹⁰⁷⁵ The effect of changing the width of the proposal function is highlighted in Figure 4.3.
¹⁰⁷⁶ Three scenarios, each with the same underlying stationary distribution (A Gaussian of
¹⁰⁷⁷ width 1.0 and mean 0.), are presented. The only difference between the three scenarios
¹⁰⁷⁸ is the width of the proposal function, colloquially known as the ‘step size σ ’. Each
¹⁰⁷⁹ scenario starts at an initial parameter value of 10.0 which would be considered an
¹⁰⁸⁰ extreme variation. For the case where $\sigma = 0.1$, it is clear to see that the chain takes
¹⁰⁸¹ a long time to reach the expected region of the parameter. This indicates that this
¹⁰⁸² chain would have a large burn-in period and does not converge to the stationary
¹⁰⁸³ distribution until step ~ 500 . Furthermore, whilst the chain does move towards the
¹⁰⁸⁴ expected region, each step is significantly correlated with the previous. Considering
¹⁰⁸⁵ the case where $\sigma = 5.0$, the chain approaches the expected parameter region almost
¹⁰⁸⁶ instantly meaning that the burn-in period is not significant. However, there are clearly
¹⁰⁸⁷ large regions of steps where the chain does not move. This is likely due to the chain
¹⁰⁸⁸ proposing steps in the tails of the distribution which have a low probability of being

1089 accepted. Consequently, this chain would take a significant number of steps to fully
 1090 span the allowable parameter region. For the final scenario, where $\sigma = 0.5$, you can see
 1091 a relatively small burn-in period of approximately 100 steps. Once the chain reaches
 1092 the stationary distribution, it moves throughout the expected region of parameter
 1093 values many times, sufficiently sampling the full parameter region. This example is a
 1094 single parameter varying across a continuous distribution and does not fully reflect
 1095 the difficulties in the many-hundred multi-variate parameter distribution used within
 1096 this analysis. However, it does give a conceptual idea of the importance of selecting
 1097 the proposal function and associated step size.

1098 As discussed, step size tuning directly correlates to the average step acceptance
 1099 rate. If the step size is too small, many steps will be accepted but the chain moves
 1100 slowly. If the opposite is true, many steps will be rejected as the chain proposes steps
 1101 in the tails of the distribution. Discussion in [138] suggests that the ‘ideal’ acceptance
 1102 rate of a high dimension MCMC chain should be approximately $\sim 25\%$. An “ideal”
 1103 step size [138] of

$$\sigma = \frac{2.4}{N_p}, \quad (4.6)$$

1104 where N_p is the number of parameters included in the MCMC fit. However, the
 1105 complex correlations between systematics mean that some parameters have to be hand
 1106 tuned and many efforts have been taken to select a set of parameter-by-parameter step
 1107 sizes to approximately reach the ideal acceptance rate.

1108 Figure 4.3 highlights the likelihood as calculated by the fit in [DB: Link to AsimovA](#)
 1109 **Sensitivity Section** as a function of the number of steps in each chain. In practice,
 1110 many independent MCMC chains are run simultaneously to parallelise the task of

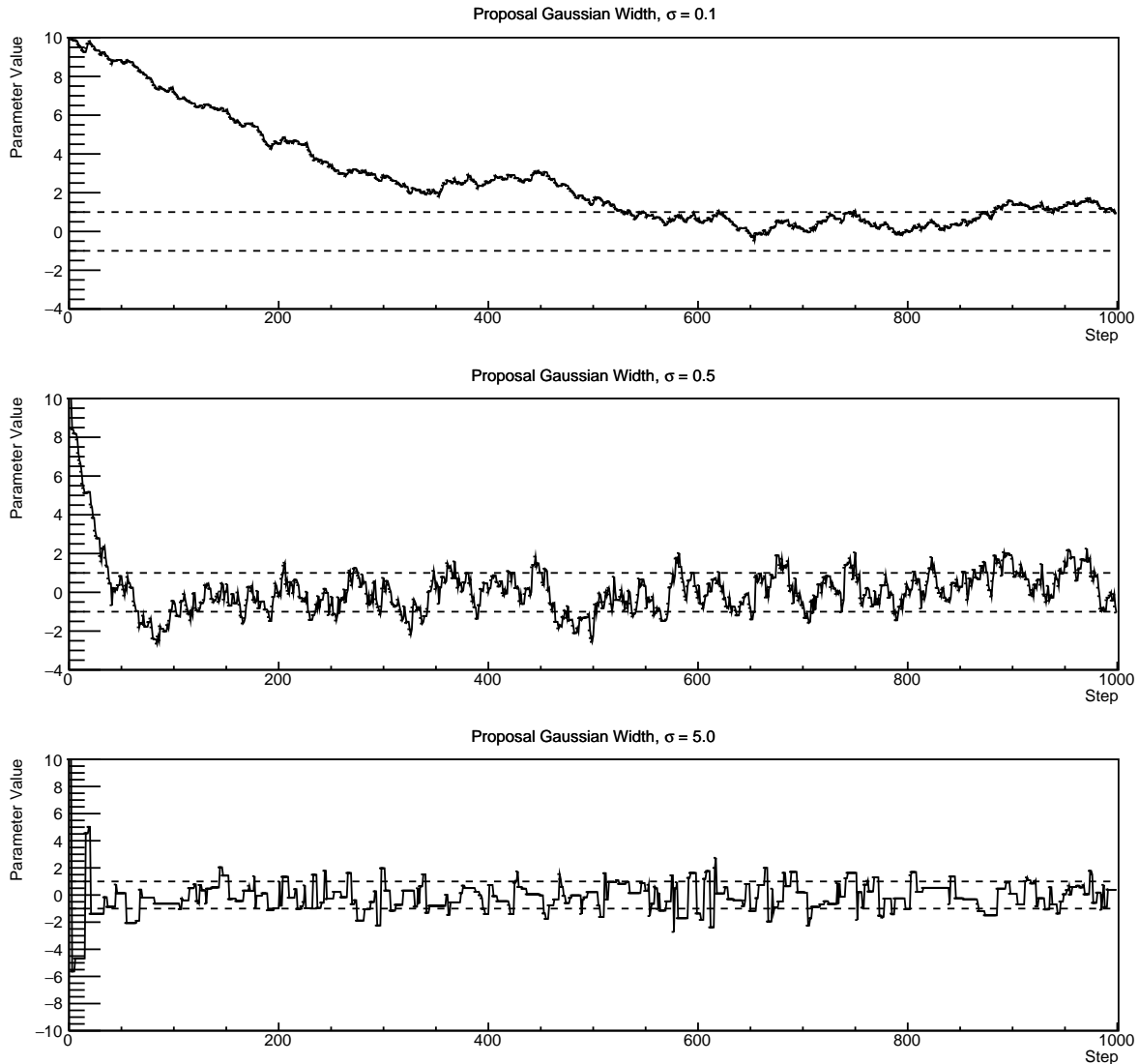


Figure 4.3: Three MCMC chains, each with a stationary distribution equal to a Gaussian centered at 0 and width 1 (As indicated by the black dotted lines). All of the chains use a Gaussian proposal function but have different widths (or ‘step size σ ’). The top panel has $\sigma = 0.1$, middle panel has $\sigma = 0.5$ and the bottom panel has $\sigma = 5.0$.

1111 performing the fit. This figure overlays the distribution found in each chain. As seen,
 1112 the likelihood decreases from its initial value and converges towards a stationary
 1113 distribution after $\sim 1 \times 10^5$ steps.

1114 Multiple configurations of this analysis have been performed throughout this thesis
 1115 where different samples or systematics have been used. For all of these configurations,
 1116 it was found that a burnin period of 1×10^5 was sufficient in all cases.

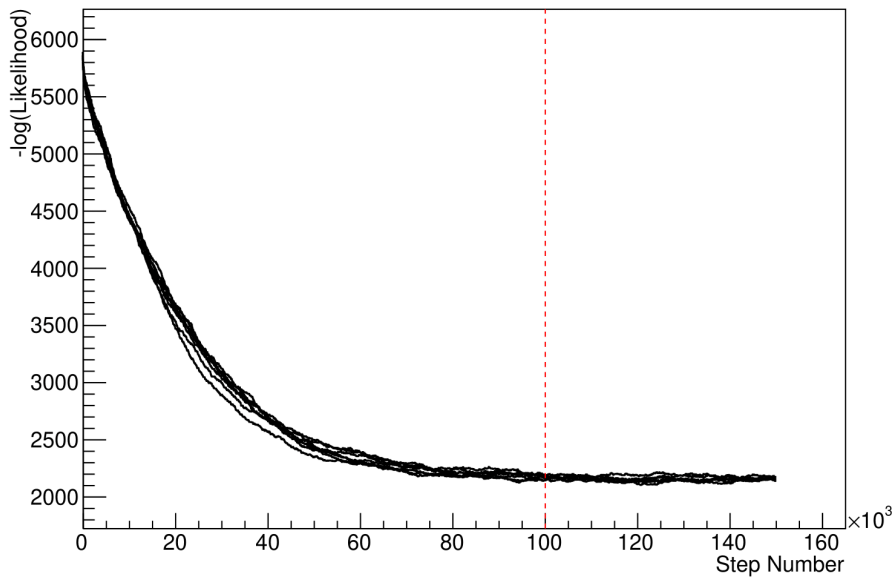


Figure 4.4: The log-likelihood from the fit detailed in DB: [Link to AsimovA Sensitivity Section](#) as a function of the number of steps accumulated in each fit. Many independent MCMC chains were run in parallel and overlaid on this plot. The red line indicates the 1×10^5 step burn-in period after which the log-likelihood becomes stable.

1117 4.3 Understanding the MCMC Results

1118 The previous sections have described how to generate the posterior probability distri-
1119 bution using Bayesian MCMC techniques. However, this analysis focuses on oscillation
1120 parameter determination. The posterior distribution output from the chain is a high
1121 dimension object, with as many dimensions as there are parameters included in the os-
1122 cillation analysis. However, this multi-dimensional object is difficult to conceptualize
1123 so parameter estimations are often presented in one or two-dimensional projections
1124 of this probability distribution. To do this, we invoke the marginalisation technique
1125 highlighted in subsection 4.3.1.

¹¹²⁶ 4.3.1 Marginalisation

¹¹²⁷ The output of the MCMC chain is a highly dimensional probability distribution
¹¹²⁸ which is very difficult to interpret. From the standpoint of an oscillation analysis
¹¹²⁹ experiment, the one or two-dimensional ‘projections’ of the oscillation parameters of
¹¹³⁰ interest are most relevant. Despite this, the best fit values and uncertainties on the
¹¹³¹ oscillation parameters of interest should correctly encapsulate the correlations to the
¹¹³² other systematic uncertainties (colloquially called ‘nuisance’ parameters). For this joint
¹¹³³ beam and atmospheric analysis, the oscillation parameters of interest are $\sin^2(\theta_{23})$,
¹¹³⁴ $\sin^2(\theta_{13})$, Δm_{23}^2 , and δ_{CP} . All other parameters (Including the oscillation parameter
¹¹³⁵ this fit is insensitive to) are deemed nuisance parameters. To generate these projections,
¹¹³⁶ we rely upon integrating the posterior distribution over all nuisance parameters. This
¹¹³⁷ is called marginalisation. A simple example of this technique is to imagine the scenario
¹¹³⁸ where two coins are flipped. To determine the probability that the first coin returned
¹¹³⁹ a ‘head’, the exact result of the second coin flip is disregarded and simply integrated
¹¹⁴⁰ over. For the parameters of interest, $\vec{\theta}_i$, we can calculate the marginalised posterior by
¹¹⁴¹ integrating over the nuisance parameters, $\vec{\theta}_n$. In this case, Equation 4.2 becomes

$$P(\vec{\theta}_i|D) = \frac{\int P(D|\vec{\theta}_i, \vec{\theta}_n)P(\vec{\theta}_i, \vec{\theta}_n)d\vec{\theta}_n}{\int P(D|\vec{\theta})P(\vec{\theta})d\vec{\theta}} \quad (4.7)$$

¹¹⁴² Where $P(\vec{\theta}_i, \vec{\theta}_n)$ encodes the prior knowledge about the uncertainty and correlations
¹¹⁴³ between the parameters of interest and the nuisance parameters. In practice, this
¹¹⁴⁴ is simply taking the one or two-dimensional projection of the multi-dimensional
¹¹⁴⁵ probability distribution.

Whilst in principle an easy solution to a complex problem, correlations between the interesting and nuisance parameters can bias the marginalised results. A similar effect is found when the parameters being marginalised over have non-Gaussian probability distributions. For example, Figure 4.5 highlights the marginalisation bias in the probability distribution found for a parameter when requiring a correlated parameter to have a positive parameter value. Due to the complex nature of this oscillation parameter fit presented in this thesis, there are correlations occurring between the oscillation parameters of interest and the other nuisance parameters included in the fit.

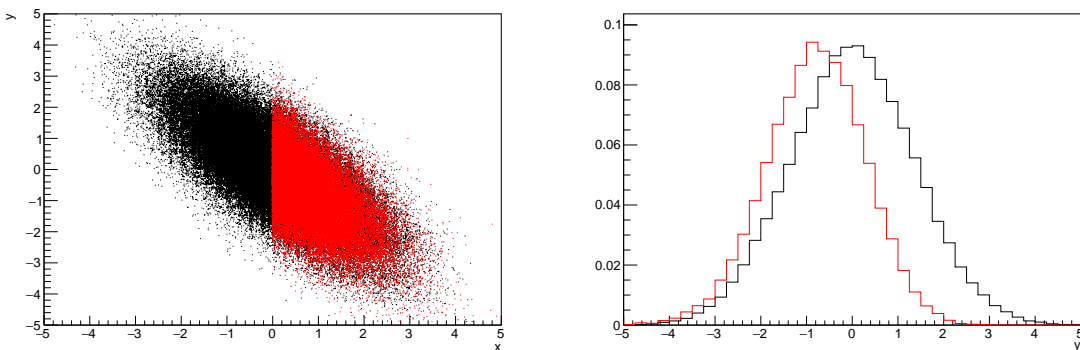


Figure 4.5: Left: The two dimensional probability distribution for two correlated parameters x and y . The red distribution shows the two dimensional probability distribution when $0 \leq x \leq 5$. Right: The marginalised probability distribution for the y parameter found when requiring the x to be bound between $-5 \leq x \leq 5$ and $0 \leq x \leq 5$ for the black and red distribution, respectively.

4.3.2 Parameter Estimation and Credible Intervals

The purpose of this analysis is to determine the best fit values for the oscillation parameters that the beam and atmospheric samples are sensitive to: $\sin^2(\theta_{23})$, $\sin^2(\theta_{13})$, Δm_{23}^2 , and δ_{CP} . Typically, the results presented take the form of one or two-dimension marginalised probability distributions for the appearance ($\sin^2(\theta_{13})$ and δ_{CP}) and disappearance ($\sin^2(\theta_{23})$ and Δm_{23}^2) parameters. The posterior probability density

₁₁₆₁ taken from the output MCMC chain is binned in these parameters. The parameter
₁₁₆₂ best-fit point is then taken to be the value that has the highest posterior probability.
₁₁₆₃ This is performed in both one and two-dimensional projections.

₁₁₆₄ However, the single best-fit point in a given parameter is not of much use on its
₁₁₆₅ own. We would also like to determine the uncertainty, or credible interval, on that
₁₁₆₆ best-fit point. The definition of the 1σ credible interval is that we have 68% belief that
₁₁₆₇ the parameter is within those bounds. For a more generalised definition, the credible
₁₁₆₈ interval is the region, R , of the posterior distribution that contains a specific fraction of
₁₁₆₉ the total probability, such that

$$\int_R P(\theta|D)d\theta = \alpha \quad (4.8)$$

₁₁₇₀ Where θ is the parameter on which we calculate the credible interval. This technique
₁₁₇₁ then calculates the $\alpha \times 100\%$ credible interval.

₁₁₇₂ In practice, this analysis uses the highest posterior density (HPD) credible intervals
₁₁₇₃ which are calculated through the following method. First, the probability distribution
₁₁₇₄ is area-normalised such that it has an integrated area equal to 1.0. The bins of proba-
₁₁₇₅ bility are then summed from the highest to lowest until the sum exceeds the 1σ level
₁₁₇₆ (0.68 in this example). This process is repeated for a range of credible intervals, notably
₁₁₇₇ the 1σ , 2σ and 3σ along with other levels where the critical values for each level can
₁₁₇₈ be found in [139]. This process can be repeated for the two-dimensional probability
₁₁₇₉ distributions by creating two-dimensional contours of credible intervals rather than a
₁₁₈₀ one-dimensional result.

¹¹⁸¹ 4.3.3 Bayesian Model Comparisons

¹¹⁸² Due to the matter resonance, this analysis has some sensitivity to the mass hierarchy
¹¹⁸³ of neutrino states (whether Δm_{23}^2 is positive or negative) and the octant of $\sin^2(\theta_{23})$
¹¹⁸⁴ . The Bayesian approach utilised within this analysis gives an intuitive method of
¹¹⁸⁵ model comparison by determining which hypothesis is most favourable. Taking the
¹¹⁸⁶ ratio of Equation 4.3 for the two hypotheses of normal hierarchy, NH , and inverted
¹¹⁸⁷ hierarchy, IH , gives

$$\frac{P(\vec{\theta}_{NH}|D)}{P(\vec{\theta}_{IH}|D)} = \frac{P(D|\vec{\theta}_{NH})}{P(D|\vec{\theta}_{IH})} \times \frac{P(\vec{\theta}_{NH})}{P(\vec{\theta}_{IH})}. \quad (4.9)$$

¹¹⁸⁸ The middle term defines the Bayes factor which is a data-driven interpretation of
¹¹⁸⁹ how strong the data prefers one hierarchy to the other. For this analysis, equal priors
¹¹⁹⁰ on both mass hierarchy hypotheses are chosen ($P(\vec{\theta}_{NH}) = P(\vec{\theta}_{IH}) = 0.5$). In practice,
¹¹⁹¹ the MCMC chain proposes a value of $|\Delta m_{23}^2|$ and then applies a 50% probability
¹¹⁹² that the value is sign flipped. Consequently, the Bayes factor can be calculated from
¹¹⁹³ the ratio of the probability density in either hypothesis. This equates to counting the
¹¹⁹⁴ number of steps taken in the normal and inverted hierarchies and taking the ratio. The
¹¹⁹⁵ same approach can be taken to compare the upper octant (UO) compared to the lower
¹¹⁹⁶ octant (LO) hypothesis of $\sin^2(\theta_{23})$.

¹¹⁹⁷ Whilst the value of the Bayes factor should always be shown, the Jeffreys scale [140]
¹¹⁹⁸ (highlighted in Table 4.1) gives an indication of the strength of preference for one model
¹¹⁹⁹ compared to the other. Other interpretations of the strength of preference of a model
¹²⁰⁰ exist, e.g. the Kass and Raferty Scale [141].

$\log_{10}(B_{AB})$	B_{AB}	Strength of Preference
< 0.0	< 1	No preference for hypothesis A (Supports hypothesis B)
0.0 – 0.5	1.0 – 3.16	Preference for hypothesis A is weak
0.5 – 1.0	3.16 – 10.0	Preference for hypothesis A is substantial
1.0 – 1.5	10.0 – 31.6	Preference for hypothesis A is strong
1.5 – 2.0	31.6 – 100.0	Preference for hypothesis A is very strong
> 2.0	> 100.0	Decisive preference for hypothesis A

Table 4.1: Jeffreys scale for strength of preference for two models A and B as a function of the calculated Bayes factor ($B_{AB} = B(A/B)$) between the two models [140]. The original scale is given in terms of $\log_{10}(B(A/B))$ but converted to linear scale for easy comparison throughout this thesis.

1201 4.3.4 Comparison of MCMC Output to Expectation

1202 To ensure the fit is performing well, a best-fit spectrum is produced using the pos-
 1203 terior probability distribution and compared with the data, allowing easy by-eye
 1204 comparisons to be made. A simple method of doing this is to perform a comparison
 1205 in the fitting parameters (For instance, the reconstructed neutrino energy and lepton
 1206 direction for T2K far detector beam samples) of the spectra generated by the MCMC
 1207 chain to ‘data’. This ‘data’ could be true data or some variation of Monte Carlo predic-
 1208 tion. This allows easy comparison of the MCMC probability distribution to the data.
 1209 To perform this, N steps from the post burn-in MCMC chain are randomly selected
 1210 (Where for all plots of this style in this thesis, $N = 3000$). From these, the Monte Carlo
 1211 prediction at each step is generated by reweighting the model parameters to the values
 1212 specified at that step. Due to the probability density being directly correlated with
 1213 the density of steps in a certain region, parameter values close to the best fit value are
 1214 most likely to be selected.

1215 In practice, for each bin of the fitting parameters has a probability distribution
 1216 of event rates, with one entry per sampled MCMC step. This distribution is binned
 1217 where the bin with the highest probability is selected as the mean and an error on

1218 the width of this probability distribution is calculated using the approach highlighted
1219 in subsection 4.3.2. Consequently, the best fit distribution in the fit parameter is not
1220 necessarily that which would be attained by reweighting the Monte Carlo prediction
1221 to the most probable parameter values.

1222 A similar study can be performed to illustrate the freedom of the model parameter
1223 space prior to the fit. This can be done by throwing parameter values from the prior
1224 uncertainty of each parameter. This becomes troublesome for parameters with no
1225 prior uncertainty as the range is technically infinite. Where applicable solutions to
1226 remove these have been addressed.

1227 **Chapter 5**

1228 **Simulation, Reconstruction, and Event
Reduction**

1230 As a crucial part of the oscillation analysis, an accurate prediction of the expected
1231 neutrino spectrum at the far detector is required. This includes modeling the flux
1232 generation, neutrino interactions, and detector effects. All of the simulation packages
1233 required to do this are briefly described in section 5.1. The reconstruction of neutrino
1234 events inside the far detector, including the `fitQun` algorithm, is documented in
1235 section 5.2. This also includes data quality checks of the SK-V data which the author
1236 performed for the T2K oscillation analysis presented at Neutrino 2020 [80]. Finally,
1237 section 5.3 describes the steps taken in the SK detector to trigger on events of interest
1238 whilst removing the comparatively large rate of cosmic ray muon events.

1239 **5.1 Simulation**

1240 In order to generate a Monte Carlo prediction of the expected event rate at the far
1241 detector, all the processes in the beam and atmospheric flux, neutrino interaction, and
1242 detector need to be modeled. Each of these parts is individually modeled and each of
1243 them is detailed below.

1244 The beamline simulation consists of three distinct parts: the initial hadron inter-
1245 action modeled by FLUKA [142], the target station geometry and particle tracking

1246 performed by JNUBEAM, [143, 144] and any hadronic re-interactions simulated by
1247 GCALOR [145]. The primary hadronic interactions are $O(10)\text{GeV}$, where FLUKA
1248 matches external cross-section data better than GCALOR [146]. However, FLUKA
1249 is not very adaptable so a small simulation is built to model the interactions in the
1250 target and the output is then passed to JNUBEAM and GCALOR for propagation.
1251 The hadronic interactions are tuned to data from the NA61/SHINE [147–149] and
1252 HARP [150] experiments. The tuning is done by reweighting the FLUKA and GCALOR
1253 predictions to match the external data multiplicity and cross-section measurements,
1254 based on final state particle kinematics [146]. The culmination of this simulation
1255 package generates the predicted flux for neutrino and antineutrino beam modes which
1256 are illustrated in Figure 3.7.

1257 The atmospheric neutrino flux predictions are simulated by the HKKM model
1258 [43, 45]. The primary cosmic ray flux is tuned to AMS [151] and BESS [152] data assum-
1259 ing the US-standard atmosphere '76 [153] density profile and includes geomagnetic
1260 field effects. The primary cosmic rays interact to generate pions and muons. The
1261 interaction of these secondary particles to generate neutrinos is handled by DPMJET-
1262 III [154] for energies above 32GeV and JAM [45, 155] for energies below that value **DB:**
1263 **Question for Giles: Why different generators for above/below 32GeV?** These hadronic
1264 interactions are tuned to BESS and L3 data [156, 157] using the same methodology
1265 as the tuning of the beamline simulation. The energy and cosine zenith predictions
1266 of $\nu_e, \bar{\nu}_e, \nu_\mu, \bar{\nu}_\mu$ flux are given in Figure 2.3 and Figure 2.5, respectively. The flux is
1267 approximately symmetrical and peaked around the horizon ($\cos(\theta_Z) = 0.0$). This is be-
1268 cause horizontally-going pions and kaons can travel further than their vertically-going
1269 counterparts resulting in a larger probability of decaying to neutrinos. The symmetry
1270 is broken in low-energy neutrinos due to geomagnetic effects, which modify the track
1271 of the primary cosmic rays. Updates to the HKKM model are currently ongoing [158].

Once a flux prediction has been made for all three detectors, NEUT 5.4.0 [159, 160] models the interactions of the neutrinos in the detectors. For the purposes of this analysis, quasi-elastic (QE), meson exchange (MEC), single meson production (PROD), coherent pion production (COH), and deep inelastic scattering (DIS) interactions are simulated. These interaction categories can be further broken down by whether they were propagated via a W^\pm boson in Charged Current (CC) interactions or via a Z^0 boson in Neutral Current (NC) interactions. CC interactions have a charged lepton in the final state, which can be flavour-tagged in reconstruction to determine the flavour of the neutrino. In contrast, NC interactions have a neutrino in the final state so no flavour information can be determined from the observables left in the detector after an interaction. This is the reason why NC events are assumed to not oscillate within this analysis. Both CC and NC interactions are modeled for all the above interaction categories, other than MEC interactions which are only modeled for CC events. The SK detector is only sensitive to charged particles, so all charged current interactions are simulated whilst only neutral current processes that produce charged mesons (NCDIS, NCCOH, and NCProd) are modeled. NC MEC interactions can only produce charged particles through secondary re-interactions which is a low cross-section process.

As illustrated in Figure 5.1, CC QE interactions dominate the low-energy cross-section of neutrino interactions. The NEUT implementation adopts the Llewellyn Smith [161] model for neutrino-nucleus interactions, where the nuclear ground state of any bound nucleons (neutrino-oxygen interactions) is approximated by a spectral-function [162] model that simulates the effects of Fermi momentum and Pauli blocking. The cross-section of QE interactions are controlled by vector and axial-vector form factors parameterised by the BBBA05 [163] model and a dipole form factor with $M_A^{QE} = 1.21\text{GeV}$ fit to external data [164], respectively. NEUT implements the Valencia [165] model to simulate MEC events, where two nucleons and two holes in the nuclear target are produced (Often called 2p2h interactions).

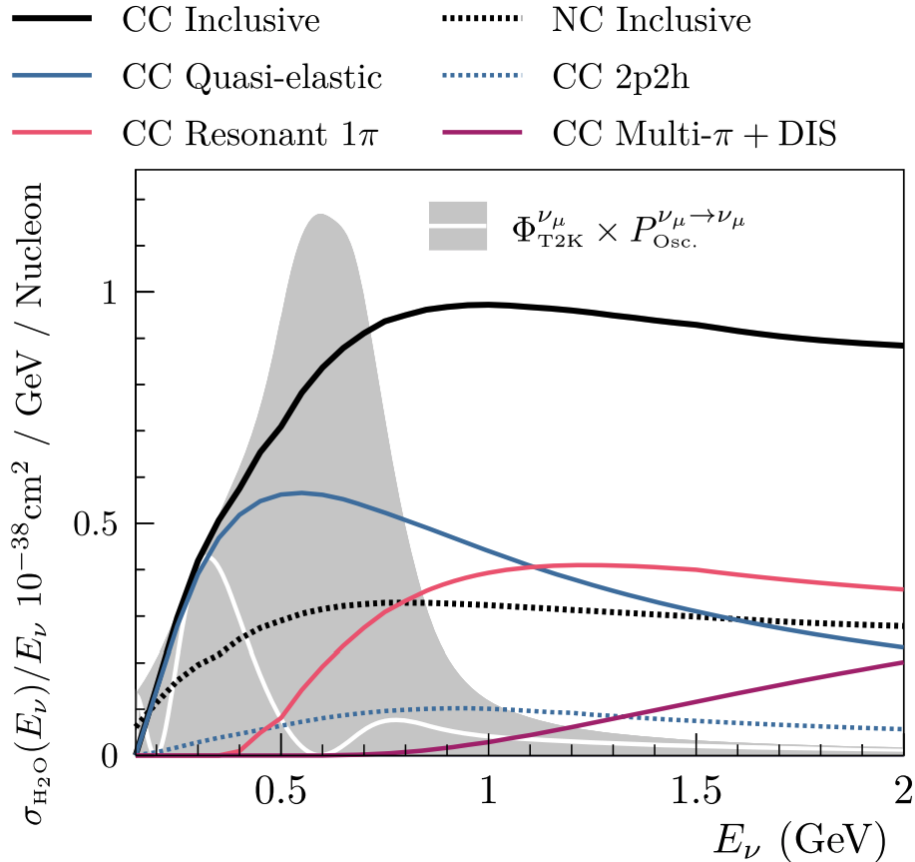


Figure 5.1: The NEUT prediction of the ν_μ -H₂O cross-section overlaid on the T2K ν_μ flux. The charged current (black, solid) and neutral current (black, dashed) inclusive, charged current quasi-elastic (blue, solid), charged current 2p2h (blue, dashed), charged current single pion production (pink), and charged current multi- π and DIS (Purple) cross-sections are illustrated. Figure taken from [159].

1299 For neutrinos of energy $O(1)\text{GeV}$, PROD interactions become dominant. These
 1300 predominantly produce charged and neutral pions although γ , kaon, and η production
 1301 is also considered. To simulate these interactions, the Berger-Sehgal [166] model is
 1302 implemented within NEUT. It simulates the excitation of a nucleon from a neutrino
 1303 interaction, production of an intermediate baryon, and the consequential decay to a
 1304 single meson or γ . Pions can also be produced through COH interactions, which occur
 1305 when the incoming neutrino interacts with the entire oxygen nuclei target leaving a
 1306 single pion outside of the nucleus. NEUT utilises the Berger-Sehgal [167] model to
 1307 simulate these COH interactions.

1308 DIS and multi- π producing interactions become the most dominant for energies
1309 $> O(5)\text{GeV}$. PYTHIA [168] is used to simulate any interaction with invariant mass,
1310 $W > 2\text{GeV}/c^2$, which produces at least one meson. For any interaction which produces
1311 at least two mesons but has $W < 2\text{GeV}/c^2$, the Bronner model is invoked [169].
1312 Both of these models use Parton distribution functions based on the Bodek-Yang
1313 model [170–172].

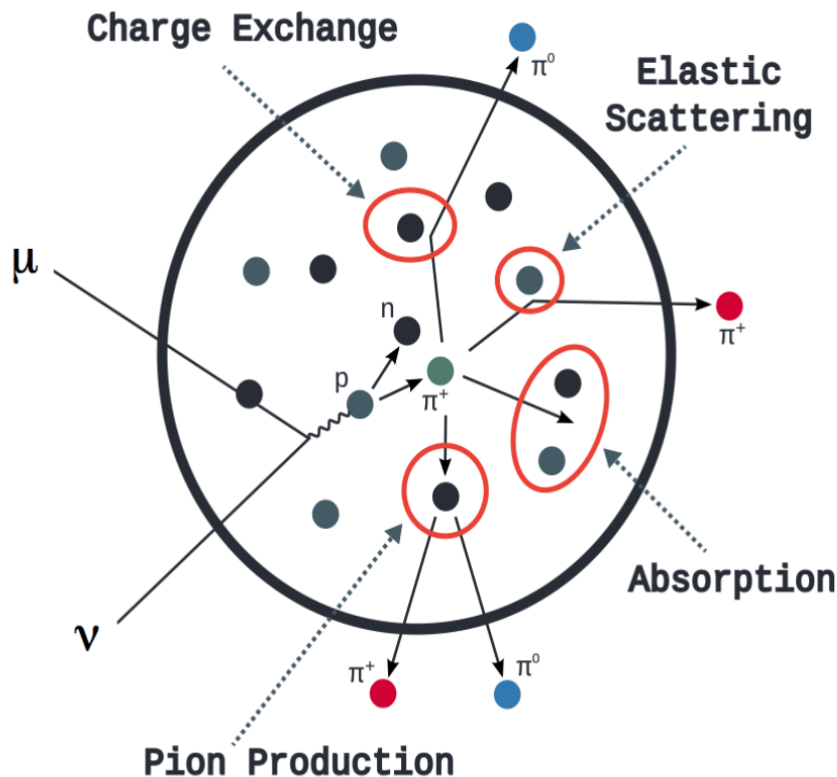


Figure 5.2: Illustration of the various processes which a pion can undergo before exiting the nucleus. Taken from [173].

1314 Any pion which is produced within the nucleus can re-interact through final state
1315 interactions before it exits, as illustrated by the scattering, absorption, production, and
1316 exchange interactions in Figure 5.2. These re-interactions alter the observable particles
1317 within the detector. For instance, if the charged pion from a CC PROD interaction is
1318 absorbed, the observables would mimic a CC QE interaction. To simulate these effects,

1319 NEUT uses a semi-classical intranuclear cascade model [159]. This cascade functions by
1320 stepping the pion through the nucleus in fixed-length steps equivalent to $dx = R_N/100$,
1321 where R_N is the radius of the nucleus. At each step, the simulation allows the pion
1322 to interact through scattering, charged exchange, absorption, or production with an
1323 interaction-dependent probability calculated from a fit to external data [174]. This
1324 cascade continues until the pion is absorbed or exits the nucleus.

1325 Once the final state particle kinematics have been determined from NEUT, they
1326 are passed into the detector simulation. The near detectors, ND280 and INGRID, are
1327 simulated using a GEANT4 package [118,175] to simulate the detector geometry, particle
1328 tracking, and energy deposition. The response of the detectors is simulated using
1329 the elecSim package [118]. The far detector simulation is based upon the original
1330 Kamiokande experiment software which uses the GEANT3-based SKDETSIM [118,176]
1331 package. This controls the interactions of particles in the water as well as Cherenkov
1332 light production. The water quality and PMT calibration measurements detailed in
1333 subsection 3.1.2 are also used within this simulation to make accurate predictions of
1334 the detector response.

1335 5.2 Event Reconstruction at SK

1336 Any above Cherenkov threshold event which occurs in SK will be recorded by the
1337 PMT array, where each PMT records the time and accumulated charge. This recorded
1338 information is shown in event displays similar to those illustrated in Figure 5.3. To
1339 be useful for physics analyses, this series of PMT hit information needs to be recon-
1340 structed to determine the particle's identity and kinematics (or track parameters):
1341 four-vertex, direction, and momenta. This is because the charge and timing distribu-
1342 tion of photons generated by a particular particle in an event is dependent upon its

1343 initial kinematics. The concept of distinguishing electron and muon events is from the
 1344 “fuzziness” of the ring. Muons are heavier and less affected by scattering or showering
 1345 meaning they typically produce “crisp” rings. Electrons are more likely to interact
 1346 via electromagnetic showering or scattering which results in larger variations of their
 1347 direction from the initial direction. Consequently, electrons typically produce “fuzzier”
 1348 rings compared to muons.

1349 For the purposes of this analysis, the `fitQun` reconstruction algorithm is utilised.
 1350 Its core function is to compare a prediction of the accumulated charge and timing
 1351 distribution from each PMT, generated for a particular particle identity and track
 1352 parameters, to that observed in the neutrino event. It determines the preferred values
 1353 by minimising a likelihood function which includes information from PMTs which
 1354 were hit and those that were not hit. The `fitQun` algorithm improves upon the APFit
 1355 reconstruction algorithm which has been used for many previous SK analyses. APFit
 1356 fits the vertex from timing information and then fits the momentum and direction
 1357 of the particle from PMT hits within a 43 deg Cherenkov cone (which assumes an
 1358 ultra-relativistic particle). It then fits the particle identity once the track parameters
 1359 have been fit. Conversely, `fitQun` performs a simultaneous fit of particle kinematics
 1360 and identity, improving both the accuracy of the fit parameters and the rejection of
 1361 neutral current π^0 events [177,178]. The `fitQun` algorithm is based on the key concepts
 1362 of the MiniBooNE reconstruction algorithm [179] and is described in [180] which is
 1363 summarised below.

1364 An event in SK can consist of multiple particles. For example, a charge current
 1365 muon neutrino interaction can generate two particles that have the potential of gen-
 1366 erating Cherenkov photons: the primary muon, and the secondary decay-electron
 1367 from the muon. To ensure both subevents are reconstructed separately, each event is
 1368 divided into time clusters which are called “subevents”. The number of subevents is

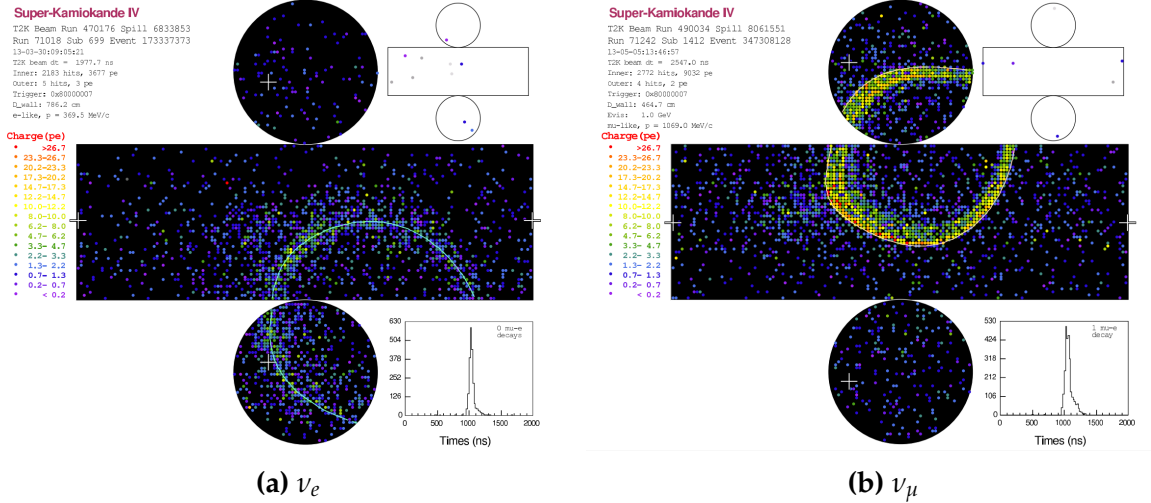


Figure 5.3: Event displays from Super Kamiokande illustrating the “crisp” ring from a muon and the typically “fuzzy” electron ring. Each pixel represents a PMT and the color scheme denotes the accumulated charge deposited on that PMT. Figures taken from [181].

equal to the number of decay electrons minus one (the primary event). To find all the subevents in an event, a vertex goodness metric is calculated for some vertex position \vec{x} and time t ,

$$G(\vec{x}, t) = \sum_i^{\text{hit PMTs}} \exp \left(-\frac{1}{2} \left(\frac{T_{Res}^i(\vec{x}, t)}{\sigma} \right)^2 \right) \quad (5.1)$$

where

$$T_{Res}^i(\vec{x}, t) = t^i - t - |R_{PMT}^i - \vec{x}| / c_n \quad (5.2)$$

is the residual hit time. It is the difference in time between the PMT hit time, t^i , of the i^{th} PMT and the expected time of the PMT hit if the photon was emitted at the start of the vertex. R_{PMT}^i is the position of the i^{th} PMT, c_n is the speed of light in

water and $\sigma = 4\text{ns}$ which is comparable to the time resolution of the PMT. When the proposed fit values of time and vertex are close to the true values, $T_{Res}^i(\vec{x}, t)$ tends to zero resulting in subevents appearing as spikes in the goodness metric. The proposed fit vertex and time are grid-scanned, and the values which maximise the goodness metric are selected as the “pre-fit vertex”. Whilst this predicts a vertex for use in the clustering algorithm, the final vertex is fit using the higher-precision maximum likelihood method described below.

Once the pre-fit vertex has been determined, the goodness metric is scanned as a function of t to determine the number of subevents. A peak-finding algorithm is then used on the goodness metric, requiring the goodness metric to exceed some threshold and drop below a reduced threshold before any subsequent additional peaks are considered. The thresholds are set such that the rate of false peak finding is minimised while still attaining good data to Monte Carlo agreement. To improve performance, the pre-fit vertex for each delayed subevent is re-calculated after PMT hits from the previous subevent are masked. This improves the decay-electron tagging performance. Once all subevents have been determined, the time window around each subevent is then defined by the earliest and latest time which satisfies $-180 < T_{Res}^i < 800\text{ns}$. The subevents and associated time windows are then used as seeds for further reconstruction.

For a given subevent, the `fiTQun` algorithm constructs a likelihood based on the accumulated charge q_i and time information t_i from the i^{th} PMT,

$$L(\Gamma, \vec{\theta}) = \prod_j^{\text{unhit}} P_j(\text{unhit}|\Gamma, \vec{\theta}) \prod_i^{\text{hit}} \{1 - P_i(\text{unhit}|\Gamma, \vec{\theta})\} f_q(q_i|\Gamma, \vec{\theta}) f_t(t_i|\Gamma, \vec{\theta}), \quad (5.3)$$

1397 where $\vec{\theta}$ defines the track parameters; vertex position, direction vector and mo-
 1398 ments, and Γ represents the particle hypothesis. $P_i(\text{unhit}|\Gamma, \vec{\theta})$ defines the probability
 1399 of the i^{th} tube to not register a hit given the track parameters and particle hypothesis.
 1400 The charge likelihood, $f_q(q_i|\Gamma, \vec{\theta})$, and time likelihood, $f_t(t_i|\Gamma, \vec{\theta})$, represent the prob-
 1401 ability density function of observing charge q_i and time t_i on the i^{th} PMT given the
 1402 specified track parameters and particle hypothesis.

1403 As the generation and propagation of the optical photons are independent of the
 1404 PMT and electronics response, it is natural to split the calculation into two. Firstly,
 1405 the expected number of photoelectrons (or predicted charge), $\mu_i = \mu_i(\vec{\theta}, \Gamma)$, at the i^{th}
 1406 PMT is calculated. This value is then substituted into the likelihood function. This
 1407 allows the charge likelihood density $f_q(q_i|\mu_i)$ and unhit probability $P_i(\text{unhit}|\mu_i)$ to be
 1408 expressed via quantities that are only dependent on the response of the PMT.

1409 The predicted charge is calculated based on contributions from both the direct
 1410 light and the scattered light. The direct light contribution is determined based on the
 1411 integration of the Cherenkov photon profile along the track. PMT angular acceptance,
 1412 water quality, and calibration measurements discussed in subsection 3.1.2 are included
 1413 to accurately predict the charge probability density at each PMT. The scattered light
 1414 is calculated in a similar way, although it includes a scattering function that depends
 1415 on the vertex of the particle and the position of the PMT. The charge likelihood is
 1416 calculated by comparing the prediction to the observed charge in the PMT.

1417 The time likelihood is approximated to depend on the vertex \vec{x} , direction \vec{d} , and
 1418 time t of the track parameters as well as the particle hypothesis. The expected time
 1419 for PMT hits is calculated by assuming unscattered photons being emitted from the
 1420 midpoint of the track, S_{mid} ,

$$t_{exp}^i = t + S_{mid}/c + |R_{PMT}^i - \vec{x} - S_{mid}\vec{d}|/c_n, \quad (5.4)$$

where c is the speed of light in a vacuum. The time likelihood is then expressed in terms of the residual difference between the PMT hit time and the expected hit time, $t_{Res}^i = t^i - t_{exp}^i$. The particle hypothesis and momentum also affect the Cherenkov photon distribution. These parameters modify the shape of the time likelihood density since in reality not all photons are emitted at the midpoint of the track. As with the charge likelihood, the contributions from both the direct and scattered light to the time likelihood density are calculated separately, which are both calculated from particle gun studies.

The track parameters and particle identity which maximise $L(\Gamma, \vec{\theta})$ are defined as the best-fit parameters. In practice MINUIT [182] is used to minimise the value of $-\ln L(\Gamma, \vec{\theta})$. The `fitQun` algorithm considers an electron-like, muon-like, and charged pion-like hypothesis for events with a single final state particle, denoted “single-ring events”. The particle’s identity is determined by taking the ratio of the likelihood of each of the hypotheses. For instance, electrons and muons are distinguished by considering the value of $\ln(L(e, \vec{\theta}_e)/L(\mu, \vec{\theta}_\mu))$ in comparison to the reconstructed momentum of the electron hypothesis [180]. This distance from this criteria is termed the PID parameter and is illustrated in Figure 5.4.

DB: Mentiton Pi0 rejection and mu/pip separation cuts

The `fitQun` algorithm also considers a π^0 hypothesis. To do this, it performs a fit looking for two standard electron-hypothesis tracks which point to the same four-vertex. This assumes the electron tracks are generated from photon-conversion so the electron tracks actually appear offset from the proposed π^0 vertex. For these fits, the

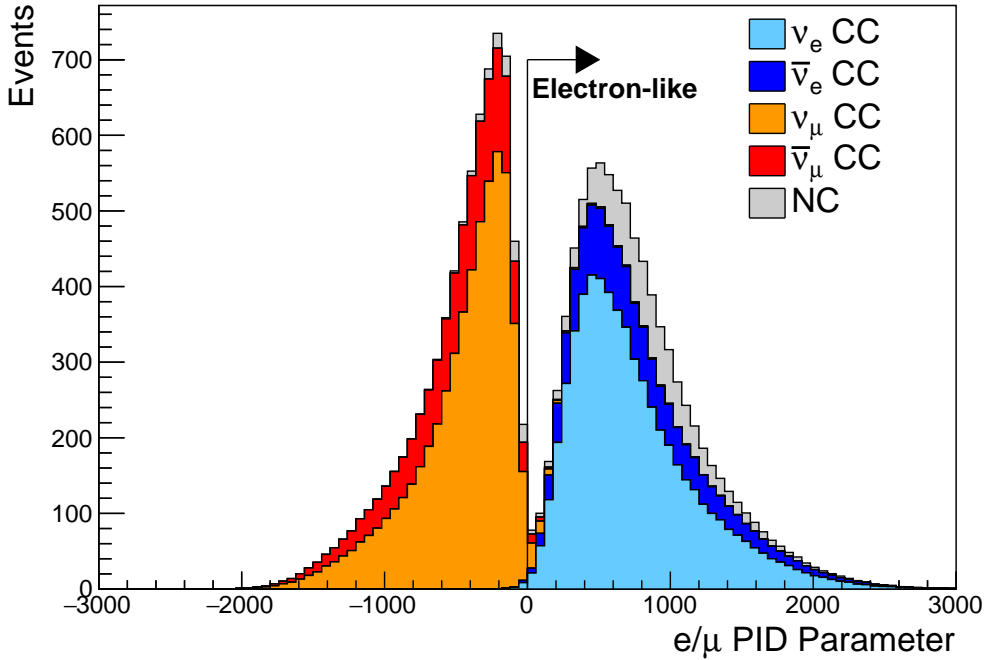


Figure 5.4: The electron/muon PID separation parameter for all sub-GeV single-ring events in SK-IV. The charged current (CC) component is broken down in four flavours of neutrino (ν_μ , $\bar{\nu}_\mu$, ν_e and $\bar{\nu}_e$). Events with positive values of the parameter are determined to be electron-like.

¹⁴⁴³ conversion length, direction, and momenta of each photon are also considered as track
¹⁴⁴⁴ parameters which are then fit in the same methodology as the standard single-ring
¹⁴⁴⁵ hypotheses.

¹⁴⁴⁶ Whilst low energy events are predominately single-ring events, higher energy
¹⁴⁴⁷ neutrino events can generate final states with multiple particles which generate
¹⁴⁴⁸ Cherenkov photons. These “multi-ring” hypotheses are also considered in the `fitQun`
¹⁴⁴⁹ algorithm. When calculating the charge likelihood density, the predicted charge
¹⁴⁵⁰ associated with each ring is calculated separately and then merged to calculate the
¹⁴⁵¹ total accumulated charge on each PMT. Similarly, the time likelihood for the multi-ring
¹⁴⁵² hypothesis is calculated assuming each ring is independent. Each track is time-ordered
¹⁴⁵³ based on the time of flight from the center of the track to the PMT and the direct light
¹⁴⁵⁴ from any ring incident on the PMT is assumed to arrive before any scattered light. To

reduce computational resources, the multi-ring fits only consider electron-like and charged pion-like rings as the pion fit can be used as a proxy for a muon fit due to their similar mass.

Multi-ring fits proceed by proposing another ring to the previous fit and then fitting the parameters in the method described above. Typically, multi-ring fits have the largest likelihood because of the additional degrees of freedom introduced. Consequently, the additional ring is only added if the ratio of likelihoods passes a criterion, which is determined by Monte Carlo studies.

As an example of how the reconstruction depends on the detector conditions, the author of this thesis assessed the quality of event reconstruction for SK-V data. The detector systematics invoked within the T2K-only oscillation analysis are determined using data to Monte Carlo comparisons using the SK-IV data [183]. Due to tank-open maintenance occurring between SK-IV and SK-V, the dark rate of each PMT was observed to increase in SK-V due to light exposure for a significant time during the repairs. This increase can be seen in Figure 5.5. Run-10 of the T2K experiment was conducted in the SK-V period, so the consistency of SK-IV and SK-V data needs to be studied to determine whether the SK-IV-defined systematics can be applied to the run-10 data. This comparison study was performed using the stopping muon data set for both the SK-IV and SK-V periods. This data sample is used due to the high rate of interactions ($O(200)$ events per hour) as well as having similar energies to muons from CCQE ν_μ interactions from beam interactions. The rate of cosmic muons does depend on the solar activity cycle [184] but has been neglected in this comparison study. This is because the shape of the distributions is most important for the purposes of being compared to the detector systematics. The SK-IV and SK-V data samples consist of 2398.42 and 626.719 hours of data which equates to 686k and 192k events respectively.

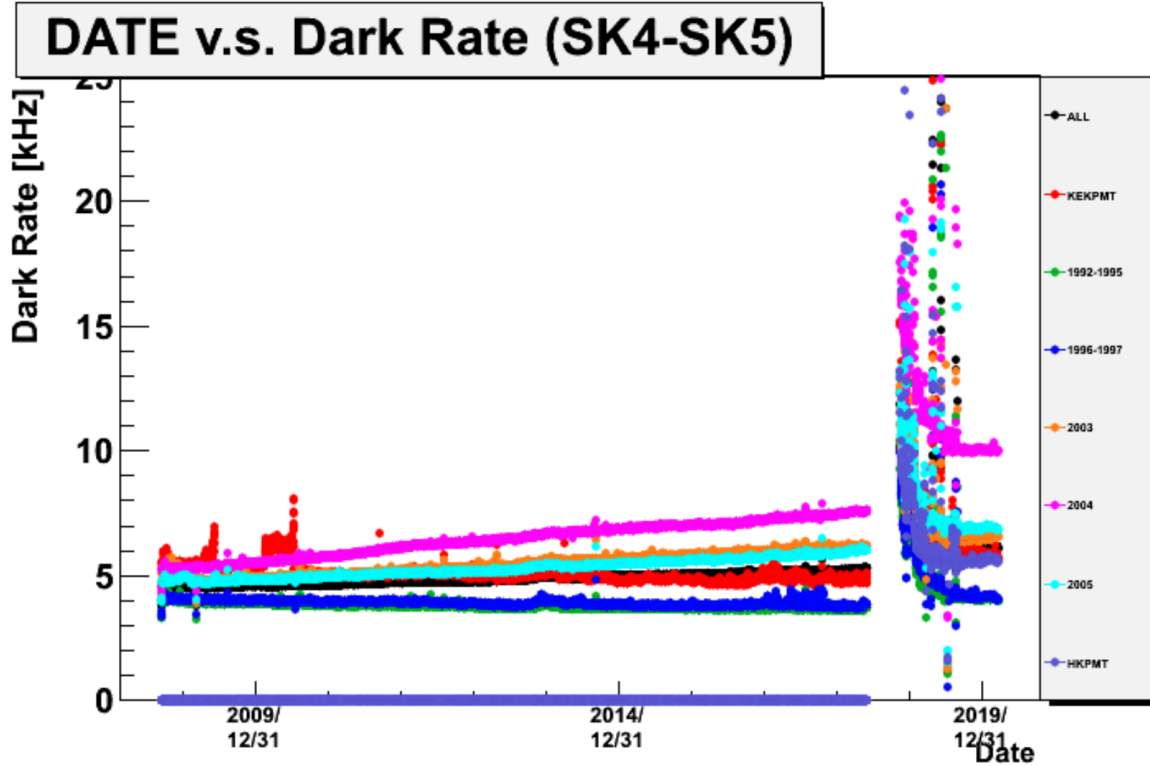


Figure 5.5: The variation of the measured dark rate as a function of date, broken down by PMT type. The SK-IV and SK-V periods span September 2008 to May 2018 and January 2019 to July 2020, respectively. The break in measurement in 2018 corresponds to the period of tank repair and refurbishment. Figure adapted from [183].

The predicted charge calculated in the `fitQun` charge likelihood prediction includes a contribution from the photoelectron emission due to dark noise. Therefore, the increase in the SK-V dark rate needs to be accounted for. In practice, the average dark rate in each SK period is calculated and used as an input in the reconstruction. This is calculated by averaging the dark rate per run for each period separately, using the calibration measurements detailed in subsection 3.1.2. The average dark rate from SK-IV and SK-V were found to be 4.57kHz and 6.30kHz, respectively. The associated charge with the muon and decay electron subevents are illustrated in Figure 5.6. The photoelectron emission from dark noise will be more noticeable for events that have lower energy. This is because this contribution becomes more comparable to the number of photoelectrons emitted from incident photons in low-energy events. This

1491 behaviour is observed in the data, where the charge deposited by the muon subevent
 1492 is mostly unaffected by the increase in dark rate, whilst the charge associated with the
 1493 decay-electron is clearly affected.

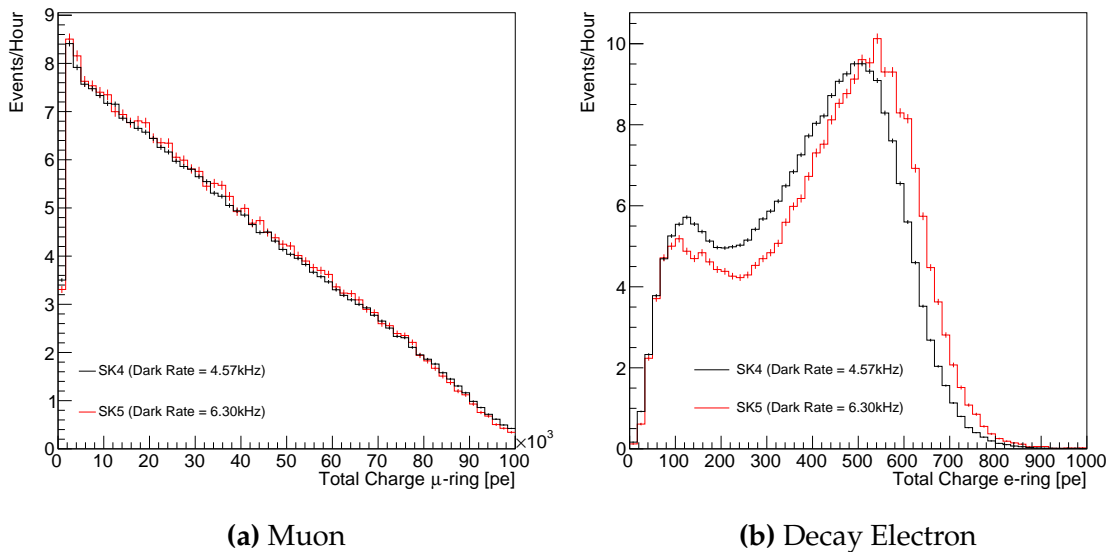


Figure 5.6: Comparison of the measured raw charge deposited per event from the stopping muon data samples between SK-IV (Blue) and SK-V (Red), split by the primary muon subevent and the associated decay electron subevent.

1494 The energy scale systematic for the SK-IV period was determined to be 2.1% [185].
 1495 It is defined to be equal to the difference between data and Monte Carlo prediction
 1496 in the stopping muon data sample. To determine the consistency of the SK-IV and
 1497 SK-V with respect to the energy scale systematic, the muon momentum distribution is
 1498 compared between the two SK periods. As the total number of Cherenkov photons
 1499 is integrated across the track length, the reconstructed momentum divided by track
 1500 length (or range) is compared between SK-IV and SK-V as illustrated in Figure 5.7.

1501 The consistency between these distributions has been computed in two ways.
 1502 Firstly, a Gaussian is fit to each distribution separately. The mean of which is found to
 1503 be $(2.272 \pm 0.003)\text{MeV/cm}$ and $(2.267 \pm 0.006)\text{MeV/cm}$ for SK-IV and SK-V respec-
 1504 tively. The ratio of these is equal to 1.002 ± 0.003 . The mean of the Gaussian fits are

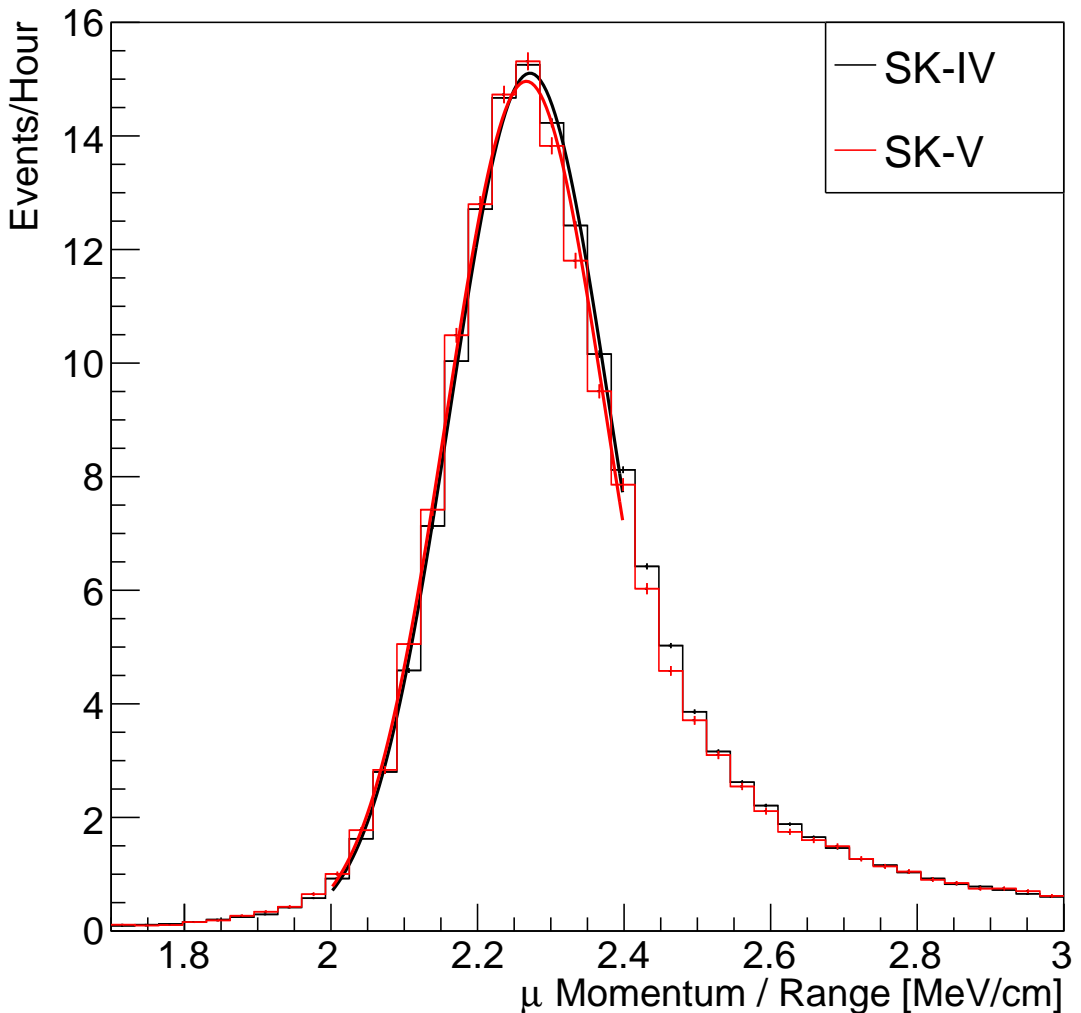


Figure 5.7: The distribution of the reconstructed momentum from the muon ring divided by the distance between the reconstructed muon and decay electron vertices as found in the stopping muon data sets of SK-IV (Black) and SK-IV (Red). Only events with one tagged decay electron are considered. A Gaussian fit is considered in the range [2.0, 2.4] MeV/cm and illustrated as the solid curve.

consistent with the expected stopping power of a minimum ionising muon for a target material (water) with $Z/A \sim 0.5$ [186]. The second consistency check is performed by introducing a nuisance parameter, α , which modifies the SK-V distribution. The value of α which minimises the χ^2 value between the SK-IV and SK-V is determined by scanning across a range of values. This is repeated by applying the nuisance parameter as both a multiplicative factor and an additive shift. The χ^2 distributions for different

₁₅₁₁ values of α is illustrated in Figure 5.8. The values which minimise the χ^2 are found to
₁₅₁₂ be 0.0052 and 1.0024 for the additive and multiplicative implementations, respectively.
₁₅₁₃ No evidence of shifts larger than the 2.1% uncertainty on the energy scale systematic
₁₅₁₄ has been found in the reconstructed momentum distribution of SK-IV and SK-V.

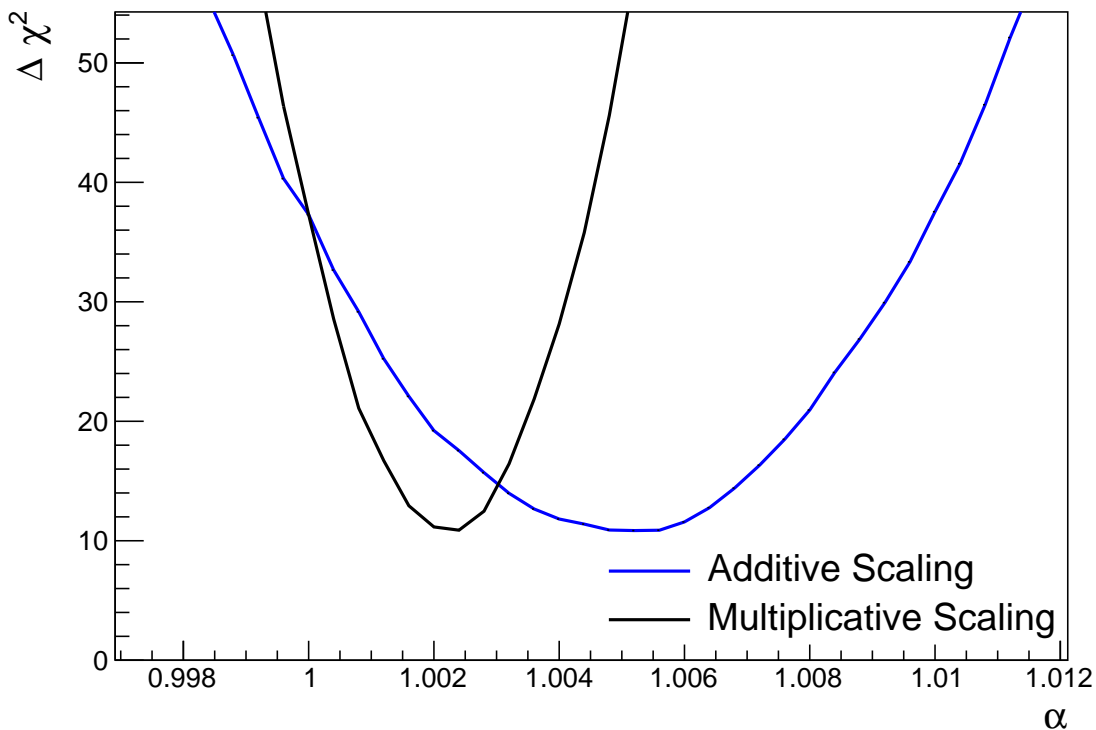


Figure 5.8: The χ^2 difference between the SK-IV and SK-V reconstructed muon momentum divided by range when the SK-V is modified by the scaling parameter α . Both additive (Blue) and multiplicative (Black) scaling factors have been considered. In practice, the additive scaling factor actually uses the value of $(\alpha - 1.0)$ but is illustrated like this so the results can be shown on the same axis range.

₁₅₁₅ 5.3 Event Reduction at SK

₁₅₁₆ Atmospheric neutrino events observed in the SK detector are categorised into three
₁₅₁₇ different types of samples: fully contained (FC), partially contained (PC) and up-
₁₅₁₈ going muon ($\text{Up-}\mu$), using PMT hit signatures in the inner and outer detector (ID

and OD, respectively). To identify FC neutrino events, it is required that the neutrino interacts inside the fiducial volume of the ID such that no significant OD activity is observed. For this analysis, an event is defined to be in the fiducial volume providing the event vertex is at least 0.5m away from the ID walls. PC events have the same ID requirements but can have a larger signal present inside the OD. Typically these events are higher energy muon interactions that penetrate the ID walls. The Up- μ sample contains events where muons are created from neutrino interactions in the OD water or rock below the tank. They then propagate upwards through the detector. The reason downward-going muons generated from neutrino interactions above the tank are neglected is due to the difficulty in separating their signature from the cosmic muon shower background. The sample categories are visually depicted in Figure 5.9.

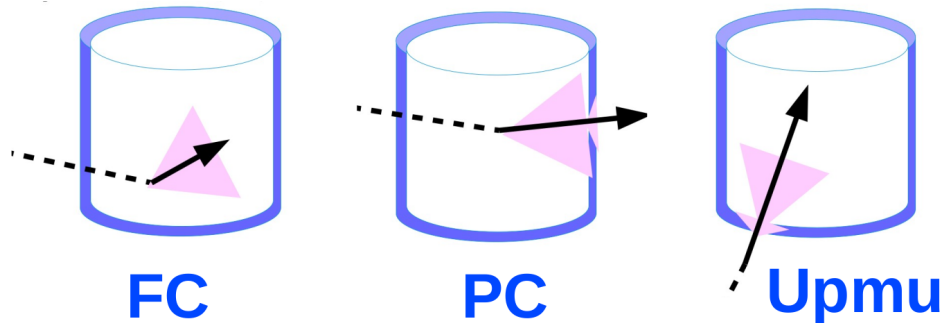


Figure 5.9: A depiction of the topology patterns for fully-contained (FC), partially-contained (PC) and up-going muon (Up- μ) samples included in this analysis.

Based on the event characteristics, as defined by the `fitQun` event reconstruction software, the FC events are categorised by

- **Visible Energy:** equal to the sum of the reconstructed kinetic energy above the Cerenkov threshold for all rings present in the event. The purpose is to separate events into sub-GeV and multi-GeV categories.
- **Number of observed Cerenkov rings.** The purpose is to separate single-ring and multi-ring events, where single-ring events predominantly consist of quasi-elastic

interactions and multi-ring events are typically resonant pion production or deep inelastic scattering events.

- **Particle identification parameter of the most energetic ring:** A value determined from the maximum likelihood value based on `fitQun`'s electron, muon, or pion hypothesis. The purpose is to separate electron-like and muon-like events.
- **Number of decay electrons:** The purpose is to separate quasi-elastic events (which have one decay electron emitted from the muon decay) and resonant pion production events (which have two decay electrons emitted from the muon and pion).

The PC and Up- μ categories are broken down into “through-going” and “stopping” samples depending on whether the muon left the detector. This is because the stopping events deposit the entire energy of the interaction into the detector, resulting in better reconstruction. The energy of events that exit the detector has to be estimated which introduces much larger systematic uncertainties. Through-going Up- μ samples are further broken down by whether any hadronic showering was observed in the event which typically indicates DIS interactions. The expected neutrino energy for the different categories is given in Figure 5.10. FC sub-GeV and multi-GeV events peak around 0.7GeV and 3GeV respectively, with slightly different peak energies for $\nu_x \rightarrow \nu_e$ and $\nu_x \rightarrow \nu_\mu$ oscillation channels. PC and Up- μ are almost entirely comprised of $\nu_x \rightarrow \nu_\mu$ events and peak around 7GeV and 100GeV, respectively.

In normal data-taking operations, the SK detector observes many background events alongside the beam and atmospheric neutrino signal events of physics interest. Cosmic ray muons and flasher events, which are the spontaneous discharge of a given PMT, contribute the largest amount of background events in the energy range relevant to any analysis searching for neutrino events. Lower energy analyses like DSNB searches are also subject to radioactive backgrounds [187]. Therefore the data recorded

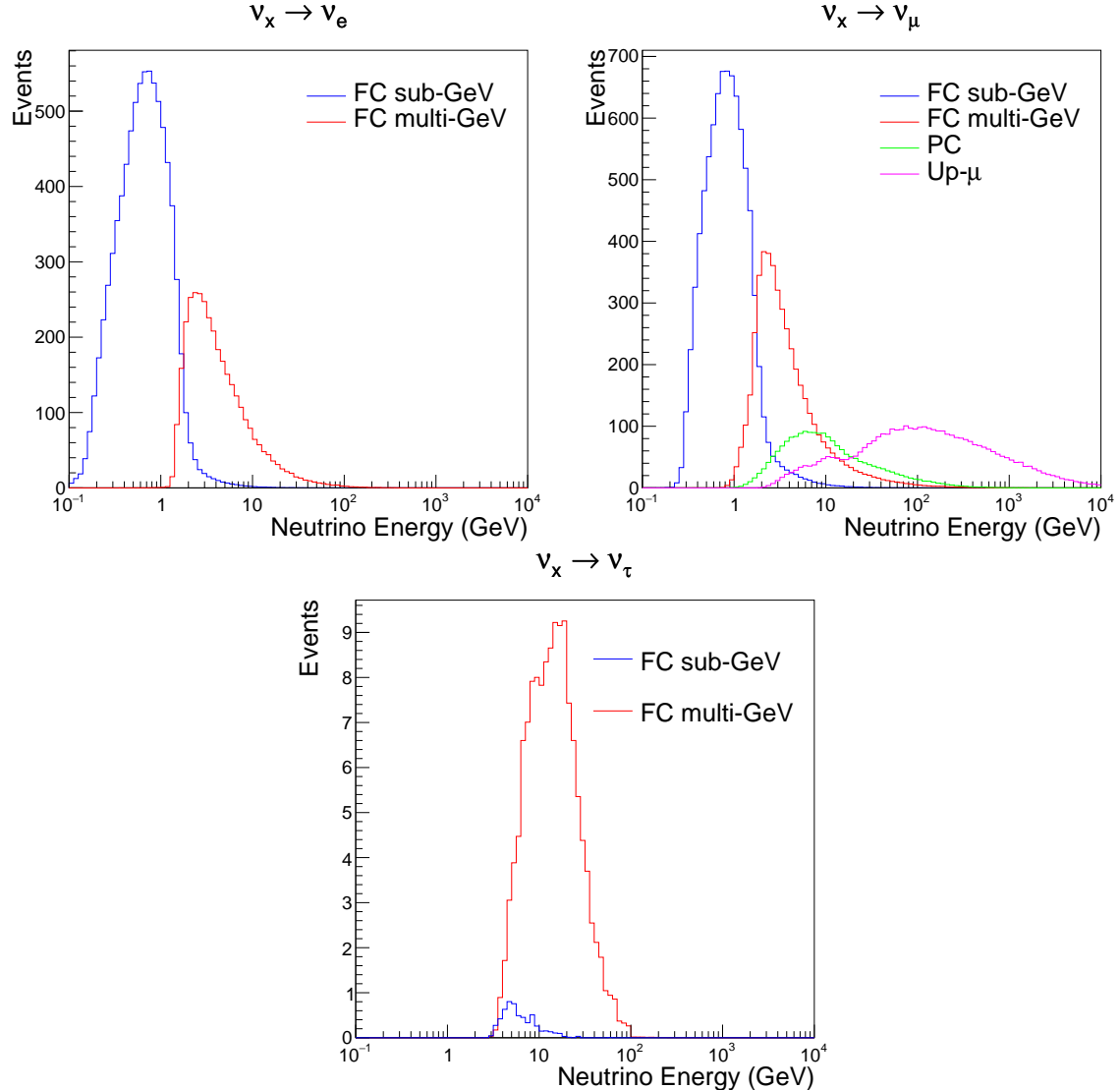


Figure 5.10: The predicted neutrino flux of the fully contained (FC) sub-GeV and multi-GeV, partially contained (PC), and upward-going muon (Up- μ) events. The prediction is broken down by the $\nu_x \rightarrow \nu_e$ prediction (top left), $\nu_x \rightarrow \nu_\mu$ prediction (top right) and $\nu_x \rightarrow \nu_\tau$ prediction (bottom). All systematic dials are set to their nominal values and the Asimov A oscillation parameters are assumed.

is reduced with the aim of removing these background events. The reduction process

is detailed in [47, 89] and briefly summarised below.

The first two steps in the FC reconstruction remove the majority of cosmic ray

muons by requiring a significant amount of ID activity compared to that measured in

the OD. Events that pass this cut are typically very high momentum muons or events

that leave very little activity in the OD. Consequently, a third reduction step is then

1569 applied to select cosmic-ray muons that pass the initial reduction step. A purpose-built
 1570 cosmic muon fitter is used to determine the entrance (or exit) position of the muon and
 1571 a cut is applied to OD activity contained within 8m of this position. Flasher events are
 1572 removed in the fourth reduction step which is based on the close proximity of PMT
 1573 hits surrounding the PMT producing the flash. Events that pass all these reduction
 1574 steps are reconstructed with the APFit algorithm. The fifth step of the reduction uses
 1575 information from the more precise fitter to repeat the previous two steps with tighter
 1576 cuts. Muons below the Cherenkov threshold can not generate optical photons in the
 1577 ID but the associated decay electron can due to its lower mass. These are the types of
 1578 events targeted in the fifth reduction step. The final cuts require the event vertex to be
 1579 within the fiducial volume (0.5m from the wall although the nominal distance is 2.0m),
 1580 visible energy $E_{vis} > 30\text{MeV}$ and fewer than 16 hits within the higher energy OD
 1581 cluster. The culmination of the fully contained reduction results in 8.09 events/day in
 1582 the nominal fiducial volume [188]. The uncertainty in the reconstruction is calculated
 1583 by comparing Monte Carlo prediction to data. The largest discrepancy is found to be
 1584 1.3% in the fourth reduction step.

1585 The PC and Up- μ events are processed through their own reduction processes
 1586 detailed in [47]. Both of these samples are reconstructed with the APFit algorithm
 1587 rather than `fiTQun`. This is because the efficiency of reconstructing events that leave
 1588 the detector has not been sufficiently studied for reliable systematic uncertainties. The
 1589 PC and Up- μ samples attain events at approximately 0.66 and 1.44 events/day.

1590 Events due to beam neutrinos undergo the same reduction steps as FC events and
 1591 are then subject to further cuts [189]. The GPS system which links the timing between
 1592 the beam facility and SK needs to be operating correctly and there should be no activity
 1593 within the detector in the previous $100\mu\text{s}$ before the trigger. The events then need to
 1594 triggered between $-2\mu\text{s}$ and $10\mu\text{s}$ of the expected spill timing.

1595 Due to the lower energy beam neutrinos, the T2K samples are not dependent
 1596 upon the visible energy neutrino as the range of neutrino energies are smaller than
 1597 that found in atmospheric neutrinos. Furthermore, the 2020 T2K-only oscillation
 1598 analysis only considers events which contain a single ring. Similar to atmospheric
 1599 event selection, the number of decay electrons is used as a proxy for distinguishing
 1600 CCQE and CCRES events. The expected neutrino energy, broken down by number of
 1601 decay electrons, is given in Figure 5.11.

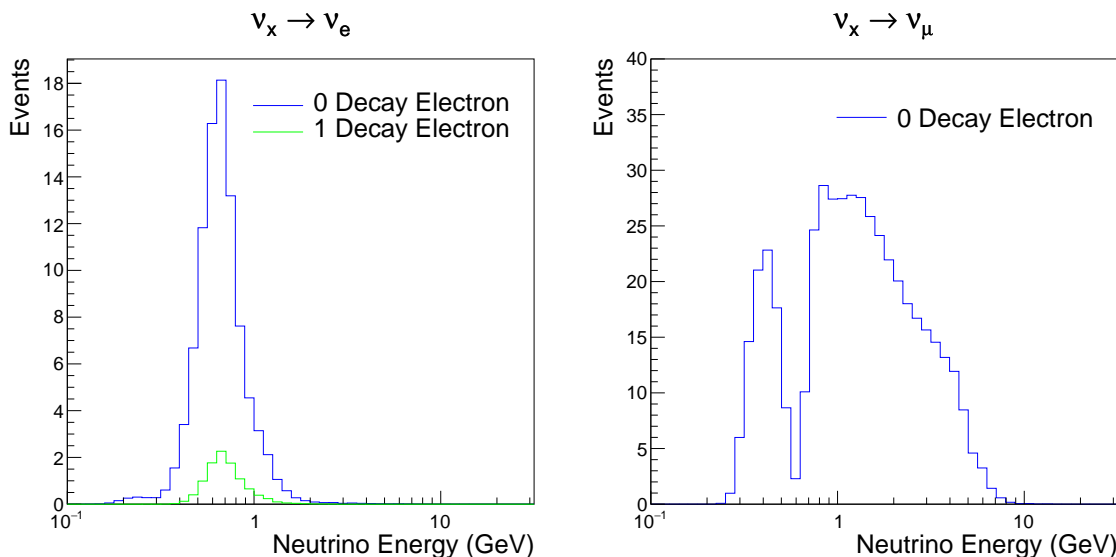


Figure 5.11: The predicted neutrino flux of the beam neutrinos, illustrated as a function of neutrino energy. The predictions are broken down by the number of decay electrons associated with the particular events. All systematic dials are set to their nominal values and the Asimov A oscillation parameters are assumed.

₁₆₀₂ **Chapter 6**

₁₆₀₃ **Sample Selections and Systematics**

₁₆₀₄ The oscillation analysis presented within this thesis is built upon a simultaneous
₁₆₀₅ fit to atmospheric data at SK, neutrino beam data in the near detector and beam
₁₆₀₆ data measured at SK. The definitions of these samples are documented in section 6.1,
₁₆₀₇ section 6.2, and section 6.3, respectively. The data collected and used within this
₁₆₀₈ analysis is detailed in Table 6.1. The near and far detector data corresponds to T2K
₁₆₀₉ runs 2-9 and runs 1-10, respectively. The accumulated POT and beam power for runs
₁₆₁₀ 1 – 10 is illustrated in Figure 6.1.

Data Type	Total
Near Detector FHC	1.15×10^{21} POT
Near Detector RHC	8.34×10^{20} POT
Far Detector FHC	1.97×10^{21} POT
Far Detector RHC	1.63×10^{21} POT
Atmospheric SK-IV	3244.4 days

Table 6.1: The amount of data collected in each detector used within this analysis. The data collected at the near and far detector, for both neutrino beam (FHC) and antineutrino beam (RHC), is measured as the amount of protons on target (POT).

₁₆₁₁ The difference in POT recorded at the near and far detector is due to the difference
₁₆₁₂ in downtime of the respective detector. The SK detector is very stable with almost 100%
₁₆₁₃ of data recorded during beam operation. Due to various technical and operational
₁₆₁₄ issues, the downtime of the near detector is significantly higher due to its more
₁₆₁₅ complex design and operating requirements.

1616 The systematic parameters invoked within the flux, detector, and interaction models
 1617 used within this analysis are documented in section 6.4. The standard configuration of
 1618 the joint beam and atmospheric data fit utilises far detector systematics provided in
 1619 the official inputs from the two experiments. Additionally, a correlated detector model
 1620 which fits the parameters used in sample selections to data has been developed and
 1621 documented in subsection 6.4.5.

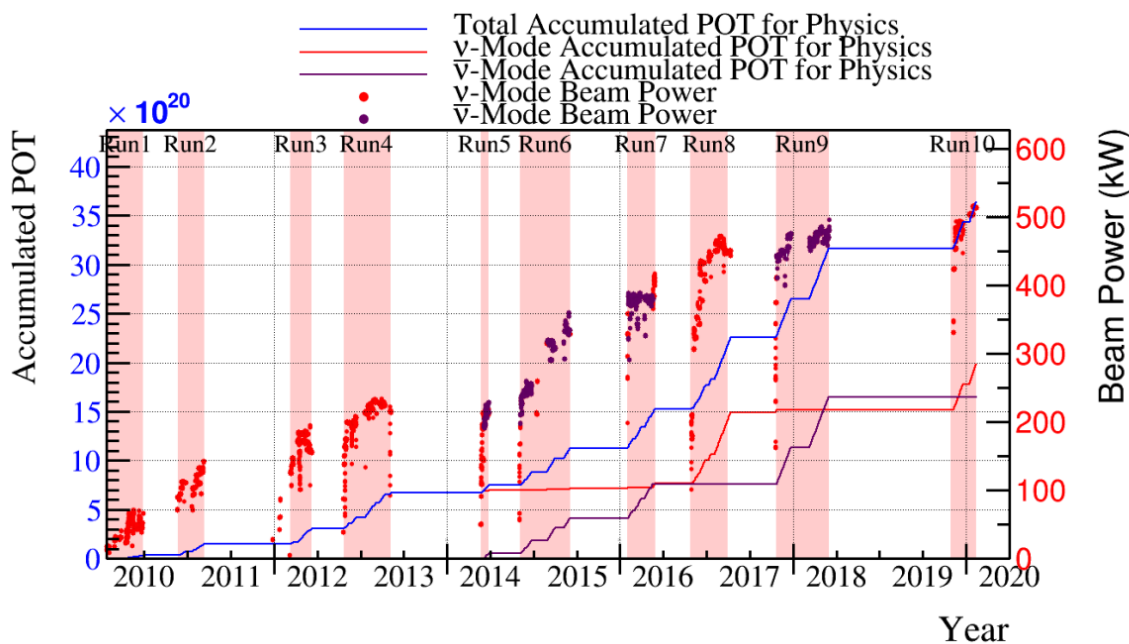


Figure 6.1: The accumulated beam data, measured as the number of protons on target (POT). The total data (blue) is given which comprises of the neutrino beam (red) and antineutrino (purple) components. The beam power for neutrino and antineutrino beams is given as the markers using the same colourscheme. The timescale runs from Run 1 which started in January 2010 until Run 10 which ended in February 2020. The ratio of accumulated data in neutrino and antineutrino beam is 54.7% : 45.3%.

1622 6.1 Atmospheric Samples

1623 The atmospheric event selection follows the official SK-IV analysis presented in [89]
1624 and is documented below. The Monte Carlo prediction used within this analysis
1625 corresponds to 500 years worth of neutrino events, which is scaled down to match the
1626 SK-IV livetime of 3244.4 days.

1627 The fully contained (FC), partially contained (PC), and upward going muon events
1628 ($\text{up-}\mu$) which pass the reduction cuts discussed in section 5.3 are further broken down
1629 into different samples based on reconstruction information. This section details the
1630 samples used within this oscillation analysis, alongside the chosen binning, used
1631 within the fit.

1632 FC events are first separated by the visible energy deposited within the detector.
1633 This is calculated as the sum of the reconstructed kinetic energy above the Cherenkov
1634 threshold for all rings present in the event. Events are separated by whether they were
1635 above or below $E_{\text{vis}} = 1.33\text{GeV}$. This separates “subGeV” and “multiGeV” events.
1636 Typically, lower energy events consist of charge current quasi-elastic (CCQE) inter-
1637 actions which are better understood and simpler to reconstruct resulting in smaller
1638 systematic uncertainties. Events are further separated by the number of rings as-
1639 sociated with the event due to similar reasoning. As the oscillation probability is
1640 dependent upon the flavour of neutrino, electron and muon events are separated
1641 using a similar likelihood method to that discussed in section 5.2. To reduce computa-
1642 tional resources required for the reconstruction, only electron and pion hypotheses are
1643 considered so this separation cut depends on the ratio of the electron to pion likeli-
1644 hoods, $\log(L_e/L_\pi)$. Finally, the number of decay electrons is used to classify events.
1645 Charged current resonant pion production (CCRES) interactions generate a final-state
1646 pion. This can decay, mostly likely through a muon, into a decay electron. Therefore

- ¹⁶⁴⁷ any electron-like event with one decay electron or muon-like event with two decay
¹⁶⁴⁸ electrons was most likely produced by a CCRES interaction. Consequently, the number
¹⁶⁴⁹ of decay electrons can be used to distinguish CCQE and CCRES interaction modes.
¹⁶⁵⁰ Ultimately, FC subGeV events are separated into the samples listed in Table 6.2.

Sample Name	Description
SubGeV-e-like-0dcy	Single ring e -like events with zero decay electrons
SubGeV-e-like-1dcy	Single ring e -like events with one or more decay electrons
SubGeV-mulike-0dcy	Single ring μ -like events with zero decay electrons
SubGeV-mulike-1dcy	Single ring μ -like events with one decay electrons
SubGeV-mulike-2dcy	Single ring μ -like events with two or more decay electrons
SubGeV-pi0like	Two e -like ring events with zero decay electrons and reconstructed π^0 mass $85 \leq m_{\pi^0} < 215\text{MeV}$

Table 6.2: The fully contained subGeV samples, defined as events with visible energy $E_{vis} < 1.33\text{GeV}$, used within this oscillation analysis.

- ¹⁶⁵¹ In addition to the cuts discussed above, multiGeV samples also have additional cuts
¹⁶⁵² to separate samples which target neutrino and antineutrino separation. As discussed
¹⁶⁵³ in section 7.1, the matter resonance only occurs for neutrinos in normal hierarchy and
¹⁶⁵⁴ antineutrinos in inverted mass hierarchy. Therefore, having flavour-enriched samples
¹⁶⁵⁵ aids in the determination of the mass hierarchy. For a CCRES interaction,

$$\begin{aligned}
 \bar{\nu}_e + N &\rightarrow e^+ + N' + \pi^-, \\
 \nu_e + N &\rightarrow e^- + N' + \pi^+ \\
 &\quad \downarrow \mu^+ + \nu_\mu \\
 &\quad \downarrow e^+ + \nu_e + \bar{\nu}_\mu.
 \end{aligned} \tag{6.1}$$

- ¹⁶⁵⁶ The π^- emitted from a $\bar{\nu}_e$ interaction is more likely to be absorbed within the
¹⁶⁵⁷ oxygen nucleus compared to the π^+ from ν_e interactions [190]. These pions then

1658 decay, mostly through muons, to electrons. Therefore the number of tagged decay
 1659 electrons associated with an event gives an indication of whether the interaction
 1660 was due to a neutrino or antineutrino: zero for $\bar{\nu}_e$ events, and one for ν_e events.
 1661 The ability to separate neutrino from antineutrino events is illustrated in Table 6.4,
 1662 where the MultiGeV-*e*like-nue has 78% purity of neutrino interactions with only 7%
 1663 antineutrino background in that sample and the rest of the sample comprising of
 1664 neutral current backgrounds.

1665 This relatively simple discriminator works reasonably well for single-ring events.
 1666 However, this is not the case for multi-ring events. A multiGeV multiring separation
 1667 (MME) likelihood cut which specifically targets multiGeV multiRing electron-like
 1668 events was introduced in [191, 192]. This is a two stage likelihood selection cut. Four
 1669 observables are used within the first likelihood cut to distinguish CC ν_e and CC $\bar{\nu}_e$
 1670 events from background:

- 1671 • The number of decay electrons
- 1672 • The maximum distance between the vertex of the neutrino and the decay electrons
- 1673 • The energy deposited by the leading energy ring
- 1674 • The reconstructed particle identification of that highest energy ring

1675 Background events consist of CC ν_μ and NC interactions. Typically these produce
 1676 events where the majority of the energy is carried by the hadronic system. Additionally,
 1677 muons tend to travel further than the pions from CC ν_e before decaying. Consequently,
 1678 the parameters used within the likelihood cut target the typical background interaction
 1679 kinematics.

1680 Neutrino and antineutrino events are then separated by a second likelihood method
 1681 ($\nu/\bar{\nu}$ separation) detailed in [52]. This uses the number of decay electrons, the number
 1682 of reconstructed rings, and the event's transverse momentum. The last two parameter

Sample Name	Description
MultiGeV- <i>e</i> -like-nue	Single ring <i>e</i> -like events with zero decay electrons
MultiGeV- <i>e</i> -like-nuebar	Single ring <i>e</i> -like events with one or more decay electrons
MultiGeV- <i>μ</i> -like	Single ring <i>μ</i> -like events
MultiRing- <i>e</i> -like-nue	Two or more ring events with leading energy <i>e</i> -like ring and passed both MME and $\nu/\bar{\nu}$ separation cuts
MultiRing- <i>e</i> -like-nuebar	Two or more ring events with leading energy <i>e</i> -like ring and passed MME and failed $\nu/\bar{\nu}$ separation cuts
MultiRing- <i>μ</i> -like	Two or more ring events with leading energy <i>μ</i> -like ring and only requires $E_{vis} > 0.6\text{GeV}$ DB: Why?
MultiRing-Other1	Two or more ring events with leading energy <i>e</i> -like ring and failed the MME likelihood cut

Table 6.3: The fully contained multiGeV samples used within this oscillation analysis. Both the sample name and description are given.

1683 are used because higher-energy samples tend to have more pions produced above
 1684 the Cherenkov threshold which results in more rings compared to an antineutrino
 1685 interaction. Furthermore, the angular distribution also tends to be more forward
 1686 peaked in antineutrino interactions as compared to neutrino interactions [89]. These
 1687 FC multiGeV sample definitions are detailed in Table 6.3.

1688 The PC and up- μ events are split by the amount of energy deposited within the
 1689 outer detector, into “stopping” and “through-going” samples. This is because the
 1690 momentum of events leaving the detector have to be approximated, which increases
 1691 the systematic uncertainty. This estimate is particularly poor for very high energy
 1692 events. This is why up- μ through-going events are not binned in reconstructed
 1693 momentum. If an event leaves the detector, the energy it takes with it has to be
 1694 estimated which increases the systematic uncertainty compared to events entirely
 1695 contained within the inner detector. The through-going up- μ are further separated by
 1696 the presence of any electromagnetic showering in the event, as the assumption of non-

₁₆₉₇ showering muon does not give reliable reconstruction for these types of events [47]. In
₁₆₉₈ total, 13 FC, 2 PC, and 3 up- μ atmospheric samples are included within this analysis.

Sample	CC ν_e	CC $\bar{\nu}_e$	CC($\nu_\mu + \bar{\nu}_\mu$)	CC($\nu_\tau + \bar{\nu}_\tau$)	NC
SubGeV-elike-0dcy	72.17	23.3	0.724	0.033	3.77
SubGeV-elike-1dcy	86.81	1.773	7.002	0.062	4.351
SubGeV-mulike-0dcy	1.003	0.380	90.07	0.036	8.511
SubGeV-mulike-1dcy	0.023	0.	98.46	0.029	1.484
SubGeV-mulike-2dcy	0.012	0.	99.25	0.030	0.711
SubGeV-pi0like	6.923	2.368	0.928	0.011	89.77
MultiGeV-elike-nue	78.18	7.041	3.439	1.886	9.451
MultiGeV-elike-nuebar	56.68	37.81	0.174	0.614	4.718
MultiGeV-mulike	0.024	0.005	99.67	0.245	0.058
MultiRing-elike-nue	59.32	12.39	4.906	3.385	20
MultiRing-elike-nuebar	52.39	31.03	1.854	1.585	13.14
MultiRing-mulike	0.673	0.080	97.33	0.342	1.578
MultiRingOther-1	27.98	2.366	34.93	4.946	29.78
PCStop	8.216	3.118	84.45	0.	4.214
PCThrus	0.564	0.207	98.65	0.	0.576
UpStop-mu	0.829	0.370	98.51	0.	0.289
UpThruNonShower-mu	0.206	0.073	99.62	0.	0.103
UpThruShower-mu	0.128	0.054	99.69	0.	0.132

Table 6.4: The purity of each atmospheric sample used within this analysis, broken down by charged current (CC) and neutral current (NC) interactions and which neutrino flavour interacted within the detector. Asimov A oscillation parameter sets are assumed (given in Table 2.2). Electron neutrino and antineutrino events are separated to illustrate the ability of the separation likelihood cuts used within the multiGeV and multiring sample selections.

₁₆₉₉ The atmospheric samples are binned in direct observables: reconstructed lepton
₁₇₀₀ momentum and direction, as given by Table 6.5. The distribution of the reconstructed
₁₇₀₁ lepton momentum (for samples that only have one bin reconstructed zenith angle)
₁₇₀₂ and reconstructed direction for each atmospheric sample used within this analysis is
₁₇₀₃ illustrated in Figure 6.2.

Sample	$\cos(\theta_Z)$ Bins	Momentum Bin Edges ($\log_{10}(P)$ MeV)
SubGeV- <i>e</i> like-0dcy	10	2.0, 2.4, 2.6, 2.8, 3.0, 3.2
SubGeV- <i>e</i> like-1dcy	1	2.0, 2.4, 2.6, 2.8, 3.0, 3.2
SubGeV- <i>m</i> ulike-0dcy	10	2.0, 2.4, 2.6, 2.8, 3.0, 3.2
SubGeV- <i>m</i> ulike-1dcy	10	2.0, 2.4, 2.6, 2.8, 3.0, 3.2
SubGeV- <i>m</i> ulike-2dcy	1	2.0, 2.4, 2.6, 2.8, 3.0, 3.2
SubGeV- <i>p</i> i0like	1	2.0, 2.2, 2.4, 2.6, 2.8, 3.2
MultiGeV- <i>e</i> like-nue	10	3.0, 3.4, 3.7, 4.0, 5.0
MultiGeV- <i>e</i> like-nuebar	10	3.0, 3.4, 3.7, 4.0, 5.0
MultiGeV- <i>m</i> ulike	10	3.0, 3.4, 5.0
MultiRing- <i>e</i> like-nue	10	3.0, 3.4, 3.7, 5.0
MultiRing- <i>e</i> like-nuebar	10	3.0, 3.4, 3.7, 5.0
MultiRing- <i>m</i> ulike	10	2.0, 3.124, 3.4, 3.7, 5.0
MultiRing- <i>O</i> ther1	10	3.0, 3.4, 3.7, 4.0, 5.0
PC-Stop	10	2.0, 3.4, 5.0
PC-Through	10	2.0, 3.124, 3.4, 3.7, 5.0
Upmu-Stop	10	3.2, 3.4, 3.7, 8.0
Upmu-Through-Showering	10	2.0, 8.0
Upmu-Through-NonShowering	10	2.0, 8.0

Table 6.5: The reconstructed cosine zenith and lepton momentum binning assigned to the atmospheric samples. The “ $\cos(\theta_Z)$ Bins” column illustrates the number of bins uniformly distributed over the $-1.0 \leq \cos(\theta_Z) \leq 1.0$ region for fully and partially contained samples and $-1.0 \leq \cos(\theta_Z) \leq 0.0$ region for up- μ samples. **DB: Does this belong in the appendix?**

1704

DB: By-mode spectra of each sample needed?

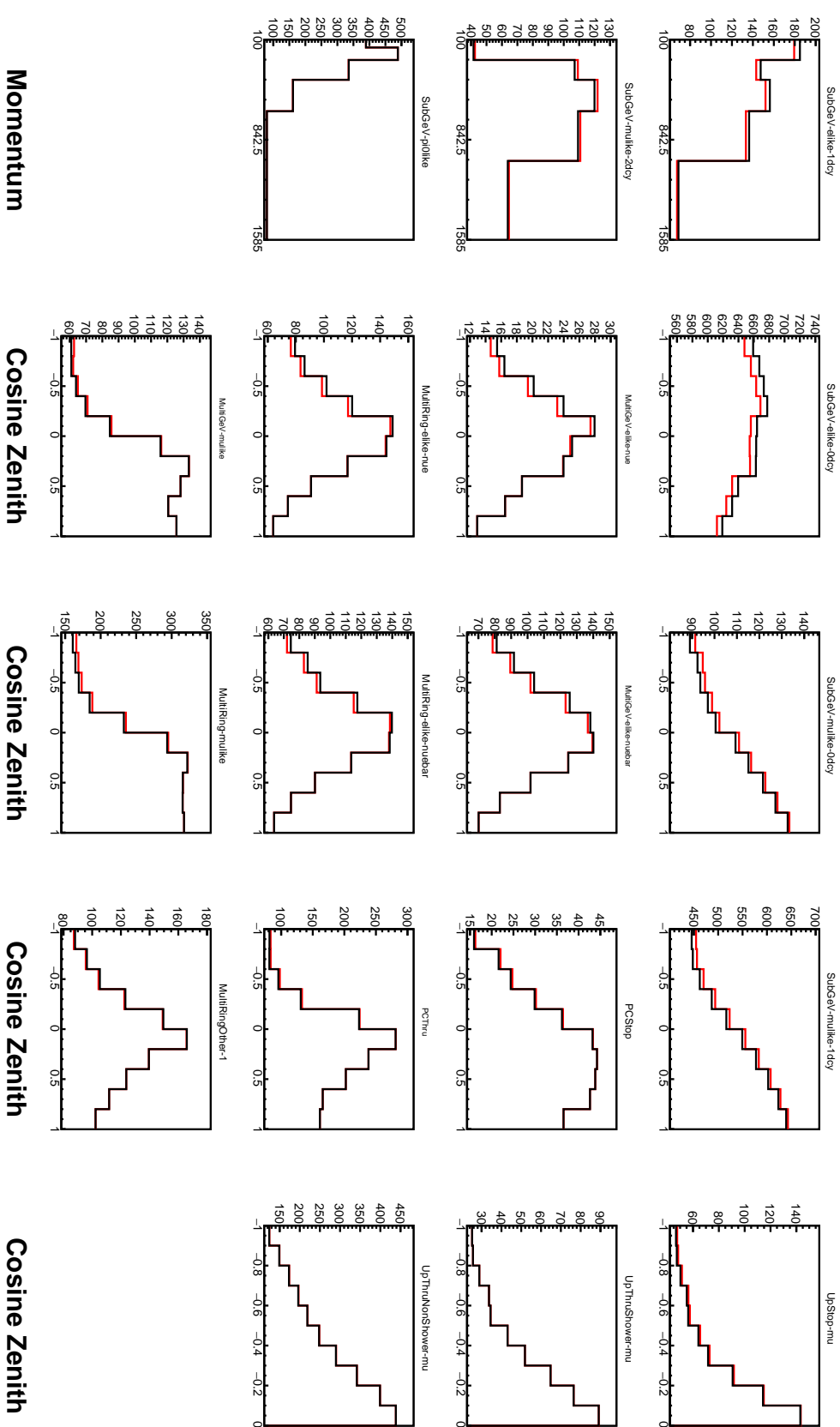


Figure 6.2: Comparison of the SK-IV atmospheric samples between predictions made with the CP-violating Asimov A (Black) and CP-conserving Asimov B (Red) oscillation parameter sets (given in Table 2.2). The subGeV samples CCRES and π^0 -like samples are given in their reconstructed lepton momentum. All other samples are presented in their reconstructed zenith angle projection.

1705 6.2 Near Detector Beam Samples

1706 The near detector sample selections are documented in detail within [193] and sum-
1707 marised below. Samples are selected based upon the particular FGD in which the
1708 vertex of the neutrino interaction is in as well as the operating mode of the beam:
1709 FHC or RHC. For additional constraints on model parameters, wrong-sign neutrino
1710 samples are also considered when the beam is operating in RHC mode. Samples
1711 from the wrong-sign component of the FHC beam mode are not included as they are
1712 statistically insignificant compared to those samples already listed.

1713 Before being assigned a sample, all events must undergo CC-inclusive cuts, as
1714 defined in [194]:

- 1715 • Event Timing: The DAQ must be operational and the event must occur within
1716 the expected beam time window
- 1717 • TPC Requirement: The track path must intercept one or more TPCs
- 1718 • Fiducial volume: The event must originate from within the fiducial volume. The
1719 fiducial volumes are defined as a region within each sub-detector [195].
- 1720 • Upstream Background: Remove events which have muons tracks that originate
1721 upstream of the FGDs by requiring no high-momentum tracks within 150mm
1722 upstream of the candidate vertex. Additionally, events that occur within the
1723 downstream FGD are vetoed if a secondary track starts within the upstream FGD
- 1724 • Broken track removal: All candidates where the muon candidate is broken in two
1725 are removed
- 1726 • Muon PID: Measurements of dE/dx in a TPC are used to distinguish muon-like
1727 events using a likelihood cut

₁₇₂₈ In addition to these cuts, RHC neutrino events also have to undergo the following
₁₇₂₉ cuts to aid in the separation of neutrino and antineutrino [196]:

- ₁₇₃₀ • TPC Requirement: The track path must intercept TPC2
- ₁₇₃₁ • Positive Track: The highest momentum track must be positive
- ₁₇₃₂ • TPC1 Veto: Remove any events originating upstream of TPC1

₁₇₃₃ Once all CC-inclusive events have been determined, they are further segregated
₁₇₃₄ into sub-samples that target the constraints on interaction modes most relevant at the
₁₇₃₅ far detector. They are split by pion ultiplicity: CC0 π , CC1 π , and CCOther. These target
₁₇₃₆ specific interaction modes CCQE, CCRES, and other CC background interactions,
₁₇₃₇ respectively. Pions in the TPCs and FGDs are selected by requiring a secondary track
₁₇₃₈ to be observed, which is separate from the muon track and is in the same beam spill
₁₇₃₉ window and sub-detector. If the pion originated within a FGD, it must also pass
₁₇₄₀ through the sequential downstream TPC (TPC2 for FGD1, TPC3 for FGD2).

₁₇₄₁ CC0 π , CC1 π , and CCOther samples are defined with the following cuts:

- ₁₇₄₂ • ν_μ **CC0 π Selection:** No electrons in TPC and no charged pions or decay electrons
₁₇₄₃ within the TPC or FGD
- ₁₇₄₄ • ν_μ **CC1 π Selection:** Exactly one charged pion in either the TPC or FGD,
₁₇₄₅ where the number of charged pions in the FGD is equal to the number of decay
₁₇₄₆ electrons
- ₁₇₄₇ • ν_μ **CCOther Selection:** All events which are not classified into the above two
₁₇₄₈ selections.

₁₇₄₉ Counting the three selections for each FGD in FHC and RHC running, including
₁₇₅₀ the wrong-sign background in RHC, 18 near detector samples are used within this
₁₇₅₁ analysis. These samples are binned in reconstructed lepton momentum (illustrated in

Figure 6.3) and direction with respect to the beam. The binning is chosen such that each event has at least 20 Monte Carlo events in each bin [195]. This is to ensure that the bins are coarse enough to ensure the reduction of statistical errors, whilst also being fine enough to sample the high-resolution peak regions. The exact binning is detailed in [195].

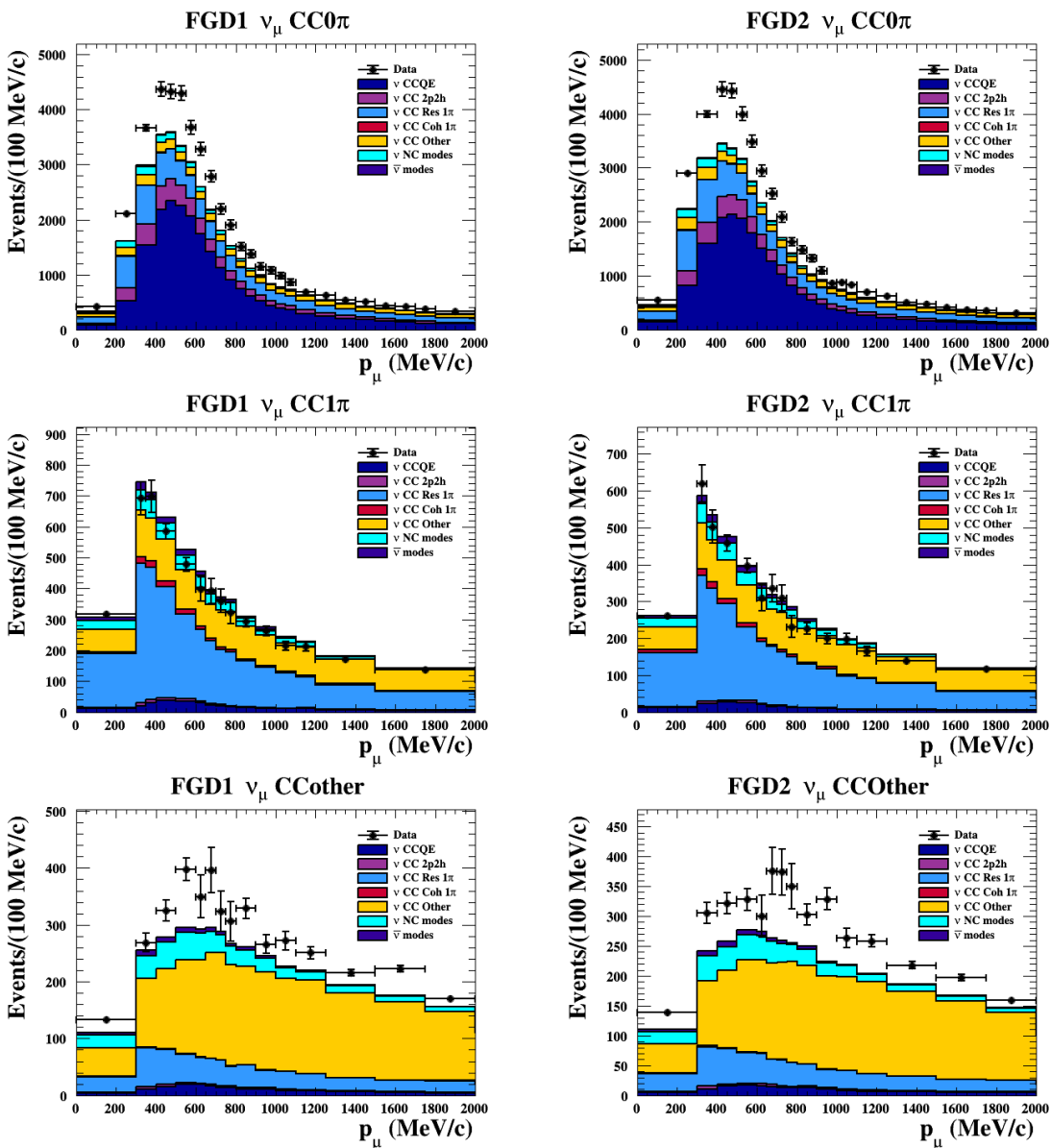


Figure 6.3: The nominal Monte Carlo predictions for the FGD1 and FGD2 samples in neutrino beam mode, broken down into the $CC\nu_\mu 0\pi$, $CC\nu_\mu 1\pi$ and $CC\nu_\mu$ Other categories. Figures taken from [193].

¹⁷⁵⁷ 6.3 Far Detector Beam Samples

¹⁷⁵⁸ The beam neutrino events which occur at the SK detector, which pass the reduction cuts
¹⁷⁵⁹ detailed in section 5.3, are separated depending on whether the beam was operating
¹⁷⁶⁰ in FH or RHC mode. The events are then separated into three samples: electron-like
¹⁷⁶¹ ($1Re$), muon-like ($1R\mu$), and CC1 π^+ -like ($1Re1de$) which are observed as electron-like
¹⁷⁶² events with an associated decay electron [183]. As discussed in section 6.1, positively
¹⁷⁶³ charged pions emitted from neutrino interactions are more likely to produce decay
¹⁷⁶⁴ electrons than negatively charged pions. Consequently, the CC1 π^+ -like sample is
¹⁷⁶⁵ only selected when the beam is operating in FHC mode. Therefore, five beam samples
¹⁷⁶⁶ measured at SK are used in this analysis.

¹⁷⁶⁷ The fiducial volume definition for beam samples is slightly different from that used
¹⁷⁶⁸ within the atmospheric samples. It uses both the distance to the closest wall (d_{Wall})
¹⁷⁶⁹ and the distance to the wall along the trajectory of the particle (to_{Wall}). This allows
¹⁷⁷⁰ events that originate close to the wall but are facing into the tank to be included within
¹⁷⁷¹ the analysis, which would have otherwise been removed. These additional events are
¹⁷⁷² beneficial for a statistics-limited experiment. The exact cut values for both d_{Wall} and
¹⁷⁷³ to_{Wall} are different for each of the three types of sample and are optimised based on
¹⁷⁷⁴ T2K sensitivity to δ_{CP} [197, 198]. They are:

¹⁷⁷⁵ DB: Diagram of d_{Wall} and to_{Wall} ?

¹⁷⁷⁶ **1Re event selection** For an event to be classified as a $1Re$ -like, the event must follow:

- ¹⁷⁷⁷ • Fully-contained and within $d_{Wall} > 80\text{cm}$ and $to_{Wall} > 170\text{cm}$
- ¹⁷⁷⁸ • Total of one ring which is reconstructed as electron-like with reconstructed mo-
¹⁷⁷⁹ mentum $P_e > 100\text{MeV}$

- 1780 • Zero decay electrons are associated with the event
1781 • Passes π^0 rejection cut discussed in section 5.2

1782 The zero decay electron cut specifically targets CCQE interactions. Whereas, the π^0
1783 rejection cut is designed to remove neutral current π^0 background events which can
1784 be easily reconstructed as 1Re-like events.

1785 **CC1 π^+ event selection** This event selection is very similar to that of the 1Re sample.
1786 The only difference is that the dWall and toWall criteria are changed to $> 50\text{cm}$ and
1787 $> 270\text{cm}$, respectively. Furthermore, exactly one decay electron is required from the
1788 π^+ decay.

1789 **1R μ event selection** A 1R μ -like event is determined by the following cuts:

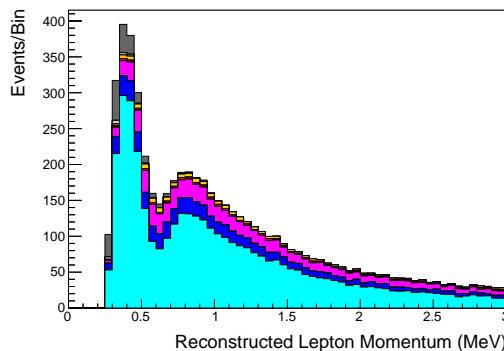
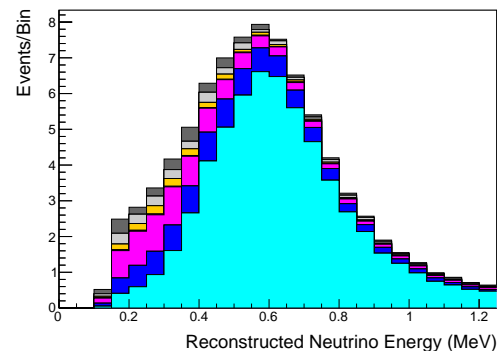
- 1790 • Fully-contained and within $\text{dWall} > 50\text{cm}$ and $\text{toWall} > 250\text{cm}$
1791 • Total of one ring which is reconstructed as muon-like with reconstructed momen-
1792 tum $P_\mu > 200\text{MeV}$
1793 • Fewer than two decay electrons are associated with the event
1794 • Passes π^+ rejection cut discussed in section 5.2

1795 As pions and muons have similar masses, the Cherenkov rings they generate have
1796 similar opening angles. To enhance purity, the events have to pass the π^+ rejection cut
1797 which is specifically optimised to separate the two types of events.

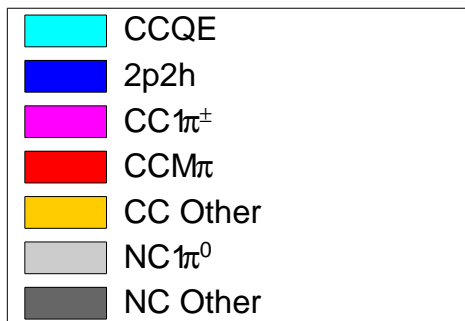
1798 All of these samples are binned in reconstructed neutrino energy. This is possible
1799 as the direction from the source is known extremely well. This value is calculated for
1800 the 1Re-like and 1R μ -like samples assuming CCQE interactions,

$$E_\nu^{rec} = \frac{(M_N - V_{nuc})E_l - m_l^2/2 + M_N V_{nuc} - V_{nuc}^2/2 + (M_P^2 + M_N^2)/2}{M_N - V_{nuc} - E_l + P_l \cos(\theta_{beam})} \quad (6.2)$$

1801 Where M_N , M_P and m_l are the masses of the neutron, proton and outgoing lepton,
 1802 respectively. $V_{nuc} = 27\text{MeV}$ is the binding energy of the oxygen nuclei [183], θ_{beam} is
 1803 the angle between the beam and the direction of the outgoing lepton, and E_l and P_l
 1804 are the energy and momentum of that outgoing lepton.

(a) FHC 1R μ 

(b) FHC 1Re



(c)

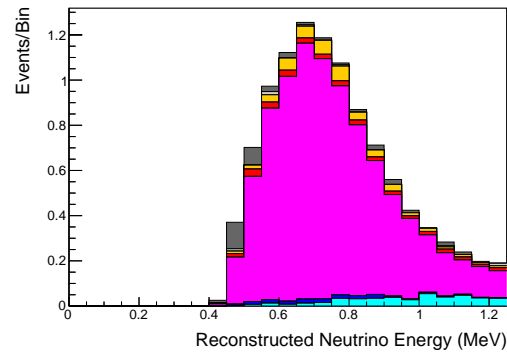
(d) FHC CC1 π^+

Figure 6.4: The reconstructed neutrino energy, as defined by Equation 6.2 and Equation 6.3, for the 1R μ -like, 1Re-like and CC1 π^+ -like samples. Asimov A oscillation parameter sets are assumed (given in Table 2.2). These samples are the FHC mode samples. For ease of viewing, the 1R μ sample only shows the $0. \leq E_\nu^{rec} < 3.0\text{GeV}$ but the binning extends to 30.0GeV.

₁₈₀₅ The reconstructed neutrino energy of the CC1 π^+ -like events is modified to include
₁₈₀₆ the delta resonance produced within the interaction,

$$E_\nu^{rec} = \frac{2M_N E_l + M_{\Delta^{++}}^2 - M_N^2 - m_l^2}{2(M_N - E_l + P_l \cos(\theta_{beam}))} \quad (6.3)$$

₁₈₀₇ Where $M_{\Delta^{++}}$ is the mass of the delta baryon. Binding energy effects are not
₁₈₀₈ considered as a two-body process with the delta baryon is assumed. [DB: Link to](#)
₁₈₀₉ [OA2022 which has ResEB](#)

₁₈₁₀ The reconstructed neutrino energy for the FHC samples is illustrated in Figure 6.4.
₁₈₁₁ As expected, the 1R μ -like and 1Re-like samples are heavily dominated by CCQE in-
₁₈₁₂ teractions, with smaller contributions from 2p2h meson exchange and resonant pion
₁₈₁₃ production interactions. The CC1 π^+ -like sample predominantly consists of charged
₁₈₁₄ current resonant pion production interactions. The 1Re-like and CC1 π^+ -like samples
₁₈₁₅ are also binned by the angle between the neutrino beam and the reconstructed lepton
₁₈₁₆ momentum. This is to aid in charged current and neutral current separation, as indi-
₁₈₁₇ cated in Figure 6.5. This is because the neutral current backgrounds are predominantly
₁₈₁₈ due to π^0 -decays, where the opening angle of the two gammas alongside the different
₁₈₁₉ final state kinematics produces a slightly broader angular distribution compared to
₁₈₂₀ the final state particles originating from charged current ν_e interactions.

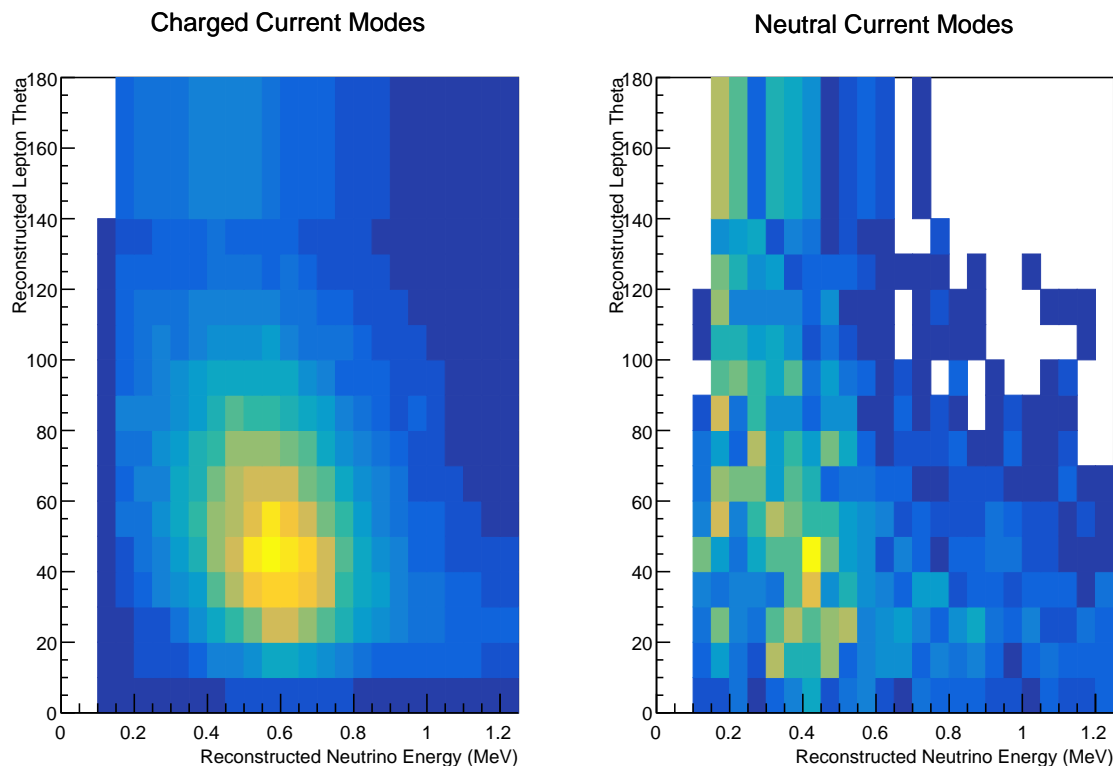


Figure 6.5: The distribution of the angle between the neutrino beam direction and the reconstructed final state lepton, for the FHC 1Re-like sample. The distribution is broken down by neutrino interaction mode into charged current (left) and neutral current (right) components. Asimov A oscillation parameter sets are assumed (given in Table 2.2). DB: Is this needed? If so, a COLZ is required

¹⁸²¹ 6.4 Systematic Uncertainties

¹⁸²² The systematics for this analysis are split into groups, or blocks, depending on their
¹⁸²³ purpose. They consist of flux uncertainties, neutrino-matter interaction systematics,
¹⁸²⁴ and detector efficiencies. There are also uncertainties on the oscillation parameters
¹⁸²⁵ which this analysis will not be sensitive to, Δm_{12}^2 and $\sin^2(\theta_{12})$. As described in
¹⁸²⁶ chapter 4, each model parameter used within this analysis requires a prior uncertainty.
¹⁸²⁷ This is provided via separate covariance matrices for each block. The covariance
¹⁸²⁸ matrices can include prior correlations between parameters within a single block, but
¹⁸²⁹ the separate treatment means prior uncertainties can not be included for parameters
¹⁸³⁰ in different groups. Alternatively, some parameters have no reasonably motivated
¹⁸³¹ uncertainties. These parameters are assigned flat priors which do not change the
¹⁸³² likelihood penalty. The flux, neutrino interaction, and detector modeling have already
¹⁸³³ been discussed in section 5.1. The uncertainties invoked within these models are
¹⁸³⁴ described below.

¹⁸³⁵ 6.4.1 Beam Flux

¹⁸³⁶ The neutrino beam flux systematics is based upon our uncertainty in the modeling of
¹⁸³⁷ the components of the beam. This includes the hadron production model and their re-
¹⁸³⁸ interactions, the shape, intensity, and alignment of the beam with respect to the target,
¹⁸³⁹ and the uniformity of the magnetic field produced by the horn, alongside other effects.
¹⁸⁴⁰ The uncertainty, as a function of neutrino energy, is illustrated in Figure 6.6 which
¹⁸⁴¹ includes the total uncertainty as well as the individual components. The uncertainty
¹⁸⁴² for events below, and much higher than, the peak neutrino energy is dominated by
¹⁸⁴³ hadron production and re-interaction systematics. The beam profile and alignment of
¹⁸⁴⁴ the proton beam dominate the systematic uncertainty for events with $E_\nu \sim 1\text{GeV}$.

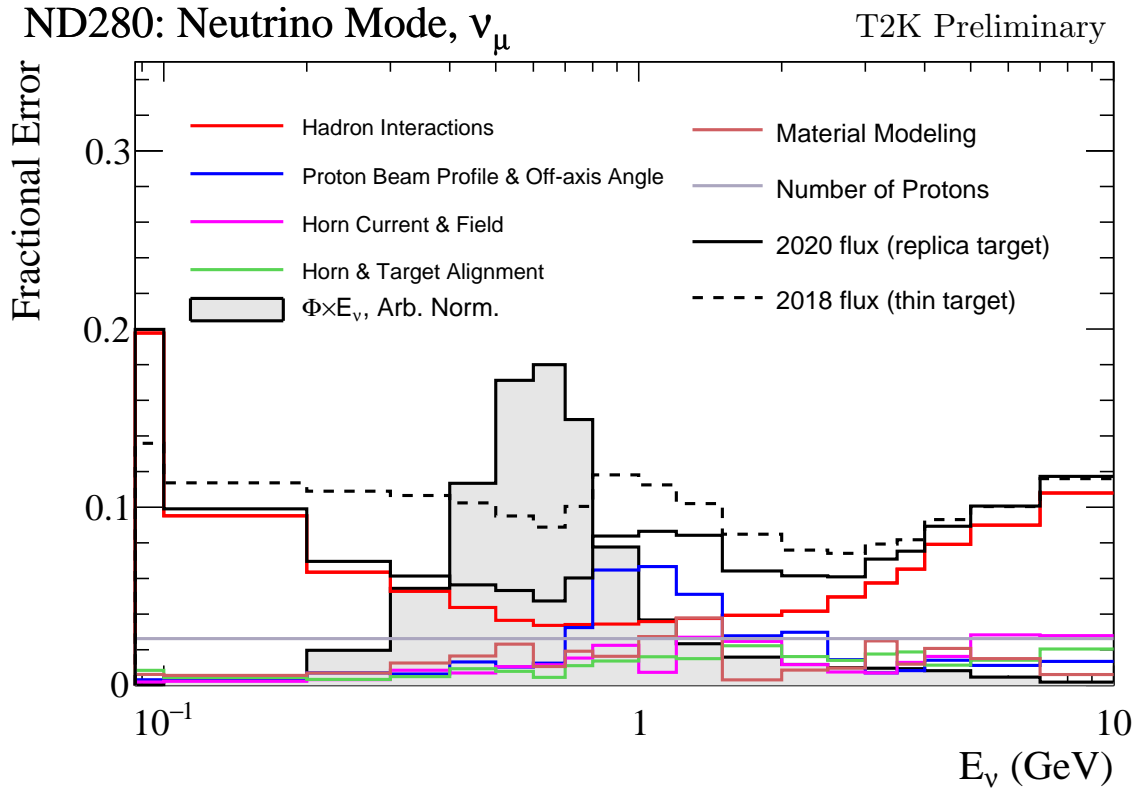


Figure 6.6: The total uncertainty evaluated on the near detector ν_μ flux prediction constrained by the replica-target data, illustrated as a function of neutrino energy. The solid(dashed) line indicates the uncertainty used within this analysis(the T2K 2018 analysis). The solid histogram indicates the neutrino flux as a function of energy. Figure taken from [199].

1845 The beam flux uncertainties are described by one hundred parameters. They are
 1846 split between both ND280 and SK detectors and binned by neutrino flavour: ν_μ , $\bar{\nu}_\mu$, ν_e
 1847 and $\bar{\nu}_e$. The response is then broken down as a function of neutrino energy. The bin
 1848 density in the neutrino energy is the same for the FHC- ν_μ and RHC- $\bar{\nu}_\mu$, and narrows
 1849 for neutrino energies close to the oscillation maxima of $E_\nu = 0.6\text{GeV}$. This binning is
 1850 specified in Table 6.6. All of these systematic uncertainties are applied as normalisation
 1851 parameters with Gaussian priors centered at 1.0 and error specified from a covariance
 1852 matrix provided by the T2K beam group.

Neutrino Flavour	Sign	Neutrino Energy Bin Edges (GeV)
μ	Right	0., 0.4, 0.5, 0.6, 0.7, 1., 1.5, 2.5, 3.5, 5., 7., 30.
μ	Wrong	0., 0.7, 1., 1.5, 2.5, 30.
e	Right	0., 0.5, 0.7, 0.8, 1.5, 2.5, 4., 30.
e	Wrong	0., 2.5, 30.

Table 6.6: The neutrino energy binning for the different neutrino flavours. “Right” sign indicates neutrinos in the FHC beam and antineutrinos in the RHC beam mode. “Wrong” sign indicates antineutrinos in the FHC beam and neutrinos in the RHC beam mode. The binning of the detector response is identical for the FHC and RHC modes as well as at ND280 and SK.

1853 6.4.2 Atmospheric Flux

1854 The atmospheric neutrino flux is modeled by the HKKM model, however, 16 system-
 1855 atic uncertainties are applied to control the normalisation of each neutrino flavour,
 1856 energy, and direction. All of the parameters are given Gaussian priors centered at 0
 1857 and width 1.. They are summarised below:

- 1858 • **Absolute Normalisation:** The overall normalisation of each neutrino flavour is
 1859 controlled by two independent systematic uncertainties, for $E_\nu < 1\text{GeV}$ and $E_\nu >$
 1860 1GeV , respectively. This is driven mostly by hadronic interaction uncertainties for
 1861 the production of pions and kaons [43]. The strength of the response is dependent
 1862 upon the neutrino energy.
- 1863 • **Relative Normalisation:** Uncertainties on the ratio of $(\nu_\mu + \bar{\nu}_\mu) / (\nu_e + \bar{\nu}_e)$ are
 1864 controlled by the difference between the HKKM model [43], FLUKA [46] and
 1865 Bartol models [42]. Three independent parameters are applied in the energy
 1866 ranges: $E_\nu < 1\text{GeV}$, $1\text{GeV} < E_\nu < 10\text{GeV}$, and $E_\nu > 10\text{GeV}$.
- 1867 • **$\nu/\bar{\nu}$ Normalisation:** The uncertainties in the π^+/π^- (and kaon equivalent) pro-
 1868 duce uncertainties in the flux of $\nu/\bar{\nu}$. The response is applied in the same way as
 1869 the relative normalisation parameters.

1870 • **Up/Down and Vertical/Horizontal Ratio:** Similar to the above two systematics,
1871 the difference between the HKKM, FLUKA, and Bartol model predictions, as a
1872 function of $\cos(\theta_Z)$, is used to control the normalisation of events as a function of
1873 zenith angle.

1874 • **K/π Ratio:** Higher energy neutrinos ($E_\nu < 10\text{GeV}$) become dependent upon
1875 kaon decay as the dominant source of neutrinos. Measurements of the ratio of
1876 K/π [200] are used to control the systematic uncertainty of the expected ratio of
1877 pion and kaon production.

1878 • **Solar Activity:** As the 11-year solar cycle can affect the Earth's magnetic field, the
1879 flux of primary cosmic rays is modulated across the same period. The uncertainty
1880 is calculated by taking a ± 1 year variation, equating to a 10% uncertainty for the
1881 SK-IV period.

1882 • **Atmospheric Density:** The height of the interaction of the primary cosmic rays is
1883 dependent upon the atmospheric density. The HKKM assumes the US standard
1884 1976 [153] profile. This systematic controls the uncertainty in that model.

1885 Updates to the HKKM and Bartol models are underway to use a similar tuning
1886 technique to that used in the beam flux predictions. After those updates, it may be
1887 possible to include correlations in the hadron production uncertainty systematics for
1888 beam and atmospheric flux predictions.

1889 6.4.3 Neutrino Interaction

1890 The neutrino interactions which occur within all the detectors are modeled by NEUT.
1891 The two independent oscillation analyses, T2K beam only and the SK atmospheric
1892 only, have developed separate interaction models. The T2K-only analysis uses the
1893 systematics model defined in [201] and the SK-only analysis uses the uncertainties

1894 detailed in [52]. To leverage the most sensitivity out of this joint beam and atmospheric
1895 analysis, a correlated interaction model has been defined. Where applicable, these
1896 correlations allow the systematic uncertainties applied to the atmospheric samples to
1897 be constrained by measurements of the near detector in the beam experiment leading
1898 to stronger sensitivity to oscillation parameters as compared to an uncorrelated model.
1899 An in-depth discussion of the reasoning and validity of enforcing correlations is
1900 documented in [202] and briefly summarised below.

1901 The low energy T2K systematic model has a more sophisticated treatment of CCQE,
1902 CCMEC, and CCRES uncertainties which is due to the purpose-made cross-section
1903 measurements made by the near detector. Furthermore, extensive testing of this model
1904 has been performed by the working group responsible for this model [201]. However,
1905 it is not designed for the high-energy atmospheric events illustrated in Figure 5.10.
1906 Therefore the high energy systematic model from the SK-only analysis is implemented
1907 for the relevant multiGeV samples. The CCQE systematic parameters invoked within
1908 the SK high energy model are actually contained within T2K's CCQE model. Conse-
1909 quently, the more sophisticated CCQE and CCMEC T2K model parameters have been
1910 incorporated into the high energy model but are uncorrelated from the low energy
1911 counterparts. This results in a more complete model but without any constraint from
1912 the near detector measurements.

1913 The high energy systematic model includes parameters developed from compar-
1914 isons of Nieves and Rein-Seghal models which affect CCRES interactions, comparisons
1915 of the GRV98 and CKMT models which control DIS interactions, and hadron multipli-
1916 city measurements which modulate the normalisation of $CCN\pi$ events. The uncertainty
1917 of the ν_τ cross-section is particularly large and is controlled by a 25% normalisation
1918 uncertainty. These parameters are applied via normalisation or shape parameters.
1919 The former linearly scales the weight of all affected Monte-Carlo events, whereas the

latter can increase or decrease a particular event's weight depending on its neutrino energy and mode of interaction. The response of the shape parameters are defined by third-order polynomial splines which return a weight for a particular neutrino energy. In total, 17 normalisation and 15 shape parameters are included in the more sophisticated high-energy model.

Figure 6.7 indicates the predicted neutrino energy distribution for both beam and subGeV atmospheric samples, and Figure 6.8 illustrates the fractional contribution of the different interaction modes per sample. There is clearly significant overlap in neutrino energy between the subGeV atmospheric and beam samples, allowing similar kinematics in the final state particles. Comparing beam samples with zero decay electrons and atmospheric electron-like(muon-like) samples with zero(zero or one) decay electrons, there is a very similar contribution of CCQE, CC 2p2h, and CC1 π^\pm interactions. The samples which target CC1 π^\pm interactions, FHC 1Re1de beam sample and atmospheric electron-like(muon-like) samples with one(two) decay electrons, also consist of very similar mode interactions. As a consequence of the similarity in energy and mode contributions, correlating the systematic model between the beam and subGeV atmospheric samples ensures that this analysis attains the largest sensitivity to oscillation parameters while still ensuring neutrino interaction systematics are correctly accounted for. Due to its sophisticated CCQE model, the T2K systematic model was chosen as the basis of the correlated model.

The T2K uncertainty model is applied in a similar methodology to the SK model parameters. It consists of 19 shape parameters applied via third-order polynomial splines and 24 normalisation parameters. Four additional parameters, which model the uncertainty in the binding energy, are applied in a way to shift the momentum of the lepton emitted from a nucleus. The majority of these parameters are assigned a Gaussian prior uncertainty. Those that have no theoretical reasoning, or those which

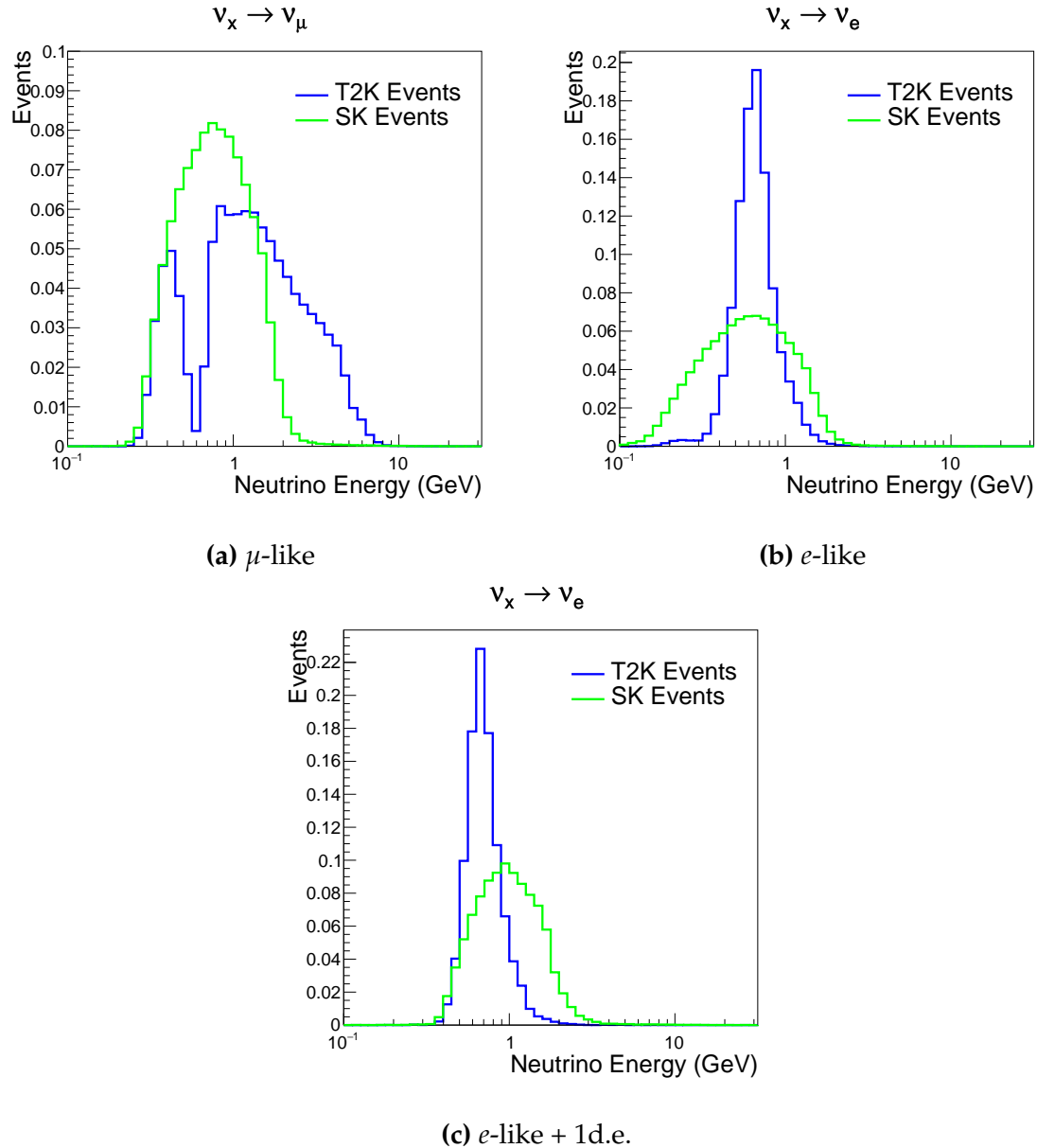


Figure 6.7: The prediction neutrino energy distribution for subGeV atmospheric and beam samples, given for muon-like samples FHC+RHC 1R μ beam samples compared to the subGeV μ -like 0+1 decay electrons (d.e.) atmospheric samples, electron-like 0d.e. samples FHC+RHC 1Re beam samples compared to the subGeV e -like 1d.e. sample, and electron-like 1d.e. sample FHC1Re1de beam sample compared to the subGeV e -like 1d.e. atmospheric sample.

¹⁹⁴⁶ have not been fit to external data, are assigned a flat prior which does not affect the
¹⁹⁴⁷ penalty term. The CCQE model parameters were tuned to MiniBooNE [203] and
¹⁹⁴⁸ MINER ν A [204] measurements and CCRES model parameters are tuned to ANL and
¹⁹⁴⁹ BNL experiments [205].

	CC QE	CC 2p2h	CC $1\pi^\pm$	CC $M\pi$	CC Other	NC π^0	NC $1\pi^\pm$	NC $M\pi$	NC Coh.	NC Other
FHC 1R+1d.e. e-like	0.04	0.02	0.83	0.03	0.04	0.01	0.01	0.01	0.00	0.01
RHC 1R e-like	0.62	0.12	0.11	0.01	0.02	0.06	0.01	0.01	0.01	0.04
FHC 1R e-like	0.68	0.12	0.10	0.00	0.02	0.04	0.01	0.00	0.00	0.02
RHC 1R μ -like	0.62	0.13	0.17	0.02	0.03	0.00	0.02	0.00	0.00	0.00
FHC 1R μ -like	0.62	0.12	0.16	0.02	0.03	0.00	0.03	0.00	0.00	0.00
S.G. π^0 -like	0.05	0.01	0.02	0.00	0.01	0.68	0.06	0.07	0.06	0.04
S.G. μ -like 2de	0.04	0.01	0.80	0.10	0.04	0.00	0.00	0.00	0.00	0.00
S.G. μ -like 1de	0.72	0.11	0.12	0.01	0.02	0.00	0.01	0.00	0.00	0.00
S.G. μ -like 0de	0.68	0.11	0.10	0.01	0.02	0.01	0.05	0.01	0.00	0.02
S.G. e-like 1de	0.05	0.01	0.75	0.10	0.05	0.00	0.01	0.02	0.00	0.01
S.G. e-like 0de	0.73	0.11	0.10	0.01	0.02	0.02	0.00	0.00	0.00	0.00

Figure 6.8: The interaction mode contribution of each sample given as a fraction of the total event rate in that sample. All systematic dials are set to their nominal values and the Asimov A oscillation parameters are assumed. The Charged Current (CC) modes are broken into quasi-elastic (QE), meson exchange (2p2h), resonant charged pion production ($1\pi^\pm$), multi-pion production ($M\pi$), and other interaction categories. Neutral Current (NC) interaction modes are given in interaction mode categories: π^0 production, resonant charged pion production, multi-pion production, and others.

There are three particular tunes of the T2K low energy cross section model typically considered. Firstly, the “generated” tune which is the set of dial values with which the Monte Carlo was generated. Secondly, the set of dial values which are taken from external data measurements and used as inputs. These are the “pre-fit” dial values. The reason these two sets of dial values are different is that the external data measurements are continually updated but it is very computationally intensive to regenerate a Monte Carlo prediction after each update. Consequently, the pre-fit and generated dial values differ. The final tune is the “post-fit” or “post-BANFF” dial values. These are the values taken from a fit to the beam near detector data. This fit is

1959 performed by two independent fitting frameworks, MaCh3 and BANFF, which ensures
1960 reliable measurements. The output of each fitter is converted into a covariance matrix
1961 to describe the error and correlations between all the cross-section parameters. This is
1962 then propagated to the far-detector oscillation analysis group for use in the P-Theta
1963 fitting framework. As MaCh3 can perform a near detector fit, it is included within
1964 the simultaneous fit of the far-detector beam and atmospheric oscillation analysis.
1965 This is because this technique does not require any assumption of Gaussian posterior
1966 distributions which is required in the covariance matrix methodology.

1967 On top of the combination of the SK and T2K interaction models, several other
1968 parameters have been specifically developed for the joint oscillation analysis. As
1969 the majority of the atmospheric samples' δ_{CP} sensitivity comes from the normali-
1970 sation of subGeV electron-like events, an additional dial that models an alternative
1971 Continous Random Phase Approximation (CRPA) nuclear ground state has been im-
1972 plemented [202]. As the near detector can not sufficiently constrain the model, this
1973 dial approximates the event weights if a CRPA model had been assumed rather than a
1974 spectral function. This dial only effects ν_e and $\bar{\nu}_e$ and is applied as a shape parameter.

1975 Further additions to the model have been included due to the subGeV π^0 atmo-
1976 spheric sample. This particularly targets charged current and neutral current π^0
1977 producing interactions to constrain the systematic uncertainties. However, there
1978 is no analogous sample in the T2K beam-only analysis so no significant effort has
1979 been placed into building a sufficient uncertainty model. Therefore, an uncertainty
1980 that affects neutral current resonant π^0 production is incorporated in this analysis.
1981 Comparisons of NEUT's NC resonant pion production predictions have been made
1982 to MiniBooNE [206] data and a consistent 16% to 21% underprediction is observed.
1983 Consequently, a conservative 30% normalisation is invoked.

1984 Events which originate from above the detector and travel downward are very
 1985 insensitive to oscillation parameters and act similar to the near detector within an
 1986 accelerator experiment (Details are illustrated in chapter 7). Consequently, the applica-
 1987 tion of the T2K low energy cross section and the effect of the near detector constraint
 1988 on the atmospheric samples can be studied through these events, without biasing
 1989 the results from oscillation effects. The downward going predictives are illustrated
 1990 in Figure 6.9. For samples that target CCQE interactions (electron-like with 0 decay
 1991 electrons and muon-like with 0 or 1 decay electrons), the application of the near
 1992 detector constraint is well within statistical fluctuation of the down-going data and
 1993 no significant tension is observed between the data and the Monte Carlo prediction
 1994 with the T2K near detector constraint. This is not the case for samples with target
 1995 CCRES interactions (electron-like with 1 decay electron and muon-like with 2 decay
 1996 electrons). The electron-like data is consistent with the constrained prediction at higher
 1997 reconstructed momenta but diverges at lower momentum, whereas the muon-like
 1998 sample is under-predicted throughout the range of momenta. To combat this disagree-
 1999 ment, an additional cross-section systematic dial, specifically designed to inflate the
 2000 low pion momentum systematics was developed in [202]. This is a shape parameter
 2001 implemented through a splined response.

2002 6.4.4 Near Detector

2003 The systematics applied due to uncertainties arising from the response of the near
 2004 detector is contained within 574 normalisation parameters binned in momentum and
 2005 angle, $P_\mu \text{ ad } \cos(\theta_\mu)$, of the final-state muon. These are applied via a covariance
 2006 matrix with each parameter being assigned a Gaussian prior from that covariance
 2007 matrix. These normalisation parameters are built from underlying systematics, e.g.
 2008 pion secondary interaction systematics, which are randomly thrown and the variation

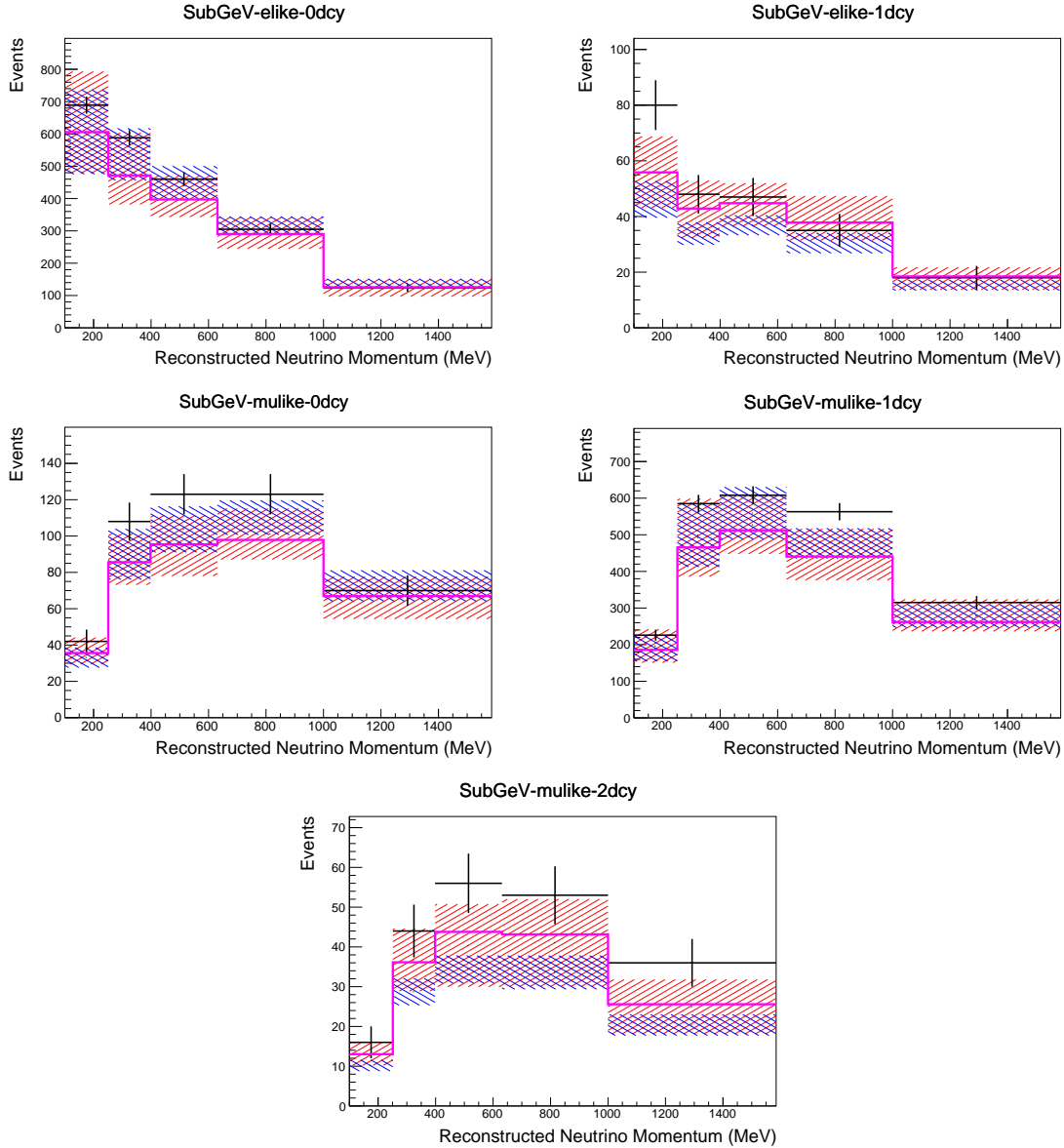


Figure 6.9: Down-going atmospheric subGeV single-ring samples comparing the mean and error of the pre-fit and post-fit Monte Carlo predictions in red and blue, respectively. The magenta histogram illustrates the Monte Carlo prediction using the generated dial values. The black points illustrate the down-going data with statistical errors given. The mean and errors of the Monte Carlo predictions are calculated by the techniques documented in subsection 4.3.4. The cross-section and atmospheric flux parameters are either thrown from their pre-fit uncertainties (denoted pre-fit band), or the cross section dial values are randomly sampled from a MCMC chain whilst the atmospheric flux parameters are thrown from their pre-fit distributions (denoted post-fit band).

²⁰⁰⁹ in each $P_\mu \times \cos(\theta_\mu)$ bin is determined. This is performed 2000 times and a covariance matrix response is created. This allows significant correlations between FGD1 and

2011 FGD2 samples, as well as adjacent bins. Statistical uncertainties are accounted for by
2012 including fluctuations of each event's weight from a Poisson distribution.

2013 Similar to the cross-section systematics, MaCh3 and BANFF are used to constrain
2014 the uncertainty of these systematics through independent validations. Each fitter
2015 generates a post-fit covariance matrix which is compared and passed to the far-detector
2016 oscillation analysis working group. However, as the analysis presented within this
2017 thesis uses the MaCh3 framework, a joint oscillation analysis fit of all three sets of
2018 samples is performed. From the T2K-only perspective, this joint analysis including
2019 atmospheric samples allows additional constraints on the systematic uncertainties
2020 where correlations have been invoked.

2021 **6.4.5 Far Detector**

2022 Two configurations of the far detector systematic model implementation have been
2023 considered. Firstly, the far detector systematic uncertainties for beam and atmospheric
2024 samples are taken from their respective analysis inputs, denoted “official inputs” anal-
2025 ysis. Consequently, no correlations are assumed between the beam and atmospheric
2026 samples. The generation of the beam- and atmospheric-specific inputs are documented
2027 in subsubsection 6.4.5.1 and subsubsection 6.4.5.2 for the beam and atmospheric sam-
2028 ples, respectively. Secondly, a correlated detector model has been considered. Here, the
2029 distribution of parameters used for applying event cuts (e.g. electron-muon separation)
2030 is modified within the fit, following a similar methodology to the beam far detector
2031 systematics model implementation. However, it has been designed to ensure that the
2032 atmospheric data is not double-counted, which would be the case for the official-inputs
2033 analysis. This alternative implementation is detailed in subsubsection 6.4.5.3.

2034 **6.4.5.1 Beam Samples**

2035 There are 45 systematics which describes the response of the far detector, specifically for
2036 beam sample neutrino events. 44 of these parameters are normalisation parameters and
2037 are split by the interaction mode, true neutrino flavour, reconstructed neutrino energy,
2038 and sample which they affect. The final parameter is the energy scale uncertainty. It is
2039 applied as a multiplicative factor to the reconstructed neutrino energy. The value of
2040 the systematic is taken from Monte Carlo to data differences illustrated in [185]. The
2041 normalisation parameters are assigned a Gaussian error centralised at 1.0 and a width
2042 taken from the covariance matrix. A detailed breakdown of the following procedure is
2043 found in [197]. To build the covariance matrix, a fit is performed on atmospheric data
2044 which has been selected using beam sample selection cuts. The variable which defines
2045 each cut, L (e.g. the electron-muon PID parameter) is assigned a smear, α , and shift, β
2046 parameter such that,

$$L_j^i \rightarrow \bar{L}_j^i = \alpha_j^i L + \beta_j^i \quad (6.4)$$

2047 Where L_j^i (\bar{L}_j^i) correspond to nominal(varied) PID cut parameters given in Table 6.7.
2048 The shift and smear parameters are binned by final-state topology, j , where the binning
2049 is given in Table 6.8. This approach is used to allow the cut parameter distributions to
2050 be modified within the fit which allows better data to Monte Carlo agreement.

2051 Beyond the uncertainty on the PID cut criteria, the mis-modeling of π^0 events is also
2052 considered. If one of the two rings from a π^0 event is missed, this will be reconstructed
2053 as a $CC\nu_e$ event. This is one of the largest systematics hindering the electron neutrino
2054 appearance analyses. Consequently, a systematic has been introduced to constrain
2055 the mis-modeling of π^0 events in SK. To evaluate this systematic uncertainty, a set of

Cut Variable	Parameter Name
0	<code>fitQun e/μ PID</code>
1	<code>fitQun e/π⁰ PID</code>
2	<code>fitQun μ/π PID</code>
3	<code>fitQun Ring-Counting Parameter</code>

Table 6.7: List of cut variables that are included within the shift/smear fit documented in [197].

Category	Description
1e	Only one electron above Cherenkov threshold in the final state
1μ	Only one muon above Cherenkov threshold in the final state
1e+other	One electron and one or more other charged particles above Cherenkov threshold in the final state
1μ+other	One muon and one or more other charged particles above Cherenkov threshold in the final state
1π ⁰	Only one π ⁰ in the final state
1π [±] or 1p	Only one hadron (typically charged pion or proton) in the final state
Other	Any other final state

Table 6.8: Reconstructed event topology categories on which the SK detector systematics [197] are based.

“hybrid- π^0 samples is constructed. These events are built by overlaying one electron-like ring from the SK atmospheric neutrino samples or decay electron ring from a stopping cosmic ray muon with one simulated photon ring. Both rings are chosen so that momenta and opening angle follow the decay kinematics of NC π^0 events from the T2K-MC. Hybrid- π^0 Monte Carlo samples with both rings from the SK Monte Carlo are produced to compare with the hybrid- π^0 data samples and the difference in the fraction of events that pass the ν_e selection criteria is used to assign the systematic error. In order to investigate any data to Monte Carlo differences that may originate from either the higher energy ring or lower energy ring, two samples are built; a sample in which the electron constitutes the higher energy ring from the π^0 decay called the primary sample and another one in which it constitutes the lower energy

2067 ring called the secondary sample. The standard T2K ν_e `fiTQun` event selection criteria
2068 are used to select events.

2069 Final contributions to the covariance matrix are determined by supplementary
2070 uncertainties attained by comparing stopping muon data to Monte Carlo prediction,
2071 as first introduced in section 5.2. The efficiency of tagging decay electrons is estimated
2072 by the stopping muon data/Monte Carlo differences by comparing the number of
2073 one decay electron events to the number of events with one or fewer decay electrons.
2074 The rate at which fake decay electrons are reconstructed by `fiTQun` is estimated in a
2075 similar way with the only difference being the ratio compares the number of two decay
2076 electron events to the number of events with one or two reconstructed decay electrons.
2077 The two sources of systematics are added in quadrature weighted by the number of
2078 events with one true decay electron yielding a 0.2% systematic uncertainty. The muon
2079 misidentification rate is estimated by comparing the number of electron-like events
2080 which have one decay electron to the total number of events with one decay electron.
2081 This systematic is estimated as a 30% effect in the rate of muon misidentification.
2082 A fiducial volume systematic of $\pm 2.5\text{cm}$ which corresponds to a 0.5% shift in the
2083 normalisation of events. Additional normalisation uncertainties based on neutrino
2084 flavour and interaction mode are also defined in [183, 207, 208].

2085 This covariance matrix is then added in quadrature with two other covariance ma-
2086 trices. These are matrices that describe the uncertainties due to secondary interactions
2087 which modify the final state kinematics and the photo-nucleon interactions. These
2088 are generated by studying the effect of each sample's event rates when considering
2089 variations of the underlying parameters.

2090 **6.4.5.2 Atmospheric Samples**

2091 The systematic parameters which control the detector systematics are split into two
2092 sub-groups. Those which are related to particle identification and ring counting
2093 systematics and those which are related to calibration measurements.

2094 The particle identification systematics consist of five parameters. The ring sepa-
2095 ration systematic enforces an anti-correlated response between the single-ring and
2096 multi-ring samples. This is implemented as a fractional increase/decrease in the over-
2097 all normalisation of each sample, depending on the distance to the nearest wall from an
2098 event's vertex. The coefficients of the normalisation are estimated prior to the fit and
2099 depend on the atmospheric sample. The single-ring and multi-ring PID systematics
2100 encode the detector's ability to separate electron-like and muon-like events and are
2101 implemented in an identical way to the ring separation systematic.

2102 The multi-ring electron-like separation systematics encode the ability of the detector
2103 to separate neutrino from anti-neutrino events. As an important systematic in the mass
2104 hierarchy determination, this systematic controls the relative normalisation's of the ν_e
2105 and $\bar{\nu}_e$ enriched samples. A two-stage approach is implemented in the event selection
2106 and a systematic is implemented for both stages. The first stage in the event selection
2107 is to confirm that the most energetic ring, which is required to be electron-like, is from
2108 the neutrino interaction rather than a pion decay from any hadronic system present
2109 in the event. The second stage of separation uses a likelihood-based cut to separate
2110 $\nu_e/\bar{\nu}_e$ events. This takes the typical properties of ν_e scattering events into account;
2111 e.g. less forward-going, with larger energy fractions in the hadronic system. These
2112 parameters are implemented via normalisation parameters which vary the event rate
2113 of each multi-ring sample, whilst ensuring the total event rate is conserved.

²¹¹⁴ There are 22 systematics related to calibration measurements, including effects
²¹¹⁵ from backgrounds, reduction, and showering effects. They are documented in [89] and
²¹¹⁶ briefly summarised in Table 6.9. They are applied via normalisation parameters, with
²¹¹⁷ the separation systematics requiring the conservation of event rate across all samples.

Table 6.9: Sources of systematic errors specified within the grouped into the “calibration” systematics model.

Index	Description
0	Partially contained reduction
1	Fully contained reduction
2	Separation of fully contained and partially contained events
3	Separation of stopping and through-going partially contained events in top of detector
4	Separation of stopping and through-going partially contained events in barrel of detector
5	Separation of stopping and through-going partially contained events in bottom of detector
6	Background due to cosmic rays
7	Background due to flasher events
8	Vertex systematic moving events into and out of fiducial volume
9	Upward going muon event reduction
10	Separation of stopping and through-going in upward going muon events
11	Energy systematic in upward going muon events
12	Reconstruction of the path length of upward going muon events
13	Separation of showering and non-showering upward going muon events
14	Background of stopping upward going muon events
15	Background of non-showering through-going upward going muon events
16	Background of showering through-going upward going muon events
17	Efficiency of tagging two rings from π^0 decay
18	Efficiency of decay electron tagging
19	Background from downgoing cosmic muons
20	Asymmetry of energy deposition in tank
21	Energy scale deposition

2118 6.4.5.3 Correlated Detector Model

2119 A complete uncertainty model of the SK detector would be able to determine the
2120 systematic shift on the sample spectra for a variation of the underlying parameters, e.g.
2121 PMT angular acceptance. However, this is computationally intensive, requiring Monte
2122 Carlo predictions to be made for each plausible variation. Consequently, an effective
2123 parameter model has been utilised for a correlated detector model. This follows from
2124 the T2K-only model implementation documented in subsubsection 6.4.5.1. The T2K-
2125 only implementation can not be used for atmospheric sample systematics because it
2126 is built upon a fit to atmospheric data. Consequently, an implementation where the
2127 cut distributions (given in Table 6.7) from both beam and atmospheric samples are fit,
2128 whilst simultaneously fitting for oscillation parameters. The fit to the cut variables
2129 performs a shape-only fit to ensure that no double-counting occurs.

2130 The correlated detector model utilises the same smear and shift parameters doc-
2131 umented in subsubsection 6.4.5.1, split by final state topology. This splitting is done
2132 because the detector will respond differently to events that have one or multiple rings.
2133 For example, the detector will be able to distinguish single-ring events better than
2134 two overlapping ring events, resulting in smaller systematic uncertainty for one-ring
2135 events compared to two-ring events. Furthermore, the shift and smear parameters
2136 are split by visible energy deposited within the tank has been included, with bin-
2137 ning specified in Table 6.10. This is because atmospheric events are categorised by
2138 subGeV and multiGeV events based on visible energy, so this splitting is required
2139 when correlating the systematic model for beam and atmospheric events. Alongside
2140 the technical requirement, higher energy events will be better reconstructed due to
2141 fractionally less noise within the detector. Consequently, this analysis correlates the
2142 detector systematics between the far-detector beam and subGeV atmospheric samples

2143 due to their similar energies and interaction types. As a result of the inclusion of
2144 visible energy binning, Equation 6.4 becomes

$$L_{jk}^i \rightarrow \bar{L}_{jk}^i = \alpha_{jk}^i L + \beta_{jk}^i, \quad (6.5)$$

2145 where k is the visible energy bin. The multi-GeV, multi-ring, PC, and Up- μ samples
2146 will be subject to the ATMPD particle identification systematics implementation as
2147 described in subsubsection 6.4.5.2 rather than using this correlated detector model.
2148 The calibration systematics also described in the aforementioned chapter still apply to
2149 all atmospheric samples.

Index	Range (MeV)
0	$30 \geq x > 300$
1	$300 \geq x > 700$
2	$700 \geq x > 1330$
3	$1330 \geq x$

Table 6.10: Reconstructed event topology categories on which the SK detector systematics are based

2150 The implementation of this systematic model takes the events reconstructed values
2151 of the cut parameters, modifies them by the particular shift and smear parameter for
2152 that event, and then re-applies event selection. This invokes event migration, which is
2153 a new feature incorporated into the MaCh3 framework which is only achievable due
2154 to the event-by-event reweighting scheme.

2155 Particular care has to be taken when varying the ring counting parameter. This
2156 is because the number of rings is a finite value (one-ring, two-rings, etc.) which
2157 can not be continuously varied. Consequently a ring counting parameter, RC_i , is
2158 calculated for the i^{th} event, following the definition in [209]. The likelihood from

2159 all considered one-ring ($1R$) and two-ring ($2R$) fits are compared to determine the
 2160 preferred hypothesis. This is done by searching for the minimum log-likelihoods,
 2161 $\log(L_{1R})$ and $\log(L_{2R})$. The difference is computed as $\Delta_{LLH} = \log(L_{1R}) - \log(L_{2R})$.
 2162 The ring counting parameter is then defined as,

$$RC_i = \text{sgn}(\Delta_{LLH} - C_{Thres}) \times \sqrt{|\Delta_{LLH} - C_{Thres}|}, \quad (6.6)$$

2163 where $C_{Thres} = 150.0 - 0.6 \times P_{2R}$, and P_{2R} is the momentum of the preferred two-
 2164 ring hypothesis, and $\text{sgn}(x) = x/|x|$. The coefficients used within the definition of
 2165 C_{Thres} are calculated based on Monte Carlo studies. This ring counting parameter
 2166 corresponds to an intermediate likelihood value used within the `fitQun` algorithm
 2167 to decide the number of rings associated with a particular event. However, fake-ring
 2168 merging algorithms are applied after this likelihood value is used to determine the
 2169 number of rings associated with an event. Consequently, this ring counting parameter
 2170 does not always exactly correspond to the number of reconstructed rings. This can be
 2171 seen in Figure 6.10.

2172 As the `fitQun` algorithm does not provide a likelihood value after the fake-ring
 2173 algorithms have been applied, the ring counting parameter distribution is connected to
 2174 the final number of reconstructed rings through “maps”. These are two-dimensional
 2175 distributions linking the ring counting parameter and the final number of recon-
 2176 structed rings. An example is illustrated in Figure 6.11. In principle, the `fitQun`
 2177 reconstruction algorithm should be re-run after the variation in the ring counting
 2178 parameter. However, this is not computationally viable. Therefore the “maps” are
 2179 used as a reweighting template.

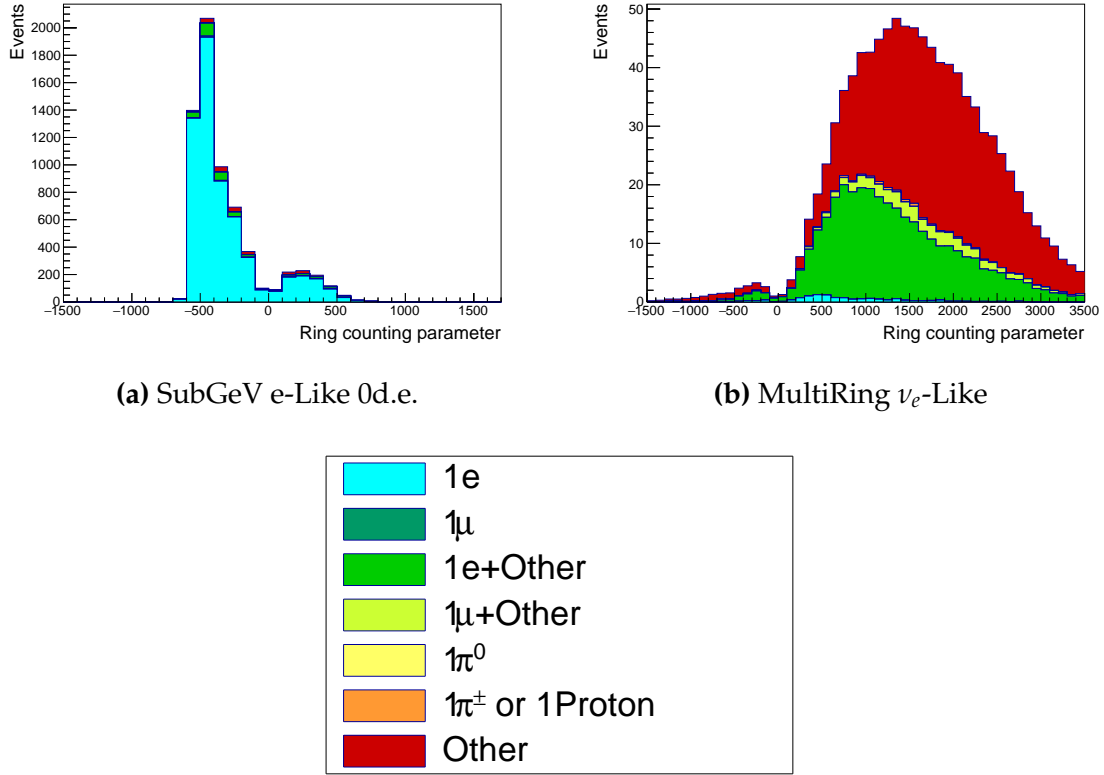


Figure 6.10: The ring counting parameter, as defined in Equation 6.6, for the subGeV electron-like zero decay electron and multi-ring ν_e -like samples.

The maps are split by final state topology and true neutrino flavour and all fiTQun-reconstructed Monte Carlo events are used to fill them. To ensure the conservation of event rate, the maps are normalised such that the total event rate across all number of reconstructed rings is equal to one. Prior to the fit, an event's nominal weight is calculated as $W(N_{Rings}^i, L_{jk}^i)$, where N_{Rings}^i is the reconstructed number of rings for the i^{th} event and $W(x, y)$ is the bin content in the associated map for x number of rings and ring counting parameter L . Then during the fit, the value of $R = W(N_{Rings}^i, \bar{L}_{jk}^i)/W(N_{Rings}^i, L_{jk}^i)$ is calculated as the ring-counting weight for the i^{th} event. This is the only cut variable that uses a reweighting scheme rather than event migration.

The π^0 systematics introduced in subsection 6.4.4 were expected to be applied via a covariance matrix. As this alternative technique performs a simultaneous fit

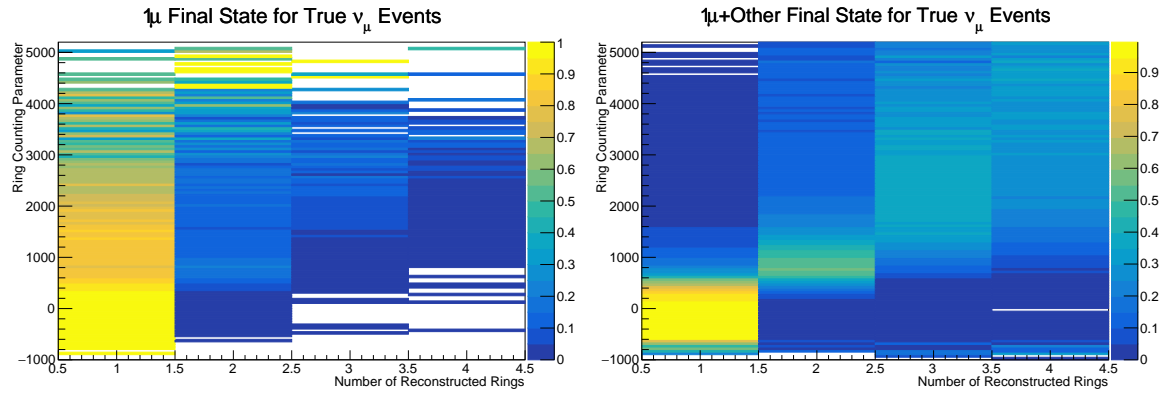


Figure 6.11: The ring counting parameter, defined in Equation 6.6, as a function of the number of reconstructed rings as found by the `fitQun` algorithm. Left: true ν_μ events with only one muon above the Cherenkov threshold in the final state. Right: true ν_μ events with one muon and at least one other charged particle above the Cherenkov threshold in the final state.

2192 between detector distributions and oscillation parameters, the implementation of the
 2193 π^0 systematics has been modified. In practice, the inputs from the hybrid π^0 sample
 2194 is included via the use of “ χ^2 maps”, which are two dimensional histograms in α
 2195 and β parameters over some range. Illustrative examples of the χ^2 maps are given
 2196 in Figure 6.12. Due to their nature, the shift and smear parameters are typically very
 2197 correlated.

2198 The maps are filled through the χ^2 comparison of the hybrid π^0 Monte Carlo and
 2199 data in the particle identification parameters documented in Table 6.7. The Monte
 2200 Carlo distribution is modified with the α and β scaling, whilst cross-section and flux
 2201 nuisance parameters are thrown from their prior uncertainties, and the χ^2 between
 2202 the scaled Monte Carlo and data is calculated and the relevant point in the χ^2 map is
 2203 filled. Then in the fit, the likelihood penalty term is found for the particular particle
 2204 identification parameter by using the value of the relevant χ^2 map for the α and β
 2205 parameter at that step in the MCMC fit. For this fit, only $1\pi^0$ final state topology shift
 2206 and smear parameters use the hybrid $\pi^0 \chi^2$ prior uncertainty.

2207 Similarly, the supplementary systematics which are added into the covariance from
 2208 stopping muon and decay electron studies need to be included. A new framework

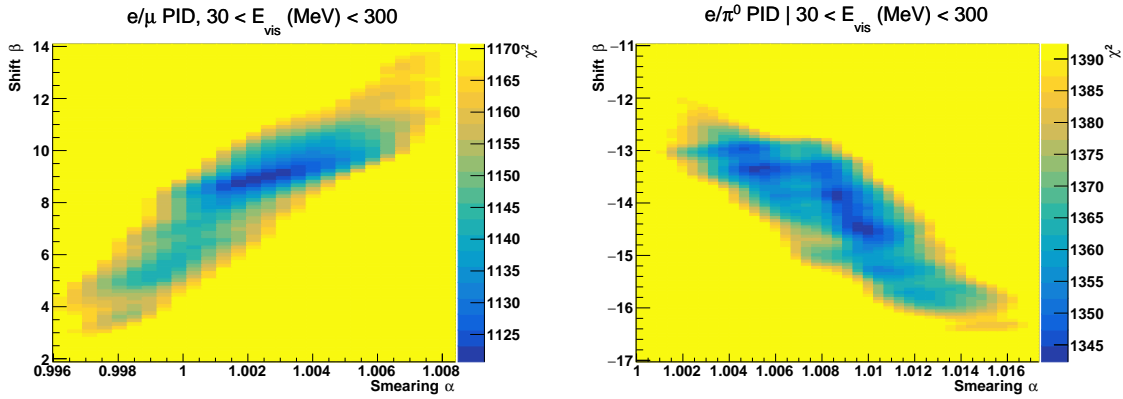


Figure 6.12: The χ^2 between the hybrid- π^0 Monte Carlo and data samples, as a function of smear (α) and shift (β) parameters, for events which have $1\pi^0$ final state topology. Left: Electron-muon separation PID parameter for events with $30 \geq E_{vis}(\text{MeV}) < 300$. Right: Electron- π^0 separation PID parameter for events with $30 \geq E_{vis}(\text{MeV}) < 300$.

[210] was built in tandem with the T2K-SK working group [183] so the additional parameters can be incorporated into the MaCh3 framework. These are applied as normalisation parameters, depending on the particular interaction mode, number of tagged decay electrons, and whether the primary particle generated Cherenkov light. They are assigned Gaussian uncertainties with widths described by a covariance matrix.

Finally, the secondary interaction and photo-nuclear effects need to be accounted for in this detector model. In the T2K-only analysis, a covariance matrix was built to describe the response of the samples to variations of these parameters which was then added in quadrature to the detector covariance matrix. However, this technique can not be applied in the correlated detector model. Consequently, a binned response of each of the secondary interaction systematic parameters and the photo-nuclear response was generated and included through splined shape parameters, similar to the application of shape parameters in the cross-section model (see subsection 6.4.3).

There are a total of 224 α_{jk}^i and β_{jk}^i parameters, of which 32 have prior constraints from the hybrid π^0 samples.

2225 One final complexity of this correlated detector model is that the two sets of sam-
 2226 ples, beam and subGeV atmospheric, use slightly different parameters to distinguish
 2227 electron and muon-like events. The beam-only events use the $\log(L_e/L_\mu)$ whereas
 2228 the atmospheric samples use $\log(L_e/L_\pi)$, where L_X is the likelihood for hypothesis X.
 2229 This is because the beam-only fits use single-ring `fitQun` fitting techniques, whereas
 2230 multi-ring fits are applied to the atmospheric samples where only the electron and
 2231 pion hypothesis are considered. As discussed in section 5.2, the pion hypothesis is
 2232 a very good approximation of the muon hypothesis due to their similar mass. The
 2233 correlation between the two likelihood ratios is illustrated in Figure 6.13. A very
 2234 strong correlation is clearly shown. Consequently, using the same shift and smear
 2235 parameters correlated between the beam and subGeV atmospheric samples is a good
 2236 approximation.

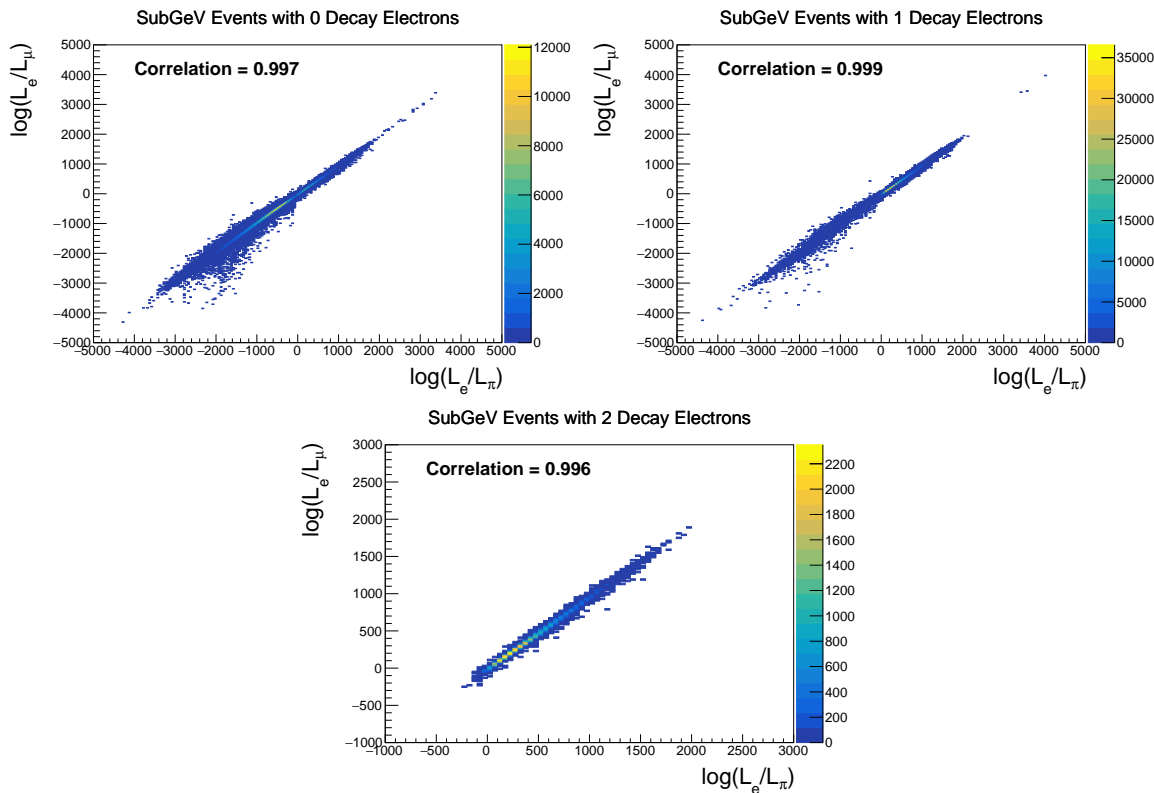


Figure 6.13: The distribution of $\log(L_e/L_\mu)$ compared to $\log(L_e/L_\pi)$ for subGeV events with zero (top left), one (top right) or two (bottom) decay electrons. The correlation in the distribution is calculated as 0.997, 0.999 and 0.996, respectively.

2237

Chapter 7

2238

Oscillation Probability Calculation

2239 It is important to understand how and where the sensitivity to the oscillation pa-
2240 rameters comes from for both atmospheric and beam samples. An overview of how
2241 these samples observe changes in δ_{CP} , Δm_{23}^2 , and $\sin^2(\theta_{23})$ is given in section 7.1. It
2242 also explains the additional complexities involved when performing an atmospheric
2243 neutrino analysis as compared to a beam-only analysis.

2244 Without additional techniques, atmospheric sub-GeV upward-going neutrinos
2245 ($E_\nu < 1.33\text{GeV}, \cos(\theta_Z) < 0.$) can artificially inflate the sensitivity to δ_{CP} due to the
2246 quickly varying oscillation probability in this region. Therefore, a “sub-sampling”
2247 approach has been developed to reduce these biases ensuring accurate and reliable
2248 sensitivity measurements. This technique ensures that small-scale unresolvable fea-
2249 tures of the oscillation probability have been averaged over whilst the large-scale
2250 features in the oscillation probability are unaffected. The documentation and valida-
2251 tion of this technique are found in section 7.2. The oscillation probability calculation is
2252 computationally intensive due to the large number of matrix multiplications needed.
2253 Consequently, the CUDAProb3 implementation choice made within the fitting frame-
2254 work, as detailed in section 7.3, ensures that the analysis can be done in a timely
2255 manner.

2256 Whilst the beam neutrinos are assumed to propagate through a constant density
2257 slab of material, the density variations through the Earth result in more complex
2258 oscillation patterns. Furthermore, the uncertainty in the electron density can modify
2259 the oscillation probability for the denser core layers of the Earth. The model of the

2260 Earth used within this analysis is detailed in section 7.4. This includes information
 2261 about the official SK-only methodology as well as improvements that can be made
 2262 to remove some of the approximations made in that analysis. Another complexity of
 2263 atmospheric neutrinos oscillation studies is that the height of production in the atmo-
 2264 sphere is not known on an event-by-event basis. An analytical averaging technique
 2265 that approximates the uncertainty of the oscillation probability has been followed,
 2266 with the author of this thesis being responsible for the implementation and validation.
 2267 This implementation of an external technique is illustrated in section 7.5.

2268 7.1 Overview

2269 DB: Should this be moved into an earlier chapter? The selections chapter references
 2270 the matter resonance which has not yet been explained at that point

2271 The analysis presented within this thesis focuses on the determination of oscillation
 2272 parameters from atmospheric and beam neutrinos. Whilst subject to the same oscil-
 2273 lation formalism, the way in which the two samples have sensitivity to the different
 2274 oscillation parameters differs quite significantly.

2275 Atmospheric neutrinos have a varying baseline, or “path length”, L , such that
 2276 the distance each neutrino travels before interacting is dependent upon the zenith
 2277 angle, θ_Z . As primary cosmic rays can interact anywhere between the Earth’s surface
 2278 and $\sim 50\text{km}$ above that, the height, h , in the atmosphere at which the neutrino was
 2279 generated also affects the path length,

$$L = \sqrt{(R_E + h)^2 - R_E^2 (1 - \cos^2(\theta_Z))} - R_E \cos(\theta_Z). \quad (7.1)$$

2280 Where $R_E = 6,371\text{km}$ is the Earth's radius. Consequently, the oscillation probabil-
 2281 ity is dependent upon two parameters, $\cos(\theta_Z)$ and E_ν .

2282 The oscillation probability used within this analysis is based on [21]. The neutrino
 2283 wavefunction in the vacuum Hamiltonian evolves in each layer of constant matter
 2284 density via

$$i \frac{d\psi_j(t)}{dt} = \frac{m_j^2}{2E_\nu} \psi_j(t) - \sum_k \sqrt{2} G_F N_e U_{ej} U_{ke}^\dagger \psi_k(t), \quad (7.2)$$

2285 where m_j^2 is the square of the j^{th} vacuum eigenstate mass, E_ν is the neutrino
 2286 energy, G_F is Fermi's constant, N_e is the electron number density and U is the PMNS
 2287 matrix. The transformation $N_e \rightarrow -N_e$ and $\delta_{CP} \rightarrow -\delta_{CP}$ is applied for antineutrino
 2288 propagation. Thus, a model of the Earth's density is required for atmospheric neutrino
 2289 propagation. Following the official SK-only methodology [211], this analysis uses the
 2290 Preliminary Reference Earth Model (PREM) [212]. This model provides piecewise cubic
 2291 polynomials as a function of the Earth's radius which results in the density profile
 2292 illustrated in Figure 7.1. As discussed, the propagator requires layers of constant
 2293 density. The SK methodology approximates the PREM model by using four layers of
 2294 constant density [211]. The details of these layers are detailed in Table 7.1.

Layer	Outer Radius [km]	Density [g/cm^3]	Chemical composition (Z/A)
Inner Core	1220	13	0.468 ± 0.029
Outer Core	3480	11.3	0.468 ± 0.029
Lower Mantle	5701	5.0	0.496
Transition Zone	6371	3.3	0.496

Table 7.1: Description of the four layers of the Earth invoked within the constant density approximation of the PREM model [212].

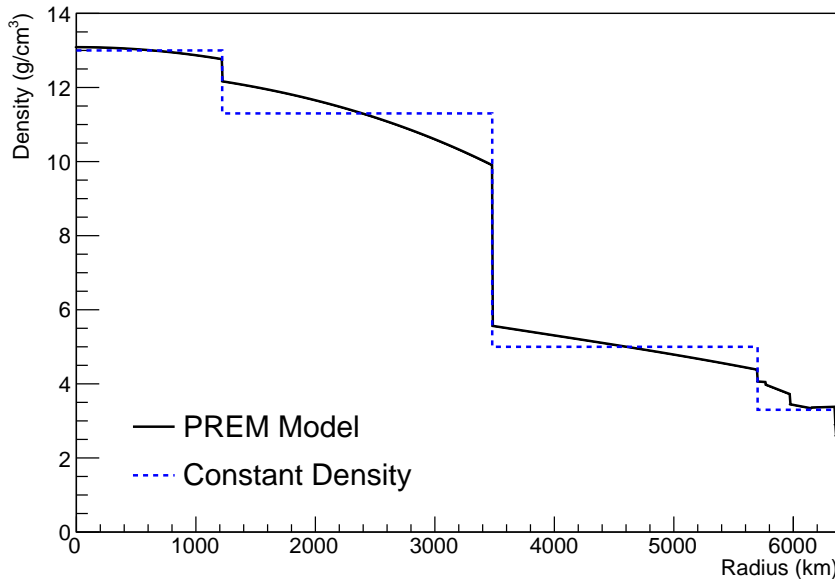


Figure 7.1: The density of the Earth given as a function of the radius, as given by the PREM model (Black), and the constant density four-layer approximation (Blue), as used in the official SK-only analysis.

2295 The atmospheric neutrino oscillation probabilities can be presented as two dimen-
 2296 sional “oscillograms” as illustrated in Figure 7.2. The distinct discontinuities, as a
 2297 function of $\cos(\theta_Z)$, are due to the discrete change in density invoked within the PREM
 2298 model.

2299 Atmospheric neutrinos do have sensitivity to δ_{CP} through a normalisation term.
 2300 Figure 7.3 illustrates the difference in oscillation probability between CP-conserving
 2301 ($\delta_{CP} = 0$) and a CP-violating ($\delta_{CP} = -1.601$) value taken from Asimov A oscillation
 2302 parameter set (Table 2.2). The result is a complicated oscillation pattern in the appear-
 2303 ance probability for sub-GeV upgoing neutrinos. The detector does not have sufficient
 2304 resolution to resolve these individual patterns so the sensitivity to δ_{CP} for atmospheric
 2305 neutrinos comes via the overall normalisation of these events.

2306 The presence of matter means that the effect δ_{CP} has on the oscillation probability
 2307 is not equal between neutrinos and antineutrinos, which would be expected when
 2308 propagating through a vacuum. This is further extenuated by the fact that SK can

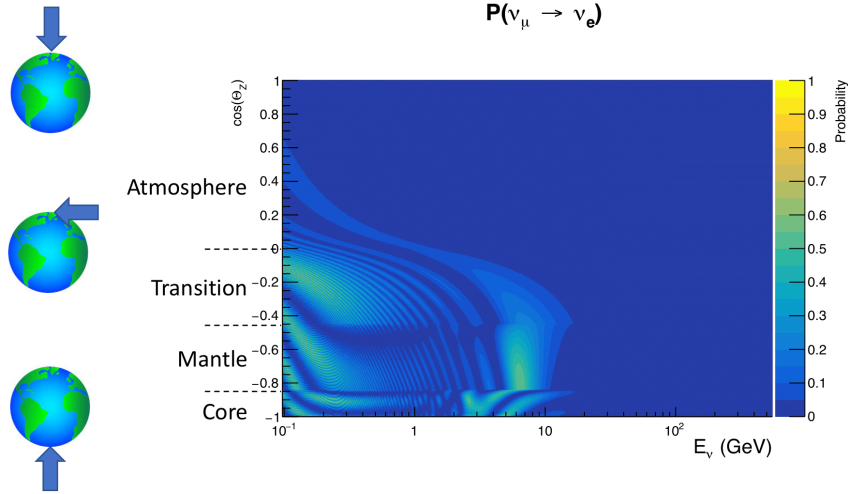


Figure 7.2: An “oscillogram” that depicts the $P(\nu_\mu \rightarrow \nu_e)$ oscillation probability as a function of neutrino energy and cosine of the zenith angle. The zenith angle is defined such that $\cos(\theta_Z) = 1.0$ represents neutrinos that travel from directly above the detector. The four-layer constant density PREM model approximation is used and Asimov A oscillation parameters are assumed (Table 2.2).

not distinguish neutrinos and antineutrinos well and that the cross-section neutrino interaction is larger than that for antineutrinos. Finally, sample selections (discussed in section 6.1) targeting different neutrino interaction modes result in an imbalance in the percentage of neutrinos to anti-neutrinos. This is because negatively charged pions from antineutrino interactions are more likely to be captured by a nucleus compared to a positively charged pion. All of these effects lead to a difference in the number of neutrinos detected compared to antineutrinos. This changes how the δ_{CP} normalisation term is observed, resulting in a very complex sensitivity to δ_{CP} .

Atmospheric neutrinos are subject to matter effects as they travel through the dense matter in the Earth. The vacuum and matter oscillation probabilities for $P(\nu_e \rightarrow \nu_e)$ and $P(\bar{\nu}_e \rightarrow \bar{\nu}_e)$ are presented in Figure 7.4, where the PREM model has been assumed. The oscillation probability for both neutrinos and antineutrinos is affected in the presence of matter. However, the resonance effects around $O(5)\text{GeV}$ only occur for neutrinos in normal mass hierarchy and antineutrinos in inverse mass hierarchy. The

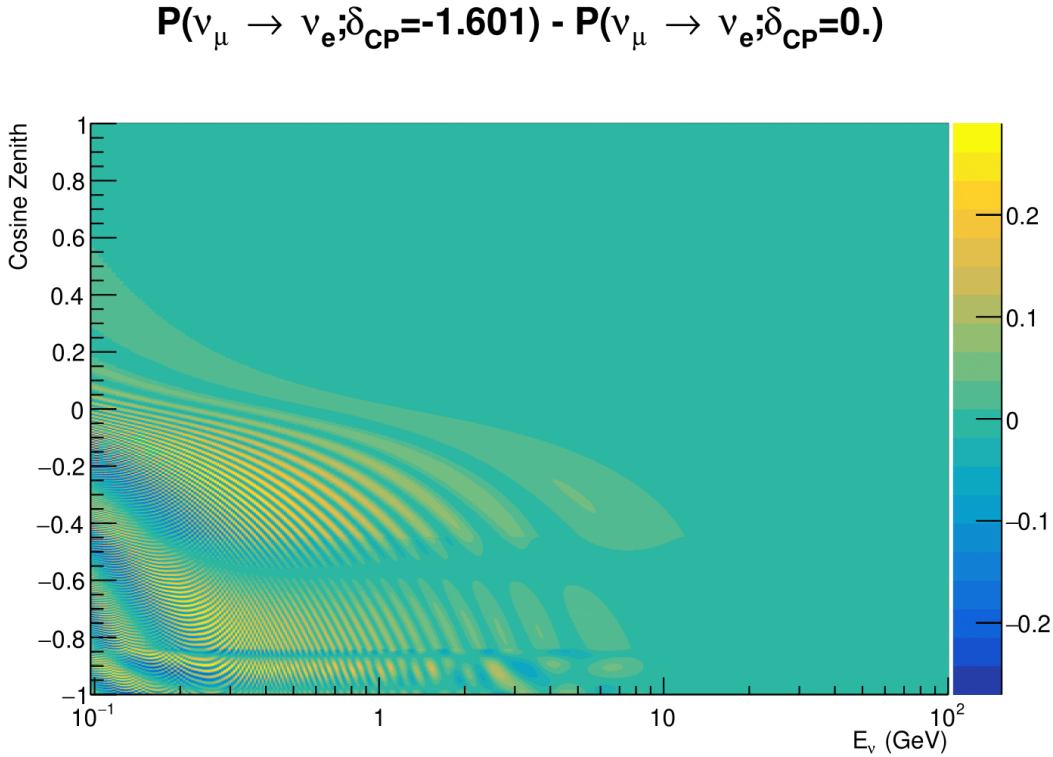


Figure 7.3: The effect of δ_{CP} for atmospheric neutrinos given in terms of the neutrino energy and zenith angle. This oscillogram compares the $P(\nu_\mu \rightarrow \nu_e)$ oscillation probability for a CP conserving ($\delta_{CP} = 0.0$) and a CP violating ($\delta_{CP} = -1.601$) value taken from the Asimov A parameter set. The other oscillation parameters assume the Asimov A oscillation parameter set given in Table 2.2.

exact position and amplitude of the resonance depend on $\sin^2(\theta_{23})$ meaning that the atmospheric neutrinos have sensitivity to $\sin^2(\theta_{23})$.

As the T2K beam flux is centered at the first oscillation maximum ($E_\nu = 0.6\text{GeV}$), the sensitivity to δ_{CP} is predominantly observed as a change in the event-rate of e-like samples in $\nu/\bar{\nu}$ modes. Figure 7.5 illustrates the $P(\nu_\mu \rightarrow \nu_e)$ oscillation probability for a range of δ_{CP} values. A circular modulation of the first oscillation peak (in both magnitude and position) is observed when varying throughout the allowable values of δ_{CP} . The CP-conserving values of $\delta_{CP} = 0, \pi$ have a lower(higher) oscillation maximum than the CP-violating values of $\delta_{CP} = -\pi/2(\delta_{CP} = \pi/2)$. A sub-dominant

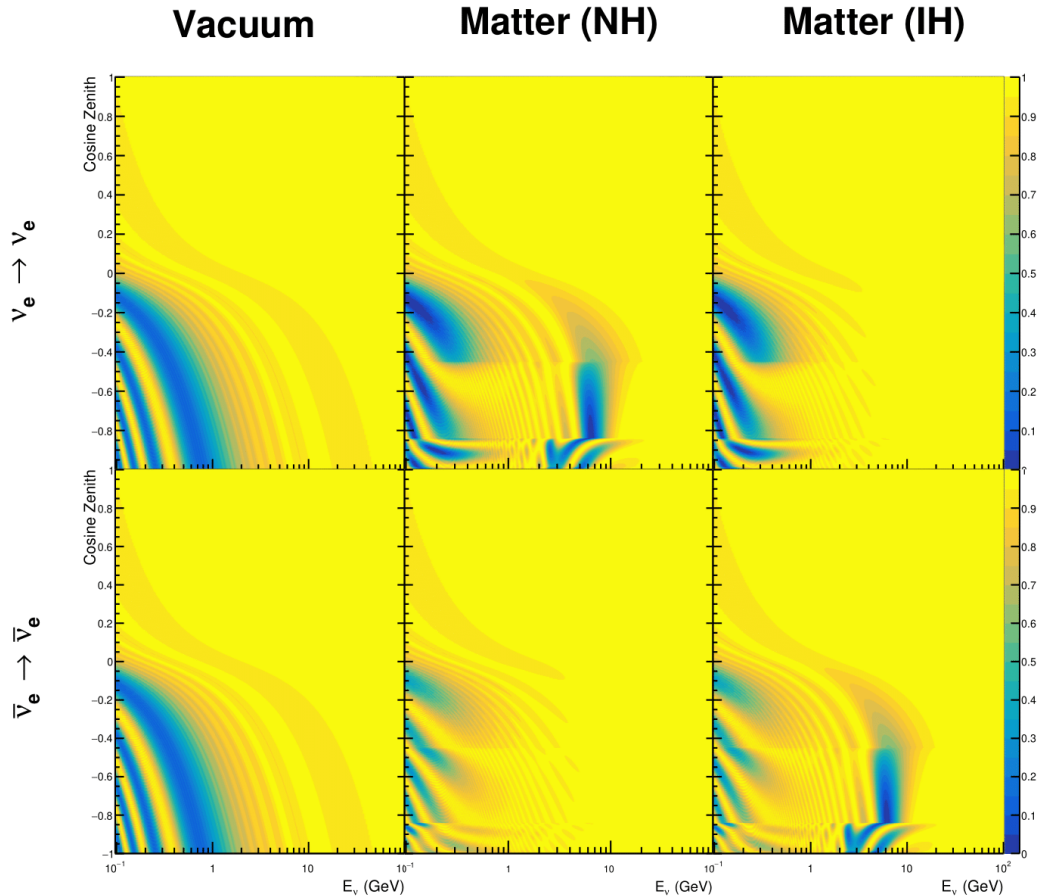


Figure 7.4: An illustration of the matter-induced effects on the oscillation probability, given as a function of neutrino energy and zenith angle. The top row of panels gives the $P(\nu_e \rightarrow \nu_e)$ oscillation probability and the bottom row illustrates the $P(\bar{\nu}_e \rightarrow \bar{\nu}_e)$ oscillation probability. The left column highlights the oscillation probability in a vacuum, whereas the middle and right column represents the oscillation probabilities when the four-layer fixed density PREM model is assumed. All oscillation probabilities assume the “Asimov A” set given in Table 2.2, but importantly, the right column sets an inverted mass hierarchy. The “matter resonance” effects at $E_\nu \sim 5\text{GeV}$ can be seen in the $P(\nu_e \rightarrow \nu_e)$ for normal mass hierarchy and $P(\bar{\nu}_e \rightarrow \bar{\nu}_e)$ for inverted hierarchy.

shift in the energy of the oscillation peak is also present to aid in separating the two

CP-conserving values of δ_{CP} .

T2K’s sensitivity to the $\sin^2(\theta_{23})$ and Δm_{23}^2 is observed as a shape-based variation

of the muon-like samples, as illustrated in Figure 7.5. The value of Δm_{32}^2 laterally shifts

the position of the oscillation dip (around $E_\nu \sim 0.6\text{GeV}$) in the $P(\nu_\mu \rightarrow \nu_\mu)$ oscillation

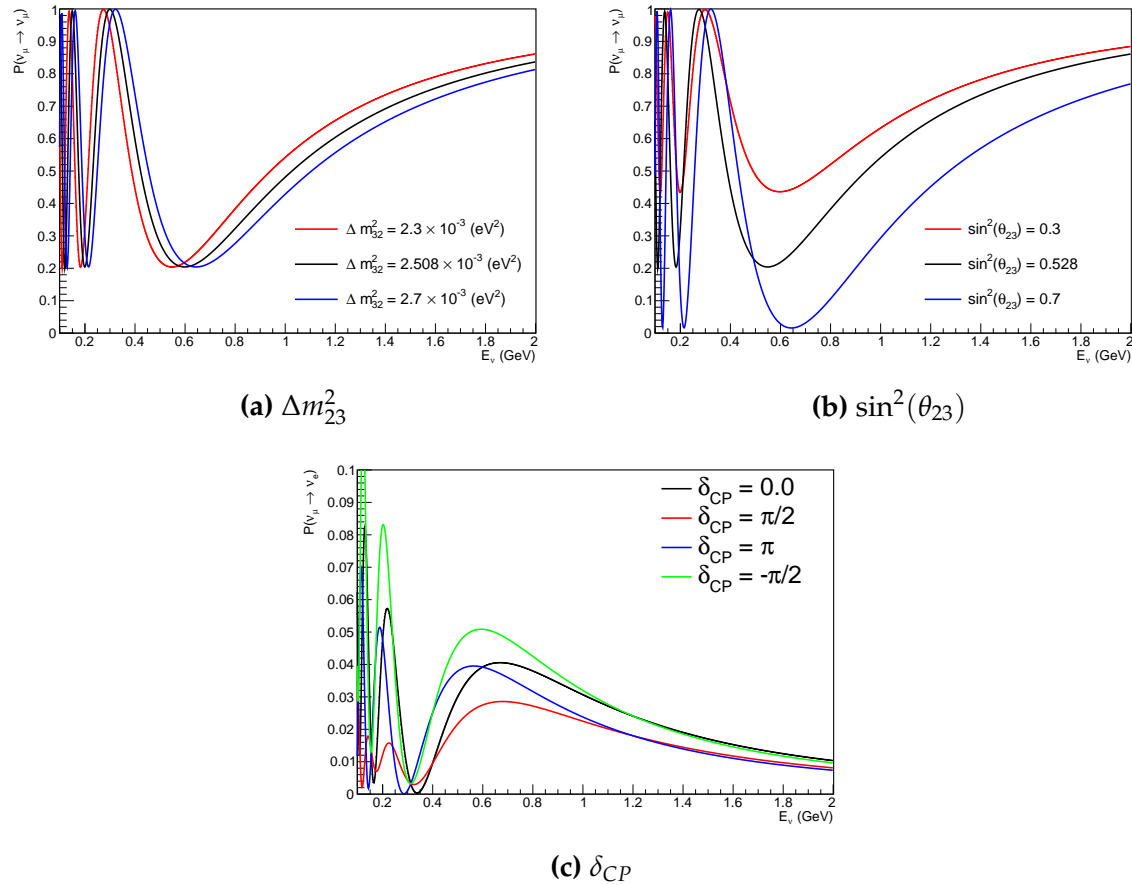


Figure 7.5: The oscillation probability for beam neutrino events given as a function of neutrino energy. All oscillation parameters assume the “Asimov A” set given in Table 2.2 unless otherwise stated. Each panel represents a change in one of the oscillation parameters whilst keeping the remaining parameters fixed.

probability. A variation of $\sin^2(\theta_{23})$ is predominantly observed as a vertical shift of the oscillation dip with second-order horizontal shifts being due to matter effects. The beam neutrinos have limited sensitivity to matter effects due to the relatively shorter baseline as well as the Earth’s mantle being a relatively low-density material (as compared to the Earth’s core). For some values of δ_{CP} , the degeneracy in the number of e-like events allows the mass hierarchy to be resolved. This leads to a δ_{CP} -dependent mass hierarchy sensitivity which can be seen in Figure 7.6.

Whilst all oscillation channels should be included for completeness, the computational resources required to run a fit are limited and any reasonable approximations

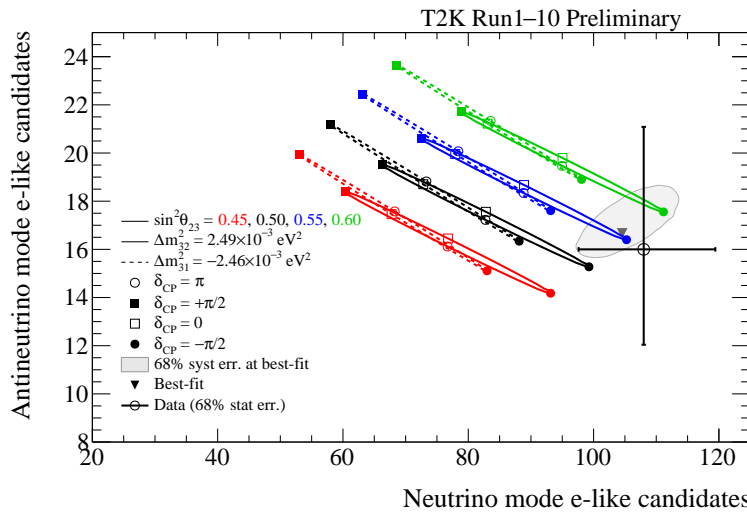


Figure 7.6: The number of electron-like events in the FHC and RHC operating mode of the beam, as a function of the oscillation probabilities. Both normal hierarchy (Solid) and inverse hierarchy (Dashed) values of Δm_{23}^2 are given.

which reduce the number of oscillation probability calculations that need to be made should be applied. The $\nu_e \rightarrow \nu_{e,\mu,\tau}$ (and antineutrino equivalent) oscillations can be ignored for beam neutrinos as the $\nu_e/\bar{\nu}_e$ fluxes are approximately two orders of magnitude smaller than the corresponding $\nu_\mu/\bar{\nu}_\mu$ flux. Furthermore, as the peak neutrino energy of the beam is well below the threshold for charged current tau production ($E_\nu = 3.5 \text{ GeV}$ [51], only a small proportion of the neutrinos produced in the beam have the required energy. For the few neutrinos that have sufficient energy, the oscillation probability is very small due to the short baseline. Whilst these approximations can be made for the beam neutrinos, the atmospheric flux of ν_e is of the same order of magnitude as the ν_μ flux and the energy distribution of atmospheric neutrinos extends well above the tau production threshold.

2357 7.2 Treatment of Fast Oscillations

2358 As shown in Figure 7.7, atmospheric neutrino oscillations have a significantly more
2359 complex structure for upgoing neutrinos with energy below 1GeV. This is because the
2360 L/E dependence of the oscillation probability in this region induces rapid variations
2361 for small changes in L or E . As discussed in section 7.1, this is also the region in which
2362 atmospheric neutrinos have sensitivity to δ_{CP} . In practice, the direction of the neutrino
2363 is inferred from the direction of the final state particles traveling in the detector, which
2364 can be poor for low-energy neutrino interactions. This creates a distinct difference
2365 from the beam neutrinos where the position of the source is very precisely known.

2366 As a consequence of the unresolvable structure, an average oscillation probability
2367 is observed in the subGeV upgoing region. This creates a computational problem; A
2368 significantly large amount of Monte Carlo statistics would be required to accurately
2369 predict the number of events if Monte Carlo averaging was the only technique used.
2370 This section describes the ‘sub-sampling’ approach developed for this analysis and
2371 compares it to the methodology used within the SK-only analysis.

2372 The official SK-only analysis uses the osc3++ oscillation parameter fitter [211].
2373 To perform the fast oscillation averaging, it uses a ‘nearest-neighbour’ technique.
2374 For a given neutrino event, the nearest twenty neighbours in reconstructed lepton
2375 momentum and zenith angle are found and a distribution of their neutrino energies is
2376 built. The RMS, σ , of this distribution is then used to compute an average oscillation
2377 probability for the given neutrino Monte Carlo event.

2378 For the i^{th} event, the oscillation weight is calculated as

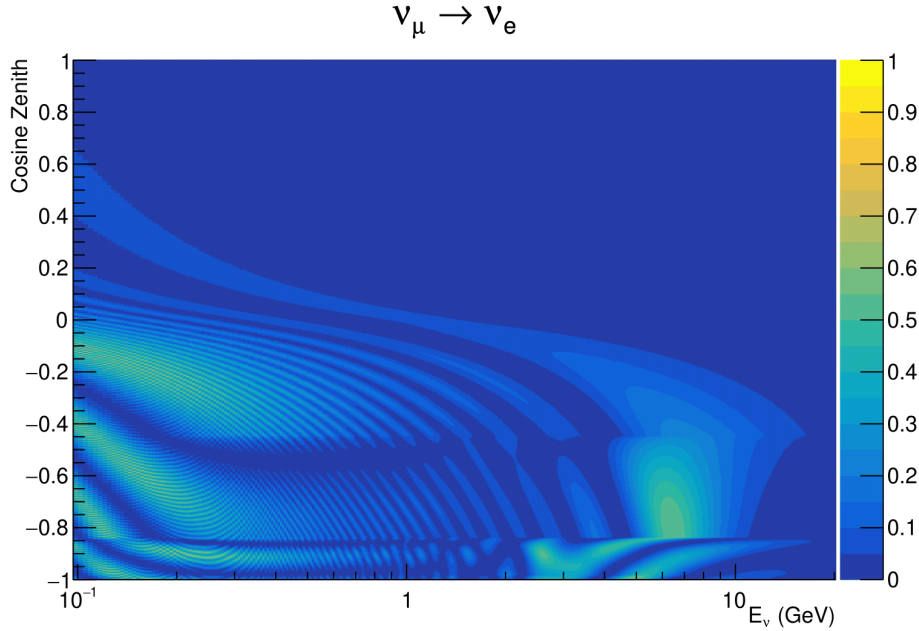


Figure 7.7: The oscillation probability $P(\nu_\mu \rightarrow \nu_e)$, given as a function of neutrino energy and zenith angle, which highlights an example of the “fast” oscillations in the sub-GeV upgoing region.

$$W_i = \frac{1}{5}P(E_i, \bar{L}_i) + \frac{1}{5} \sum_{\beta=-1,-0.5,0.5,1} P(E_i + \beta\sigma_i, L_\beta), \quad (7.3)$$

where $P(E, L)$ is the oscillation probability calculation for neutrino energy E and path length L and the two path lengths, \bar{L}_i and L_β are discussed below. All of the oscillation probability calculations are performed with a fixed zenith angle such that the same density profile is used.

The uncertainty in the production height is controlled by using an “average” production height, \bar{L}_i , which represents the average path length computed using twenty production heights taken from the Honda flux model’s prediction [45]. For a given event, the production heights are sampled in steps of 5% of their cumulative distribution function. L_β values are similarly calculated but instead use different combinations of four production heights,

$$\begin{aligned}
 L_{-1.0} &= \frac{1}{4}L(45, 50, 55, 60), \\
 L_{-0.5} &= \frac{1}{4}L(35, 40, 65, 70), \\
 L_{+0.5} &= \frac{1}{4}L(25, 30, 75, 68), \\
 L_{+1.0} &= \frac{1}{4}L(15, 20, 85, 89).
 \end{aligned} \tag{7.4}$$

2389 This averaging technique works because of the inference between the zenith angle
 2390 and the reconstructed direction of final state particles in the detector. For low-energy
 2391 neutrinos, where the resolution of the true neutrino direction is poor, σ_i will be large,
 2392 resulting in significant averaging effects. Contrary to this, the inferred direction of
 2393 high-energy neutrinos will be much closer to the true value, meaning that σ_i will be
 2394 smaller, culminating in small averaging effects.

2395 In practice, this technique is performed before the fit in order to deal with the
 2396 computational cost. This is possible as the Osc3++ framework uses binned oscillation
 2397 parameters rather than continuous so the oscillation parameters used in the fit are
 2398 known prior to run-time. The framework used in this analysis uses continuous
 2399 oscillation parameters, and due to the MCMC fitting technique, there is no way to
 2400 know which oscillation parameter values will be selected *a priori*. Therefore, the
 2401 oscillation parameter calculation has to be performed at run-time. Computing five
 2402 oscillation probabilities per event would require far too many computational resources
 2403 to be viable. Therefore SK technique can not be used within this analysis. However,
 2404 the concept of the averaging technique can be taken from it.

2405 To perform a similar averaging as the SK analysis, a sub-sampling approach using
 2406 binned oscillograms has been devised. The technique can be explained by considering
 2407 a “fine” and “coarse” oscillogram. The fine oscillograms are used to define the array of

2408 $\cos(\theta_Z)$ and E_ν used in the oscillation engine. The coarse oscillograms cover the same
2409 phase-space but have fewer bins, where the value of a particular coarse bin is taken
2410 as the linear average (flat prior in E_ν and $\cos(\theta_Z)$) of all fine bins which falls into it.
2411 The coarse oscillogram is then used for determining the oscillation weight for a given
2412 event. The binning which is used to calculate the oscillation probabilities, known as
2413 the ‘fine’ binning, has $N \times N$ subdivisions per coarse bin. Figure 7.8 illustrates the
2414 $N = 2$ example where the assigned value to a coarse bin is the average of the four fine
2415 bins which fall in that coarse bin. Whilst the coarse bin edges do not have to be linear
2416 on either axis, the sub-division of the fine bins is linear over the range of a coarse bin.

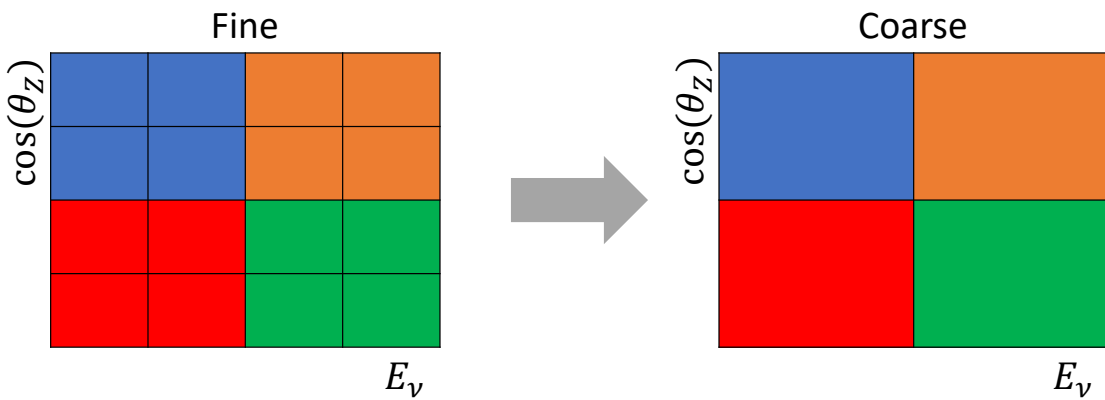


Figure 7.8: Illustration of the averaging procedure for $N = 2$. The oscillation probabilities calculated on the finer left binning are averaged to obtain the oscillation probabilities in the coarser right binning. These averaged oscillation probabilities with the coarser binning are then applied to each event during the fit.

2417 The coarse binning is defined with 67×52 bins in true neutrino energy \times cosine
2418 zenith. It is picked to be identical to that provided in [213]. In general, the binning is
2419 logarithmically spaced in neutrino energy but has some hand-picked bin edges. Firstly,
2420 the bin density around the matter resonance is smoothly increased around the matter
2421 resonance region. This is to avoid smearing this region which can be well sampled by
2422 the Monte Carlo. Secondly, bin edges are selected to hit $0.4, 0.6, 1, 10, 30, 50, 100\text{GeV}$.
2423 This is to ensure that the Coulomb correction systematic and the atmospheric flux
2424 systematics definitions in neutrino energy can be hit. The cosine zenith binning is

approximately linearly spaced across the allowable range but the values of layer transitions are hit precisely: -0.8376 (core-mantle) and -0.4464 (mantle/transition zone). Bins are spread further apart for downgoing events as this is a region unaffected by the fast oscillation wavelengths and reduces the total number of calculations required to perform the calculation.

The choice of N is justified based on two studies. Firstly, the variation of event rates of each sample is studied as a function of N . For a given set of oscillation parameters thrown from the PDG prior constraints (detailed in Table 2.1), the oscillation probabilities are calculated using a given value of N . Each sample is re-weighted and the event rate is stored. The value of N is scanned from 1, which corresponds to no averaging, to 24, which corresponds to the largest computationally viable subdivision binning. The event rate of each sample at large N is expected to converge to a stationary value due to the fine binning fully sampling the small-scale structure. Figure 7.9 illustrates this behaviour for the SubGeV_elike_0dcy sample for 30 different throws of the oscillation parameters.

Denoting the event rate for one sample for a given throw t at each N by λ_t^N , the average over all considered N values ($\bar{\lambda}_t = \frac{1}{24} \sum_{N=1}^{24} \lambda_t^N$) is computed. The variance in the event rate at each N is then calculated as

$$\text{Var}[\lambda^N] = \frac{1}{N_{\text{throws}}} \sum_{t=1}^{N_{\text{throws}}} (\lambda_t^N - \bar{\lambda}_t)^2 - \left[\frac{1}{N_{\text{throws}}} \sum_{t=1}^{N_{\text{throws}}} (\lambda_t^N - \bar{\lambda}_t) \right]^2. \quad (7.5)$$

The aim of the study is to find the lowest value of N such that this variance is below 0.001. This is the typical threshold used by T2K fitters to validate systematic implementation so has been set as the same criteria. The results of this study for each atmospheric sample used within this thesis are illustrated in Figure 7.10 for

SubGeV-elike-0dcy

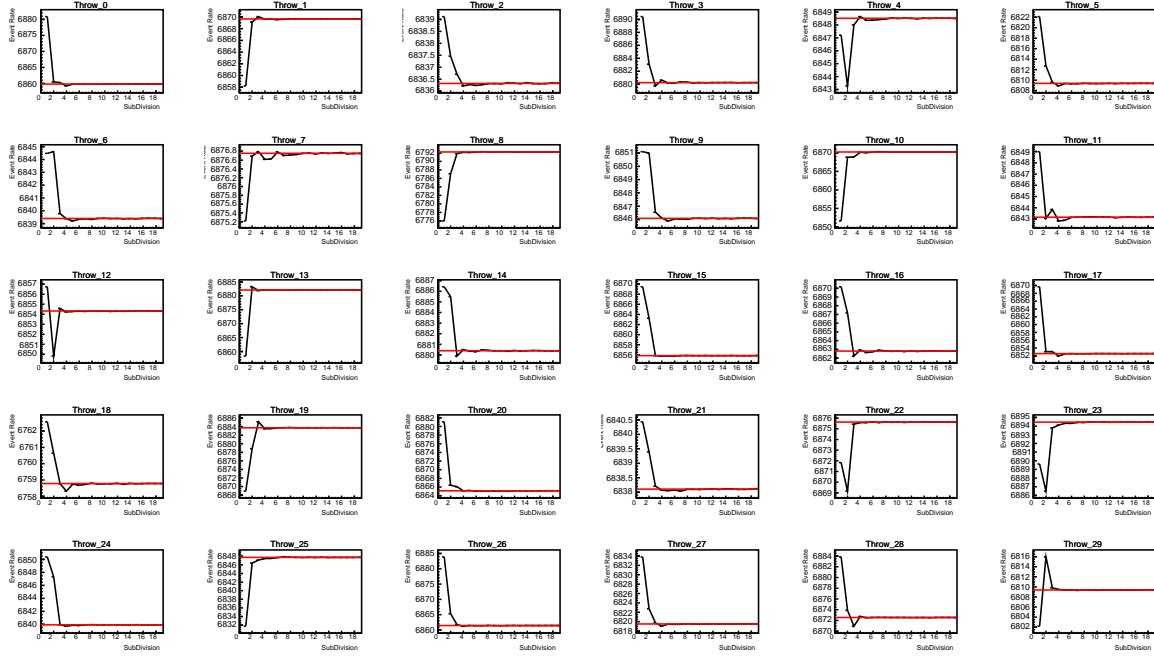


Figure 7.9: Event rate of the SubGeV_elike_0dcy sample as a function of the number of subdivisions per coarse bin. Each subplot represents the event rate of the sample at a different oscillation parameter set thrown from the PDG priors detailed in Table 2.1. The red line in each subplot represents the mean of the event rate over the different values of sub-divisions for that particular oscillation parameter throw.

2447 2000 throws of the oscillation parameters. As can be seen, the variance is below
 2448 the threshold at $N = 10$, and is driven primarily by the SubGeV_mulike_1dcy and
 2449 SubGeV_elike_0dcy samples.

2450 The second study to determine the value of N is as follows. The likelihood for each
 2451 sample is computed against an Asimov data set created with Asimov A oscillation
 2452 parameters (Table 2.2). Following Equation 7.5, the variance of the log-likelihood over
 2453 all considered N is computed. The results are shown in Figure 7.11.

2454 A choice of $N = 10$ sub-divisions per coarse bin has a variance in both event rate
 2455 and log-likelihood residuals less than the required threshold of 0.001. The largest
 2456 value of the likelihood variance is of order 10^{-7} , corresponding to an error on the log-

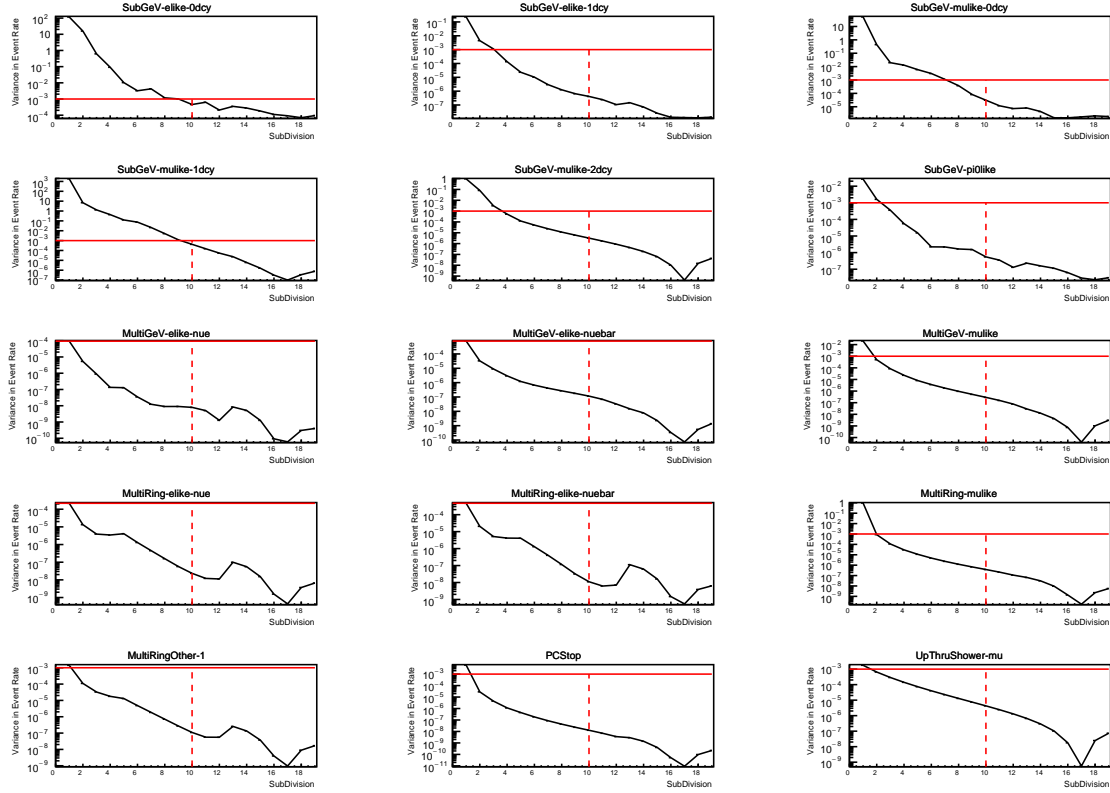


Figure 7.10: Variance of event rate for each atmospheric sample as a function of the number of sub-divisions per coarse bin. The solid red line indicates the 0.1% threshold and the dashed red line indicates the variance at a sub-division $N = 10$.

likelihood of about 3×10^{-4} which is small enough to be negligible for the oscillation analysis.

Figure 7.12 illustrates the effect of the smearing using $N = 10$. The fast oscillations in the sub-GeV upgoing region have been replaced with a normalisation effect whilst the large matter resonance structure remains.

7.3 Calculation Engine

As previously discussed in section 7.2, the calculation of oscillation probabilities is performed at run-time due to utilising continuous oscillation parameters. Consequently, the time per calculation is crucial for fit performance. The initial fitting framework

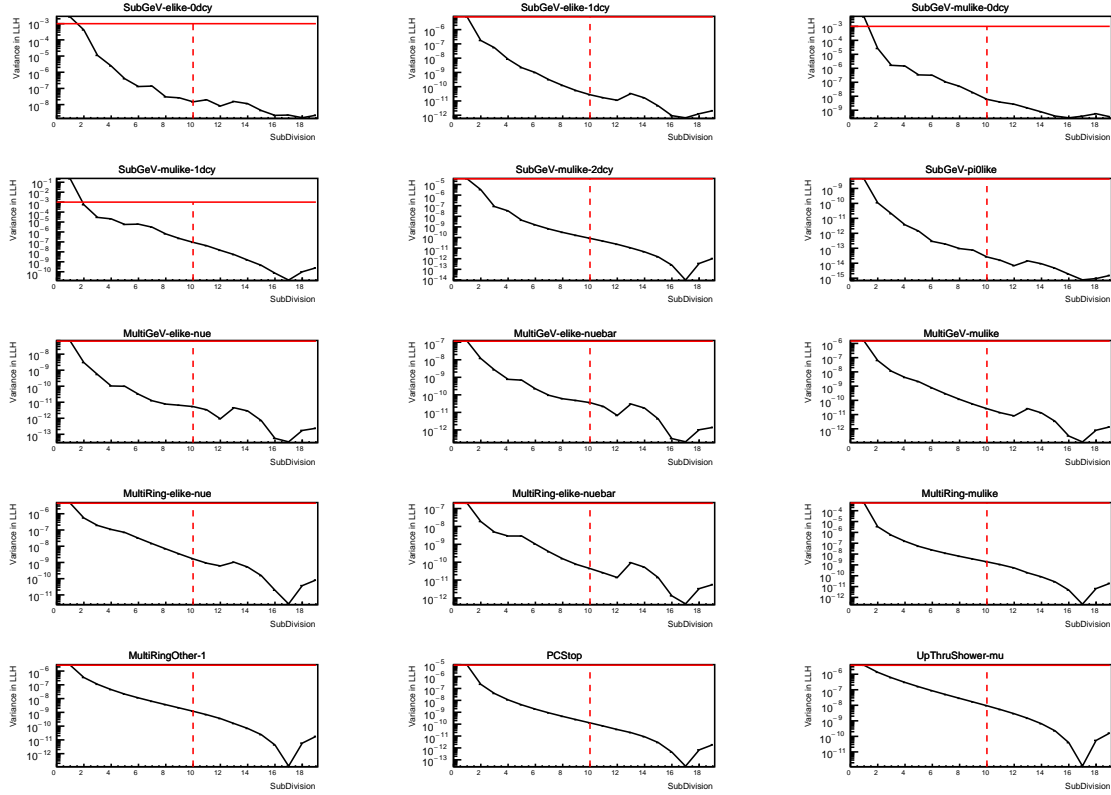


Figure 7.11: Variance of sample likelihood, when compared to ‘Asimov data’ set at Asimov A, for each atmospheric sample as a function of the number of sub-divisions per coarse bin. The solid red line indicates the 0.1% threshold and the dashed red line is a graphical indication of the variance at a sub-division $N = 10$.

used for this analysis was developed with ProbGPU [214]. This is a GPU-only implementation of the prob3 engine [215]. It is primarily designed for neutrino propagation in a beam experiment (single layer of constant density) with the atmospheric propagation code not being used prior to the analysis in this thesis.

Another engine, CUDAProb3 [216], has been implemented within the fitting framework used in this analysis. It has been specifically optimised for atmospheric neutrino oscillation calculation so does not contain the code to replace the beam oscillation calculation. The engine utilises object-orientated techniques as compared to the functional implementation of ProbGPU. This allows the energy and cosine zenith arrays to be kept on GPU memory, rather than having to load these arrays onto GPU memory for each calculation. General memory interfacing is one of the slowest tasks which

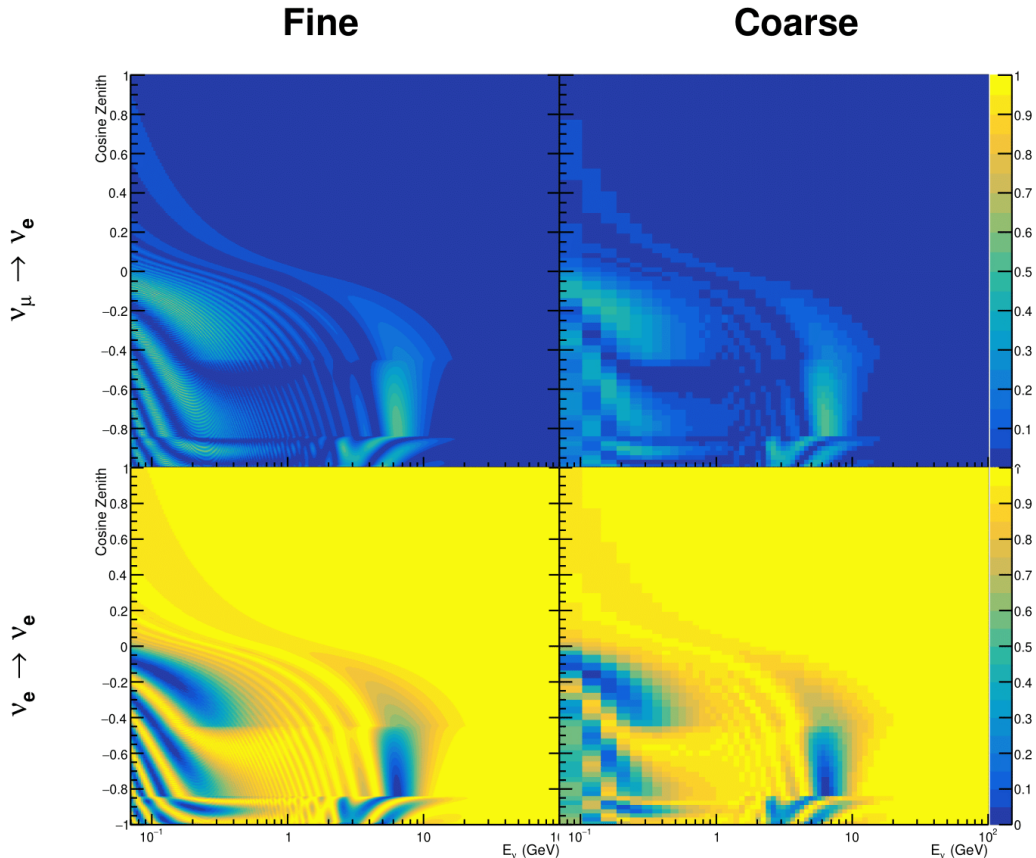


Figure 7.12: The oscillation probability, $P(\nu_\mu \rightarrow \nu_e)$ (top row) and $P(\nu_e \rightarrow \nu_e)$ (bottom row), given as a function of neutrino energy and zenith angle. The left column gives the “fine” binning used to calculate the oscillation probabilities and the right column illustrates the “coarse” binning used to reweight the Monte Carlo events. The fine binning choice is given with $N = 10$, which was determined to be below the threshold from Figure 7.10 and Figure 7.11.

2477 GPUs can do, so being able to eliminate this significantly reduces the time required
 2478 for calculation. This can be seen in Figure 7.13, where the GPU implementation of
 2479 CUDAProb3 is approximately three times faster than the ProbGPU engine.

2480 Another significant advantage of CUDAProb3 is that it contains a CPU multithreaded
 2481 implementation which is not possible with the ProbGPU or prob3 engines. This elimi-
 2482 nates the requirement for GPU resources when submitting jobs to batch systems. As
 2483 illustrated in Figure 7.13, the calculation speed depends on the number of available

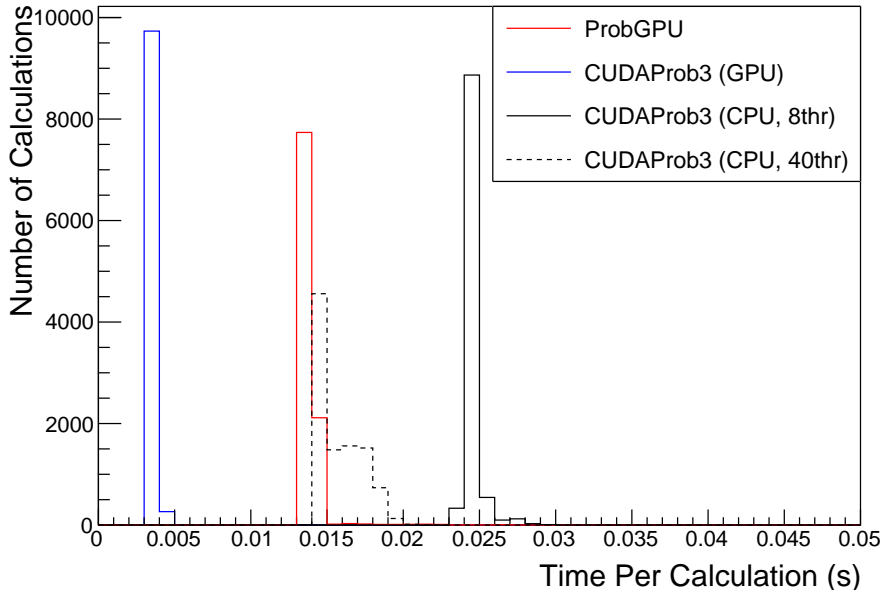


Figure 7.13: The calculation time taken to both calculate the oscillation probabilities and fill the “coarse” oscilloscopes, following the technique given in section 7.2, for the CUDAProb3 and ProbGPU (Red) calculation engines. CUDAProb3 has both a GPU (Blue) and CPU (Black) implementation, where the CPU implementation is multithreaded. Therefore, 8-threads (solid) and 40-threads (dashed) configurations have been tested. Prob3, which is a CPU single-thread implementation has a mean step time of 1.142s.

2484 threads. Using 8 threads (which is typical of the batch systems being used) is ap-
2485 proximately twice as slow as the ProbGPU engine implementation, but would allow
2486 the fitting framework to be run on many more resources. This fact is utilised for any
2487 SK-only fits but GPU resources are required for any fits which include beam samples
2488 due to the ProbGPU requirement. Based on the benefits shown by the implementation
2489 in this section, efforts are being placed into including linear propagation for beam
2490 neutrino propagation into the engine [217].

2491 7.4 Matter Density Profile

2492 For an experiment observing atmospheric neutrinos propagating through the Earth, a
2493 model of the Earth’s density profile is required. The model used within this analysis is

the Preliminary Reference Earth Model (PREM) [212], as illustrated in Figure 7.1. As discussed in section 7.1, the propagator used within the calculation engine requires constant density layers. To follow the official SK-only analysis [211], the average density of each layer has been taken from the PREM model. Table 7.1 documents the density and radii of the layers used within this approximation. The density measurements provided in the PREM model are provided in terms of mass density, whereas neutrino oscillations are sensitive to the electron number density. This value can be computed as the product of the chemical composition, or the Z/A value, and the mass density of each layer. Currently, the only way to calculate the chemical composition value for layers close to the Earth’s core is through neutrino oscillations.

The chemical composition of the upper layers of the Earth’s Mantle and the Transition zone is well known due to it being predominantly pyrolite which has a chemical composition value of 0.496 [218]. The components of the Earth’s core region are less well known. Consequently, the chemical composition dial for the core layers is set to a value of 0.468, as calculated in [219]. This value is assigned a Gaussian error with a standard deviation equivalent to the difference in chemical composition in core and mantle layers. Figure 7.14 illustrates the effect of moving from the $Z/A = 0.5$ method which is used in the official SK-only analysis [211] to these more precise values.

The beam oscillation probability in this thesis uses a baseline of 295km, density $2.6\text{g}/\text{cm}^3$, and chemical composition 0.5 as is done by the official T2K-only analysis [220].

Whilst the propagator requires a fixed density layer model of the Earth, the density only has to be fixed for a specific $E_\nu \times \cos(\theta_Z)$ bin in a given layer. As the density is a function of radius, which is a function of the direction in which a neutrino propagates, a better approximation of the PREM model can be made if a $\cos(\theta_Z)$ -specific density is calculated.

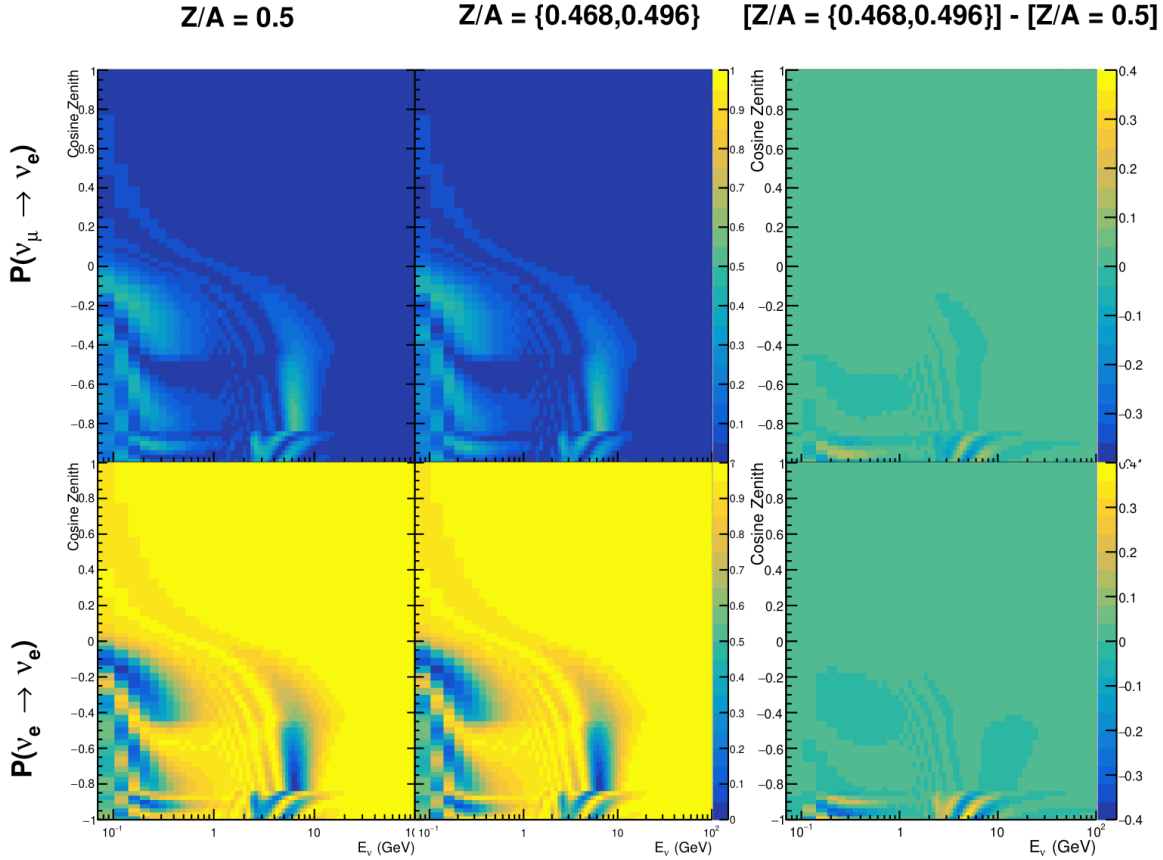


Figure 7.14: The oscillation probability, $P(\nu_\mu \rightarrow \nu_e)$ (top row) and $P(\nu_e \rightarrow \nu_e)$ (bottom row), given as a function of neutrino energy and zenith angle. The left column gives probabilities where the constant $Z/A = 0.5$ approximation which is used in the official SK-only analysis. The middle column gives the probabilities where $Z/A = [0.468, 0.498]$ values are used, as given in Table 7.1. The right column illustrates the difference in oscillation probability between the two different techniques.

2520 To achieve this, the average density, $\langle \rho \rangle_i$, in the i^{th} layer, is calculated as the density,
 2521 $\rho(t)$, integrated over the track a given $\cos(\theta_Z)$,

$$\langle \rho \rangle_i = \frac{1}{t_{i+1} - t_i} \int_{t_i}^{t_{i+1}} \rho(t) dt \quad (7.6)$$

2522 where t_i are the intersection points between each layer and t is the path length of
 2523 the trajectory across the layer.

2524 The oscillation probability calculation speed is approximately linear in the number
 2525 of layers invoked within the Earth model. Therefore a four-layer model is still utilized
 2526 with the only difference to the official SK-only analysis being that the four-layer model
 2527 used for each value of $\cos(\theta_Z)$ is different. Following the method outlined in [221],
 2528 a four-layer piecewise quadratic polynomial is fit to the PREM model for the four
 2529 layers defined in Table 7.1. This fit was not performed by the author of the thesis
 2530 and is documented in [213]. The coefficients of the quadratic fit to each layer are
 2531 given in Table 7.2 with the final distribution illustrated in Figure 7.15. The quadratic
 2532 approximation is clearly much closer to the PREM model as compared to the constant
 2533 density approximation.

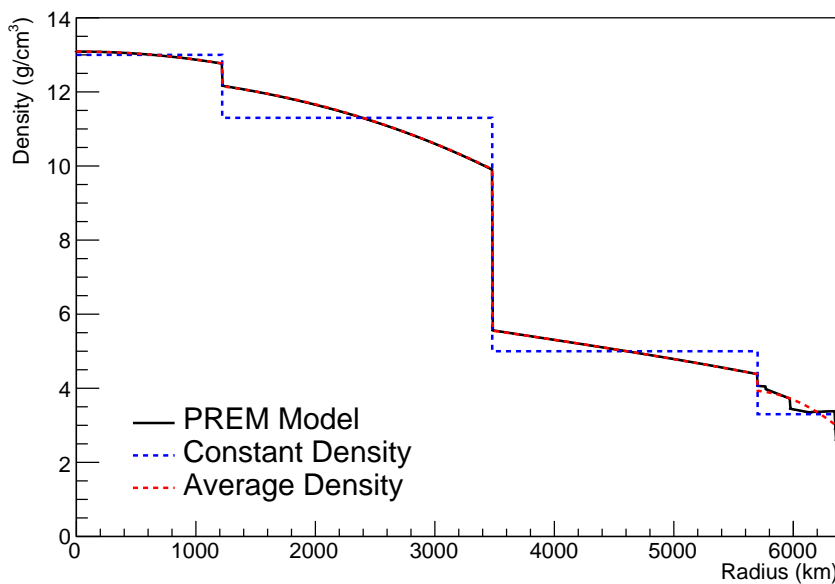


Figure 7.15: The density of the Earth given as a function of the radius, as given by the PREM model (Black), the constant density four-layer approximation (Blue), as used in the official SK-only analysis, and the quadratic approximation of the PREM model (Red).

Layer	Outer Radius [km]	Density [g/cm ³]
Inner Core	1220	$13.09 - 8.84x^2$
Outer Core	3480	$12.31 + 1.09x - 10.02x^2$
Lower Mantle	5701	$6.78 - 1.56x - 1.25x^2$
Transition Zone	6371	$-50.42 + 123.33x - 69.95x^2$

Table 7.2: The quadratic polynomial fits to the PREM model for four assumed layers of the PREM model. The fit to calculate the coefficients is given in [213], where $x = R/R_{Earth}$.

The effect of using the quadratic density per $\cos(\theta_Z)$ model is highlighted in Figure 7.16. The slight discontinuity in the oscillation probability around $\cos(\theta_Z) \sim -0.45$ in the fixed density model, which is due to the transition to mantle layer boundary, has been reduced. This is expected as the difference in the density across this boundary is significantly smaller in the quadratic density model as compared to the constant density model. Whilst the difference in density across the other layer transitions is reduced, there is still a significant difference. This means the discontinuities in the oscillation probabilities remain but are significantly reduced. However, as the quadratic density approximation matches the PREM model well in this region, these discontinuities are due to the Earth model rather than an artifact of the oscillation calculation.

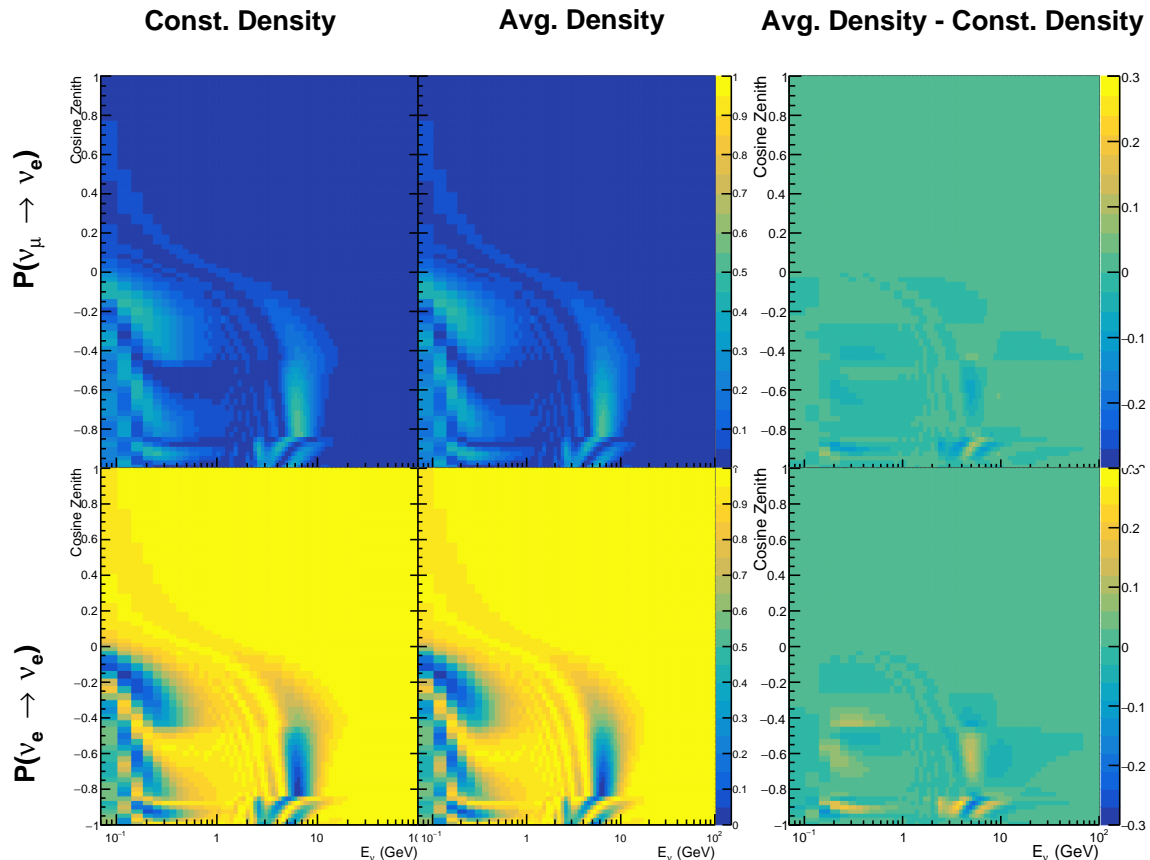


Figure 7.16: The oscillation probability, $P(\nu_\mu \rightarrow \nu_e)$ (top row) and $P(\nu_e \rightarrow \nu_\mu)$ (bottom row), given as a function of neutrino energy and zenith angle. The left column gives probabilities where the four-layer constant density approximation is used. The middle column gives the probabilities where the density is integrated over the trajectory, using the quadratic PREM approximation, for each $\cos(\theta_Z)$ is used. The right column illustrates the difference in oscillation probability between the two different techniques.

2545 7.5 Production Height Averaging

2546 As discussed in section 7.1, the height at which the cosmic ray flux interacts in the
2547 atmosphere is not known on an event-by-event basis. The production height can vary
2548 from the Earth’s surface to $\sim 50\text{km}$ above that. The SK-only analysis methodology
2549 (described in section 7.2) for including the uncertainty on the production height is
2550 to include variations from the Honda model when pre-calculating the oscillation
2551 probabilities prior to the fit. This technique is not possible for this analysis which
2552 uses continuous oscillation parameters that can not be known prior to the fit. Conse-
2553 quently, an analytical averaging technique was developed in [213]. The author of this
2554 thesis was not responsible for the derivation of the technique but has performed the
2555 implementation and validation of the technique for this analysis alone.

2556 Using the 20 production heights per Monte Carlo neutrino event, provided as 5%
2557 percentiles from the Honda flux model, a production height distribution $p_j(h|E_\nu, \cos \theta_Z)$
2558 is built for each neutrino flavour $j = \nu_e, \bar{\nu}_e, \nu_\mu, \bar{\nu}_\mu$. In practice, a histogram is filled with
2559 20 evenly spaced bins in production height h between 0 and 50km. The neutrino energy
2560 and cosine zenith binning of the histogram is the same as that provided in section 7.2.
2561 The average production height, $\bar{h} = \int dh \frac{1}{4} \sum_j p_j(h|E_\nu, \cos(\theta_Z))$, is calculated. The
2562 production height binning of this histogram is then translated into $\delta t(h) = t(\bar{h}) - t(h)$,
2563 where $t(h)$ is the distance travelled along the trajectory.

2564 For the i^{th} traversed layer, the transition amplitude, $D_i(t_{i+1}, t_i)$, is computed. The
2565 time-ordered product of these is then used as the overall transition amplitude via

$$A(t_{n+1}, t_0) = D_n(t_{n+1}, t_n) \dots D_1(t_2, t_1) D_0(t_1, t_0), \quad (7.7)$$

2566

where,

$$\begin{aligned} D_n(t_{n+1}, t_n) &= \exp[-iH_n(t_{n+1} - t_n)] \\ &= \sum_{k=1}^3 C_k \exp[ia_k(t_{n+1} - t_n)] \end{aligned} \quad (7.8)$$

2567

is expressed as a diagonalised time-dependent solution to the Schrodinger equation.

2568

The 0^{th} layer is the propagation through the atmosphere and is the only term that depends on the production height. Using the substitution $t_0 = t(\bar{h}) - \delta t(h)$, it can be shown that

2570

$$D_0(t_1, t_0) = D_0(t_1, \bar{h})D_0(\delta t). \quad (7.9)$$

2571

Thus Equation 7.7 becomes

$$\begin{aligned} A(t_{n+1}, t_0) &= D_n(t_{n+1}, t_n) \dots D_1(t_2, t_1) D_0(t_1, \bar{h}) D(\delta t) \\ &= A(t_{n+1}, \bar{h}) \sum_{k=1}^3 C_k \exp[ia_k \delta t], \\ &= \sum_{k=1}^3 B_k \exp[ia_k \delta t]. \end{aligned} \quad (7.10)$$

2572

The oscillation probability averaged over production height is then calculated as

$$\begin{aligned}
 \bar{P}(\nu_j \rightarrow \nu_i) &= \int d(\delta t) p_j(\delta t | E_\nu, \cos \theta_Z) P(\nu_j \rightarrow \nu_i) \\
 &= \int d(\delta t) p_j(\delta t | E_\nu, \cos \theta_Z) A(t_{n+1}, t_0) A^*(t_{n+1}, t_0) \\
 &= \sum_{km} (B_k)_{ij} (B_m)_{ij}^* \int d(\delta t) p_j(\delta t | E_\nu, \cos \theta_Z) \exp[i(a_k - a_m)\delta t]
 \end{aligned} \tag{7.11}$$

2573 In practice, implementation in CUDAProb3 [216] is relatively straightforward as
 2574 the majority of these terms are already calculated in the standard oscillation calculation.
 2575 Figure 7.17 illustrates the results of the production height averaging. As expected,
 2576 the main effect is observed in the low-energy downward-going and horizontal-going
 2577 events. Upward-going events have to travel the radius of the Earth, $R_E = 6371\text{km}$,
 2578 where the production height uncertainty is a small fraction of the total path length.

2579

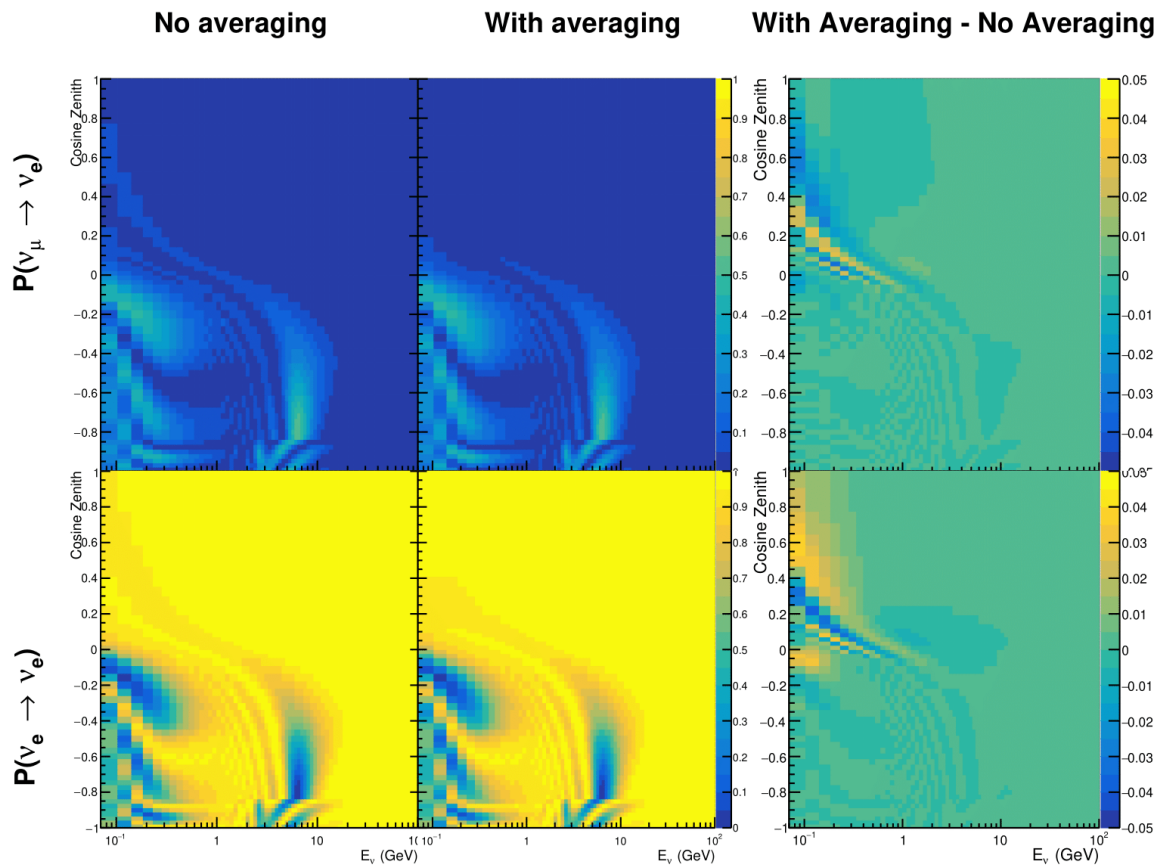


Figure 7.17: The oscillation probability, $P(\nu_\mu \rightarrow \nu_e)$ (top row) and $P(\nu_e \rightarrow \nu_\mu)$ (bottom row), given as a function of neutrino energy and zenith angle. The left column gives probabilities where a fixed production height of 25km is used. The middle column gives the probabilities where the production height is analytically averaged. The right column illustrates the difference in oscillation probability between the two different techniques.

2580 **Bibliography**

- 2581 [1] J. Chadwick, Verhandl. Dtsc. Phys. Ges. **16**, 383 (1914).
- 2582 [2] C. D. Ellis and W. A. Wooster, Proc. R. Soc. Lond. A Math. Phys. Sci. **117**, 109
2583 (1927).
- 2584 [3] W. Pauli, Phys. Today **31N9**, 27 (1978).
- 2585 [4] E. Fermi, Z. Phys. **88**, 161 (1934).
- 2586 [5] F. Reines and C. L. Cowan, Phys. Rev. **92**, 830 (1953).
- 2587 [6] C. L. Cowan, F. Reines, F. B. Harrison, H. W. Kruse, and A. D. McGuire, Science
2588 **124**, 103 (1956), <http://science.sciencemag.org/content/124/3212/103.full.pdf>.
- 2589 [7] G. Danby *et al.*, Phys. Rev. Lett. **9**, 36 (1962).
- 2590 [8] K. Kodama *et al.*, Physics Letters B **504**, 218 (2001).
- 2591 [9] LSND, A. Aguilar-Arevalo *et al.*, Phys. Rev. **D64**, 112007 (2001), hep-ex/0104049.
- 2592 [10] MiniBooNE Collaboration, A. A. Aguilar-Arevalo *et al.*, Phys. Rev. Lett. **110**,
2593 161801 (2013).
- 2594 [11] Planck Collaboration *et al.*, aap **641** (2020).
- 2595 [12] The ALEPH Collaboration, The Delphi Collaboration, The L3 Collaboration, The
2596 SLD Collaboration, The LEP Electroweak Working Group, The SLD Electroweak
2597 and Heavy Flavour Groups, J. A. Bagger *et al.*, Physics Reports **427**, 257 (2006).
- 2598 [13] B. Pontecorvo, Sov. Phys. JETP **26**, 984 (1968), [Zh. Eksp. Teor. Fiz. 53, 1717 (1967)].
- 2599 [14] B. Pontecorvo, Sov. Phys. JETP **7**, 172 (1958), [Zh. Eksp. Teor. Fiz. 34, 247 (1957)].
- 2600 [15] M. Kobayashi and T. Maskawa, Progress of Theoretical Physics **49**, 652 (1973).
- 2601 [16] N. Cabibbo, Phys. Rev. Lett. **10**, 531 (1963).
- 2602 [17] A. M. and, Journal of Physics: Conference Series **587**, 012030 (2015).
- 2603 [18] A. Y. Smirnov, (2003).
- 2604 [19] S. Mikheyev and A. Smirnov, Soviet Journal of Nuclear Physics **42**, 913 (1985).

- 2605 [20] L. Wolfenstein, Phys. Rev. D **17**, 2369 (1978).
- 2606 [21] V. D. Barger, K. Whisnant, S. Pakvasa, and R. J. N. Phillips, Phys. Rev. D **22**, 2718
2607 (1980).
- 2608 [22] The Super-Kamiokande Collaboration, Y. Ashie *et al.*, Phys. Rev. Lett. **93**, 101801
2609 (2004).
- 2610 [23] SNO Collaboration, Q. R. Ahmad *et al.*, Phys. Rev. Lett. **89**, 011301 (2002).
- 2611 [24] 2015 Nobel prize in Physics as listed by Nobelprize.org, [https://www.](https://www.nobelprize.org/nobel_prizes/physics/laureates/2015/)
2612 [nobelprize.org/nobel_prizes/physics/laureates/2015/](https://www.nobelprize.org/nobel_prizes/physics/laureates/2015/), Accessed: 22-06-
2613 2022.
- 2614 [25] J. A. Formaggio and G. P. Zeller, Rev. Mod. Phys. **84**, 1307 (2012), 1305.7513.
- 2615 [26] A. Bellerive, Int. J. Mod. Phys. A **19**, 1167 (2004).
- 2616 [27] R. Davis, D. S. Harmer, and K. C. Hoffman, Phys. Rev. Lett. **20**, 1205 (1968).
- 2617 [28] N. Vinyoles *et al.*, Astrophys. J. **835**, 202 (2017).
- 2618 [29] V. Gribov and B. Pontecorvo, Phys. Lett. B **28**, 493 (1969).
- 2619 [30] K. S. Hirata *et al.*, Phys. Rev. Lett. **63**, 16 (1989).
- 2620 [31] W. Hampel *et al.*, Phys. Lett. B **447**, 127 (1999).
- 2621 [32] SAGE Collaboration, J. N. Abdurashitov *et al.*, Phys. Rev. C **60**, 055801 (1999).
- 2622 [33] Q. R. Ahmad *et al.*, Phys. Rev. Lett. **89** (2002).
- 2623 [34] Borexino Collaboration, Nature **562**, 505 (2018).
- 2624 [35] B. Aharmim *et al.*, Astrophys. J. **653**, 1545 (2006).
- 2625 [36] M. Agostini *et al.*, (2020).
- 2626 [37] S. Andringa *et al.*, Adv. High Energy Phys. **2016**, 1 (2016).
- 2627 [38] J. F. Beacom *et al.*, Chin. phys. C **41**, 023002 (2017).
- 2628 [39] F. An *et al.*, J. Phys. G Nucl. Part. Phys. **43**, 030401 (2016).
- 2629 [40] J. Aalbers *et al.*, (2020), 2006.03114.
- 2630 [41] T. K. Gaisser and M. Honda, (2002).

- 2631 [42] G. D. Barr, T. K. Gaisser, P. Lipari, S. Robbins, and T. Stanev, Physical Review D
2632 **70** (2004).
- 2633 [43] M. Honda, T. Kajita, K. Kasahara, S. Midorikawa, and T. Sanuki, Physical Review
2634 D **75** (2007).
- 2635 [44] M. Honda, T. Kajita, K. Kasahara, and S. Midorikawa, Phys. Rev. D **70**, 043008
2636 (2004).
- 2637 [45] M. Honda, T. Kajita, K. Kasahara, and S. Midorikawa, Phys. Rev. D **83**, 123001
2638 (2011).
- 2639 [46] A. Fasso, A. Ferrari, P. R. Sala, and J. Ranft, (2001).
- 2640 [47] Y. Ashie *et al.*, Physical Review D **71** (2005).
- 2641 [48] F. Reines *et al.*, Phys. Rev. Lett. **15**, 429 (1965).
- 2642 [49] D. Casper *et al.*, Phys. Rev. Lett. **66**, 2561 (1991).
- 2643 [50] K. S. Hirata *et al.*, Phys. Lett. B **280**, 146 (1992).
- 2644 [51] Z. Li *et al.*, Physical Review D **98** (2018).
- 2645 [52] Kamiokande Collaboration *et al.*, (2017).
- 2646 [53] T2K Collaboration, Nature **580**, 339 (2020).
- 2647 [54] M. A. Acero *et al.*, Phys. Rev. Lett. **123**, 151803 (2019).
- 2648 [55] M. G. Aartsen *et al.*, Phys. Rev. Lett. **120** (2018).
- 2649 [56] P. Adamson *et al.*, Phys. Rev. Lett. **112** (2014).
- 2650 [57] M. S. Athar *et al.*, Progress in Particle and Nuclear Physics **124**, 103947 (2022).
- 2651 [58] G. Danby *et al.*, Phys. Rev. Lett. **9**, 36 (1962).
- 2652 [59] K. Abe *et al.*, Physical Review D **87** (2013).
- 2653 [60] MINOS Collaboration, D. G. Michael *et al.*, Phys. Rev. Lett. **97**, 191801 (2006).
- 2654 [61] G. Danby *et al.*, Phys. Rev. Lett. **9**, 36 (1962).
- 2655 [62] NOvA Collaboration, M. A. Acero *et al.*, Phys. Rev. Lett. **123**, 151803 (2019).
- 2656 [63] B. Abi, R. Acciarri, M. A. Acero, and G. e. a. Adamov, Eur. Phys. J. C Part. Fields

- 2657 **80** (2020).
- 2658 [64] Hyper-Kamiokande Proto-Collaboration *et al.*, Prog. Theor. Exp. Phys. **2015**,
2659 53C02 (2015).
- 2660 [65] C. Blanco, D. Hooper, and P. Machado, Physical Review D **101** (2020).
- 2661 [66] MicroBooNE Collaboration *et al.*, Search for an Excess of Electron Neutrino
2662 Interactions in MicroBooNE Using Multiple Final State Topologies, 2021.
- 2663 [67] KARMEN Collaboration, B. Armbruster *et al.*, Phys. Rev. D **65**, 112001 (2002).
- 2664 [68] S.-B. Kim, T. Lasserre, and Y. Wang, Adv. High Energy Phys. **2013**, 1 (2013).
- 2665 [69] M. Sajjad Athar *et al.*, Prog. Part. Nucl. Phys. **124**, 103947 (2022), 2111.07586.
- 2666 [70] K. Abe *et al.*, Nucl. Instrum. Methods Phys. Res. A **1027**, 166248 (2022).
- 2667 [71] F. P. An *et al.*, Phys. Rev. Lett. **108**, 171803 (2012).
- 2668 [72] RENO Collaboration, J. K. Ahn *et al.*, Phys. Rev. Lett. **108**, 191802 (2012).
- 2669 [73] Double Chooz Collaboration, Y. Abe *et al.*, Phys. Rev. Lett. **108**, 131801 (2012).
- 2670 [74] J. Collaboration *et al.*, TAO Conceptual Design Report: A Precision Measurement
2671 of the Reactor Antineutrino Spectrum with Sub-percent Energy Resolution, 2020,
2672 2005.08745.
- 2673 [75] for the RENO Collaboration, New results from RENO and the 5 MeV excess,
2674 AIP Publishing LLC, 2015.
- 2675 [76] Y. Abe *et al.*, Journal of High Energy Physics **2014** (2014).
- 2676 [77] Daya Bay Collaboration, D. Adey *et al.*, Phys. Rev. Lett. **123**, 111801 (2019).
- 2677 [78] M. P. Decowski, Nucl. Phys. B. **908**, 52 (2016).
- 2678 [79] The KamLAND Collaboration, A. Gando *et al.*, Phys. Rev. D **83**, 052002 (2011).
- 2679 [80] P. Dunne, Latest Neutrino oscillation results from T2K, 2020.
- 2680 [81] M. Tanabashi *et al.*, Phys. Rev. D. **98** (2018).
- 2681 [82] Particle Data Group, R. L. Workman and Others, PTEP **2022**, 083C01 (2022).
- 2682 [83] T2K Collaboration, K. Abe *et al.*, Phys. Rev. Lett. **112**, 181801 (2014).

- 2683 [84] Y. Fukuda *et al.*, Phys. Rev. Lett. **81**, 1562 (1998).
- 2684 [85] Linyan Wan, (2022).
- 2685 [86] K. Abe *et al.*, Nuclear Instruments and Methods in Physics Research Section
2686 A: Accelerators, Spectrometers, Detectors and Associated Equipment **737**, 253
2687 (2014).
- 2688 [87] S. Fukuda *et al.*, Nucl. Instrum. Methods Phys. Res. A **501**, 418 (2003).
- 2689 [88] Y. Itow *et al.*, (2001).
- 2690 [89] M. Jiang *et al.*, Prog. Theor. Exp. Phys. **2019** (2019).
- 2691 [90] S. Fukuda *et al.*, Nuclear Instruments and Methods in Physics Research Section
2692 A: Accelerators, Spectrometers, Detectors and Associated Equipment **501**, 418
2693 (2003), <http://www.sciencedirect.com/science/article/pii/S016890020300425X>.
- 2694 [91] Y. Nakano *et al.*, Nucl. Instrum. Methods Phys. Res. A **977**, 164297 (2020).
- 2695 [92] Hamamatsu, Hamamatsu Photonics Photomultiplier Tubes Handbook.
- 2696 [93] K. Abe *et al.*, Nucl. Instrum. Methods Phys. Res. A **1027**, 166248 (2022).
- 2697 [94] J. F. Beacom and M. R. Vagins, Phys. Rev. Lett. **93**, 171101 (2004).
- 2698 [95] L. Marti *et al.*, Nucl. Instrum. Methods Phys. Res. A **959**, 163549 (2020).
- 2699 [96] L. Marti *et al.*, (2019).
- 2700 [97] M. Vagins, Solar/DSNB Neutrino_SK-Gd, 2022.
- 2701 [98] J. Focht, PhD thesis, Massachusetts Institute of Technology, 2004.
- 2702 [99] T. Tanimori *et al.*, IEEE Transactions on Nuclear Science **36**, 497 (1989).
- 2703 [100] Super-Kamiokande Collaboration, J. Hosaka *et al.*, Phys. Rev. D **73**, 112001
2704 (2006).
- 2705 [101] H. Nishino *et al.*, Nucl. Instrum. Methods Phys. Res. A **610**, 710 (2009).
- 2706 [102] S. Yamada *et al.*, IEEE Transactions on Nuclear Science **57**, 428 (2010).
- 2707 [103] S. Yamada, Y. Hayato, Y. Obayashi, and M. Shiozawa, New online system
2708 without hardware trigger for the Super-Kamiokande experiment, in *2007 IEEE
2709 Nuclear Science Symposium Conference Record*, IEEE, 2007.

- [2710] [104] G. Carminati, Phys. Procedia **61**, 666 (2015).
- [2711] [105] P. A. Čerenkov, Phys. Rev. **52**, 378 (1937).
- [2712] [106] I. Frank and I. Tamm, Coherent visible radiation of fast electrons passing through matter, in *Selected Papers*, pp. 29–35, Springer Berlin Heidelberg, Berlin, Heidelberg, 1991.
- [2715] [107] The T2K Collaboration, KEK Proposal (2001),
[2716] <http://neutrino.kek.jp/jhfnu/loi/loi.v2.030528.pdf>.
- [2717] [108] Y. Itow *et al.*, (2001), hep-ex/0106019.
- [2718] [109] The K2K Collaboration and S. H. Ahn, (2001), hep-ex/0103001.
- [2719] [110] The T2K Collaboration, KEK Proposal (2006), http://j-parc.jp/researcher/Hadron/en/pac_0606/pdf/p11-Nishikawa.pdf.
- [2721] [111] C. Bronner, Accelerator Neutrino I_Recent results from T2K, 2022.
- [2722] [112] T2K Collaboration, K. Abe *et al.*, Phys. Rev. Lett. **112**, 061802 (2014),
[2723] <https://link.aps.org/doi/10.1103/PhysRevLett.112.061802>.
- [2724] [113] NINJA Collaboration, T. Fukuda *et al.*, Proposal for precise measurement of
[2725] neutrino-water cross-section in NINJA physics run, Proposal for J-PARC and
[2726] KEK, 2017.
- [2727] [114] T. Ovsiannikova *et al.*, Physics of Particles and Nuclei **48**, 1014 (2017),
[2728] <https://doi.org/10.1134/S1063779617060478>.
- [2729] [115] M. Antonova *et al.*, Journal of Instrumentation **12**, C07028 (2017),
[2730] <http://stacks.iop.org/1748-0221/12/i=07/a=C07028>.
- [2731] [116] The T2K Collaboration, K. Abe *et al.*, Phys. Rev. D **102**, 012007 (2020).
- [2732] [117] K. Abe *et al.*, Progress of Theoretical and Experimental Physics **2021** (2021).
- [2733] [118] The T2K Collaboration, K. Abe *et al.*, Nuclear Instruments
[2734] and Methods in Physics Research Section A: Accelerators, Spectrometers,
[2735] Detectors and Associated Equipment **659**, 106 (2011),
[2736] <http://www.sciencedirect.com/science/article/pii/S0168900211011910>.
- [2737] [119] K. Matsuoka *et al.*, Nuclear Instruments and Methods in Physics Research Section
[2738] A: Accelerators, Spectrometers, Detectors and Associated Equipment **624**, 591

- 2739 (2010), <http://www.sciencedirect.com/science/article/pii/S016890021002098X>.
- 2740 [120] K. Abe *et al.*, Phys. Rev. D. **103** (2021).
- 2741 [121] T. Vladisavljevic, *Predicting the T2K neutrino flux and measuring oscillation parameters* Springer theses, 1 ed. (Springer Nature, Cham, Switzerland, 2020).
- 2742
- 2743 [122] D. Beavis, A. Carroll, and I. Chiang, (1995).
- 2744 [123] P.-A. Amaudruz *et al.*, Nuclear Instruments and Methods in Physics Research
2745 Section A: Accelerators, Spectrometers, Detectors and Associated Equipment
2746 **696**, 1 (2012).
- 2747 [124] N. Abgrall *et al.*, Nuclear Instruments and Methods in Physics Research Section
2748 A: Accelerators, Spectrometers, Detectors and Associated Equipment **637**, 25
2749 (2011).
- 2750 [125] S. Assylbekov *et al.*, Nuclear Instruments and Methods in Physics Research
2751 Section A: Accelerators, Spectrometers, Detectors and Associated Equipment
2752 **686**, 48 (2012).
- 2753 [126] D. Allan *et al.*, Journal of Instrumentation **8**, P10019 (2013).
- 2754 [127] F. Vannucci, Advances in High Energy Physics **2014**, 1 (2014).
- 2755 [128] UA1 magnet sets off for a second new life, 2022.
- 2756 [129] S. Aoki *et al.*, Nuclear Instruments and Methods in Physics Research Section
2757 A: Accelerators, Spectrometers, Detectors and Associated Equipment **698**, 135
2758 (2013).
- 2759 [130] K. Suzuki *et al.*, Progress of Theoretical and Experimental Physics **2015**, 53C01
2760 (2015).
- 2761 [131] S. Brooks, A. Gelman, G. L. Jones, and X.-L. Meng, *Handbook of Markov Chain
Monte Carlo* (CRC Press, 2011).
- 2762
- 2763 [132] W. R. Gilks, S. Richardson, and D. J. Spiegelhalter, *Markov Chain Monte Carlo in
Practice* (Chapman & Hall/CRC Interdisciplinary Statistics, 1995).
- 2764
- 2765 [133] C. Wret, *Minimising systematic uncertainties in the T2K experiment using near-
detector and external data*, PhD thesis, Imperial College London, 2018.
- 2766
- 2767 [134] K. E. Duffy, *Measurement of the Neutrino Oscillation Parameters $\sin^2 \theta_{23}$, Δm_{32}^2 ,*

- 2768 $\sin^2 \theta_{13}$, and δ_{CP} in Neutrino and Antineutrino Oscillation at T2K, PhD thesis, Oriel
2769 College, University of Oxford, 2016.
- 2770 [135] T. Bayes, Rev. Phil. Trans. Roy. Soc. Lond. **53**, 370 (1764).
- 2771 [136] N. Metropolis, A. W. Rosenbluth, M. N. Rosenbluth, A. H. Teller, and E. Teller,
2772 Journal of Chemical Physics **21** (1970).
- 2773 [137] W. K. Hastings, Biometrika **57** (1970).
- 2774 [138] J. Dunkley, M. Bucher, P. G. Ferreira, K. Moodley, and C. Skordis, Mon. Not. R.
2775 Astron. Soc. **356**, 925 (2005).
- 2776 [139] Particle Data Group *et al.*, Prog. Theor. Exp. Phys. **2020** (2020).
- 2777 [140] H. Jeffreys, *The Theory of Probability* Oxford Classic Texts in the Physical Sciences
2778 (, 1939).
- 2779 [141] R. E. Kass and A. E. Raftery, J. Am. Stat. Assoc. **90**, 773 (1995).
- 2780 [142] T. Böhlen *et al.*, Nuclear Data Sheets **120**, 211 (2014),
2781 <http://www.sciencedirect.com/science/article/pii/S0090375214005018>.
- 2782 [143] R. Brun *et al.*, GEANT: Detector Description and Simulation Tool; Oct 1994 CERN
2783 Program Library (CERN, Geneva, 1993), <http://cds.cern.ch/record/1082634>,
2784 Long Writeup W5013.
- 2785 [144] T2K Collaboration, K. Abe *et al.*, Phys. Rev. D **87**, 012001 (2013).
- 2786 [145] C. Zeitnitz and T. Gabriel, Nuclear Instruments and Methods in
2787 Physics Research Section A: Accelerators, Spectrometers,
2788 Detectors and Associated Equipment **349**, 106 (1994),
2789 <http://www.sciencedirect.com/science/article/pii/0168900294906130>.
- 2790 [146] A. Fiorentini *et al.*, T2K Technical Note **217** (2017).
- 2791 [147] N. Abgrall *et al.*, Physical Review C **84** (2011).
- 2792 [148] N. Abgrall *et al.*, Physical Review C **85** (2012).
- 2793 [149] N. Abgrall *et al.*, Nuclear Instruments and Methods in Physics Research Section
2794 A: Accelerators, Spectrometers, Detectors and Associated Equipment **701**, 99
2795 (2013), <http://www.sciencedirect.com/science/article/pii/S016890021201234X>.

- 2796 [150] HARP Collaboration, M. Apollonio *et al.*, Phys. Rev. C **80**, 035208 (2009),
2797 <https://link.aps.org/doi/10.1103/PhysRevC.80.035208>.
- 2798 [151] B. Blau *et al.*, Nuclear Physics B - Proceedings Supplements **113**, 125 (2002).
- 2799 [152] S. Haino *et al.*, Physics Letters B **594**, 35 (2004).
- 2800 [153] NASA, U.S. Standard Atmosphere, 1976, 1976.
- 2801 [154] S. Roesler, R. Engel, and J. Ranft, The Monte Carlo Event Generator DPMJET-III,
2802 in *Advanced Monte Carlo for Radiation Physics, Particle Transport Simulation and*
2803 *Applications*, pp. 1033–1038, Springer Berlin Heidelberg, 2001.
- 2804 [155] K. Niita *et al.*, Radiation Measurements **41**, 1080 (2006).
- 2805 [156] T. Sanuki *et al.*, Physics Letters B **541**, 234 (2002).
- 2806 [157] P. Achard *et al.*, Physics Letters B **598**, 15 (2004).
- 2807 [158] K. Sato, Atmospheric Neutrino_Reviews on neutrino fluxes (low E atm nu),
2808 2022.
- 2809 [159] Y. Hayato and L. Pickering, The European Physical Journal Special Topics **230**,
2810 4469 (2021).
- 2811 [160] Y. Hayato, Acta Physica Polonica B **40** (2009).
- 2812 [161] C. L. Smith, Physics Reports **3**, 261 (1972),
2813 <http://www.sciencedirect.com/science/article/pii/0370157372900105>.
- 2814 [162] O. Benhar, A. Fabrocini, and S. Fantoni, Nuclear Physics A **497**, 423 (1989).
- 2815 [163] R. Bradford, A. Bodek, H. Budd, and J. Arrington, Nuclear Physics B - Proceedings Supplements **159**, 127 (2006),
2816 <http://www.sciencedirect.com/science/article/pii/S0920563206005184>,
2817 Proceedings of the 4th International Workshop on Neutrino-Nucleus Interac-
2818 tions in the Few-GeV Region.
- 2819
- 2820 [164] A. A. Aguilar-Arevalo *et al.*, Physical Review D **81** (2010).
- 2821 [165] R. Gran, J. Nieves, F. Sanchez, and M. J. V. Vacas, Phys. Rev. D **88**, 113007 (2013),
2822 <https://link.aps.org/doi/10.1103/PhysRevD.88.113007>.
- 2823 [166] C. Berger and L. M. Sehgal, Phys. Rev. D **76**, 113004 (2007).

- 2824 [167] C. Berger and L. M. Sehgal, Phys. Rev. D **79**, 053003 (2009),
2825 <https://link.aps.org/doi/10.1103/PhysRevD.79.053003>.
- 2826 [168] T. Sjöstrand, Computer Physics Communications **82**, 74 (1994).
- 2827 [169] C. Bronner and M. Hartz, Tuning of the Charged Hadrons Multiplicities for Deep
2828 Inelastic Interactions in NEUT, in *Proceedings of the 10th International Workshop on*
2829 *Neutrino-Nucleus Interactions in Few-GeV Region (NuInt15)*, Journal of the Physical
2830 Society of Japan, 2016.
- 2831 [170] M. Glück, E. Reya, and A. Vogt, The European Physical Journal C **5**, 461 (1998).
- 2832 [171] A. Bodek and U.-k. Yang, Axial and Vector Structure Functions for Electron- and
2833 Neutrino- Nucleon Scattering Cross Sections at all Q^2 using Effective Leading
2834 order Parton Distribution Functions, 2010.
- 2835 [172] A. Bodek and U.-K. Yang, (2010).
- 2836 [173] S. Gollapinni, (2016).
- 2837 [174] E. S. P. Guerra *et al.*, Phys. Rev. D **99**, 052007 (2019).
- 2838 [175] GEANT4, S. Agostinelli *et al.*, Nucl. Instrum. Meth. **A506**, 250 (2003).
- 2839 [176] R. Brun, F. Bruyant, M. Maire, A. C. McPherson, and P. Zanarini, (1987).
- 2840 [177] K. Abe *et al.*, Physical Review Letters **121** (2018).
- 2841 [178] K. Abe *et al.*, Physical Review D **91** (2015).
- 2842 [179] R. Patterson *et al.*, Nuclear Instruments and Methods in Physics Research Section
2843 A: Accelerators, Spectrometers, Detectors and Associated Equipment **608**, 206
2844 (2009).
- 2845 [180] e. a. S. Berkman, T2K Technical Note **146** (2013).
- 2846 [181] e. a. A. Himmel, T2K Technical Note **219** (2015).
- 2847 [182] F. a. James, (1998), CERN Program Library Long Writeups.
- 2848 [183] e. a. D. Barrow, T2K Technical Note **399** (2020).
- 2849 [184] A. Maghrabi, A. Aldosari, and M. Almutairi, Advances in Space Research **68**,
2850 2941 (2021).

- 2851 [185] Super-Kamiokande Collaboration, K. Abe *et al.*, Phys. Rev. D **97**, 072001 (2018),
2852 <https://link.aps.org/doi/10.1103/PhysRevD.97.072001>.
- 2853 [186] Particle Data Group, J. Beringer *et al.*, Phys. Rev. D **86**, 010001 (2012).
- 2854 [187] Y. N. and, Journal of Physics: Conference Series **888**, 012191 (2017).
- 2855 [188] M. Jiang, *Study of the neutrino mass hierarchy with the atmospheric neutrino data*
2856 *collected in Super-Kamiokande IV*, PhD thesis, Kyoto University, 2019.
- 2857 [189] S. N. K. Iyogi and Y. Obayashi., T2K Technical Note **027** (2011).
- 2858 [190] LeeKaPik, *Study of the neutrino mass hierarchy with the atmospheric neutrino data*
2859 *observed in Super-Kamiokande*, PhD thesis, Tokyo University, 2012.
- 2860 [191] The Super-Kamiokande Collaboration, R. Wendell *et al.*, Phys. Rev. D **81**, 092004
2861 (2010).
- 2862 [192] Super-Kamiokande Collaboration, J. Hosaka *et al.*, Phys. Rev. D **74**, 032002
2863 (2006).
- 2864 [193] L. M. et al, T2K Technical Note **395** (2020).
- 2865 [194] P. B. et al., T2K Technical Note **212** (2015).
- 2866 [195] W. Parker, *Constraining Systematic Uncertainties at T2K using Near Detector Data*,
2867 PhD thesis, Royal Holloway University of London, 2020.
- 2868 [196] V. B. et al., T2K Technical Note **246** (2015).
- 2869 [197] J. Misset, T2K Technical Note **318** (2017).
- 2870 [198] X. Li and M. Wilking, T2K Technical Note **319** (2017).
- 2871 [199] e. a. Tomislav Vladisavljevic, T2K Technical Note **354** (2020).
- 2872 [200] G. Ambrosini *et al.*, Phys. Lett. B **420**, 225 (1998).
- 2873 [201] e. a. Edward Atkin, T2K Technical Note **344** (2019).
- 2874 [202] e. a. D. Barrow, T2K Technical Note **422** (2022).
- 2875 [203] MiniBooNE Collaboration, A. A. Aguilar-Arevalo *et al.*, Phys. Rev. D **81**, 092005
2876 (2010), <https://link.aps.org/doi/10.1103/PhysRevD.81.092005>.
- 2877 [204] MINERvA Collaboration, L. Fields *et al.*, Phys. Rev. Lett. **111**, 022501 (2013),

- 2878 <https://link.aps.org/doi/10.1103/PhysRevLett.111.022501>.
- 2879 [205] C. Wilkinson, P. Rodrigues, S. Cartwright, L. Thompson,
2880 and K. McFarland, Phys. Rev. D **90**, 112017 (2014),
2881 <https://link.aps.org/doi/10.1103/PhysRevD.90.112017>.
- 2882 [206] The MiniBooNE Collaboration, A. A. Aguilar-Arevalo *et al.*, Phys. Rev. D **81**,
2883 013005 (2010), <https://link.aps.org/doi/10.1103/PhysRevD.81.013005>.
- 2884 [207] P. de Perio and J. Imber, T2K Technical Note **186** (2014).
- 2885 [208] P. de Perio and J. Imber, T2K Technical Note **107** (2012).
- 2886 [209] S. Tobayama, *An Analysis of the Oscillation of Atmospheric Neutrinos*, PhD thesis,
2887 British Columbia U., 2016.
- 2888 [210] C. V. Daniel Barrow, T2K-SK Detector Matrix Uncertainties - MaCh3 In-
2889 tegration, <https://git.t2k.org/t2k-sk/t2ksk-detcovmat/-/tree/feature/MaCh3Integration>, Accessed: 22-06-2022.
- 2891 [211] R. Wendell, *Three Flavor Oscillation Analysis of Atmospheric Neutrinos in Super-*
2892 *Kamiokande*, PhD thesis, University of North Carolina, 2008.
- 2893 [212] A. M. Dziewonski and D. L. Anderson, Phys. Earth Planet. Inter. **25**, 297 (1981).
- 2894 [213] e. a. D. Barrow, T2K Technical Note **425** (2022).
- 2895 [214] R. G. Calland, A. C. Kaboth, and D. Payne, **9**, P04016 (2014).
- 2896 [215] R. Wendell, <http://www.phy.duke.edu/raw22/public/Prob3++/>.
- 2897 [216] F. Kallenborn, C. Hundt, S. Böser, and B. Schmidt, Computer Physics Communi-
2898 cations **234**, 235 (2019).
- 2899 [217] L. Warsame, MaCh3 Analysis Progress.
- 2900 [218] S. Bourret, J. A. B. Coelho, and V. V. E. and, Journal of Physics: Conference Series
2901 **888**, 012114 (2017).
- 2902 [219] C. Rott, A. Taketa, and D. Bose, Scientific Reports **5** (2015).
- 2903 [220] K. Hagiwara, N. Okamura, and K. ichi Senda, Journal of High Energy Physics
2904 **2011** (2011).
- 2905 [221] D. Typinski, Earth Gravity, <http://www.typnet.net/Essays/>

2906

EarthGravGraphics/EarthGrav.pdf, Accessed: 24-06-2022.

²⁹⁰⁷ List of Figures

²⁹⁰⁸	2.1	The cross-section of neutrinos from various natural and man-made sources as a function of neutrino energy. Taken from [25]	10
²⁹⁰⁹			
²⁹¹⁰	2.2	The solar neutrino flux as a function of neutrino energy for various fusion reactions and decay chains as predicted by the Standard Solar Model. Taken from [26].	11
²⁹¹¹			
²⁹¹²			
²⁹¹³	2.3	Left panel: The atmospheric neutrino flux for different neutrino flavours as a function of neutrino energy as predicted by the 2007 Honda model (“This work”) [43], the 2004 Honda model (“HKKM04”) [44], the Bartol model [42] and the FLUKA model [46]. Right panel: The ratio of the muon to electron neutrino flux as predicted by all the quoted models. Both figures taken from [43].	14
²⁹¹⁴			
²⁹¹⁵			
²⁹¹⁶			
²⁹¹⁷			
²⁹¹⁸			
²⁹¹⁹	2.4	A diagram illustrating the definition of zenith angle as used in the Super Kamiokande experiment [47].	14
²⁹²⁰			
²⁹²¹	2.5	Prediction of $\nu_e, \bar{\nu}_e, \nu_\mu, \bar{\nu}_\mu$ fluxes as a function of zenith angle as calculated by the HKKM model [45]. The left, middle and right panels represent three values of neutrino energy, 0.32GeV, 1.0GeV and 3.2GeV respectively. Predictions for other models including Bartol [42], Honda [43] and FLUKA [46] are given in [47].	15
²⁹²²			
²⁹²³			
²⁹²⁴			
²⁹²⁵			
²⁹²⁶	2.6	Constraints on the atmospheric oscillation parameters, $\sin^2(\theta_{23})$ and Δm_{23}^2 , from atmospheric and long baseline experiments: SK [52], T2K [53], NO ν A [54], IceCube [55] and MINOS [56]. Figure taken from [57].	16
²⁹²⁷			
²⁹²⁸			
²⁹²⁹	2.7	Reactor electron antineutrino fluxes for ^{235}U (Black), ^{238}U (Green), ^{239}Pu (Purple), and ^{241}Pu (Orange) isotopes. The inverse β -decay cross-section (Blue) and corresponding measurable neutrino spectrum (Red) are also given. Top panel: Schematic of Inverse β -decay interaction including the eventual capture of the emitted neutron. This capture emits a γ -ray which provides a second signal of the event. Taken from [69].	19
²⁹³⁰			
²⁹³¹			
²⁹³²			
²⁹³³			
²⁹³⁴			
²⁹³⁵	3.1	A schematic diagram of the Super-Kamiokande Detector. Taken from [88].	25

2936	3.2	The location of “standard PMTs” (red) inside the SK detector. Taken from [86].	29
2937			
2938	3.3	Schematic view of the data flow through the data acquisition and online system. Taken from [102].	32
2939			
2940	3.4	The cross-section view of the Tokai to Kamioka experiment illustrating the beam generation facility at J-PARC, the near detector situated at a baseline of 280m and the Super Kamiokande far detector situated 295km from the beam target.	35
2941			
2942			
2943			
2944	3.5	The near detector suite for the T2K experiment showing the ND280 and INGRID detectors. The distance between the detectors and the beam target is 280m.	36
2945			
2946			
2947	3.6	Top panel: Bird’s eye view of the most relevant part of primary and secondary beamline used within the T2K experiment. The primary beamline is the main-ring proton synchrotron, kicker magnet, and graphite target. The secondary beamline consists of the three focusing horns, decay volume, and beam dump. Figure taken from [118]. Bottom panel: The side-view of the secondary beamline including the focusing horns, beam dump and neutrino detectors. Figure taken from [119].	38
2948			
2949			
2950			
2951			
2952			
2953			
2954	3.7	The Monte Carlo prediction of the energy spectrum for each flavour of neutrino (ν_e , $\bar{\nu}_e$, ν_μ and $\bar{\nu}_\mu$) in the neutrino dominated beam FHC mode (Left) and antineutrino dominated beam RHC mode (Right) expected at SK. Taken from [120].	39
2955			
2956			
2957			
2958	3.8	Top panel: T2K muon neutrino disappearance probability as a function of neutrino energy. Middle panel: T2K electron neutrino appearance probability as a function of neutrino energy. Bottom panel: The neutrino flux distribution for three different off-axis angles (Arbitrary units) as a function of neutrino energy.	41
2959			
2960			
2961			
2962			
2963	3.9	The components of the ND280 detector. The neutrino beam travels from left to right. Taken from [118].	42
2964			
2965	3.10	Comparison of data to Monte Carlo prediction of integrated deposited energy as a function of track length for particles that stopped in FGD1. Taken from [123].	44
2966			
2967			

2968	3.11 Schematic design of a Time Projection Chamber detector. Taken from [124].	45
2969	3.12 The distribution of energy loss as a function of reconstructed momentum for charged particles passing through the TPC, comparing data to Monte Carlo prediction. Taken from [124].	45
2970		
2971		
2972	3.13 A schematic of the P0D side-view. Taken from [125].	47
2973	3.14 Left panel: The Interactive Neutrino GRID on-axis Detector. 14 modules are arranged in a cross-shape configuration, with the center modules being directly aligned with the on-axis beam. Right panel: The layout of a single module of the INGRID detector. Both figures are recreated from [118].	49
2974		
2975		
2976		
2977		
2978	4.1 Example of using Monte Carlo techniques to find the area under the blue line. The gradient and intercept of the line are 0.4 and 1.0 respectively. The area found to be under the curve using one thousand samples is 29.9 units.	54
2979		
2980		
2981		
2982	4.2 The area under a line of gradient 0.4 and intercept 1.0 for the range $0 \leq x \leq 10$ as calculated using Monte Carlo techniques as a function of the number of samples used in each repetition. The analytical solution to the area is 30 units as given by the red line.	54
2983		
2984		
2985		
2986	4.3 Three MCMC chains, each with a stationary distribution equal to a Gaussian centered at 0 and width 1 (As indicated by the black dotted lines). All of the chains use a Gaussian proposal function but have different widths (or 'step size σ '). The top panel has $\sigma = 0.1$, middle panel has $\sigma = 0.5$ and the bottom panel has $\sigma = 5.0$.	60
2987		
2988		
2989		
2990		
2991	4.4 The log-likelihood from the fit detailed in DB: Link to AsimovA Sensitivity Section as a function of the number of steps accumulated in each fit. Many independent MCMC chains were run in parallel and overlaid on this plot. The red line indicates the 1×10^5 step burn-in period after which the log-likelihood becomes stable.	61
2992		
2993		
2994		
2995		

2996	4.5	Left: The two dimensional probability distribution for two correlated parameters x and y . The red distribution shows the two dimensional probability distribution when $0 \leq x \leq 5$. Right: The marginalised probability distribution for the y parameter found when requiring the x to be bound between $-5 \leq x \leq 5$ and $0 \leq x \leq 5$ for the black and red distribution, respectively.	63
3002	5.1	The NEUT prediction of the ν_μ -H ₂ O cross-section overlaid on the T2K ν_μ flux. The charged current (black, solid) and neutral current (black, dashed) inclusive, charged current quasi-elastic (blue, solid), charged current 2p2h (blue, dashed), charged current single pion production (pink), and charged current multi- π and DIS (Purple) cross-sections are illustrated. Figure taken from [159].	71
3008	5.2	Illustration of the various processes which a pion can undergo before exiting the nucleus. Taken from [173].	72
3010	5.3	Event displays from Super Kamiokande illustrating the “crisp” ring from a muon and the typically “fuzzier” electron ring. Each pixel represents a PMT and the color scheme denotes the accumulated charge deposited on that PMT. Figures taken from [181].	75
3014	5.4	The electron/muon PID separation parameter for all sub-GeV single-ring events in SK-IV. The charged current (CC) component is broken down in four flavours of neutrino (ν_μ , $\bar{\nu}_\mu$, ν_e and $\bar{\nu}_e$). Events with positive values of the parameter are determined to be electron-like. . .	79
3018	5.5	The variation of the measured dark rate as a function of date, broken down by PMT type. The SK-IV and SK-V periods span September 2008 to May 2018 and January 2019 to July 2020, respectively. The break in measurement in 2018 corresponds to the period of tank repair and refurbishment. Figure adapted from [183].	81
3023	5.6	Comparison of the measured raw charge deposited per event from the stopping muon data samples between SK-IV (Blue) and SK-V (Red), split by the primary muon subevent and the associated decay electron subevent.	82

3027	5.7 The distribution of the reconstructed momentum from the muon ring divided by the distance between the reconstructed muon and decay electron vertices as found in the stopping muon data sets of SK-IV (Black) and SK-IV (Red). Only events with one tagged decay electron are considered. A Gaussian fit is considered in the range [2.0, 2.4] MeV/cm and illustrated as the solid curve.	83
3033	5.8 The χ^2 difference between the SK-IV and SK-V reconstructed muon momentum divided by range when the SK-V is modified by the scaling parameter α . Both additive (Blue) and multiplicative (Black) scaling factors have been considered. In practice, the additive scaling factor actually uses the value of $(\alpha - 1.0)$ but is illustrated like this so the results can be shown on the same axis range.	84
3039	5.9 A depiction of the topology patterns for fully-contained (FC), partially-contained (PC) and up-going muon (Up- μ) samples included in this analysis.	85
3042	5.10 The predicted neutrino flux of the fully contained (FC) sub-GeV and multi-GeV, partially contained (PC), and upward-going muon (Up- μ) events. The prediction is broken down by the $\nu_x \rightarrow \nu_e$ prediction (top left), $\nu_x \rightarrow \nu_\mu$ prediction (top right) and $\nu_x \rightarrow \nu_\tau$ prediction (bottom). All systematic dials are set to their nominal values and the Asimov A oscillation parameters are assumed.	87
3048	5.11 The predicted neutrino flux of the beam neutrinos, illustrated as a function of neutrino energy. The predictions are broken down by the number of decay electrons associated with the particular events. All systematic dials are set to their nominal values and the Asimov A oscillation parameters are assumed.	89

3053	6.1	The accumulated beam data, measured as the number of protons on target (POT). The total data (blue) is given which comprises of the neutrino beam (red) and antineutrino (purple) components. The beam power for neutrino and antineutrino beams is given as the markers using the same colourscheme. The timescale runs from Run 1 which started in January 2010 until Run 10 which ended in February 2020. The ratio of accumulated data in neutrino and antineutrino beam is 54.7% : 45.3%.	91
3061	6.2	Comparison of the SK-IV atmospheric samples between predictions made with the CP-violating Asimov A (Black) and CP-conserving Asimov B (Red) oscillation parameter sets (given in Table 2.2). The subGeV samples CCRES and π^0 -like samples are given in their reconstructed lepton momentum. All other samples are presented in their reconstructed zenith angle projection.	98
3067	6.3	The nominal Monte Carlo predictions for the FGD1 and FGD2 samples in neutrino beam mode, broken down into the $CC\nu_\mu 0\pi$, $CC\nu_\mu 1\pi$ and $CC\nu_\mu$ Other categories. Figures taken from [193].	101
3070	6.4	The reconstructed neutrino energy, as defined by Equation 6.2 and Equation 6.3, for the $1R\mu$ -like, $1Re$ -like and $CC1\pi^+$ -like samples. Asimov A oscillation parameter sets are assumed (given in Table 2.2). These samples are the FHC mode samples. For ease of viewing, the $1R\mu$ sample only shows the $0. \leq E_\nu^{rec} < 3.0\text{GeV}$ but the binning extends to 30.0GeV	104
3075	6.5	The distribution of the angle between the neutrino beam direction and the reconstructed final state lepton, for the FHC $1Re$ -like sample. The distribution is broken down by neutrino interaction mode into charged current (left) and neutral current (right) components. Asimov A oscillation parameter sets are assumed (given in Table 2.2). DB: Is this needed? If so, a COLZ is required	106
3081	6.6	The total uncertainty evaluated on the near detector ν_μ flux prediction constrained by the replica-target data, illustrated as a function of neutrino energy. The solid(dashed) line indicates the uncertainty used within this analysis(the T2K 2018 analysis). The solid histogram indicates the neutrino flux as a function of energy. Figure taken from [199].	108

- 3086 6.7 The prediction neutrino energy distribution for subGeV atmospheric
 3087 and beam samples, given for muon-like samples FHC+RHC 1R μ beam
 3088 samples compared to the subGeV μ -like 0+1 decay electrons (d.e.) at-
 3089 mospheric samples, electron-like 0d.e. samples FHC+RHC 1Re beam
 3090 samples compared to the subGeV e -like 1d.e. sample, and electron-like
 3091 1d.e. sample FHC1Re1de beam sample compared to the subGeV e -like
 3092 1d.e. atmospheric sample. 113
- 3093 6.8 The interaction mode contribution of each sample given as a fraction
 3094 of the total event rate in that sample. All systematic dials are set to
 3095 their nominal values and the Asimov A oscillation parameters are as-
 3096 sumed. The Charged Current (CC) modes are broken into quasi-elastic
 3097 (QE), meson exchange (2p2h), resonant charged pion production ($1\pi^\pm$),
 3098 multi-pion production ($M\pi$), and other interaction categories. Neutral
 3099 Current (NC) interaction modes are given in interaction mode cate-
 3100 gories: π^0 production, resonant charged pion production, multi-pion
 3101 production, and others. 114
- 3102 6.9 Down-going atmospheric subGeV single-ring samples comparing the
 3103 mean and error of the pre-fit and post-fit Monte Carlo predictions in
 3104 red and blue, respectively. The magenta histogram illustrates the Monte
 3105 Carlo prediction using the generated dial values. The black points illus-
 3106 trate the down-going data with statistical errors given. The mean and
 3107 errors of the Monte Carlo predictions are calculated by the techniques
 3108 documented in subsection 4.3.4. The cross-section and atmospheric flux
 3109 parameters are either thrown from their pre-fit uncertainties (denoted
 3110 pre-fit band), or the cross section dial values are randomly sampled
 3111 from a MCMC chain whilst the atmospheric flux parameters are thrown
 3112 from their pre-fit distributions (denoted post-fit band). 117
- 3113 6.10 The ring counting parameter, as defined in Equation 6.6, for the subGeV
 3114 electron-like zero decay electron and multi-ring ν_e -like samples. 127
- 3115 6.11 The ring counting parameter, defined in Equation 6.6, as a function of
 3116 the number of reconstructed rings as found by the `fitQun` algorithm.
 3117 Left: true ν_μ events with only one muon above the Cherenkov threshold
 3118 in the final state. Right: true ν_μ events with one muon and at least one
 3119 other charged particle above the Cherenkov threshold in the final state. 128

3120	6.12 The χ^2 between the hybrid- π^0 Monte Carlo and data samples, as a function of smear (α) and shift (β) parameters, for events which have 1 π^0 final state topology. Left: Electron-muon separation PID parameter for events with $30 \geq E_{vis}(\text{MeV}) < 300$. Right: Electron- π^0 separation PID parameter for events with $30 \geq E_{vis}(\text{MeV}) < 300$	129
3121		
3122		
3123		
3124		
3125	6.13 The distribution of $\log(L_e/L_\mu)$ compared to $\log(L_e/L_\pi)$ for subGeV events with zero (top left), one (top right) or two (bottom) decay electrons. The correlation in the distribution is calculated as 0.997, 0.999 and 0.996, respectively.	130
3126		
3127		
3128		
3129	7.1 The density of the Earth given as a function of the radius, as given by the PREM model (Black), and the constant density four-layer approximation (Blue), as used in the official SK-only analysis.	134
3130		
3131		
3132	7.2 An “oscillogram” that depicts the $P(\nu_\mu \rightarrow \nu_e)$ oscillation probability as a function of neutrino energy and cosine of the zenith angle. The zenith angle is defined such that $\cos(\theta_Z) = 1.0$ represents neutrinos that travel from directly above the detector. The four-layer constant density PREM model approximation is used and Asimov A oscillation parameters are assumed (Table 2.2).	135
3133		
3134		
3135		
3136		
3137		
3138	7.3 The effect of δ_{CP} for atmospheric neutrinos given in terms of the neutrino energy and zenith angle. This oscillogram compares the $P(\nu_\mu \rightarrow \nu_e)$ oscillation probability for a CP conserving ($\delta_{CP} = 0.0$) and a CP violating ($\delta_{CP} = -1.601$) value taken from the Asimov A parameter set. The other oscillation parameters assume the Asimov A oscillation parameter set given in Table 2.2.	136
3139		
3140		
3141		
3142		
3143		

3144	7.4 An illustration of the matter-induced effects on the oscillation probability, given as a function of neutrino energy and zenith angle. The top row of panels gives the $P(\nu_e \rightarrow \nu_e)$ oscillation probability and the bottom row illustrates the $P(\bar{\nu}_e \rightarrow \bar{\nu}_e)$ oscillation probability. The left column highlights the oscillation probability in a vacuum, whereas the middle and right column represents the oscillation probabilities when the four-layer fixed density PREM model is assumed. All oscillation probabilities assume the “Asimov A” set given in Table 2.2, but importantly, the right column sets an inverted mass hierarchy. The “matter resonance” effects at $E_\nu \sim 5\text{GeV}$ can be seen in the $P(\nu_e \rightarrow \nu_e)$ for normal mass hierarchy and $P(\bar{\nu}_e \rightarrow \bar{\nu}_e)$ for inverted hierarchy.	137
3155	7.5 The oscillation probability for beam neutrino events given as a function of neutrino energy. All oscillation parameters assume the “Asimov A” set given in Table 2.2 unless otherwise stated. Each panel represents a change in one of the oscillation parameters whilst keeping the remaining parameters fixed.	138
3160	7.6 The number of electron-like events in the FHC and RHC operating mode of the beam, as a function of the oscillation probabilities. Both normal hierarchy (Solid) and inverse hierarchy (Dashed) values of Δm_{23}^2 are given.	139
3164	7.7 The oscillation probability $P(\nu_\mu \rightarrow \nu_e)$, given as a function of neutrino energy and zenith angle, which highlights an example of the “fast” oscillations in the sub-GeV upgoing region.	141
3167	7.8 Illustration of the averaging procedure for $N = 2$. The oscillation probabilities calculated on the finer left binning are averaged to obtain the oscillation probabilities in the coarser right binning. These averaged oscillation probabilities with the coarser binning are then applied to each event during the fit.	143
3172	7.9 Event rate of the SubGeV_elike_0dcy sample as a function of the number of sub-divisions per coarse bin. Each subplot represents the event rate of the sample at a different oscillation parameter set thrown from the PDG priors detailed in Table 2.1. The red line in each subplot represents the mean of the event rate over the different values of subdivisions for that particular oscillation parameter throw.	145

- | | | |
|------|---|-----|
| 3178 | 7.10 Variance of event rate for each atmospheric sample as a function of the number of sub-divisions per coarse bin. The solid red line indicates the 0.1% threshold and the dashed red line indicates the variance at a sub-division $N = 10$ | 146 |
| 3179 | | |
| 3180 | | |
| 3181 | | |
| 3182 | 7.11 Variance of sample likelihood, when compared to ‘Asimov data’ set at Asimov A, for each atmospheric sample as a function of the number of sub-divisions per coarse bin. The solid red line indicates the 0.1% threshold and the dashed red line is a graphical indication of the variance at a sub-division $N = 10$ | 147 |
| 3183 | | |
| 3184 | | |
| 3185 | | |
| 3186 | | |
| 3187 | 7.12 The oscillation probability, $P(\nu_\mu \rightarrow \nu_e)$ (top row) and $P(\nu_e \rightarrow \nu_e)$ (bottom row), given as a function of neutrino energy and zenith angle. The left column gives the “fine” binning used to calculate the oscillation probabilities and the right column illustrates the “coarse” binning used to reweight the Monte Carlo events. The fine binning choice is given with $N = 10$, which was determined to be below the threshold from Figure 7.10 and Figure 7.11. | 148 |
| 3188 | | |
| 3189 | | |
| 3190 | | |
| 3191 | | |
| 3192 | | |
| 3193 | | |
| 3194 | 7.13 The calculation time taken to both calculate the oscillation probabilities and fill the “coarse” oscillograms, following the technique given in section 7.2, for the CUDAProb3 and ProbGPU (Red) calculation engines. CUDAProb3 has both a GPU (Blue) and CPU (Black) implementation, where the CPU implementation is multithreaded. Therefore, 8-threads (solid) and 40-threads (dashed) configurations have been tested. Prob3, which is a CPU single-thread implementation has a mean step time of 1.142s. | 149 |
| 3195 | | |
| 3196 | | |
| 3197 | | |
| 3198 | | |
| 3199 | | |
| 3200 | | |
| 3201 | | |
| 3202 | 7.14 The oscillation probability, $P(\nu_\mu \rightarrow \nu_e)$ (top row) and $P(\nu_e \rightarrow \nu_e)$ (bottom row), given as a function of neutrino energy and zenith angle. The left column gives probabilities where the constant $Z/A = 0.5$ approximation which is used in the official SK-only analysis. The middle column gives the probabilities where $Z/A = [0.468, 0.498]$ values are used, as given in Table 7.1. The right column illustrates the difference in oscillation probability between the two different techniques. | 151 |
| 3203 | | |
| 3204 | | |
| 3205 | | |
| 3206 | | |
| 3207 | | |
| 3208 | | |

- 3209 7.15 The density of the Earth given as a function of the radius, as given by
3210 the PREM model (Black), the constant density four-layer approxima-
3211 tion (Blue), as used in the official SK-only analysis, and the quadratic
3212 approximation of the PREM model (Red). 152

3213 7.16 The oscillation probability, $P(\nu_\mu \rightarrow \nu_e)$ (top row) and $P(\nu_e \rightarrow \nu_e)$ (bot-
3214 tom row), given as a function of neutrino energy and zenith angle. The
3215 left column gives probabilities where the four-layer constant density ap-
3216 proximation is used. The middle column gives the probabilities where
3217 the density is integrated over the trajectory, using the quadratic PREM
3218 approximation, for each $\cos(\theta_Z)$ is used. The right column illustrates the
3219 difference in oscillation probability between the two different techniques. 154

3220 7.17 The oscillation probability, $P(\nu_\mu \rightarrow \nu_e)$ (top row) and $P(\nu_e \rightarrow \nu_e)$ (bot-
3221 tom row), given as a function of neutrino energy and zenith angle. The
3222 left column gives probabilities where a fixed production height of 25km
3223 is used. The middle column gives the probabilities where the produc-
3224 tion height is analytically averaged. The right column illustrates the
3225 difference in oscillation probability between the two different techniques. 158

List of Tables

3227	2.1	The 2018 Particle Data Group constraints of the oscillation parameters taken from [81]. The value of Δm_{23}^2 is given for both normal hierarchy (N.H.) and inverted hierarchy (I.H.) and $\sin^2(\theta_{23})$ is broken down by whether its value is below (Q1) or above (Q2) 0.5.	21
3231	2.2	Reference values of the neutrino oscillation parameters for two different oscillation parameter sets.	22
3233	3.1	The various SK periods and respective live-time. The SK-VI live-time is calculated until 1 st April 2022. SK-VII started during the writing of this thesis.	24
3236	3.2	The trigger thresholds and extended time windows saved around an event which were utilised throughout the SK-IV period. The exact thresholds can change and the values listed here represent the thresholds at the start and end of the SK-IV period.	33
3240	3.3	The threshold momentum and energy for a particle to generate Cherenkov light in ultrapure water, as calculated in Equation 3.2 in ultrapure water which has refractive index $n = 1.33$	34
3243	4.1	Jeffreys scale for strength of preference for two models A and B as a function of the calculated Bayes factor ($B_{AB} = B(A/B)$) between the two models [140]. The original scale is given in terms of $\log_{10}(B(A/B))$ but converted to linear scale for easy comparison throughout this thesis.	66
3247	6.1	The amount of data collected in each detector used within this analysis. The data collected at the near and far detector, for both neutrino beam (FHC) and antineutrino beam (RHC), is measured as the amount of protons on target (POT).	90
3251	6.2	The fully contained subGeV samples, defined as events with visible energy $E_{vis} < 1.33\text{GeV}$, used within this oscillation analysis.	93

3253 6.3	The fully contained multiGeV samples used within this oscillation analysis. Both the sample name and description are given.	95
3254		
3255 6.4	The purity of each atmospheric sample used within this analysis, broken down by charged current (CC) and neutral current (NC) interactions and which neutrino flavour interacted within the detector. Asimov A oscillation parameter sets are assumed (given in Table 2.2). Electron neutrino and antineutrino events are separated to illustrate the ability of the separation likelihood cuts used within the multiGeV and multiring sample selections.	96
3256		
3257		
3258		
3259		
3260		
3261		
3262 6.5	The reconstructed cosine zenith and lepton momentum binning assigned to the atmospheric samples. The “ $\cos(\theta_Z)$ Bins” column illustrates the number of bins uniformly distributed over the $-1.0 \leq \cos(\theta_Z) \leq 1.0$ region for fully and partially contained samples and $-1.0 \leq \cos(\theta_Z) \leq 0.0$ region for up- μ samples. DB: Does this belong in the appendix?	97
3263		
3264		
3265		
3266		
3267		
3268 6.6	The neutrino energy binning for the different neutrino flavours. “Right” sign indicates neutrinos in the FHC beam and antineutrinos in the RHC beam mode. “Wrong” sign indicates antineutrinos in the FHC beam and neutrinos in the RHC beam mode. The binning of the detector response is identical for the FHC and RHC modes as well as at ND280 and SK.	109
3269		
3270		
3271		
3272		
3273		
3274 6.7	List of cut variables that are included within the shift/smear fit documented in [197].	120
3275		
3276 6.8	Reconstructed event topology categories on which the SK detector systematics [197] are based.	120
3277		
3278 6.9	Sources of systematic errors specified within the grouped into the “calibration” systematics model.	123
3279		
3280 6.10	Reconstructed event topology categories on which the SK detector systematics are based	125
3281		
3282 7.1	Description of the four layers of the Earth invoked within the constant density approximation of the PREM model [212].	133
3283		

